

# New physically based sub-models for the cycle-simulation of spark-ignition engine

---

**Sjerić, Momir**

**Doctoral thesis / Disertacija**

**2014**

*Degree Grantor / Ustanova koja je dodijelila akademski / stručni stupanj:* **University of Zagreb, Faculty of Mechanical Engineering and Naval Architecture / Sveučilište u Zagrebu, Fakultet strojarstva i brodogradnje**

*Permanent link / Trajna poveznica:* <https://urn.nsk.hr/urn:nbn:hr:235:552575>

*Rights / Prava:* [In copyright](#)/[Zaštićeno autorskim pravom.](#)

*Download date / Datum preuzimanja:* **2024-12-19**

*Repository / Repozitorij:*

[Repository of Faculty of Mechanical Engineering and Naval Architecture University of Zagreb](#)





University of Zagreb  
FACULTY OF MECHANICAL ENGINEERING  
AND NAVAL ARCHITECTURE

Momir Sjerić

# **NEW PHYSICALLY BASED SUB-MODELS FOR THE CYCLE-SIMULATION OF SPARK-IGNITION ENGINE**

DOCTORAL THESIS

Zagreb, 2014



Sveučilište u Zagrebu  
FAKULTET STROJARSTVA I BRODOGRADNJE

Momir Sjerić

# **NOVI FIZIKALNI POD-MODELI SIMULACIJE RADNOG CIKLUSA OTTOVOG MOTORA**

DOKTORSKI RAD

Zagreb, 2014.



University of Zagreb  
FACULTY OF MECHANICAL ENGINEERING  
AND NAVAL ARCHITECTURE

Momir Sjerić

# **NEW PHYSICALLY BASED SUB-MODELS FOR THE CYCLE-SIMULATION OF SPARK-IGNITION ENGINE**

DOCTORAL THESIS

Supervisor:  
Darko Kozarac, PhD, assistant professor

Zagreb, 2014





Sveučilište u Zagrebu  
FAKULTET STROJARSTVA I BRODOGRADNJE

MOMIR SJERIĆ

# **NOVI FIZIKALNI POD-MODELI SIMULACIJE RADNOG CIKLUSA OTTOVOG MOTORA**

DOKTORSKI RAD

Mentor:  
Doc. dr. sc. Darko Kozarac

Zagreb, 2014.

## BIBLIOGRAPHY DATA

UDC	621.43.01
Keywords:	spark-ignition engine, combustion, cycle-simulation, turbulence, ignition, cycle-to-cycle variations
Scientific area:	Technical sciences
Scientific field:	Mechanical engineering
Institution:	Faculty of Mechanical Engineering and Naval Architecture (FMENA), University of Zagreb
Supervisor:	Darko Kozarac, PhD, assistant professor
Number of pages:	189
Number of figures:	88
Number of tables:	22
Number of references:	119
Date of public defense:	27 <sup>th</sup> November 2014
Committee members:	Zoran Lulić, PhD, full professor Darko Kozarac, PhD, assistant professor Neven Duić, PhD, full professor Daniel Rolph Schneider, PhD, associate professor Reinhard Tatschl, PhD, (AVL List GmbH, Graz)
Archive:	Faculty of Mechanical Engineering and Naval Architecture (FMENA), University of Zagreb, Croatia

## Acknowledgments

„The person who never made mistakes, never tried anything new.“

*Albert Einstein*

I would first like to express my gratitude to my supervisor Darko Kozarac, PhD, assistant professor, for the unselfish guidance and support during the research that resulted with this thesis. A number of our discussions were very useful contributing to the better understanding of particular phenomena related to internal combustion engines.

The research presented in this thesis was supported by the Ministry of Science, Education and Sports of the Republic of Croatia, and by AVL AST d.o.o. Croatia through the cooperation of the Chair of IC Engines and Motor Vehicles and AVL List GmbH. This support is gratefully appreciated.

I am also very thankful to the committee members, Professor Zoran Lulić, Professor Neven Duić, Professor Daniel Rolph Schneider, and Dr. Reinhard Tatschl (AVL List GmbH) for the time to review this thesis, and for giving valuable comments that improved the final shape of dissertation.

I would also like to thank my colleagues from the Chair of IC Engines and Motor Vehicles, Goran Šagi, Rudolf Tomić, Petar Ilinčić, Ante Vučetić, Mladen Božić, Ivan Taritaš, Krunoslav Ormuž and to professor Ivan Mahalec for creating a good working atmosphere at our department, as well as to colleagues from AVL List GmbH for the given support, advice and many discussions that always resulted with new ideas and that were realized and presented in this thesis. I am very thankful to the Combustion analysis Laboratory of University of California, Berkeley, where the experimental results presented in this thesis were measured within the postdoctoral research activities of Darko Kozarac where he was as a Fulbright scholar.

At the end, the special gratitude goes to my family and to my wife Aleksandra that always supported me during my study and research at the Faculty of Mechanical Engineering and Naval Architecture in Zagreb.

Momir Sjerić

Zagreb, November 2014

# Contents

Preface.....	v
Summary .....	vi
Prošireni sažetak.....	viii
List of Figures .....	xviii
List of Tables.....	xxiii
Nomenclature .....	xxiv
Abbreviations .....	xxvii
1. Introduction .....	1
1.1. Motivation .....	3
1.2. Overview of literature.....	5
1.3. Objective and hypotheses of research .....	8
1.4. Methodology and research plan.....	9
2. Turbulent flow and modeling .....	12
2.1. Single zone $k$ - $\varepsilon$ turbulence model - high pressure cycle.....	16
2.1.1. General equations of $k$ - $\varepsilon$ model.....	16
2.1.2. Background of the $k$ - $\varepsilon$ turbulence model for 0-D applications .....	17
2.1.3. Modification of $k$ and $\varepsilon$ differential equation for 0-D model .....	19
2.2. Two zone $k$ - $\varepsilon$ turbulence model.....	23
2.3. Single zone $k$ - $\varepsilon$ turbulence model – gas exchange .....	28
3. Fundamentals of spark ignition and modeling .....	32
3.1. Ignition modeling in multidimensional models.....	33
3.2. Background of Quasi-Dimensional Ignition Model .....	34
3.3. The electric circuit sub-model .....	34
3.4. Early flame kernel growth .....	37
3.5. Modeling of electric spark and spark gap flow .....	39
3.6. Modeling of spark plug geometry .....	42
3.7. Features of the developed quasi-dimensional ignition model .....	48
4. Fundamentals of combustion in SI engines and modeling.....	49
4.1. Background of quasi-dimensional fractal combustion model .....	50
4.2. Modification and extension of the quasi-dimensional fractal combustion model.....	56
4.2.1. Ignition delay and early flame kernel growth .....	57
4.2.2. Transition of laminar to turbulent flame .....	58
4.2.3. Combustion process with single and two zone turbulence model .....	60

5.	Validation of cycle-simulation results with 3-D CFD data.....	63
5.1.	Validation of single and two zone $k-\varepsilon$ turbulence model.....	66
5.2.	Validation of full cycle $k-\varepsilon$ turbulence model .....	81
5.3.	Validation of developed QDIM and modified transition time from laminar to fully developed turbulent flame .....	90
5.3.1.	Quantitative analysis of the early combustion phase .....	101
5.3.2.	Specific results of developed QDIM.....	105
5.4.	Parameterization of turbulence and combustion model constants.....	112
5.4.1.	Parameterization of turbulence model constants.....	113
5.4.2.	Parameterization of upper limit of fractal dimension.....	115
5.5.	Optimization of turbulence model constants towards the single set of constants ...	120
5.5.1.	Optimization algorithm and definition of objective function.....	121
5.5.2.	Optimization results .....	122
5.6.	Application of single sets of constants .....	127
5.7.	Overview of validation with 3-D CFD results.....	132
6.	Validation of cycle-simulation model with the experimental data .....	134
6.1.	Cycle-to-cycle variations, background and modeling .....	134
6.2.	Modeling of CCV using cycle-simulation model.....	136
6.2.1.	Experimental setup.....	137
6.2.2.	Engine operating conditions and data processing .....	139
6.2.3.	Cycle-simulation model .....	140
6.3.	Cycle-averaged results.....	142
6.4.	Cycle-resolved results.....	144
6.5.	Influence of in-cylinder turbulence variation on CCV in combustion .....	156
6.6.	The variation of cross-flow direction at the spark plug.....	158
7.	General Overview and Conclusions .....	164
7.1.	Original scientific contribution.....	169
7.2.	Possible directions of further work.....	170
	References .....	172
	Carriculum Vitae in English.....	180
	Carriculum Vitae in Croatian .....	181
	APPENDIX .....	182

## **Preface**

This PhD thesis was written entirely by me as the summary of research work that was done during past 4 years (from 2010) within intensive cooperation of the Chair of IC Engines and Motor Vehicles with AVL List GmbH. A number of comprehensive and detail reports that were internally exchanged, every few months, were very helpful for the final dissertation shape.

All new ideas and improvements of the simulation model presented in this thesis are originally mine, and are defined by using the knowledge gained at the Faculty of Mechanical Engineering and Naval Architecture (during the undergraduate, graduate and postgraduate study), by using the specified literature and insights obtained from the attendance of international conferences related to the internal combustion engines and automotive engineering. The developed sub-models for turbulence, ignition and combustion are integrated into the development version of the cycle-simulation model of AVL BOOST and will be available in the commercial version of this software in future.

Momir Sjerić  
Zagreb, November 2014

## Summary

The research and study presented in this thesis are related to the modeling of turbulence, ignition and combustion phenomena of the cycle-simulation of SI engines. The developed sub-models for the turbulence, ignition and combustion process of SI engine are integrated into the cycle-simulation code AVL BOOST and the cycle-simulation results of several SI engines are compared with the available 3-D CFD and experimental data.

Modeling of the in-cylinder turbulence was performed with the single and two zone  $k$ - $\varepsilon$  turbulence model applicable to the 0-D approach. First, the single zone  $k$ - $\varepsilon$  turbulence model was developed and applied during the high pressure cycle with initial results of the in-cylinder turbulence at the intake valve closure specified from the 3-D CFD results. A developed two zone turbulence model was applied during the combustion period with the cylinder mixture divided into a burned and unburned zone. The calculation of combustion process was performed using the quasi-dimensional combustion model based on the fractal theory. The application of the two zone turbulence model, with unburned zone turbulence quantities used for the definition of flame front propagation properties showed significantly better, easier and physically more accurate prediction of the combustion process of SI engine at different engine operating conditions. To eliminate the model dependency on the initial conditions that had to be specified either from 3-D CFD or from the experimental data, the full  $k$ - $\varepsilon$  turbulence model for the entire engine cycle was developed. In order to avoid the manual tuning of ignition delay and the transition from laminar to fully developed turbulent flame from one operating point to another, the new quasi-dimensional ignition model was developed and a modified calculation of transition time was proposed and applied in the fractal combustion model. After that, the parameterization of the turbulence model constants and the parameterization of the upper limit of fractal dimension are introduced into the cycle-simulation model. In order to find a single set of turbulence model constants for one engine, an optimization process for calculation of model constants was applied. The validation of the cycle-simulation model that had a single set of constants related to turbulence and combustion sub-models of one engine showed a good agreement with the 3-D CFD results at several different operating conditions of SI engine.

The modeling of cycle-to-cycle variations (CCV) in combustion that occur in SI engine was performed by random variation of intake turbulence model parameter that was set to follow the Gaussian distribution around the mean value. The cycle-simulation model was also extended so that the random variation of flow angle at the spark plug location from cycle-

to-cycle can be considered. The cycle-simulation results obtained with the single set of constants and with the variation of in-cylinder turbulence level and flow angle showed very good agreement with the experimental data of Waukesha Cooperative Fuel Research (CFR) F4 engine at considered operating points that represent low and high CCV in combustion. The presented cycle-simulation model including the developed sub-models for modeling of turbulence, ignition and combustion represents simple, fast and well-promising solution for modeling of engine output performances by using a simulation of mean cycle or by using CCV if necessary.

**Keywords:** spark-ignition engine, combustion, cycle-simulation, turbulence, ignition, cycle-to-cycle variations



## Prošireni sažetak

Iako je sve više osobnih vozila pogonjenih elektromotorima i hibridnim sustavima, motori s unutarnjim izgaranjem i dalje imaju glavnu ulogu u proizvodnji mehaničkog rada potrebnog za pogon različitih vozila. Zbog sve strožih zakonskih propisa u pogledu smanjenja emisija štetnih ispušnih plinova primjenjuju se suvremeni sustavi prednabijanja i izravnog ubrizgavanja goriva s ciljem smanjenja potrošnje goriva odnosno smanjenja emisije CO<sub>2</sub>, kao i optimizacija radnih parametara Ottovih motora.

Zbog visoke cijene eksperimentalnih ispitivanja na motorima s unutarnjim izgaranjem te zbog naglog razvoja računalne snage kao logično i ekonomski prihvatljivo rješenje nameće se potreba za razvojem i korištenjem numeričkih simulacija. Prema stupnju složenosti i razini detalja korištenih pri opisu pojedinih fizikalnih pojava, numeričke simulacije u području motora s unutarnjim izgaranjem se mogu podijeliti na tri osnovne skupine:

- 1) simulacijski modeli temeljeni na metodi konačnih volumena (CFD),
- 2) simulacijski modeli radnog ciklusa temeljeni na 1-D/0-D pristupu,
- 3) simulacijski modeli u stvarnom vremenu tzv. *real-time* modeli.

Predmet ovog istraživanja su simulacijski modeli radnog ciklusa temeljeni na 1-D/0-D pristupu. Prednost ove vrste numeričkih simulacija rada motora s unutarnjim izgaranjem je mogućnost simulacije rada cjelokupnog sustava motora (uključujući usisne i ispušne sustave) uz dovoljnu razinu detalja u opisu fizikalnih procesa, a unutar prihvatljivog vremenskog okvira potrebnog za proračun. U simulacijskim modelima radnog ciklusa proračun strujanja kroz usisne i ispušne cijevi motora s unutarnjim izgaranjem provodi se metodom konačnih volumena pri čemu se diskretizacija provodi samo u uzdužnom smjeru cijevi, dok se termodinamičke značajke u cilindru motora računaju pomoću termodinamičkog pristupa primjenom jednadžbe očuvanja mase i prvog glavnog stavka termodinamike. To podrazumijeva da se prostorna diskretizacija cilindra motora ne provodi, a promjene pojedinih fizikalnih svojstava u cilindru motora računaju se kao funkcije vremena. Budući da se ne primjenjuje prostorna diskretizacija cilindra, simulacijski modeli temeljeni na ovakvom opisu se nazivaju bezdimenzijski (0-D) ili termodinamički modeli. Za izračun brzine izgaranja u 0-D modelima najčešće se koriste tzv. kvazidimenzijski modeli izgaranja. Kvizidimenzijski modeli izgaranja su pod-grupa 0-D modela jer se za proračun stanja u cilindru motora koriste osnovne termodinamičke jednadžbe, dok proračun brzine izgaranja uključuje geometrijski utjecaj, npr. pri izgaranju u Ottovom motoru slobodna ploha plamena ovisi o geometriji prostora izgaranja, položaju svjećice, itd. Zbog veće razine detalja koji mogu biti obuhvaćeni

prilikom proračuna veličina stanja u cilindru motora za vrijeme izgaranja, kvazidimenzijski modeli izgaranja postaju sve popularniji u simulacijama radnih ciklusa.

Početak izgaranja u Ottovim motorima definiran je trenutkom preskakanja iskre između elektroda svjeće. Izbojem električne iskre u smjesu goriva i zraka koja se nalazi između elektroda svjeće dolazi do brzog stvaranja jezgre plamena koja se počinje širiti i napredovati kroz prostor izgaranja. U početnoj fazi izgaranja, dok je polumjer jezgre plamena manji od 5 - 6 mm, polje strujanja u području svjeće uzrokuje pomicanje središta jezgre plamena u odnosu na početni položaj između elektroda svjeće. Istovremeno, slobodna ploha plamena, budući da se nalazi u polju turbulentnog strujanja, postaje sve više deformirana i naborana uslijed utjecaja turbulentnih vrtloga različitih veličina i intenziteta, što značajno utječe na površinu slobodne plohe plamena kojom se zahvaća svježa smjesa goriva i zraka, a time određuje i brzina izgaranja. Zbog toga je modeliranje turbulencije glavni preduvjet za detaljan proračun cjelokupnog procesa izgaranja u Ottovom motoru.

U ovom radu predstavljeni su novi fizikalni pod-modeli za opis turbulencije, stvaranja jezgre plamena i izgaranja u Ottovom motoru. Rezultati simulacija radnog ciklusa Ottovog motora uspoređeni su s dostupnim rezultatima iz 3-D CFD proračuna na nekoliko različitih Ottovih motora i pri različitim radnim parametrima motora. Za modeliranje cikličkih varijacija u izgaranju Ottovog motora predložena je nasumična varijacija produkcijske konstante turbulencije za vrijeme usisa i kuta nastrojavanja na svjećici od ciklusa do ciklusa. Uz zanemarenje prostorne nehomogenosti sastava smjese i ostalih parametara koji mogu uzrokovati cikličke varijacije u izgaranju, predloženi model radnog ciklusa Ottovog motora za simulaciju cikličkih varijacija predstavlja jednostavno, vrlo brzo i efikasno rješenje, pri čemu su rezultati statističke analize vrlo blizu eksperimentalnim rezultatima.

## Ciljevi i hipoteza istraživanja

U okviru ovog doktorskog rada može se definirati nekoliko ciljeva:

- bolje razumijevanje fizikalnih procesa koji se odvijaju u cilindru motora;
- razvoj jednozonskog i dvozonskog  $k-\varepsilon$  modela turbulencije za primjenu u bezdimenzijskim (0-D) modelima;
- razvoj novog pod-modela za proračun stvaranja ranog razvoja jezgre plamena u Ottovom motoru primjenjivog u bezdimenzijskim (0-D) modelima;
- poboljšanje modifikacijom postojećeg kvazidimenzijskog modela izgaranja;

- ugradnja razvijenih pod-modela za opis turbulencije, stvaranje jezgre plamena i izgaranja u simulacijski model radnog ciklusa Ottovog motora;
- primjena razvijenih pod-modela u simulacijama cikličkih varijacija u izgaranju u Ottovim motorima.

Hipoteza ovog doktorskog rada temelji se na pretpostavci da je moguće razviti pod-modele za opisivanje turbulencije, stvaranja jezgre plamena i izgaranja, a koji će biti ugrađeni u simulacijski model radnog ciklusa Ottovog motora. Njihova primjena u simulacijama radnog ciklusa Ottovog motora doprinijeti će boljem predviđanju pojedinih fizikalnih procesa, a čiji će rezultati biti podudarni s 3-D CFD i eksperimentalnim rezultatima. Na taj način omogućit će se vrlo brza, jednostavna i zadovoljavajuće točna analiza utjecajnih parametara na rad Ottovog motora.

## Opis turbulentnog strujanja i utjecaj na izgaranje u Ottovim motorima

Prva znanstvena istraživanja u pogledu utjecaja turbulencije na strukturu plamena i brzinu izgaranja proveo je Damköhler prije više od 70 godina. Uveo je opće prihvaćenu teoriju da turbulentni vrtlozi koji su veći od debljine plamena uzrokuju deformaciju plamena u smjeru strujanja, dok manji vrtlozi povećavaju brzinu izmjene topline i mase unutar fronte plamena te utječu na lokalnu laminarnu brzinu izgaranja [118]. Prihvaćanjem ove teorije i nastojanjem za modeliranjem izgaranja Ottovih motora stvorila se potreba za modeliranjem turbulencije. Najrašireniji pristup koji se danas koristi za opisivanje turbulencije u većini inženjerskih problema temelji se na primjeni vremenski osrednjenih Navier-Stokesovih jednadžbi (engl. *Reynolds Averaged Navier-Stokes - RANS*). Kolmogorov je razvio prvi model turbulencije s dvije jednadžbe ( $k-\omega$  model) početkom 40-ih godina prošlog stoljeća, a zbog nelinearnih diferencijalnih jednadžbi i nedostupnosti računala nije se primjenjivao do 70-ih godina prošlog stoljeća [6]. Lander i Spalding su 1972. godine razvili  $k-\varepsilon$  model turbulencije kao jedan od danas najčešće korištenih modela turbulencije s dvije diferencijalne jednadžbe [6, 7]. Početkom 80-ih godina započela je primjena  $k-\varepsilon$  modela turbulencije na modeliranje procesa u motorima s unutarnjim izgaranjem pri čemu su napravljene određene modifikacije diferencijalnih jednadžbi. Morel i Mansour [8] proširili su disipacijsku diferencijalnu jednadžbu kako bi se postigla bolja podudarnost s eksperimentalnim rezultatima turbulentnih duljina u slučaju vrlo brze kompresije u cilindru motora. Takav model poslužio je kao temelj za daljnja istraživanja u području modeliranja turbulencije u motorima s unutarnjim izgaranjem. Uz pretpostavku homogene i izotropne turbulencije u

cilindru motora pojavili su se prvi modeli turbulencije primijenjivi za simulacije radnog ciklusa Ottovog motora. Polous i Heywood [9] koristili su algebarski  $\varepsilon$  model u analizi utjecaja geometrije cilindra na razinu turbulencije. Tabaczynski [10] je primijenio algebarski  $\varepsilon$  model i potpuni  $k$ - $\varepsilon$  model turbulencije na različitim geometrijama cilindra. Rezultati provedene analize su pokazali da primijenjeni modeli turbulencije različito predviđaju razinu turbulencije te da geometrija prostora izgaranja ima značajan utjecaj na njenu veličinu. Razvojem višezonskih modela izgaranja pojavljuju se dvozonski modeli turbulencije [5]. Agarwal i dr. [11] pokazali su različite formulacije jednozonskih i dvozonskih modela turbulencije (algebarski  $\varepsilon$  model i  $k$ - $\varepsilon$  model turbulencije) koji su primijenjeni zajedno s kvazidimenzijskim modelom izgaranja Ottovog motora [12, 13]. U navedenom radu parametri modela turbulencije prilagođeni su tako da se simulacijski profil tlaka u cilindru motora što bolje podudara s profilom tlaka dobivenog mjerenjem, što je isti pristup kao i u većini novijih znanstvenih radova. Watanabe i dr. [14] razvili su 2010. god. kvazidimenzijski model izgaranja koji se može primijeniti na Ottove motore s izravnim ubrizgavanjem goriva u cilindar. Pri tome su koristili  $K$ - $k$  model turbulencije [5] koji je prilagođen i validiran za tzv. "tumble" strujanje u cilindru motora, a rezultati simulacije radnog ciklusa uspoređeni su s 3-D CFD rezultatima. Nedostatak ovakvog modela turbulencije [14] je u tome što sadrži ukupno 6 konstanti i prilagođen je samo za "tumble" strujanje u cilindru motora koje je karakteristično za klinasti prostor izgaranja.

## Izgaranje u Ottovim motorima

Fizikalni modeli izgaranja koji razmatraju strukturu plamena postali su vrlo popularni u simulacijama radnog ciklusa Ottovog motora jer uzimaju u obzir stvarno širenje fronte plamena unutar cilindra motora i obično se nazivaju kvazidimenzijskim modelima izgaranja [11-14]. Početkom 70-ih godina, u isto vrijeme kada se pojavljuje  $k$ - $\varepsilon$  model turbulencije, razvija se prvi kvazidimenzijski model izgaranja [15] koji je nazvan BK (Blizard-Keck) model. Razmatran je utjecaj intenziteta turbulencije, laminarne brzine širenja plamena i duljine turbulentnih vrtloga na brzinu izgaranja, uz pretpostavku da veliki vrtlozi ispred zone plamena zahvaćaju svježju smjesu, dok mali vrtlozi u zoni plamena sudjeluju u izgaranju laminarnom brzinom. U novije doba BK model izgaranja u literaturi se susreće kao model turbulentnog zahvaćanja (engl. *Turbulent Entrainment Model* [16]). Gouldin [17, 119] je 1987. godine predložio model izgaranja koji se temelji na konceptu fraktalne teorije opisa geometrije plamena, a njegova primjena u kvazidimenzijskim modelima izgaranja susreće se

početkom 90-ih godina. Provedeno je nekoliko istraživanja u pogledu definiranja fraktalne karakteristike (fraktalne dimenzije) turbulentnog plamena u Ottovim motorima, a rezultati su sažeti u [18]. Pokazano je da vrijednost fraktalne dimenzije ovisi o omjeru intenziteta turbulencije i laminarne brzine širenja plamena, a usvojen je heuristički pristup za definiranje njene dimenzije [19]. Poznato je da su rješenja simulacija radnog ciklusa motora prilično osjetljiva na ulazne parametre [21, 22], koji se definiraju od strane korisnika, pa je njihov broj potrebno svesti na minimum, ali istovremeno paziti da se obuhvati što više detalja fizikalnih procesa. Perini i dr. [20] su 2010. godine razvili kvazidimenzijski model izgaranja kojeg su primijenili na simulaciju CFR motora pogonjenog vodikom, metanom i njihovim mješavinama. Model izgaranja baziran je na BK modelu pri čemu je turbulentna brzina izgaranja određena fraktalnom teorijom. Detaljno modeliranje turbulencije u cilindru motora nije provedeno, a intenzitet turbulencije je aproksimiran pomoću specifične korelacije koja uključuje srednju brzinu klipa. U zaključku rada navedeno je da se točnost kvazidimenzijskog modela izgaranja može poboljšati uvođenjem dodatnih pod-modela za modeliranje stvaranja jezgre plamena i detaljnim modeliranjem turbulencije.

Proces izgaranja u Ottovim motorima započinje trenutkom preskakanja iskre između elektroda svjećice, pri čemu se vrlo brzo formira jezgra plamena jer je električna energija iskre mnogo veća od kritične vrijednosti energije potrebne za početak izgaranja. Ballal i Lafevbre [23] istraživali su efekte probojnog napona, duljine trajanja električne iskre, raspodjele energije, razmaka između elektrodi, brzine strujanja i geometrije elektrode na proces formiranja jezgre plamena. Detaljno eksperimentalno istraživanje rane faze širenja jezgre plamena, pri različitim brzinama strujanja i omjerima goriva i zraka proveo je Mensour [24]. Pischinger i Heywood [25] predložili su jednodimenzijski model formiranja jezgre plamena koji uključuje u obzir gubitke topline prema elektrodama svjećice kao i konvektivno udaljavanje jezgre plamena od inicijalnog položaja. U spomenutim istraživanjima pokazano je da električne veličine u sustavu paljenja, razmak između elektrodi, prijelaz topline i brzine strujanja oko svjećice imaju značajan utjecaj na razvoj jezgre plamena u Ottovom motoru.

Razvojem računalne snage dolazi do razvoja složenijih 3-D modela za opis formiranja jezgre plamena i njezin rast [26, 27], pa su tako Duclos i Colin [28] 2001. godine razvili AKTIM model (engl. *Arc and Kernel Tracking Ignition Model*) koji se može susresti u vodećim komercijalnim 3-D CFD programima, a koristi se za simulaciju izgaranja u Ottovim motorima. Model formiranja jezgre plamena uzima u obzir efekte sekundarnog strujnog kruga, geometrije elektrodi svjećice, brzine strujanja u području svjećice i prijelaza topline s jezgre plamena na elektrode svjećice. Jezgra plamena opisana je česticama određene mase u

području oko i između elektrodi koje imaju interakciju s poljem strujanja, a svaka od njih predstavlja potencijalnu jezgru plamena. U kvazidimenzijskim modelima izgaranja koji se primjenjuju u današnjim simulacijama radnog ciklusa Ottovog motora preskakanje električne iskre i formiranje jezgre plamena najčešće se ne modelira, a proračun izgaranja započinje s već formiranom frontom plamena određene veličine [13]. Vrijeme kašnjenja paljenja, kao period od trenutka preskakanja iskre do početka izgaranja s frontom plamena određene veličine, modelira se usvajanjem vrijednosti da taj period traje 0,2 ms. Pri različitim uvjetima u cilindru motora, vrijeme kašnjenja paljenja može biti znatno drugačije od pretpostavljene vrijednosti od 0,2 ms, pa je u postojećem modelu izgaranja potrebno prilagoditi korisnički definiranu konstantu koja definira početak izgaranja te kako bi se rezultati simulacije radnog ciklusa mogli usporediti s eksperimentalnim ili 3-D CFD rezultatima.

Prilikom izgaranju u Ottovom motoru, čak i pri konstantnim radnim uvjetima (brzina vrtnje motora, tlak i temperatura usisa, sastav smjese, itd.) dolazi do varijacija u profilu izgaranja od jednog radnog ciklusa do drugog [35, 36]. Cikličke varijacije pri izgaranju u Ottovom motoru javljaju se kao posljedica nepotpunog miješanja goriva, zraka i zaostalih produkata izgaranja, lokaciji električne iskre i njenim karakteristikama izboja kroz mješavinu goriva i zraka te stohastičkoj prirodi polja strujanja i turbulencije u cilindru motora [74] koja oscilira od jednog do drugog radnog ciklusa. Stoga je opravdano upustiti se u razvoj pod-modela za opis turbulencije, stvaranje jezgre plamena i izgaranja u Ottovim motorima.

## Pregled doktorskog rada

U doktorskom radu opisan je razvoj, validacija i primjena 0-D pod-modela turbulencije, pod-modela stvaranja jezgre plamena i pod-modela procesa izgaranja u Ottovom motoru. Razvijeni pod-modeli za proračun turbulencije, stvaranja jezgre plamena i izgaranja su ugrađeni u simulacijski model radnog ciklusa Ottovog motora koji je dostupan u programu AVL BOOST.

Razvoj  $k-\varepsilon$  modela turbulencije, opisan u drugom poglavlju rada, sastoji se od definiranja jednozonskog modela koji je primjenjiv samo na visokotlačni dio radnog ciklusa, razvoja dvozonskog modela turbulencije za vrijeme izgaranja i razvoja jednozonskog modela turbulencije koji se može primijeniti na cjelokupni radni ciklus Ottovog motora. U svrhu validacije razvijenog pod-modela za opis turbulencije u cilindru motora korišteni su 3-D CFD rezultati za nekoliko Ottovih motora i njihovih radnih točaka pri različitim radnim uvjetima. Kako bi se rezultati turbulencije izračunati primjenom simulacijskog modela radnog ciklusa

Ottovog motora mogli usporediti s dostupnim 3-D CFD rezultatima, provedena je prilagodba novih korisnički definiranih konstanti koje su uvedene u razvijeni  $k-\varepsilon$  model turbulencije.

S ciljem poboljšanja točnosti proračuna u pogledu zakašnjenja paljenja i uklanjanjem potrebe za prilagođavanje korisnički definirane konstante koja definira početak izgaranja, u trećem poglavlju rada opisan je razvoj novog fizikalnog pod-modela za formiranje jezgre plamena primjenjiv u 0-D proračunima. Budući da pod-model za proračun stvaranja jezgre plamena uzima u obzir utjecaj geometrije elektroda svjećice na razvoj jezgre plamena, nazvan je kvazidimenzijским modelom stvaranja jezgre plamena, a temelji se na AKTIM modelu koji je dostupan u 3-D CFD proračunima za proračun izgaranja u Ottovim motorima. Razvijeni pod-model za proračun stvaranja jezgre plamena uključuje utjecaj sekundarnog strujnog kruga u sustavu paljenja Ottovog motora, prijelaza topline između jezgre plamena i elektrodi svjećice, te utjecaj lokalne brzine strujanja na razvoj jezgre plamena.

U četvrtom poglavlju rada opisano je proširenje kvazidimenzijskog modela izgaranja koji se temelji na primjeni fraktalne teorije. Proširenje kvazidimenzijskog modela izgaranja uključuje integraciju razvijenog pod-modela za proračun stvaranja jezgre plamena, promjenu izračuna za period prijelaza plamena iz laminarnog u potpuno razvijeni turbulentni plamen i primjenu dvozonskog modela turbulencije pri čemu se turbulentne veličine neizgorjele zone koriste za proračun procesa turbulentnog izgaranja. U svrhu validacije proširenog kvazidimenzijskog modela izgaranja korišteni su 3-D CFD rezultati izgaranja pri čemu su konstante proširenog kvazidimenzijskog modela izgaranja prilagođene kako bi se postigla što bolja podudarnost s 3-D CFD rezultatima.

Cjelokupna validacija razvijenih pod-modela, parametrizacija konstanti modela turbulencije i maksimalne vrijednosti fraktalne dimenzije te optimizacija konstanti modela turbulencije prikazana je i opisana u petom poglavlju rada. Validacija pod-modela sastoji se od usporedbe rezultata jednozonskog i dvozonskog modela turbulencije uključujući analizu njihovog utjecaja na proračun izgaranja, validacije jednozonskog  $k-\varepsilon$  modela turbulencije koji se može primijeniti za vrijeme cjelokupnog radnog ciklusa Ottovog motora i validacije proširenog kvazidimenzijskog modela izgaranja. Na osnovu vrijednosti konstanti turbulencije i maksimalne vrijednosti fraktalne dimenzije koje su prilagođene kako bi se postigla što bolja podudarnost rezultata simulacije radnog ciklusa s 3-D CFD rezultatima, definiran je parametarski model konstanti turbulencije i maksimalne vrijednosti fraktalne dimenzije. U svrhu primjene jedinstvenog skupa konstanti za čitavo radno područje Ottovog motora, provedena je optimizacija konstanti pod-modela turbulencije te su dobivena rješenja optimizacije primjenjena zajedno s predloženim izračunom maksimalne vrijednosti fraktalne

dimenzije. Primjenom jedinstvenog skupa konstanti (5 konstanti pod-modela turbulencije, 2 konstante pod-modela izgaranja i 2 parametra pod-modela za stvaranje jezgre plamena) za radno područje pojedinog motora postignuti su simulacijski rezultati koji se vrlo dobro poklapaju s rezultatima 3-D CFD proračuna.

U zadnjem dijelu doktorskog rada, odnosno u šestom poglavlju, provedena je validacija razvijenih pod-modela pri čemu su rezultati simulacije radnog ciklusa uspoređeni s eksperimentalnim rezultatima izgaranja u Ottovom motoru. Kako bi se provela simulacija cikličkih varijacija pri izgaranju u Ottovom motoru, primijenjena je nasumična varijacija produkcijske konstante turbulencije za vrijeme usisa i varijacija kuta nastrojavanja na svjećici. Konstante razvijenih pod-modela turbulencije, stvaranja jezgre plamena i izgaranja prilagođene su usporedbom rezultata tzv. srednjeg ciklusa, dok su statistički rezultati srednjeg indiciranog tlaka (standardna devijacija i koeficijent varijacije) za nekoliko radnih točaka korišteni kako bi se prilagodila korisnički definirana konstanta kojom se modeliraju varijacije turbulencije, a time i izgaranja, u cilindru motora od jednog do drugog radnog ciklusa.

## Zaključak i doprinos rada

Razvojem jednozonskog  $k-\varepsilon$  modela turbulencije koji je primjenjen na visokotlačnom dijelu radnog ciklusa Ottovog motora moguće je postići rezultate ukupne turbulentne kinetičke energije u cilindru motora dobivene 0-D simulacijom, koji se dobro poklapaju s 3-D CFD rezultatima za različite radne uvjete motora. Pri tome je potrebno prilagoditi novu korisnički definiranu disipacijsku konstantu koja se kreće u rasponu od 2,00 do 2,55. U svrhu točnijeg proračuna izgaranja Ottovog motora, razvijen je dvozonski model turbulencije pri čemu je korišten pojednostavljeni pristup za proračun turbulentne kinetičke energije neizgorjele zone. Uz prilagodbu nove disipacijske konstante za neizgorjelu zonu koja se kreće u rasponu 3,00 do 7,50, moguće je postići rezultate turbulentne kinetičke energije neizgorjele zone koji se vrlo dobro poklapaju s 3-D CFD rezultatima, a predviđanje procesa izgaranja je znatno poboljšano. Kako bi se uklonila ovisnost jednozonskog modela primjenjenog na visokotlačni dio radnog ciklusa Ottovog motora o početnim vrijednostima turbulencije u cilindru motora, koji su korišteni iz 3-D CFD proračuna, jednozonski  $k-\varepsilon$  model turbulencije je proširen i na dio radnog ciklusa u kojem se obavlja izmjena radnog medija. Uvođenjem dvije nove konstante koje utječu na razvoj turbulentne kinetičke energije za vrijeme usisa moguće je postići 0-D rezultate turbulentne kinetičke energije koji se dobro poklapaju s 3-D CFD rezultatima, posebno tijekom procesa izgaranja. Analizom korisnički definiranih



konstanti za turbulenciju i izgaranje koje su bile prilagođene za svaku radnu točku pojedinog motora, predloženi su i primjenjeni parametarski modeli za konstante turbulencije i maksimalne vrijednosti fraktalne dimenzije. Na taj način omogućeno je da se jedinstvenim skupom konstanti za pojedini Ottov motor mogu postići zadovoljavajući rezultati izgaranja u radnom području motora.

U svrhu modeliranja cikličkih varijacija pri izgaranju u Ottovom motoru, pokazano je da varijacija produkcijske konstante za turbulenciju koja slijedi Gaussovu razdiobu oko zadane srednje vrijednosti i varijacija kuta nastrojavanja na svjećici daje vrlo dobro poklapanje 0-D rezultata u usporedbi s eksperimentalnim rezultatima CFR motora. Iako je turbulentno strujanje i izgaranje u Ottovom motoru uvijek prostornog karaktera, pokazano je da su razvijeni 0-D model turbulencije i kvazidimenzijski model stvaranja jezgre plamena i izgaranja dovoljno detaljni da mogu sa zadovoljavajućom točnošću opisati stvarne fizikalne procese koji se odvijaju u cilindru motora, a između ostalog i cikličke varijacije u izgaranju.

Istraživanje u pogledu modeliranja turbulencije, stvaranja jezgre plamena i izgaranja Ottovog motora, predstavljeno u ovom radu, rezultiralo je sljedećim znanstvenim doprinosima:

- razvoj novog jednozonskog i dvozonskog  $k-\varepsilon$  pod-modela turbulencije kojima se mogu postići simulacijski rezultati bliski rezultatima 3-D CFD proračuna, posebno za vrijeme izgaranja kada turbulencija ima značajan utjecaj na proces i tijek izgaranja;
- pojednostavljen pristup modeliranju turbulencije neizgorjele zone pri čemu je znatno poboljšano predviđanje procesa izgaranja u Ottovom motoru pri različitim radnim uvjetima motora;
- razvoj novog kvazidimenzijskog modela za proračun stvaranja jezgre plamena u Ottovom motoru koji je sposoban predvidjeti utjecaje različitih radnih parametara motora i geometrije svjećice na fazu ranog razvoja fronte plamena uključujući i utjecaje višestrukih proboja električne iskre i potpunog izostanka paljenja;
- definicija parametarskog modela za konstante razvijenog pod-modela turbulencije te parametarske funkcije za opis maksimalne vrijednosti fraktalne dimenzije. Na taj način moguće je pronaći jedinstveni skup od 9 konstanti koje se mogu primjeniti na simulaciju radnog ciklusa Ottovog motora, a čiji rezultati su usporedivi s 3-D CFD ili eksperimentalnim rezultatima;
- mogućnost simulacija cikličkih varijacija pri izgaranju u Ottovom motoru uz varijaciju ukupne razine turbulencije u cilindru motora i/ili kuta nastrojavanja na svjećici od ciklusa

do ciklusa. Na taj način moguće je postići simulacijske rezultate koji se vrlo dobro poklapaju s eksperimentalnim podacima.

- mogućnost analize efekata različitih parametara motora kao što su geometrija elektroda svjećice, raspoloživa energija sustava paljenja, prijelaza topline na svjećici, geometrija prostora izgaranja, na karakteristike motora uz prisutnost cikličkih varijacija pri izgaranju;
- bolji uvjeti za točno modeliranje detonantnog izgaranja i emisije ispušnih plinova uz prisutnost cikličkih varijacija u strujanju i izgaranju Ottovog motora.

**Ključne riječi:** Ottov motor, izgaranje, simulacija radnog ciklusa, turbulencija, zapaljenje, cikličke varijacije

## List of Figures

Figure 1. Illustration of 1-D/0-D approach of the cycle-simulation model; 1-D discretisation of intake and exhaust pipe, 0-D (thermodynamic) model of cylinder with the specification of main sub-models. ....	1
Figure 2. Example of 3-D CFD simulation model in AVL FIRE (left) and reduced cycle-simulation model in AVL BOOST (right). ....	3
Figure 3. Tuning of turbulence model constants in the original cycle-simulation model (full load case at engine speed of 2000 rpm). ....	4
Figure 4. Examples of turbulent flow in daily life [44, 45]. ....	13
Figure 5. Typical point velocity measurement in steady (left) and unsteady (right) turbulent flow field. ....	13
Figure 6. Turbulence energy spectrum and energy cascade phenomenon. ....	15
Figure 7. Illustration of axial cylinder deformation caused by piston motion (flat geometry of cylinder head and piston). ....	18
Figure 8. Example of turbulent kinetic energy (a) and its dissipation rate (b) during the high pressure cycle; recalculated dissipation rate profiles (black lines in bottom diagram) are defined from the 3-D CFD results of the turbulent kinetic energy (dashed black line in upper diagram). ....	21
Figure 9. Qualitative profiles of turbulent kinetic energies (total and unburned zone) calculated by 3D-CFD simulation during combustion. ....	24
Figure 10. Example of turbulent kinetic energy (a) and dissipation rate (b) of unburned zone during combustion. ....	27
Figure 11. Illustration of the engine intake process and turbulent eddy generated by the strong flow over the intake valve. ....	30
Figure 12. Ellipsoidal velocity distribution of in-cylinder tumble flow defined in [14]. ....	31
Figure 13. Visualization of the early flame kernel growth from the experiment [55] indicating the effects of local bulk flow and turbulence in the vicinity of the spark plug. ....	32
Figure 14. Simplified electric scheme of an engine ignition system with the spark plug. ....	34
Figure 15. Breakdown voltage as a function of in-cylinder pressure and temperature for different gap distances ( $d = 0.6 - 1.2$ mm). ....	35
Figure 16. The spark cross flow and the electric spark represented by Lagrangian particles. ..	39
Figure 17. Elongation of electric spark due to the flow velocity: photograph of curved spark channel [71] at flow velocity 7.7 m/s (left), description of spark length by the set of Lagrangian particles. ....	42
Figure 18. Description of the spark plug geometry in 0-D approach. ....	43
Figure 19. Illustration of incremental rectangular (a) and circular (b) surface area of the spark plug. ....	43

Figure 20. Illustration of early flame kernel growth; the kernel center is moved from its initial position due to the cross-flow velocity $U_{av}$ .	45
Figure 21. Effects of the spark plug geometry on the flame kernel development in the static field - Schlieren photographs at 3 ms after spark discharge; initial pressure is 1.6 bar and $\lambda=1$ [71].	47
Figure 22. Examples of the spark plug designs that can be considered with the developed quasi-dimensional ignition model: a) the standard spark plug design with single side electrode; b) spark plug with the central thin electrode.	47
Figure 23. Description of three phases of combustion process on normalized heat release curve (SOC – start of combustion, EOC – end of combustion).	49
Figure 24. Illustration of the wrinkled flame front segment of SI engine as a very thin layer that separates burned and unburned zone.	51
Figure 25. Example of typical Richardson plot to evaluate the fractal dimension $D_3$ [18].	52
Figure 26. Illustration of the free flame front surface propagation with respect to the crank angle, for the pent roof cylinder head and piston geometry [21].	55
Figure 27. Simplified geometries of the cylinder head and piston designs that can be calculated directly by AVL BOOST [86].	56
Figure 28. Integration of the newly developed QDIM with the quasi-dimensional fractal combustion model; SOC - start of combustion, EOK - end of kernel, EOC - end of combustion.	58
Figure 29. Qualitative progress of under-relaxation function for the simulation of transition time.	59
Figure 30. An example of calculated ratios of maximum to minimum integral length scale during the combustion (dashed gray line is calculated using the total in-cylinder turbulence, red solid line is defined using the unburned zone turbulence).	62
Figure 31. Intake and exhaust valve lift profiles of Engine 1 - 4.	64
Figure 32. Geometries of the considered SI engines; computational meshes are captured at TDC.	65
Figure 33. Comparison of total turbulent kinetic energy of the single zone model during the HPC (left) and results of total and unburned zone turbulent kinetic energy of the two zone model during the combustion (right); Engine 1.	68
Figure 34. Normalized heat release (left) and in-cylinder temperature (right) of Engine 1: single and two zone turbulence model.	70
Figure 35. Comparison of total turbulent kinetic energy of the single zone model during the HPC (left) and results of total and unburned zone turbulent kinetic energy of the two zone model during the combustion (right); Engine 2.	73
Figure 36. Normalized heat release (left) and in-cylinder temperature (right) of Engine 2: single and two zone turbulence model.	74
Figure 37. Comparison of total turbulent kinetic energy of the single zone model during the HPC (left) and results of total and unburned zone turbulent kinetic energy of the two zone model during the combustion (right); Engine 3.	76

Figure 38. Normalized heat release (left) and in-cylinder temperature (right) of Engine 3: single and two zone turbulence model.....	77
Figure 39. Comparison of total turbulent kinetic energy of the single zone model during the HPC (left) and results of total and unburned zone turbulent kinetic energy of the two zone model during the combustion (right); Engine 4. ....	79
Figure 40. Normalized heat release (left) and in-cylinder temperature (right) of Engine 4: single and two zone turbulence model.....	80
Figure 41. Total in-cylinder turbulent kinetic energy during the entire cycle of Engine 1 calculated by the full cycle turbulence model. ....	83
Figure 42. Total in-cylinder turbulent kinetic energy during the entire cycle of Engine 2 calculated by the full cycle turbulence model. ....	85
Figure 43. Total in-cylinder turbulent kinetic energy during the entire cycle of Engine 3 calculated by the full cycle turbulence model. ....	87
Figure 44. Total in-cylinder turbulent kinetic energy during the entire cycle of Engine 4 calculated by the full cycle turbulence model. ....	89
Figure 45. Geometry of the considered standard type of spark plug – marked dimensions are expressed in mm; figure a) y-z view, figure b) x-z view, figure c) NGK (DR8ES) standard type of the spark plug with 12 mm of shell diameter.....	91
Figure 46. Normalized heat release (left) and in-cylinder temperature (right) of Engine 1: modified fractal combustion model. ....	94
Figure 47. Normalized heat release (left) and in-cylinder temperature (right) of Engine 2: modified fractal combustion model. ....	96
Figure 48. Normalized heat release (left) and in-cylinder temperature (right) of Engine 3: two zone turbulence model and extended fractal combustion model.....	98
Figure 49. Normalized heat release (left) and in-cylinder temperature (right) of Engine 4: modified fractal combustion model. ....	100
Figure 50. Prediction of relative crank angle $\Delta\alpha_{0.1}$ at which the 0.1 % of mass is burned – comparison of 3-D CFD and 0-D simulation results. ....	101
Figure 51. Prediction of relative crank angle $\Delta\alpha_5$ at which the 5 % of mass is burned – comparison of 3-D CFD and 0-D simulation results. ....	103
Figure 52. Prediction of relative crank angle $\Delta\alpha_5$ at which the 5 % of mass is burned – the influence of ignition energy (top) and the flow angle at the spark plug (bottom) of Engine 1.....	104
Figure 53. Cycle-simulation result of electric spark length for considered operating points of Engine 1; SOI – start of ignition. ....	106
Figure 54. Visualization of the electric spark history of glow phase for Engine 1; green color of electric spark at 5500 rpm represents the sparks formed after new breakdown. Time between the electric spark profiles is 0.5 crank angle degrees. ....	108

Figure 55. Cycle-simulation result of the flame kernel radius $R_k$ , entrained spark plug surface area $S_e$ and visualization of the flame kernel at $6^\circ$ CA after SOI for all considered operating points of Engine 1. ....	109
Figure 56. Illustration of the flame kernel growth for all operating points of Engine 1 at specific times after spark onset. ....	111
Figure 57. The influence of intake $k$ production constant $S_{in}$ on engine speed. ....	113
Figure 58. The influence of intake $\varepsilon$ production constant $C_{in}$ on in-cylinder pressure at SHP - start of high pressure. ....	114
Figure 59. The values of fractal dimension during the combustion period of Engine 2. ....	116
Figure 60. Maximum values of the fractal dimension as a function of the ratio of turbulence intensity and laminar flame speed. ....	117
Figure 61. The parameterization of non-dimensional turbulent kinetic energy during the combustion period; the profile of non-dimensional turbulent kinetic energy is the same for all operating points of all engines. ....	120
Figure 62. Illustration of the objective function for optimization of turbulence model constants. ....	121
Figure 63. Turbulent kinetic energy during the expansion calculated by a single zone model that uses optimized turbulence model constants, for Engine 1 (left) and Engine 2 (right). ....	124
Figure 64. Turbulent kinetic energy during the expansion calculated by a single zone model that uses optimized turbulence model constants, for Engine 3 (left) and Engine 4 (right). ....	126
Figure 65. Normalized heat release (left) and in-cylinder temperature (right) of Engine 1 obtained by application of single set of constants. ....	128
Figure 66. Normalized heat release (left) and in-cylinder temperature (right) of Engine 2 obtained by application of single set of constants. ....	129
Figure 67. Normalized heat release (left) and in-cylinder temperature (right) of Engine 3 obtained by application of single set of constants. ....	130
Figure 68. Normalized heat release (left) and in-cylinder temperature (right) of Engine 4 obtained by application of single set of constants. ....	131
Figure 69. Relative crank angle position after start of ignition (SOI) at which the 50 % of in-cylinder mass is burned (CA50); comparison of 3-D CFD results and 0-D simulation results with the single set of constants. ....	132
Figure 70. Layout of experimental setup (left) [110] of single-cylinder Waukesha CFR F4 engine (right) from Combustion analysis Laboratory of University of California - Berkeley. ....	138
Figure 71. Experimental cylinder pressure traces for all considered operating points; black lines are individual cycle-resolved data, red lines represent averaged data (sample size = 300 cycles). ....	140

Figure 72. Reduced cycle-simulation model of CFR engine in AVL BOOST with the imposed intake pressure obtained by measurement.....	141
Figure 73. Comparison of experimental and simulation results of averaged cycle for all considered operating points. The left diagram shows the in-cylinder pressure, while the right diagram shows normalized HR. ....	143
Figure 74. Variation of intake turbulence production constant $S_{10}$ in calculation of operating point ST5 that reproduced cycle-to-cycle variations of in-cylinder turbulence. ....	145
Figure 75. Comparison of simulation results (red line) with the experimental data (black line) of IMEP over the 300 cycles. ....	147
Figure 76. Comparison of experimental and cycle-simulation results of IMEP (average value), standard deviation (StD) and coefficient of variation (CoV) of IMEP. ....	148
Figure 77. Comparison of experimental and simulation results of cycle-resolved in-cylinder pressure for all considered operating points and sample size of 300 cycles. ....	149
Figure 78. Experimental and cycle-simulation peak pressure plotted against crank angle at peak pressure (sample size = 300 cycles). ....	150
Figure 79. Comparison of experimental and simulation results of the cycle-resolved normalized HR for all considered operating points and sample size of 300 cycles. ....	151
Figure 80. Comparison of experimental and cycle-simulation statistical distribution results of CA5, CA50 and CA90 for the considered operating points and sample size of 300 cycles. ....	152
Figure 81. Comparison of experimental and cycle-simulation results of CA5 vs. CA10-90 for all considered operating points and sample size of 300 cycles.....	154
Figure 82. The statistical distribution of cross flow velocities at the spark timing, from analysis of cycle-simulation results of 300 cycles.....	155
Figure 83. Influence of relative standard deviation of turbulence production constant on the statistical results of IMEP at all considered operating points ST5 – ST20. ....	157
Figure 84. The possible cross-flow velocity directions at the spark plug (top view): $\alpha_1^*$ and $\alpha_2^*$ represent the possible angles of the velocity vector. ....	159
Figure 85. Influence of variation of the cross-flow velocity direction on the statistic results of IMEP at all considered operating points ST5 – ST20. ....	160
Figure 86. Visualization (top and isometric view) of the flame kernel shifting (at the end of kernel calculation) for the operating point ST5 ( $\sigma_{rel, S_{10}} = 0.14$ ). ....	161
Figure 87. Comparison of experimental and cycle-simulation results of CA5 vs. CA10-90 for all considered operating points and sample size of 300 cycles with the oscillation of in-cylinder turbulence and flow angle from cycle-to-cycle.....	163
Figure 88. Energy balance of the cylinder – single zone description of cylinder domain. ....	185

## List of Tables

Table 1. Main data of considered SI engines .....	63
Table 2. Values of constants of single and two zone $k-\varepsilon$ turbulence model and fractal combustion model – Engine 1 .....	67
Table 3. Values of constants of single and two zone $k-\varepsilon$ turbulence model and fractal combustion model – Engine 2 .....	72
Table 4. Values of constants of single and two zone $k-\varepsilon$ turbulence model and fractal combustion model – Engine 3 .....	75
Table 5. Values of constants of single and two zone $k-\varepsilon$ turbulence model and fractal combustion model – Engine 4 .....	78
Table 6. Values of constants of full $k-\varepsilon$ turbulence model – Engine 1 .....	82
Table 7. Values of constants of full $k-\varepsilon$ turbulence model – Engine 2.....	84
Table 8. Values of constants of full $k-\varepsilon$ turbulence model – Engine 3.....	86
Table 9. Values of constants of full $k-\varepsilon$ turbulence model – Engine 4.....	88
Table 10. Uniform operating parameters of the ignition model applied to all engines.....	91
Table 11. Values of constants of two zone $k-\varepsilon$ model and modified fractal combustion model – Engine 1 .....	93
Table 12. Values of constants of two zone $k-\varepsilon$ model and modified fractal combustion model – Engine 2 .....	95
Table 13. Values of constants of two zone $k-\varepsilon$ model and modified fractal combustion model – Engine 3 .....	97
Table 14. Values of constants of two zone $k-\varepsilon$ model and modified fractal combustion model – Engine 4 .....	99
Table 15. Overview of single set of constants for the single zone $k-\varepsilon$ turbulence model: optimization results for Engines 1 – 4 .....	123
Table 16. Overview of single set of constants for turbulence, ignition and combustion used in simulation of Engines 1 – 4 .....	127
Table 17. General specifications of the experimental Waukesha CFR F4 engine.....	138
Table 18. Main parameters of considered engine operating points.....	139
Table 19. The peak pressure and corresponding crank angle in experiment and cycle-simulation .....	143
Table 20. Overview of the cycle-simulation model constants .....	144
Table 21. Statistical results of IMEP in experiment and cycle-simulation made in AVL BOOST .....	146
Table 22. Statistical results of CA5, CA50 and CA90 – experiment vs. cycle-simulation....	153



# Nomenclature

Symbol	Unit	Description
<b><u>Latin letters</u></b>		
$A_L$	$m^2$	Laminar flame surface area
$A_T$	$m^2$	Turbulent flame surface area
$C_{bd}$	$V/\sqrt{J \cdot mm}$	Breakdown constant
$c_p$	$J/(kgK)$	Specific heat capacity at constant pressure
$d$	$m$	Distance, pipe diameter
$D_3$	-	Fractal dimension
$E_{bd}$	$J$	Breakdown energy
$E_k$	$J$	Kernel excess of energy
$F_{str}$	-	Distortion factor of free flame surface
$H$	$m$	Instantaneous cylinder height
$i_s$	$A$	Current of secondary electric circuit
$k$	$m^2/s^2$	Turbulent kinetic energy
$k_w$	$W/(m^2K)$	Heat transfer coefficient
$K$	$m^2/s^2$	Kinetic energy of mean flow
$l_k$	$m$	Kolmogorov length scale
$l_{spk}$	$m$	Electric spark length
$L_P$	$H$	Inductance of primary electric circuit
$L_S$	$H$	Inductance of secondary electric circuit
$L_I$	$m$	Integral length scale (Taylor)
$m$	$kg$	Mass
$n$	$rpm$	Engine speed
$p$	$Pa$	Pressure
$P$	$kg/(ms^3)$	Production of the turbulent kinetic energy
$Q_E$	$W$	Electric power
$Q_w$	$W$	Kernel heat loss flux
$r_0$	$m$	Assumed mean kernel radius

<b>Symbol</b>	<b>Unit</b>	<b>Description</b>
$r_f$	m	Flame front radius
$R_i$	J/(kgK)	Individual gas constant
$R_{BZ}$	J/(kgK)	Individual gas constant of burned zone
$R_k$	m	Instantaneous mean kernel radius
$R_s$	$\Omega$	Resistance of secondary electric circuit
$Re$	-	Reynolds number
$S_e$	$m^2$	Entrained spark plug surface area
$S_{ij}$	$s^{-1}$	Strain rate tensor
$S_K$	$m^2$	Kernel free flame surface area
$S_L$	m/s	Laminar flame speed
$S_T$	m/s	Turbulent flame speed
$t$	s	Time
$T$	K	Temperature
$u'$	m/s	Velocity pulsation (turbulent)
$U$	m/s	Mean flow (average) velocity
$U_{L, eff}$	m/s	Kernel expansion speed
$V_{af}$	V	Anode voltage fall
$V_{bd}$	kV	Breakdown voltage
$V_{cf}$	V	Cathode voltage fall
$V_{cg}$	V	Voltage between electrodes (after breakdown)
$x_B$	-	Mass fraction burned
$z$	m	Length

### **Greek letters**

$\alpha$	$^\circ$	Flow angle, relative crank angle
$\delta_{ij}$	-	Kronecker delta symbol
$\gamma_{wr}$	-	Non-dimensional flame wrinkling rate
$\epsilon$	$m^2/s^3$	Dissipation of the turbulent kinetic energy
$\mu$	Pa s	Dynamic viscosity

<b>Symbol</b>	<b>Unit</b>	<b>Description</b>
$\rho$	kg/m <sup>3</sup>	Density
$\sigma$	-	Prandtl number
$\tau$	s	Characteristic time of wall combustion process
$\tau_{ij}$	N/m <sup>2</sup>	Viscous stress tensor
$\nu$	m <sup>2</sup> /s	Kinematic viscosity
$\omega$	rad/s	Angular velocity

### **Subscripts**

ad	Adiabatic
av	Average
BZ	Burned zone
c	Cylinder
id	Ignition delay
in	Intake
ivcs	Intake valve cross section
k	Kernel
max	Maximum
min	Minimum
q	Quenching
ref	Reference
SOC	Start of combustion
SP	Spark plug
t	Turbulent
tot	Total
tr	Transition
UZ	Unburned zone

## Abbreviations

<b>Mark</b>	<b>Description</b>
AKTIM	Arc and Kernel Tracking Ignition Model
ATDC	After Top Dead Center
BBDC	Before Bottom Dead Center
BK	Blizard-Keck
BTDC	Before Top Dead Center
CA	Crank Angle
CCV	Cycle-to-Cycle Variations
CFD	Computational Fluid Dynamics
CFR	Cooperative Fuel Research
CFM	Coherent Flame Model
CO	Carbon Monoxide
CoV	Coefficient of Variation
DFE	Double Fine Electrode
DPIK	Discrete Particle Ignition Kernel
ECFM-3Z	Extended Coherent Flame Model – Three Zone
ECU	Engine-Control Unit
EI	Engine Interface
EOC	End of Combustion
EOK	End of Kernel
FTDC	Firing Top Dead Center
HC	Hydrocarbons
HiL	Hardware in the Loop
HR	Heat Release
IC	Internal Combustion
IVC	Intake Valve Closure
IMEP	Indicated Mean Effective Pressure
IVC	Intake Valve Closure

LDA	Laser Doppler Anemometer
MiL	Model in the Loop
NO <sub>x</sub>	Nitric Oxides
QDIM	Quasi-Dimensional Ignition Model
PT	Pressure Transducer
RANS	Reynolds Averaged Navier Stokes
RHS	Right Hand Side
RSM	Reynolds Stress Model
SB	System Boundary
SHP	Start of High Pressure
SI	Spark Ignition
SiL	Software in the Loop
SOC	Start of Combustion
SOI	Start of Ignition
StD	Standard Deviation
SVM	Support Vector Machines
TCI	Transistorized Coil Ignition
TDC	Top Dead Center
VVA	Variable Valve Actuator
0-D	Zero-dimensional
1-D	One-dimensional
2-D	Two-dimensional
3-D	Three-dimensional

# 1. Introduction

Current trends in legislation towards the reduction in fuel consumption and exhaust gas emissions lead to increased use of new SI (Spark Ignition) engine technologies, such as downsizing, charging, direct-injection, etc. Due to high costs of experiments and a rapid increase in the computer power, researchers all over the world are making great effort to develop and improve numerical simulation models.

Numerical simulations related to IC (Internal Combustion) engines can be classified into three main groups: CFD (Computational Fluid Dynamics) models, cycle-simulations and real-time capable models. CFD models are usually based on the finite volume method [1] and they hold leading position in the field of engine simulations. The technique is very powerful, involving details on the fluid flow, heat and mass transfer, and combustion-associated phenomena (chemical reactions). The cycle-simulations of IC engines are often called 1-D/0-D simulation models [2, 3] because the calculation of the flow through intake and exhaust pipes is based on 1-D finite volume method, while the cylinder domain is treated as one control volume without orientation and spatial discretization, as it is illustrated in Figure 1.

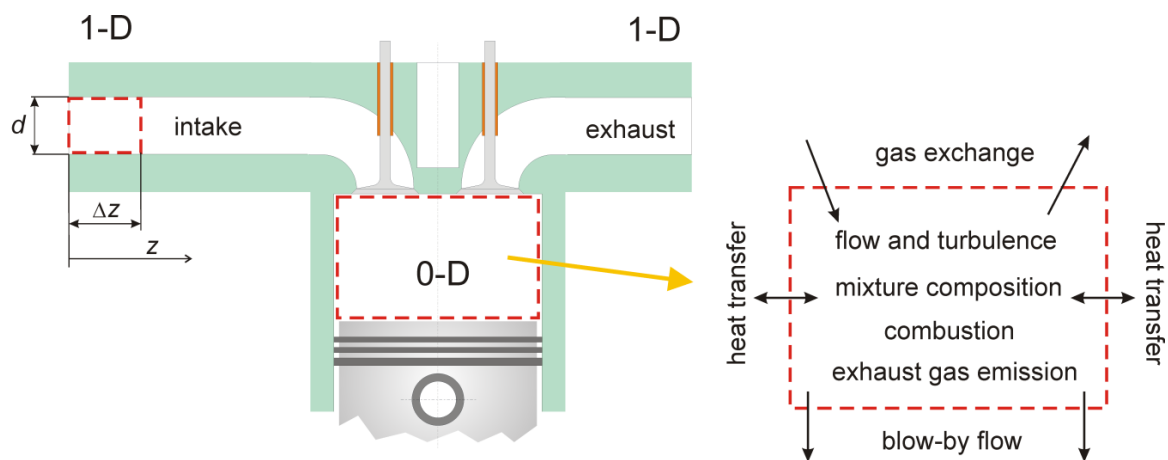


Figure 1. Illustration of 1-D/0-D approach of the cycle-simulation model; 1-D discretisation of intake and exhaust pipe, 0-D (thermodynamic) model of cylinder with the specification of main sub-models.

The last group of simulation models of IC engines is presented by real-time capable models that are usually dedicated to the investigation of transient operating conditions in desktop, MiL (Model in the Loop), SiL (Software in the Loop) and HiL (Hardware in the Loop) applications. In classical real-time capable models the basic flow characteristics are modeled by steady-state approaches and maps, while the engine characteristics are described by means of surrogate engine modeling using SVM (Support Vector Machines). The prediction of

engine characteristics using SVM is based on the data collected from the test-bed measurements or from the cycle-simulation results.

The cycle-simulation models are suitable for the analysis of key engine parameters on performance output, and for optimization with specific criteria, because the flow and combustion associated phenomena can be captured correctly with reasonable computational time. For the correct description of particular in-cylinder phenomena such as: flow, heat transfer, gas exchange and combustion, the corresponding sub-models have to be defined (see Figure 1).

The thermodynamic (0-D) combustion sub-models can be classified into two main sub-groups: single and multi zone models. In single zone models the cylinder mixture is assumed to be uniform in pressure, temperature, and composition. The main drawback of such combustion model is that the flame front propagation and combustion chamber geometry are completely neglected, although they are the most important parameters for a good prediction of the combustion process of SI engine. In the case of multi zone combustion model, the combustion chamber is generally divided into a burned and unburned zone, which are separated by a flame front. The first law of thermodynamics, equation of state and conservations of mass and volume are applied to the burned and the unburned zone. The pressure is assumed to be uniform across the combustion chamber while the burned and unburned zone are considered as two separate thermodynamic systems that are uniform in composition and temperature within themselves. A specific sub-group of multi zone combustion models are quasi-dimensional models that consider the real flame front propagation across the unburned gas mixture although a spatial discretization of the combustion chamber does not exist. The burning rate of the quasi-dimensional combustion model depends on the fundamental physical quantities such as turbulence intensity, integral length scales, turbulent time scales and kinetics of the fuel-air oxidation process. Since the fuel-air oxidation process generally depends on the mentioned turbulence quantities (intensity, time and length scales), the modeling and prediction of in-cylinder turbulence is of crucial importance for the correct prediction of turbulent combustion.

The combustion process of SI engine is initiated by electric spark discharge that occurs between the spark plug electrodes. The characteristics of electric spark discharge depend on the properties of applied engine ignition system as well as on the gas properties between the spark plug electrodes. Discharge of the electric spark defines the initial position and the initial growth of the flame kernel that starts to be wrinkled by turbulent eddies. For the simulation of

the entire combustion process typical for SI engine, the ignition associated phenomena including the electric spark discharge also have to be modeled.

The objective of the research presented in this thesis is the development and validation of turbulence, quasi-dimensional combustion and ignition sub-models that are fully integrated into a commercial cycle-simulation code. The application of the newly developed sub-models will ensure that the cycle-simulation results are comparable with the 3-D CFD results and experimental data of SI engine.

### 1.1. Motivation

The motivation for the research originated from the work that was made within the cooperation of Chair of IC Engine and Motor Vehicle with the AVL AST d.o.o. At the initial stage of the research activities, when the existing quasi-dimensional combustion model was used and analyzed, the aim was to have comparable results of turbulence and combustion between the 3-D CFD results from AVL FIRE [4] and the cycle-simulation results of AVL BOOST for the same engine and operating point. The example of 3-D CFD (computational mesh) and the cycle-simulation model of SI engine are shown in Figure 2.

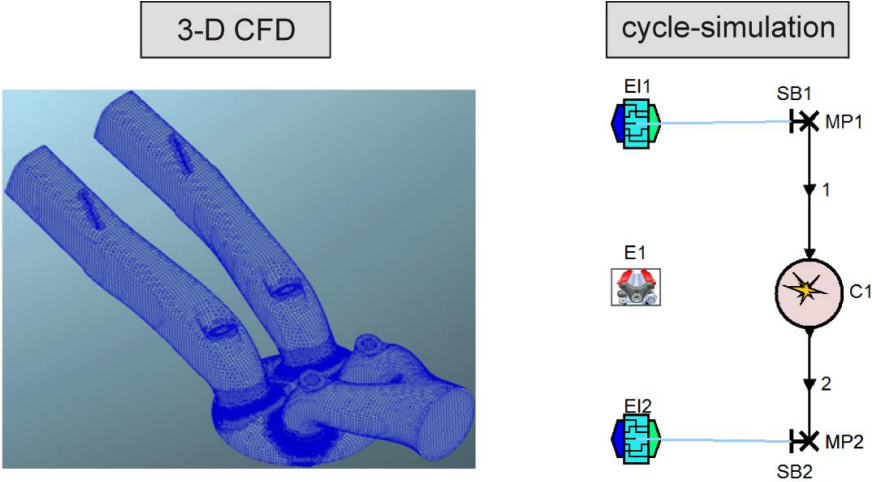


Figure 2. Example of 3-D CFD simulation model in AVL FIRE (left) and reduced cycle-simulation model in AVL BOOST (right).

The modeling of turbulence within the 3-D CFD simulation model was performed with the standard  $k-\varepsilon$  turbulence model, while the combustion process was calculated by the ECFM-3Z (Extended Coherent Flame Model – Three Zone). In the cycle-simulation model of AVL BOOST the available algebraic  $\varepsilon$  model ( $K-k$  turbulence model) for turbulence [5] and the original fractal combustion model were applied. In order to compare the cycle-simulation results of the in-cylinder turbulence with the 3-D CFD results, it was necessary to recalculate the 3-D CFD results so that the mass-averaged results of the turbulent kinetic energy from the



computational cells related to the combustion chamber are defined. The mass-averaged turbulent kinetic energy as well as the normalized HR (heat release) from 3-D CFD solution are shown with the black dashed lines in Figure 3.

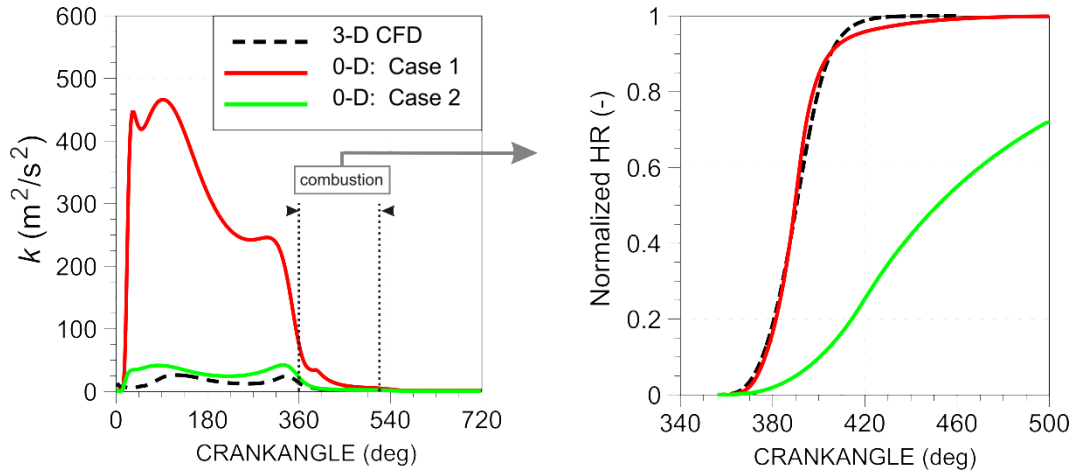


Figure 3. Tuning of turbulence model constants in the original cycle-simulation model (full load case at engine speed of 2000 rpm).

In the same figure, two cases of the cycle-simulation results are shown. The first case (red solid lines in Figure 3) represents the simulation results of in-cylinder turbulent kinetic energy and normalized heat release (HR) when the turbulence constants (production and integral length scale) are tuned so that the cycle-simulation combustion results matched well the 3-D CFD solution. In that case the turbulent kinetic energy calculated by the cycle-simulation is almost order of magnitude higher than the 3-D CFD solution. In the second case (green solid line in Figure 3) the turbulence constants were adjusted so that the best match of turbulent kinetic energies during the combustion period is achieved, but then the prediction of combustion process is not good. Any additional setting of combustion model parameters for the definition of ignition delay and combustion rate was not sufficient to speed up the combustion process to a correct levels. Obviously, the interaction between the in-cylinder turbulence and combustion was deficient. In order to improve the model and a prediction of the overall turbulence level and the interaction between the turbulence and flame of the model, the single and two zone  $k$ - $\epsilon$  turbulence models for 0-D applications are developed.

Additionally, within the previous fractal combustion model the early flame kernel formation and growth are not calculated. The combustion starts after the modeled ignition delay with the fully spherical and smooth flame with 2 mm in radius. The ignition delay is modeled with the assumption that early flame kernel growth lasts 0.2 ms when the flame kernel has grown enough to be considered as turbulent flame. By using the *Ignition Formation Multiplier* that multiplies the assumed ignition delay of 0.2 ms, it is possible to

manually tune the ignition delay for different operating conditions. In real SI engines the early flame kernel growth depends on the large number of parameters such as cross-flow velocity, spark plug design, in-cylinder pressure, temperature, mixture composition, ignition system properties, etc. In order to capture the influence of all mentioned effects on the ignition delay with the previous combustion model the *Ignition Formation Multiplier* had to be calibrated for each operating point of the considered engine. Therefore, a new ignition model is developed and integrated into the quasi-dimensional combustion model, which will physically take into account all previously mentioned effects and will model the process of early flame kernel growth.

## 1.2. Overview of literature

An influence of turbulence on the flame structure and the flame speed has been investigated by Damköhler 70 years ago. He introduced the generally accepted theory that turbulent eddies larger than the flame thickness cause the convective deformation of the flame front while the smaller eddies increase the heat and mass transfer within the flame influencing the laminar flame speed [6]. It is obvious that modeling of the turbulence is a necessary step for the modeling of the combustion process in SI engines. The most commonly used procedure for the description of turbulent flow in engineering problems is based on the averaging of Navier-Stokes equations, known as RANS approach (Reynolds Averaged Navier-Stokes). The first two-equation turbulence model ( $k$ - $\omega$  model) has been developed by Kolomogorov at the beginning of 1940's. Due to the non-linear differential equations and the computer absence such turbulence model was not applied until 1970's [6]. In 1972 Lander and Spalding [7] have developed the  $k$ - $\varepsilon$  turbulence model as one of the most commonly used two-equation turbulence model [6]. At the beginning of 1980's the  $k$ - $\varepsilon$  turbulence model was applied to the simulations of IC engines with the specific modifications of differential equations. In order to match the experimental data of turbulent length scales Morel and Mansour [8] have modified the differential equation of dissipation rate when the rapid compression of in-cylinder charge occurs. This turbulence model was used as the base model for further investigation and modeling of turbulence in the IC engines. By using the assumption of homogenous and isotropic turbulent flow field inside the engine cylinder the first turbulence models applied to the 0-D simulation of SI engine have been developed. Polous and Heywood [9] have used the algebraic  $\varepsilon$  turbulence model to study the influence of cylinder geometry on the overall in-cylinder turbulence level. Tabaczynski [10] applied the algebraic  $\varepsilon$  and the full  $k$ - $\varepsilon$  turbulence model on different cylinder geometries. The analysis of

simulation results showed that different turbulence model formulations and different cylinder geometries have significant influence on the prediction of in-cylinder turbulence level. Two zone turbulence model formulations have been developed by the application of multi-zone combustion models [5]. Agarwal et al. [11] analyzed different formulations of single and two-equation turbulence models (algebraic  $\varepsilon$  and  $k-\varepsilon$  turbulence model) that have been applied together with the quasi-dimensional combustion model of SI engine [12, 13]. In their research, the parameters of turbulence models have been adjusted so that the best match of simulated and measured pressure trace is obtained. In 2010 Watanabe et al. [14] have developed the quasi-dimensional combustion model and applied it to the direct injection gasoline engines. The modeling of turbulence was performed by the application of  $K-k$  turbulence model [5] which was adjusted and validated for the tumble type in-cylinder flow and the cycle-simulation results were compared to the 3-D CFD results. The  $K-k$  turbulence model presented in [14] used 6 tunable constants for simulating the tumble in-cylinder flow, typical for the pentroof cylinder geometry.

Physical combustion models that consider the flame structure lately became very popular for the cycle-simulation of SI engines because the real flame front propagation across the combustion chamber is considered. Therefore, such combustion models are usually called quasi-dimensional combustion models [11-14]. At the beginning of 1970's, simultaneously with the development of  $k-\varepsilon$  turbulence model, the first quasi-dimensional combustion model, known as BK (Blizard-Keck) combustion model [15] was developed. This combustion model takes into account the effects of turbulence intensity, laminar flame speed and turbulent length scales on the overall combustion rate. In the model the large turbulent eddies entrain the fresh mixture while the smaller ones wrinkle the flame and burn with the laminar flame speed. In the scientific papers published so far the BK combustion model can also be found with different names, such as turbulent entrainment model [16]. In 1987 Gouldin [17] proposed the quasi-dimensional combustion model that uses the fractal theory for the description of the flame front geometry. The application of fractal combustion model in the simulation of combustion process of SI engines can be observed at the beginning of 1990's. Several studies have been performed for the definition of fractal dimension of the turbulent flame that occurs in the SI engine and research results are summarized in [18]. It has been shown that the fractal dimension depends on the ratio of turbulence intensity and laminar flame speed and the heuristic approach in the definition of fractal dimension was adopted [19]. In 2010 Perini et al. [20] developed the quasi-dimensional combustion model that was applied on the simulation of combustion in CFR engine fueled by hydrogen, methane and their blends. The

combustion model was based on the BK model with the turbulent flame speed defined according to the fractal theory. The modeling of turbulence was significantly simplified with turbulence intensity correlated to the mean piston speed. In the conclusion remarks of their research it is mentioned that the predictive capability and accuracy of the quasi-dimensional combustion model could be improved by introducing detail sub-models for the early flame kernel growth and turbulence. On the other hand, the results of particular sub-models of the cycle-simulation are very sensitive on values of required input parameters. It was demonstrated in [21, 22] that the combustion results are sensitive on values of constants related to turbulence and combustion sub-models. Therefore, it is desirable that the number of required input parameters as well as the model sensitivity is minimized when the new sub-models are developed.

The combustion process of SI engines is initiated by the electric spark discharge that occurs between the spark plug electrodes. If the electric energy of the spark is higher than the critical energy necessary for the start of combustion, the flame kernel is formed. Ballal and Lafeyvre [23] investigated the effects of breakdown voltage, duration of electric spark, distribution of electric energy along the spark length, gap distance, flow velocity and spark plug geometry on the formation of flame kernel. An experimental study of the flame kernel propagation at different cross-flow velocities and air equivalence ratios was performed by Mansour [24]. Pischinger and Heywood [25] developed one-dimensional flame kernel model that includes the heat transfer effects and the shifting of the flame kernel center caused by the in-cylinder flow. All mentioned studies [23-25] showed that electric properties of ignition system, gap distance, heat transfer and cross-flow velocities are very important for the early flame kernel growth.

Since the computer power is getting more and more increased the modeling of comprehensive ignition phenomena and early flame kernel growth in the 3-D CFD models become possible [26, 27]. Duclos and Colin [28] developed Arc and Kernel Tracking Ignition Model (AKTIM) that can be found in the commercial 3-D CFD software for the simulation of combustion in SI engines. This ignition model takes into account the effects of secondary electric circuit, spark plug geometry, local flow velocity around the spark plug and heat transfer. The flame kernel is described by using marker particles and each of them represents the gravity center of a possible flame kernel. The modeling of detailed ignition phenomena and early flame kernel growth in the quasi-dimensional combustion models of SI engines (0-D) is usually not performed and the combustion process starts with the stable and spherically shaped flame of specific radius [13]. An ignition delay is assumed to last 0.2 ms with the

initial flame still smooth and spherical with 2 mm in radius. At different operating conditions in the cylinder, the ignition delay period can be significantly different from the assumed one. Therefore, in the previous combustion model of the cycle-simulation, the user-defined parameter that tunes the ignition delay is added, and it has to be calibrated for each operating point of the engine.

Due to extremely stochastic nature of in-cylinder flow, the in-cylinder flow field of individual cycle differs significantly from the averaged cycle. Since the combustion process of SI engine highly depends on the turbulent flow field inside the cylinder, the cycle-to-cycle variations (CCV) in combustion occur. Since CCV in combustion significantly influence the engine performance output and exhaust gas emissions the analysis and modeling of CCV in combustion is very important. The main sources of CCV have been identified by the number of physical factors: the stochastic nature of the in-cylinder fluid motion, variation of in-cylinder turbulence level and mixing of fuel, air and residual gases [29]. The work presented in [30-32] demonstrates that the oscillations in the mixture composition are not the dominant factor that causes the CCV in combustion. The main conclusion of the work presented in [31, 32] is that the oscillations in the in-cylinder turbulence between individual cycles is the most influencing factor responsible for CCV in combustion.

The literature overview showed that the detail modeling of particular phenomenon regarding the in-cylinder turbulence, ignition and combustion for cycle-simulations is necessary to capture the effects of main parameters that affect the combustion process of SI engine and CCV as well. In order to improve the prediction of entire combustion process, the new physically based turbulence, ignition model and the quasi-dimensional combustion sub-model will be developed and integrated into the cycle-simulation model. For the modeling of CCV in combustion of SI engine by using the cycle-simulation model that includes the newly developed sub-models, the variation of in-cylinder turbulence and flow angle at the spark plug from cycle-to-cycle were imposed in the model.

### **1.3. Objective and hypotheses of research**

This PhD thesis and work had several objectives:

- better understanding of physical processes that take place within the engine cylinder;
- development of a single and a two zone  $k-\varepsilon$  turbulence model for 0-D applications;
- development of new ignition model for 0-D applications;
- improvement and modification of the existing quasi-dimensional combustion model;

- implementation of developed sub-models into a software code for the cycle-simulation of SI engines;
- application of developed cycle-simulation in the prediction of cycle-to-cycle variations in combustion of SI engine.

Hypotheses of the presented research are:

1. It is assumed that simulation sub-models of turbulence, ignition and combustion phenomena can be developed and integrated into the cycle-simulation model of SI engine.
2. It is expected that the development of such sub-models and their application in the cycle-simulation will contribute to the better prediction of certain processes and that the cycle-simulation results will match well the 3-D CFD results and experimental data. This will enable the faster and more accurate analysis of main factors that affect the SI engine cycle.

#### **1.4. Methodology and research plan**

The research presented and described in this thesis is divided into five main parts:

The first part deals with the modeling of in-cylinder turbulence. Since the turbulent flow field plays a very important role in the combustion process of SI engine, modeling of the turbulence is of crucial importance. The first analysis was performed to define the single zone  $k-\varepsilon$  turbulence model that was applied during the high pressure cycle with the initial conditions at the intake valve closure (IVC) defined from the 3-D CFD results. It was shown that a turbulence model defined in this way correctly predicts the overall in-cylinder turbulence level during the high pressure cycle. The main disadvantage of the single zone turbulence model applied during the high pressure cycle is its dependency on the initial conditions that have to be imposed either from the 3-D CFD results or from the experimental data. Therefore, modeling of the turbulence was extended to the gas exchange phase that fully eliminated the requirement for initial conditions. The application of the developed full cycle  $k-\varepsilon$  turbulence model on the entire cycle of SI engine demonstrated the possibility of the model to predict the in-cylinder turbulence level that is comparable with the 3-D CFD results, especially during the combustion period when the turbulence quantities are most important. It is known from the combustion theory [33] that the state of unburned zone (in front of the flame) defines the flame front propagation and the rate of heat release. In order to predict the combustion progress correctly and physically more accurate the two zone  $k-\varepsilon$  turbulence model was developed and applied during the combustion period.

In the second part, the development of a new ignition model for the description of early flame kernel growth in a quasi-dimensional combustion model is presented. The new ignition model for the cycle-simulation of SI engine is based on the AKTIM ignition model that is available in the commercial 3-D CFD software. AKTIM takes into account the effects of spark plug geometry, secondary electric circuit, local flow velocity and heat transfer from the flame kernel to the spark plug electrodes. The modeling of the spark plug geometry is very important for the calculation of early flame kernel growth because the heat transfer significantly influences the kernel expansion speed. A specific approach is employed for a definition of the real spark plug geometry in the 0-D calculation. The local flow velocity around the spark plug influences the convective shifting of the flame kernel center from its initial position resulting in the distortion of the flame front and influencing the overall combustion process. Such phenomena are captured by the proposed ignition model, but it requires the correct prediction of in-cylinder flow and turbulence.

In the third part of the research, the quasi-dimensional combustion model [22, 34] is extended and improved. The calculation of the early flame kernel growth is performed by the application of a newly developed ignition model. When the specific portion of the cylinder mixture is burned by the newly developed ignition model, the calculation of the combustion process is switched to the fractal combustion model. The implementation of the  $k-\varepsilon$  turbulence model contributed to the better description of the flame transition from the laminar to the fully developed turbulent flame, when the maximum value of fractal dimension is reached. Also, the implementation of  $k-\varepsilon$  turbulence model enables the new definition of maximum fractal dimension that is reached during the fully developed turbulent flame. The fractal dimension defines the free flame surface that is highly wrinkled due to effects of turbulent eddies and that entrains the fresh mixture. It is shown that the modifications that were made contribute to the better prediction of combustion process, especially when the two zone turbulence model is applied. In the case of the two zone turbulence model the calculation of the combustion process is significantly simplified because the non predictive wall combustion sub-model can be fully omitted.

In the fourth part, the validation of the developed sub-models that are integrated into the cycle-simulation model of AVL BOOST and the parameterization of turbulence and combustion model are presented. The validation is performed on four engine geometries with the cycle-simulation results compared to the 3-D CFD results calculated by the AVL FIRE. The validation is performed over different engine speeds and loads. In order to achieve the best match with the 3-D CFD results the parameters of particular sub-models of cycle-

simulation are adjusted at each operating point. After that, the parameterization of turbulence and combustion model parameters is proposed, that would enable the use of single set of constants for one engine geometry and for the entire engine map.

The fifth part of this thesis presents the validation of the cycle-simulation results with the experimental results of a single cylinder SI engine fueled by gasoline. It is known that SI engine combustion shows non-repeatable behavior known as cycle-to-cycle variation (CCV) in combustion, even when the constant boundary conditions are imposed [35, 36]. Therefore, the specific approach for modeling and prediction of the CCV in combustion is proposed. In order to perform the statistical analysis of CCV in combustion it is necessary to use the sample size of several hundred cycles [37]. The modeling and analysis of CCV in combustion is performed at different operating conditions with the emphasis on the variation of spark timing. The comparison of cycle-averaged results and statistical results of indicated mean effective pressure (IMEP) and normalized HR demonstrated that the developed cycle-simulation calculation is efficient, fast, predictive and well-promising solution for modeling of SI engine combustion.



## 2. Turbulent flow and modeling

All flows that are encountered in daily life can be classified into two main groups: laminar and turbulent flows. Turbulence is a very complex physical phenomenon occurring when the Reynolds number ( $Re = UL/\nu$ , where  $U$  and  $L$  are characteristic velocity and length scale of the mean flow, and  $\nu$  is kinematic viscosity) is above the critical value [1]. Almost all fluid flows occurring in engineering practice are turbulent: flows around buildings, bridges, airplanes, cars, flows in IC engines, etc. The behavior of the turbulent flow is random and chaotic and the motion of fluid particles becomes unsteady even with constant boundary conditions [38]. The velocity and all other flow properties vary in a random and chaotic way.

The general mixture motion in internal combustion engines and the associated turbulence structures have a great influence on the combustion process. Turbulence effects include the convective deformation of the flame front, the additional transfer of momentum, heat and mass due to flow fluctuations, etc. The level of the in-cylinder turbulence is defined by velocity fluctuations, often called turbulence intensity [1, 39]. The turbulence intensity is strongly influenced by engine speed, valve timing, port geometry, compression stroke characteristics, and combustion process [9, 39, 40].

Performing of experiments is a very expensive process because it requires special equipment, laboratories and professionals who are capable to perform them correctly. Moreover, experimental measurements of turbulence intensity are difficult due to the extreme in-cylinder conditions. Hot-wire anemometers can be used for turbulence intensity measurement but in this method it is required that the engine operates only under motored conditions [41]. Laser-based methods (e.g. Laser Doppler Anemometer - LDA) can provide both spatial and temporal data on the turbulence intensity under firing conditions but with extensive engine modifications [10, 42].

Due to high costs of experimental data and increased computer power, a number of simulation software packages have been developed. CFD codes based on the finite volume method [1] hold leading position in the field of engine simulations. The technique is very powerful, involving details on the fluid flow, heat and mass transfer and combustion-associated phenomena (chemical reactions). On the other hand, there are simulation codes which are based on simplified approaches (e.g. zero dimensional approach) providing acceptable results with dramatically reduced computational time.

Typical examples of the turbulent flow in daily life are flows around buildings, airplanes, cars, as well as flows in internal combustion engines (see Figure 4). The turbulent

flow field can be described by a few characteristic features such as: irregularity, diffusivity, high Reynolds number, three-dimensionality and dissipation [43].

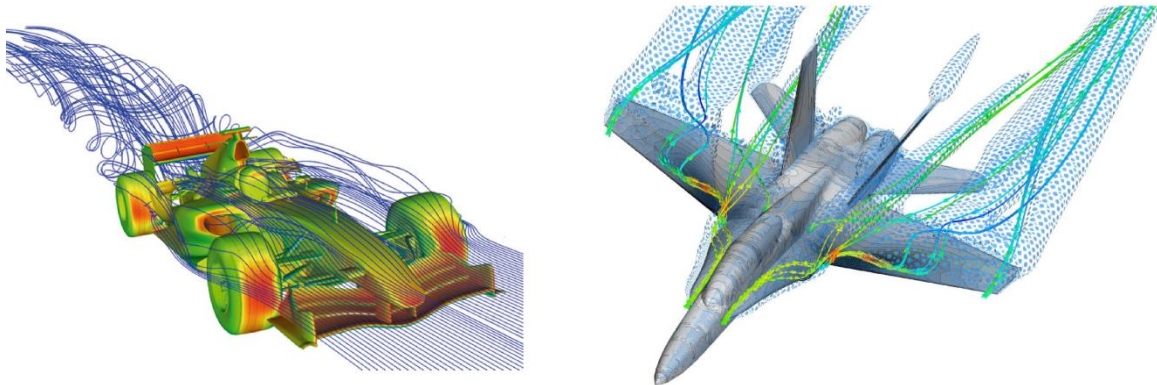


Figure 4. Examples of turbulent flow in daily life [44, 45].

Good understanding of the in-cylinder turbulent flow is one of the key factors for successful modeling of the combustion process in spark ignition (SI) engines. A turbulent flow is usually described in terms of the steady mean value of the velocity  $\bar{U}$  and its fluctuation component  $u'$  that is superimposed (Figure 5):  $u = \bar{U} + u'$ . All other quantities such as pressure and density can also be expressed as a sum of the mean and fluctuating parts. This approach was introduced by Reynolds and hence it is often called the Reynolds decomposition [1]. One reason for decomposing these quantities is that when the flow quantities are measured, one is interested in the mean values rather than in the time histories. The second reason is a possibility to solve the Navier-Stokes equations numerically without excessive spatial and temporal resolution [43].

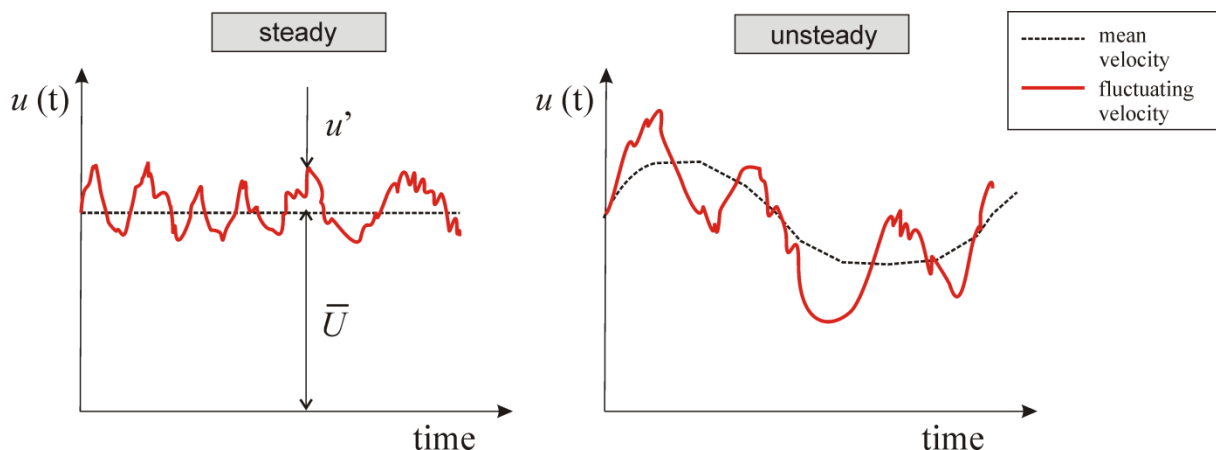


Figure 5. Typical point velocity measurement in steady (left) and unsteady (right) turbulent flow field.

Initial equations for any turbulence modeling are the continuity equation (2.1) and the Navier-Stokes equations (2.2) for a Newtonian fluid (body forces are neglected):

$$\rho_{,t} + (\rho u_i)_{,i} = 0 \quad (2.1)$$

$$(\rho u_i)_{,t} + (\rho u_i u_j)_{,j} = -p_{,i} + \tau_{ij,j} \quad (2.2)$$

where:  $\rho$  (kg/m<sup>3</sup>) is the fluid density,  $u_i$  (m/s) is the instantaneous total velocity in the  $i$  direction,  $p$  (Pa) is the pressure and  $\tau_{ij}$  (N/m<sup>2</sup>) is the viscous stress tensor. If the Reynolds decomposition is applied to equations (2.1) and (2.2) and if the fluctuations in density, pressure and viscous stress tensor are neglected, the following equations can be written (RANS):

$$\rho_{,t} + (\bar{\rho} \bar{u}_i)_{,i} = 0 \quad (2.3)$$

$$(\bar{\rho} \bar{u}_i)_{,t} + (\bar{\rho} \bar{u}_i \bar{u}_j)_{,j} = -\bar{p}_{,i} + \bar{\tau}_{ij,j} + \overline{\rho u_i' u_j'}, \quad (2.4)$$

where the term  $\overline{u_i' u_j'}$  that appears on the right-hand side (RHS) of equation (2.4) represents the Reynolds stress tensor [1, 6, 43]. The Reynolds stress tensor appears as an additional stress term due to velocity fluctuations  $u'$ . The Reynolds stress tensor is unknown and in order to close the system of equations (2.4), it has to be defined. Different approaches are taken for closing the system of equations (2.4) which distinguish turbulence models by different levels of approximation (group of RANS-based eddy viscosity models):

1. Algebraic or zero-equation models – models that do not require the solution of any additional equations. The Reynolds stress tensor is related to the velocity gradients and turbulent viscosity (eddy viscosity). These models, such as Baldwin-Lomax and Cebeci-Smith model, are quite simple to use in general situations.
2. One-equation models – models in which the transport equation for a turbulent quantity (usually the turbulent kinetic energy) is calculated. The turbulent viscosity is defined from the Boussinesq assumption [1, 43]. The well-known one-equation models are Prandtl's, the Baldwin-Barth and the Spalart-Allmaras model.
3. Two-equation models – this type of models is the most commonly used turbulence models in engineering problems. Transport of two scalars, for example the turbulent kinetic energy  $k$  and its dissipation rate  $\varepsilon$ , are defined. The Reynolds stress tensor is

related to the velocity gradients and eddy viscosity. Most often used two-equation turbulence models are:  $k-\varepsilon$  and  $k-\omega$  model [1, 6, 43].

4. Reynolds stress models (RSM) – under this modeling approach [46] eddy viscosity has been discarded and the Reynolds stresses are directly computed using additional differential transport equations.

Generally, when mass flows into the cylinder, it increases the kinetic energy of the mean flow which is represented by large scale eddies. The kinetic energy of the mean flow is handed down from large scale eddies to progressively smaller eddies. This means that the increase in the turbulent kinetic energy occurs as a result of decrease in the mean kinetic energy and that they are always closely connected. Finally, small scale eddies are dissipated into heat by the effect of viscous forces. The phenomenon of the energy transition from large eddies to smaller ones and the generation of heat from the small scale eddies decay is always a unidirectional process. An energy cascade from large scale eddies to smaller ones is defined by the production of turbulent kinetic energy, while the generation of heat caused by viscous effects is defined by the dissipation rate of turbulent kinetic energy. When the mass flows out of the cylinder, it decreases both the mean and the turbulent kinetic energy. The energy cascade process is illustrated in Figure 6.

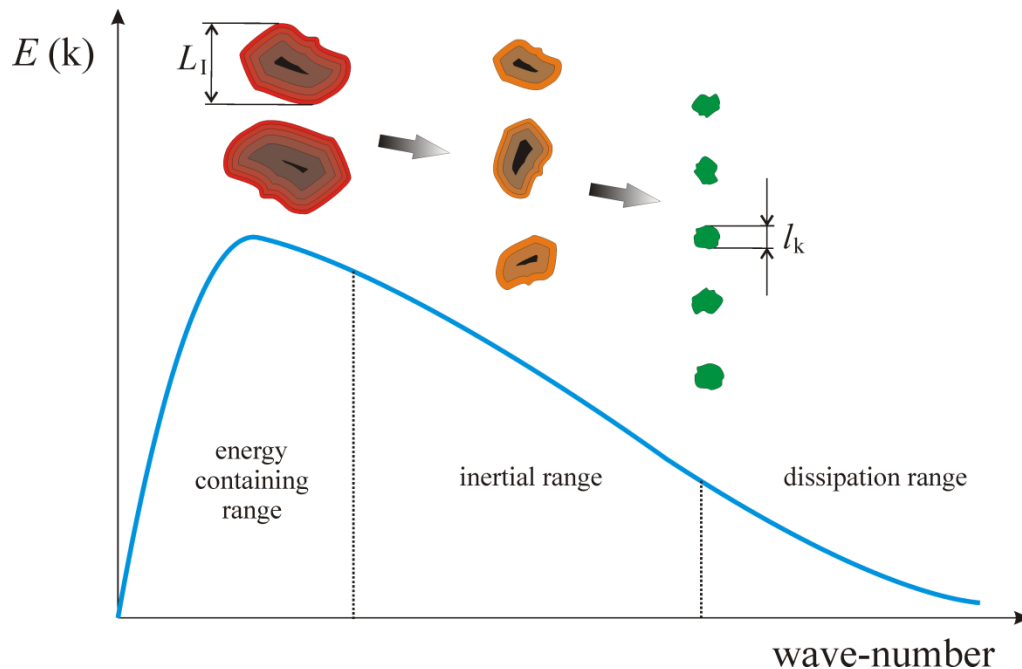


Figure 6. Turbulence energy spectrum and energy cascade phenomenon.

## 2.1. Single zone $k$ - $\varepsilon$ turbulence model - high pressure cycle

### 2.1.1. General equations of $k$ - $\varepsilon$ model

Since the  $k$ - $\varepsilon$  turbulence model is the most commonly used turbulence model in multi-dimensional codes, the main idea was to implement this model in the cycle-simulation software and to obtain turbulent quantities that match the results of the multi-dimensional model. The standard  $k$ - $\varepsilon$  turbulence model [47] includes two transport equations, one for the turbulent kinetic energy  $k$  and the other for its dissipation rate  $\varepsilon$ . The model is based on the best understanding of the relevant processes that change these variables [1]. If equation (2.4) is subtracted from equation (2.2), multiplied by  $u'$  and time averaged, it is possible to write a transport equation of the turbulent kinetic energy as:

$$(\rho k)_{,t} + (\rho k u_i)_{,i} = -\overline{\rho u_i u_j} \cdot u_{ij} - \rho \left( \frac{\overline{u'_i u'_i u'_j}}{2} \right)_{,j} - \overline{p_{,j} u'_i} + \left( \overline{\tau'_{ij} u'_i} \right)_{,j} - \overline{\tau'_{ij} u'_{i,j}} \quad (2.5)$$

The first term on the RHS of equation (2.5) represents the production of turbulent kinetic energy, the second is the molecular diffusion, the third and fourth terms are changes in the turbulent kinetic energy influenced by pressure and viscous stress pulsations (which can be neglected) and the last term is the dissipation of the turbulent kinetic energy [5]. The production term  $P$  is calculated by using the well-known Boussinesq approximation [1, 5, 43]:

$$P = -\overline{\rho u_i u_j} \cdot u_{ij} = \mu_t (u_{i,j} + u_{j,i}) \cdot u_{i,j} - \frac{2}{3} \delta_{ij} \left( \mu_t \cdot u_{k,k}^2 + \rho k u_{k,k} \right) \quad (2.6)$$

where  $\mu_t$  (Pa·s) is the turbulent (eddy) viscosity and  $\delta_{ij}$  is the Kronecker delta symbol. The first term on the RHS of equation (2.6) represents the shear effect and second is the dilatation effect on the turbulent kinetic energy [5]. The dissipation rate of the turbulent kinetic energy is defined as:

$$\varepsilon = \frac{\overline{\tau'_{ij} u'_{i,j}}}{\rho} \quad (2.7)$$

Finally, the transport equation of turbulent kinetic energy can be expressed as:

$$(\rho k)_{,t} + (\rho k u_i)_{,i} = \left( \frac{\mu_t}{\sigma_k} k_i \right)_{,i} + P - \rho \varepsilon \quad (2.8)$$

where  $k = \frac{1}{2} \overline{u_i u_i}$  represents the turbulent kinetic energy and  $\sigma_k = 1.0$  is the Prandtl number.

The transport equation of the dissipation rate  $\varepsilon$  is derived in the same manner as it is done with turbulent kinetic energy:

$$(\rho \varepsilon)_{,t} + (\rho \varepsilon u_i)_{,i} = \left( \frac{\mu_t}{\sigma_\varepsilon} \varepsilon_i \right)_{,i} + \left( C_1 \frac{\varepsilon}{k} P + C_3 \rho \varepsilon u_{i,i} \right) - C_2 \rho \frac{\varepsilon^2}{k} \quad (2.9)$$

where  $\sigma_\varepsilon = 1.3$  is the Prandtl number,  $C_1 = 1.44$ ,  $C_2 = 1.92$  and  $C_3 = -0.373$  are adjustable model constants [1, 6]. The default values of model constants previously specified are derived from the comprehensive data fitting for a wide range of turbulent flows [1, 5]. The production and dissipation of the turbulent kinetic energy are always closely connected, which means that the dissipation rate  $\varepsilon$  is higher if the value of the turbulent kinetic energy is larger. Equations (2.8) and (2.9) represent two transport equations of the standard  $k$ - $\varepsilon$  turbulence model [48].

### 2.1.2. Background of the $k$ - $\varepsilon$ turbulence model for 0-D applications

In order to transform the multi-dimensional transport equations of the  $k$ - $\varepsilon$  turbulence model into the equations of the zero dimensional model, a homogeneous and isotropic turbulent flow field [5] is assumed. The total velocity divergence can be expressed from the continuity equation if density is uniform in space but may vary in time [49]:

$$u_{i,j} = -\frac{1}{\rho} \frac{d\rho}{dt} \cdot \frac{\delta_{ij}}{3} \quad (2.10)$$

If equation (2.10) is applied to the definition of the strain rate tensor  $S_{ij}$ , only members on the main diagonal exist:

$$S_{ij} = \frac{1}{2} (u_{i,j} + u_{j,i}) = \begin{bmatrix} u_{1,1} & 0 & 0 \\ 0 & u_{2,2} & 0 \\ 0 & 0 & u_{3,3} \end{bmatrix} \quad (2.11)$$

and the total strain rate (total velocity divergence) of the cylinder for the zero dimensional approach is equal to [49]:

$$S_{ij}^{\text{tot}} = u_{i,j}^{\text{tot}} = -\frac{1}{\rho} \frac{d\rho}{dt} \quad (2.12)$$

In the case of combustion chamber, the equation (2.12) represents the total strain rate of the cylinder deformation in normal direction caused by the piston motion (Figure 7).

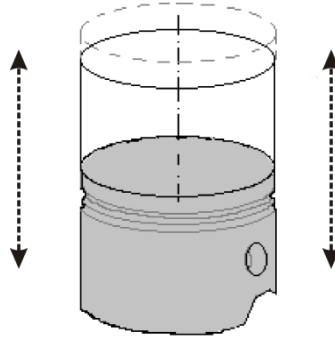


Figure 7. Illustration of axial cylinder deformation caused by piston motion (flat geometry of cylinder head and piston).

Derivation of zero dimensional equations for the  $k$ - $\varepsilon$  turbulence model is based on the sum of differential equations (2.8) and (2.9) over the index  $i$  for the three-dimensional case. If a homogeneous and isotropic flow field [39] is assumed, the convection and diffusion terms do not exist. Finally, the transport equations, with the default values of  $C_1 = 1.44$  and  $C_3 = -0.373$ , can be written as [5]:

$$\frac{dk}{dt} = \frac{2}{3} \frac{k}{\rho} \frac{d\rho}{dt} - \varepsilon \quad (2.13)$$

$$\frac{d\varepsilon}{dt} = \frac{4}{3} \frac{\varepsilon}{\rho} \frac{d\rho}{dt} - C_2 \frac{\varepsilon^2}{k} \quad (2.14)$$

where  $C_2 = 1.92$  is the tunable model constant [1, 5, 6, 10, 43-47]. First terms on the RHS of equations (2.13) and (2.14) represent rates of the production of turbulent kinetic energy and its dissipation and the last terms correspond to the destruction of both variables. Production terms of both equations are modeled according to the rapid distortion theory [50, 51]. Since equations (2.13) and (2.14) neglect convective and diffusion effects, they do not include changes in turbulent kinetic energy and its dissipation associated with combustion. By

assuming the equilibrium between the production and the dissipation of the turbulent kinetic energy, transport equations (2.13) and (2.14) can be further extended by including the diffusion term treated as a boundary flux between the burned and the unburned mass [5, 50]:

$$\frac{dk}{dt} = \frac{2}{3} \frac{k}{\rho} \frac{d\rho}{dt} - \frac{2}{3} \frac{k}{\nu} \frac{d\nu}{dt} - \varepsilon \quad (2.15)$$

$$\frac{d\varepsilon}{dt} = \frac{4}{3} \frac{\varepsilon}{\rho} \frac{d\rho}{dt} + \frac{5}{12} \frac{\varepsilon}{\nu} \frac{d\nu}{dt} - C_2 \frac{\varepsilon^2}{k} \quad (2.16)$$

where  $\nu$  (m<sup>2</sup>/s) is the kinematic viscosity of the cylinder mixture. Transport equations (2.15) and (2.16) may also be written as:

**Rate of change = Production + Diffusion – Dissipation**

(2.17)

where the diffusion term represents the rate of change in the turbulent kinetic energy or its dissipation rate associated with combustion. The full derivation of the 0-D differential equations of the  $k$ - $\varepsilon$  turbulence model from the multi-dimensional transport equations is given in the Appendix.

If the final form of the transport equations (2.15) and (2.16) of the zero dimensional model are compared to the multi-dimensional transport equations (2.8) and (2.9), one can notice that the zero dimensional model neglects the following:

- convective change in turbulent kinetic energy and its dissipation rate;
- diffusion change in turbulent kinetic energy and its dissipation rate;
- shear effect which occurs in the production term  $P$  – total tangential deformation of the cylinder do not exist;
- second order term in the dilatation effect of the production ( $u_{k,k}^2$ ).

Although the specified particular effects in the 0-D turbulence model are neglected, the differential equations of the 0-D model will be modified so that the neglected effects on the overall turbulence level will be compensated.

### 2.1.3. Modification of $k$ and $\varepsilon$ differential equation for 0-D model

The  $k$ - $\varepsilon$  turbulence model has two transport equations: one for the turbulent kinetic energy (equation (2.15)) and the other for its dissipation rate (equation (2.16)). Before the



analysis of the differential equations is made, it is necessary to express the kinematic viscosity and its time derivative that is used in equations (2.15) and (2.16). Generally, the kinematic viscosity is the ratio between the dynamic viscosity  $\mu$  and the density  $\rho$  of the fluid. Therefore, the time derivative of kinematic viscosity is equal to:

$$\frac{d\nu}{dt} = \frac{\frac{d\mu}{dt} \cdot \rho - \frac{d\rho}{dt} \cdot \mu}{\rho^2} \quad (2.18)$$

The calculation of the dynamic viscosity is based on an empirical correlation and is a function of fluid temperature  $T$ :

$$\mu = 17.1 \cdot 10^{-6} \cdot \left( \frac{T}{273.15} \right)^{\frac{3}{2}} \cdot \frac{383.15}{(T + 110.4)} \quad (2.19)$$

The time differentiation of equation (2.19) leads to:

$$\frac{d\mu}{dt} = 17.1 \cdot 10^{-6} \cdot 383.15 \cdot \left( \frac{\left( \frac{3}{546.2} \cdot \left( \frac{T}{273.15} \right)^{\frac{1}{2}} \cdot \frac{dT}{dt} \right) \cdot (T + 110.4) - \left( \frac{T}{273.15} \right)^{\frac{3}{2}} \cdot \frac{dT}{dt}}{(T + 110.4)^2} \right) \quad (2.20)$$

Temperature derivative of cylinder mixture has significant influence on the change of dynamic viscosity, which can be seen in equation (2.20). This derivative can be calculated in two ways:

- a) Temperature derivation includes the total temperature increase due to effects of:
  1. compression and expansion,
  2. combustion.
- b) Temperature derivative does not include the influence of combustion. Its calculation is based on thermodynamic changes of in-cylinder mixture caused only by compression and expansion.

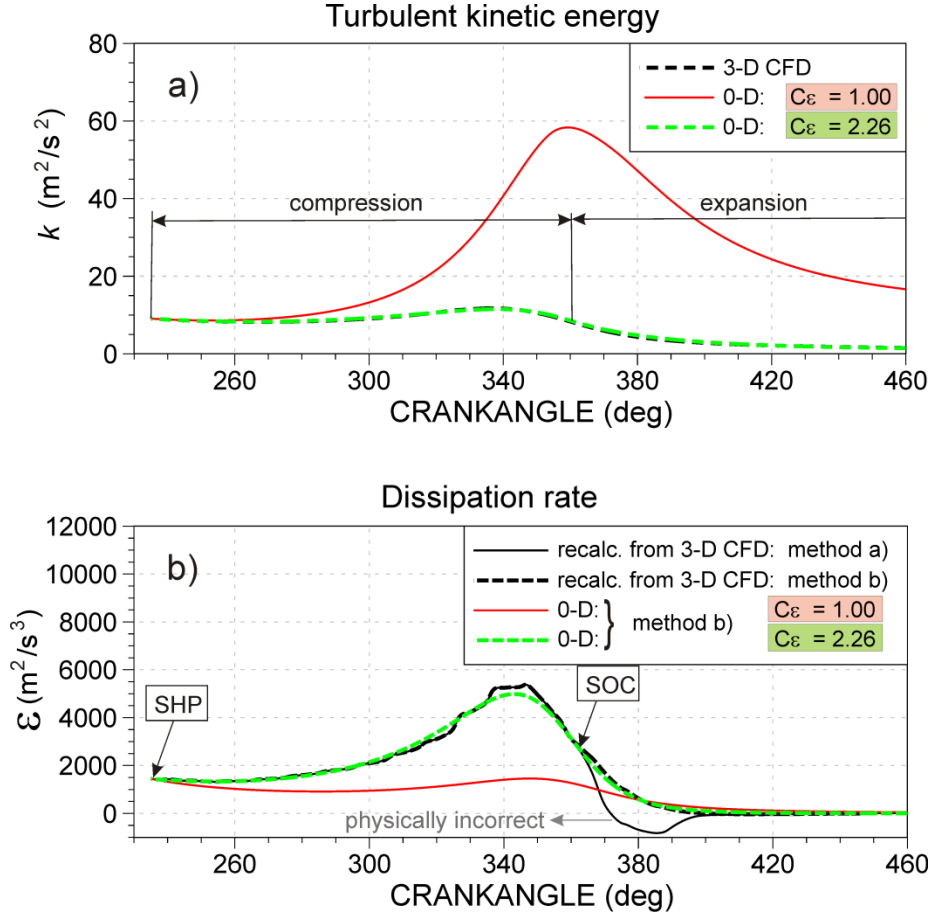


Figure 8. Example of turbulent kinetic energy (a) and its dissipation rate (b) during the high pressure cycle; recalculated dissipation rate profiles (black lines in bottom diagram) are defined from the 3-D CFD results of the turbulent kinetic energy (dashed black line in upper diagram).

During the compression, the mean kinetic energy decreases because the large scale flow structures decompose to the smaller scales increasing the turbulent kinetic energy that can be observed in upper diagram of Figure 8.

According to the energy cascade phenomenon the total production of the turbulent kinetic energy is always positive and therefore the production term of the turbulent kinetic energy in equation (2.15) is restricted only to the positive values:

$$\frac{dk}{dt} = \max \left( 0, \frac{2}{3} \frac{k}{\rho} \frac{d\rho}{dt} \right) - \frac{2}{3} \frac{k}{\nu} \frac{d\nu}{dt} - \epsilon \quad (2.21)$$

The profile of the turbulent kinetic energy during the high pressure cycle calculated by 3-D CFD is shown in Figure 8 a) with the black dashed line. The main prerequisite for correct prediction of turbulent kinetic energy is the correct calculation of its dissipation rate. By using the profile of turbulent kinetic energy calculated by 3-D CFD and by using profiles of total

fluid density, kinematic viscosity and their time derivatives calculated by 0-D simulation model, in which the in-cylinder temperature and pressure matched well with the 3-D CFD solution. By equation (2.21) it is possible to calculate the profile of dissipation rate  $\varepsilon$  that would give match to the 3-D CFD profile of turbulent kinetic energy during the high pressure cycle. In the following text this profile of  $\varepsilon$  will be called "desired" profile of  $\varepsilon$ . The "desired" profiles of dissipation rate of turbulent kinetic energy are shown with black lines in bottom diagram of Figure 8. The initial dissipation rate at the start of high pressure is calculated by equation (2.21) with the initial derivative of the turbulent kinetic energy defined by last two values of the turbulent kinetic energy calculated by 3-D CFD before the start of compression. The first profile shown with solid line is calculated by equation (2.21) with the calculation of kinematic viscosity and its time derivative that includes the overall change in temperature caused by compression (expansion) and combustion (method a) on page 19). The second profile shown with black dashed line is calculated with the temperature profile that does not include the influence of combustion (method b) on page 19). It can be observed in Figure 8 that the black solid profile of dissipation rate has negative values during the early part of expansion. Such behavior is physically incorrect because it is contradictory to the energy cascade phenomenon described previously (negative dissipation rate means that small scale turbulent eddies are generated from the internal energy of the fluid). Therefore, the adopted "desired" dissipation rate profile is the profile presented by black dashed line (Figure 8) and this profile has to be obtained from differential equation (2.16). When the equation (2.16) is applied to the 0-D model, the obtained dissipation rate is too small, and the turbulent kinetic energy is too large (red solid line in Figure 8). In order to achieve that the  $\varepsilon$  profile matches well the "desired" one, the new user-defined constant  $C_\varepsilon$  (-) that multiplies the production of the dissipation is introduced into the dissipation equation:

$$\frac{d\varepsilon}{dt} = C_\varepsilon \cdot \left( \frac{4}{3} \frac{\varepsilon}{\rho} \frac{d\rho}{dt} \right) + \frac{5}{12} \frac{\varepsilon}{\nu} \frac{d\nu}{dt} - C_2 \frac{\varepsilon^2}{k} \quad (2.22)$$

The new user-defined constant  $C_\varepsilon$  is called the dissipation constant of the high pressure cycle. It was found that by using the values of  $C_\varepsilon$  larger than 2.0 the dissipation rate profiles that the best fit "desired" profile of the dissipation and of the turbulent kinetic energy during the high pressure cycle is obtained. Such profiles are presented by dashed green lines in Figure 8. The full validation of the single zone  $k$ - $\varepsilon$  turbulence model that includes the modified differential

equations (2.21) and (2.22) and calculation of kinematic viscosity and its derivative by method b) is presented in fifth chapter.

## 2.2. Two zone $k$ - $\varepsilon$ turbulence model

As noted earlier, during the combustion period, the quasi-dimensional combustion model divides the cylinder mixture into two separate zones, burned and unburned zone. On the other hand, the turbulence model described above calculates only the mean turbulent kinetic energy and applies it to both zones. It is known from the combustion theory [33, 39] that physical properties of the unburned zone (in front of the flame) play the most important role in the combustion process. The turbulent kinetic energy of the unburned zone causes the convective deformation of the flame front, with additional transfer of momentum, heat and mass.

An analysis of single and two zone turbulence model formulations for the quasi-dimensional combustion modeling of SI engines was performed in [11]. They studied different turbulence model formulations including energy cascade (algebraic  $\varepsilon$  model I) and  $k$ - $\varepsilon$  approach. The simulation results of in-cylinder pressure achieved with the application of different formulations of single and two zone turbulence models were compared with the experimental pressure traces at several operating points. Although the rapid distortion and enhanced entrainment terms were introduced into single zone models, it was shown that the two zone turbulence models were able to predict the pressure curve during the combustion with a greater accuracy than the single zone models. It was also concluded that the two zone  $k$ - $\varepsilon$  turbulence model was consistently better in following the experimental pressure curve over the whole range of operating conditions that were analyzed [11]. Therefore, in order to be able to predict the combustion progress better and physically more accurate, the turbulence kinetic energies of both zones should be calculated separately. This section describes the extension of the single zone turbulence model into a two zone turbulence model.

The single zone model defined in Chapter 2.1.2 [52] is able to calculate the mean turbulent kinetic energy of the cylinder mixture well. This fact was exploited in the development of the two zone model. Instead of setting the model that will calculate the changes in turbulent kinetic energy of the burned and of the unburned zone [11], the two zone model calculates the total turbulent kinetic energy and the turbulent kinetic energy of the unburned zone. The turbulence values of the burned zone can then be explicitly calculated by the mean values of the cylinder mixture and by the turbulence values obtained in the unburned zone.

Results of the total turbulent kinetic energy and that of the unburned zone, calculated by 3-D CFD software, are shown qualitatively in Figure 9.

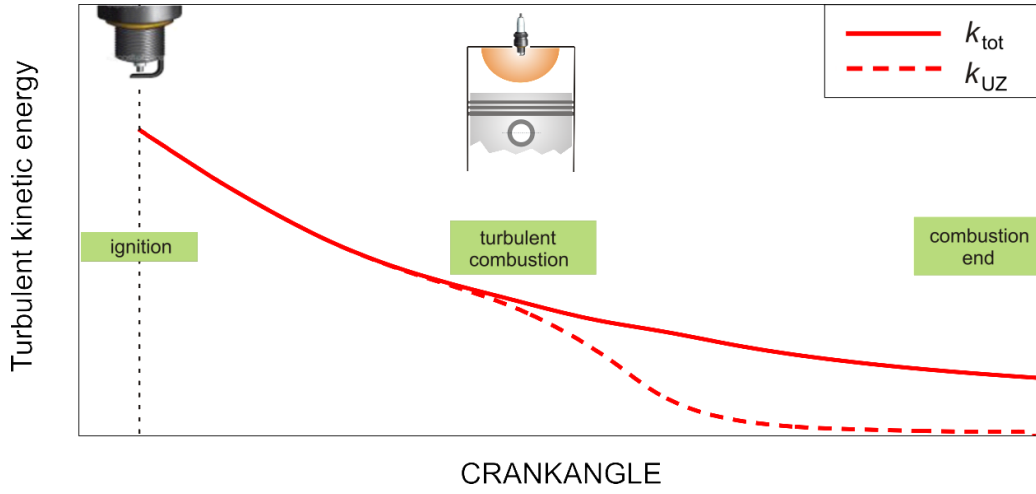


Figure 9. Qualitative profiles of turbulent kinetic energies (total and unburned zone) calculated by 3D-CFD simulation during combustion.

Before the activities on modeling of the two zone  $k$ - $\varepsilon$  turbulence model in 0-D environment are presented, a few requirements and conclusions from 3-D CFD results are shown:

1. Total turbulent kinetic energy of the cylinder mixture is equal to the sum of the turbulent kinetic energy of the burned and unburned zone:

$$k_{\text{tot}} = x_B \cdot k_{\text{BZ}} + (1 - x_B) \cdot k_{\text{UZ}} \quad (2.23)$$

where  $x_B$  (-) is burned mass ratio defined as the ratio between the burned and the total in-cylinder mass.

2. Total production of the turbulent kinetic energy of the cylinder mixture is equal to the sum of productions of the burned and unburned zone:

$$P_{\text{tot}} = x_B \cdot P_{\text{BZ}} + (1 - x_B) \cdot P_{\text{UZ}} \quad (2.24)$$

3. Total dissipation rate of the turbulent kinetic energy of the cylinder mixture is equal to the sum of dissipation rate of the burned and unburned zone:

$$\varepsilon_{\text{tot}} = x_B \cdot \varepsilon_{\text{BZ}} + (1 - x_B) \cdot \varepsilon_{\text{UZ}} \quad (2.25)$$

4. Turbulent kinetic energy of the unburned zone is always equal or lower than total turbulent kinetic energy:

$$k_{\text{UZ}} \leq k_{\text{tot}} \quad (2.26)$$

The physical quantities with the index “tot” denote specific quantities related to the total in-cylinder mass; “BZ” and “UZ” are related to the burned zone and unburned zone, respectively. When the total and unburned zone turbulent kinetic energies are known, the turbulent kinetic energy of the burned zone can easily be computed from equation (2.23).

It can be seen from Figure 9 that the turbulent kinetic energy of the unburned zone never exceeds the value of the total turbulent kinetic energy ( $k_{\text{UZ}} \leq k_{\text{tot}}$ ). If the burned and unburned zone turbulence are calculated separately by using differential equations of the turbulent kinetic energy and dissipation rate for each zone, the total in-cylinder turbulent kinetic energy is explicitly defined from equation (2.23). In order to simplify the two zone turbulence model as much as possible, the modeling strategy is based on the definition of unburned zone differential equation for  $k$  and  $\varepsilon$ , while the total in-cylinder turbulent kinetic energy is defined with the previously defined single zone turbulence model in Chapter 2.1.2. To obtain the same relation of profiles of the turbulent kinetic energy by using the 0-D simulation model, the production-to-dissipation ratio of the specific zones has to be controlled. The full control between the production-to-dissipation ratio of the total mixture and that of the unburned zone cannot be established because the burned zone turbulence quantities are unknown.

The production of turbulent kinetic energy is always positive [43]. Negative production of turbulent kinetic energy means that the small scale eddies are merged together creating large scale eddies, which is in contradiction to the energy cascade phenomenon described in the previous section. The dissipation rate of the turbulent kinetic energy is also always positive. Therefore, from equation (2.24) and (2.25), the following expressions can be written:

$$(P_{\text{tot}} - (1 - x_{\text{B}}) \cdot P_{\text{UZ}}) \geq 0 \quad (2.27)$$

$$(\varepsilon_{\text{tot}} - (1 - x_{\text{B}}) \cdot \varepsilon_{\text{UZ}}) \geq 0 \quad (2.28)$$

If conditions presented by equation (2.27) and (2.28) are not satisfied, corrections to the production and the dissipation rate of the unburned zone are made. The corrections are made by assuming that, when the conditions presented by equation (2.27) and (2.28) are not

satisfied, the production and the dissipation of the burned zone are 0. In that case, the correction to the production and the dissipation of the unburned zone is made in the following manner:

$$P_{UZ} = \left( \frac{1}{1 - x_B} \right) \cdot P_{tot} \quad (2.29)$$

$$\varepsilon_{UZ} = \left( \frac{1}{1 - x_B} \right) \cdot \varepsilon_{tot} \quad (2.30)$$

Before the specific modification and extension of differential equations for 0-D model are made, the analysis of "desired" profile of the turbulent kinetic energy calculated by 3-D CFD model is performed. The turbulent kinetic energy of unburned zone calculated by 3-D CFD model is shown with black dashed curve in Figure 10 a). In order to obtain such profile by using the 0-D two zone turbulence model, the profile of dissipation rate of the unburned zone has to follow the profile shown with the black dashed line in Figure 10 b). This profile is calculated from  $k_{UZ}$  calculated by 3-D CFD and by using following equation (similar to the procedure of calculating "desired"  $\varepsilon$  profile in the single zone model):

$$\frac{dk_{UZ}}{dt} = \max \left( 0, \frac{2}{3} \frac{k_{UZ}}{\rho_{UZ}} \frac{d\rho_{UZ}}{dt} \right) - \frac{2}{3} \frac{k_{UZ}}{\nu_{UZ}} \frac{d\nu_{UZ}}{dt} - \varepsilon_{UZ} \quad (2.31)$$

where the density  $\rho_{uz}$  (kg/m<sup>3</sup>), kinematic viscosity  $\nu_{uz}$  (m<sup>2</sup>/s) of the unburned zone and their time derivatives are taken from 0-D calculation with the combustion model constants tuned so that the in-cylinder temperature is captured well. The above equation (2.31) is similar to the equation (2.21) with the exception that all physical quantities are related to the unburned mass. The dissipation rate of the unburned zone is defined with the differential equation similar to the equation (2.16):

$$\frac{d\varepsilon_{UZ}}{dt} = \max \left( 0, \frac{4}{3} \frac{\varepsilon_{UZ}}{\rho_{UZ}} \frac{d\rho_{UZ}}{dt} \right) + \frac{5}{12} \frac{\varepsilon_{UZ}}{\nu_{UZ}} \frac{d\nu_{UZ}}{dt} - C_2 \frac{\varepsilon_{UZ}^2}{k_{UZ}} \quad (2.32)$$

where constant  $C_2$  (-) is set to 1.92. If the equation (2.32) is applied on the 0-D model without the control of conditions shown in equations (2.27) and (2.28), the obtained profile of dissipation rate is significantly different than the "desired" one, (red solid line in Figure 10). It

is evident that such profile is significantly below the desired one resulting in the higher level of turbulent kinetic energy of the unburned zone. This also has significant influence on the combustion duration because the higher turbulent kinetic energy of the unburned zone speeds up the combustion rate. Therefore, the end of combustion that can be observed in Figure 10 is much earlier than in the 3-D CFD simulation. In order to increase the dissipation of the turbulent kinetic energy of the unburned zone, the differential equation (2.32) is extended (similar to equation (2.22) in single zone model):

$$\frac{d\varepsilon_{UZ}}{dt} = \max \left[ 0, C_{\varepsilon}^{UZ} \cdot \left( \frac{4}{3} \frac{\varepsilon_{UZ}}{\rho_{UZ}} \frac{d\rho_{UZ}}{dt} \right) \right] + \frac{5}{12} \frac{\varepsilon_{UZ}}{\nu_{UZ}} \frac{d\nu_{UZ}}{dt} - C_2 \frac{\varepsilon_{UZ}^2}{k_{UZ}} \quad (2.33)$$

where  $C_{\varepsilon}^{UZ}(-)$  is a new user-defined constant that multiplies the production term of the dissipation rate of unburned zone. Therefore, this constant is called dissipation constant of unburned zone.

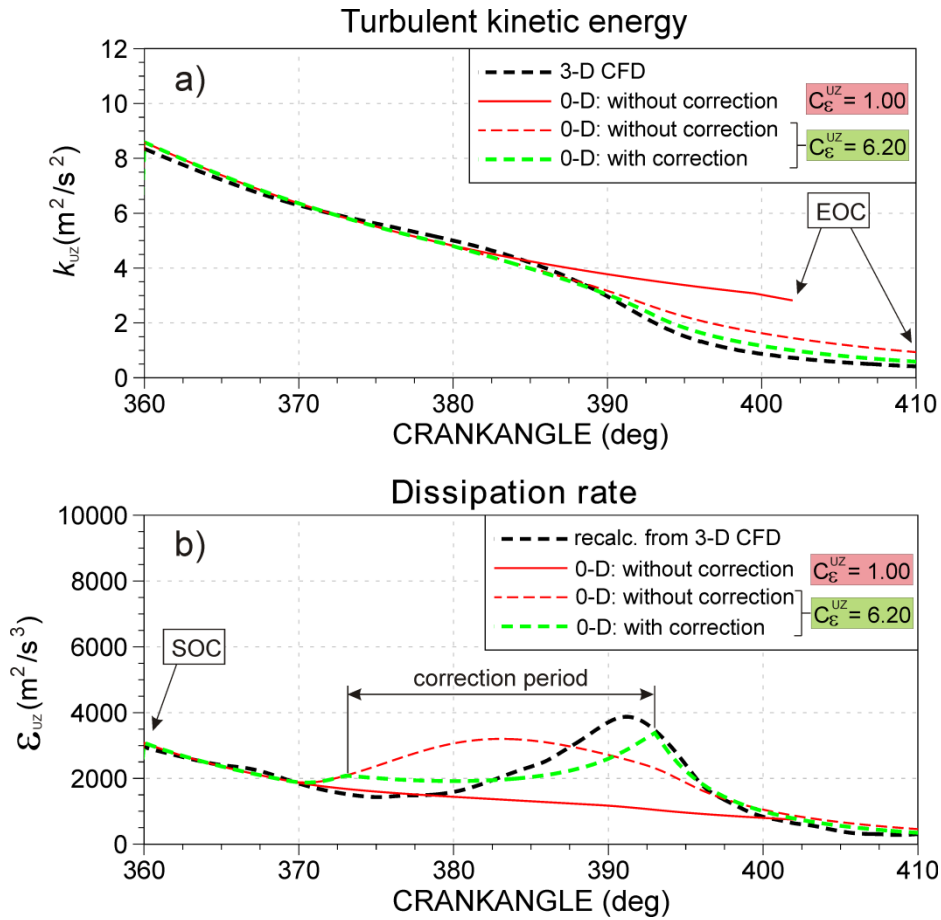


Figure 10. Example of turbulent kinetic energy (a) and dissipation rate (b) of unburned zone during combustion.



If the new user-defined constant is increased to  $C_{\epsilon}^{UZ} = 6.20$  the dissipation rate is higher which is shown with the red dashed curve in Figure 10. The dissipation rate of the unburned zone shown with the red dashed line is also calculated without the control of conditions presented by equations (2.27) and (2.28). The turbulent kinetic energy of the unburned zone in the case with  $C_{\epsilon}^{UZ} = 6.20$  and without correction is much better than the previous case, but still not close to the 3-D CFD solution. When the partial correction of production and dissipation rate of the unburned zone is performed by using the assumption that production and dissipation of burned zone are equal to 0 (equations (2.29) and (2.30)), and this corrections are applied when conditions specified in equation (2.27) and (2.28) are not satisfied, a new set of results is obtained. The results of dissipation rate and turbulent kinetic energy of unburned zone calculated by 0-D simulation model where the mentioned correction is taken into account is shown with the dashed green line in Figure 10. The obtained profiles of dissipation rate as well as the turbulent kinetic energy of the unburned zone are much closer to the "desired" 3-D CFD results than previous results.

When the two zone turbulence model is applied, the equations (2.31) and (2.33) of the turbulence of unburned zone are calculated simultaneously with the equations (2.21) and (2.22) for the total in-cylinder turbulence. The new approach for the simple calculation of unburned zone turbulence is extensively validated in the fifth chapter where 0-D results are compared with the available 3-D CFD solutions for different engines and operating conditions.

### **2.3. Single zone $k$ - $\epsilon$ turbulence model – gas exchange**

The single zone  $k$ - $\epsilon$  turbulence model described under the Chapter 2.1 was applied only during the high pressure cycle. The initial conditions (at the start of high pressure cycle) of turbulent kinetic energy and its dissipation rate were specified from the 3-D CFD results. In order to eliminate the turbulence model dependency on external specification of the initial conditions that have to be specified at IVC and to close the loop in the 0-D turbulence simulation modeling, the analysis of turbulence was extended to the gas exchange process.

The major source of in-cylinder turbulence is the shear flow around the intake valve. The recirculation flow around the intake valve is highly unstable and breaks down as soon as the intake process terminates. The strong turbulent flow during the intake significantly influences the 3-D flow structures in the cylinder, which is one of the major features of turbulence [10].

Equation (2.12) represents the total velocity divergence for the cylinder control volume that is applicable if the mass flow on the boundary of the control volume, shown in Figure 11, does not exist. During the intake process which is illustrated in Figure 11, the fresh gas mixture flows into the combustion chamber increasing the mean kinetic and turbulent kinetic energy of the in-cylinder mass. The variation of density over time takes into account the effect of the change in control volume, but cannot capture the influence of strong inflow that dominates during the intake process. In order to transform the multi-dimensional differential equations (2.8) and (2.9) into the differential equations of 0-D approach that are applicable during the gas exchange, the new source term  $S_\phi$  (kg/m<sup>3</sup>s) of continuity equation is defined:

$$\rho_{,t} + \rho u_{i,j} = S_\phi \quad (2.34)$$

With initial equation set to (2.34) the total velocity divergence of the cylinder control volume can be expressed as:

$$S_{ij}^{\text{tot}} = u_{i,j}^{\text{tot}} = -\frac{1}{\rho} \left( \frac{d\rho}{dt} + \frac{q_m^{\text{in}}}{V_c} \right) \quad (2.35)$$

where  $q_m^{\text{in}}$  (kg/s) is the intake mass flow and  $V_c$  (m<sup>3</sup>) is the instantaneous cylinder volume. By applying equation (2.35) to the transport equations (2.8) and (2.9) and by neglecting the diffusion and shear terms, the following equations are derived:

$$\frac{dk}{dt} = S_{\text{in}} \cdot \left( \frac{q_m^{\text{in}}}{m_c} U_{\text{ivcs}}^2 \right) + \frac{2}{3} \frac{k}{\rho} \frac{d\rho}{dt} - \frac{2}{3} \frac{k}{\nu} \frac{d\nu}{dt} - \varepsilon \quad (2.36)$$

$$\frac{d\varepsilon}{dt} = C_{\text{in}} \cdot \left( \frac{4}{3} \frac{q_m^{\text{in}}}{m_c} \varepsilon \right) + C_\varepsilon \left( \frac{4}{3} \frac{\varepsilon}{\rho} \frac{d\rho}{dt} \right) + \frac{5}{12} \frac{\varepsilon}{\nu} \frac{d\nu}{dt} - C_2 \frac{\varepsilon^2}{k} \quad (2.37)$$

where  $S_{\text{in}}$  (-) and  $C_{\text{in}}$  (-) are new user-defined constants, while the  $U_{\text{ivcs}}$  (m/s) is the instantaneous mean flow velocity at the intake valve cross section. The first user-defined constant  $S_{\text{in}}$  is called the intake  $k$  production constant and  $C_{\text{in}}$  is the intake  $\varepsilon$  production constant.

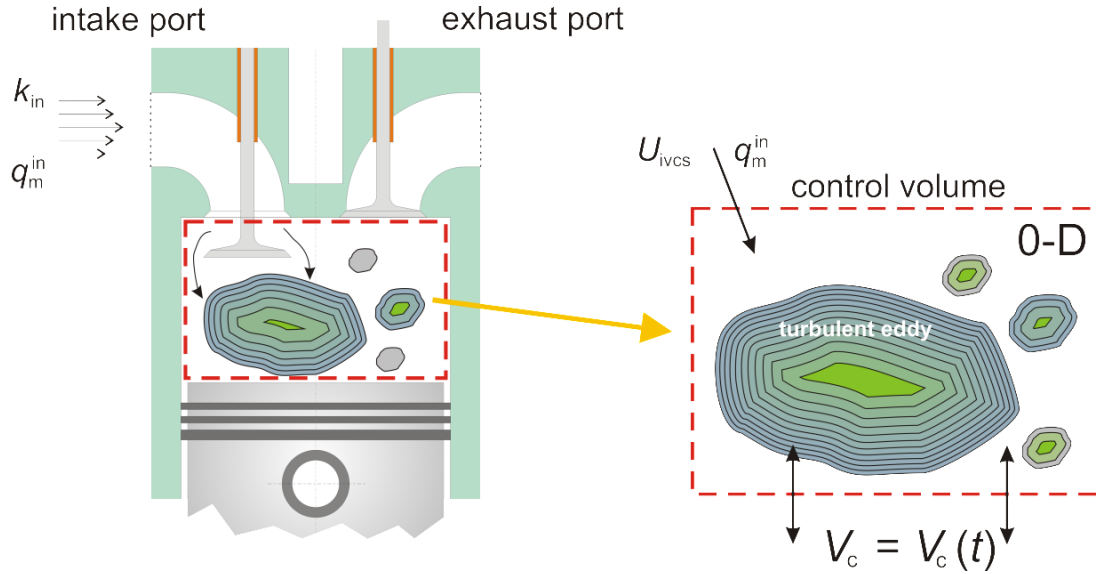


Figure 11. Illustration of the engine intake process and turbulent eddy generated by the strong flow over the intake valve.

Since the isotropic and homogeneous turbulent flow field is assumed in derivation of equation (2.36) and (2.37), the intake  $k$  production constant  $S_{in}$  and the intake  $\varepsilon$  production constant  $C_{in}$  are used to calibrate the model so that the effects of anisotropy and non-homogeneity of turbulent flow field that is dominant during the gas exchange period are captured. The new source term of equation (2.36) takes into account the influence of mean flow kinetic energy, described by the instantaneous mean velocity  $U_{ivcs}$  at the intake valve cross section, on the in-cylinder turbulent kinetic energy. The same first term of differential equation of the turbulent kinetic energy (2.36) is defined in [53] by the time derivative of kinetic energy of moving part where the intake  $k$  production constant was set to  $8 \cdot 10^{-4}$ .

The validation of the newly developed differential equations (2.36) and (2.37) is performed in fifth chapter and 0-D simulation results are compared with the 3-D CFD solutions. The approach where the 0-D results of in-cylinder turbulence were compared with the 3-D CFD results was also used in [14]. In [14] the extended 0-D turbulence model based on the  $K-k$  (algebraic  $\varepsilon$  model I) approach was employed. The model is developed and adopted only for the tumble in-cylinder flow assuming an ellipsoidal shape of the mean flow field, as it is shown in Figure 12. By assuming that the average gradient (for the entire cylinder domain) of the tumble velocity  $V_\theta$  is proportional to the ratio of mean flow velocity and integral length scale  $L_I$  that represents the averaged diameter of the turbulent eddy, Watanabe et al. [14] expressed the total production  $P_k$  of the in-cylinder turbulence as follows:

$$P_k = P_{k, \text{norm}} + P_{k, \text{shear}} = \frac{2}{3} \frac{k}{\rho} \frac{d\rho}{dt} + C_T \mu_t \left( \frac{U_1}{L_T} \right)^2 \quad (2.38)$$

where  $U_1$  (m/s) is average velocity,  $\mu_t$  (Pa·s) is turbulent viscosity and  $C_T$  (-) is model constant. The production of the turbulent kinetic energy consists of two terms where the first term represents the effects of normal fluid stress while the second takes into account the Reynolds shear stress.

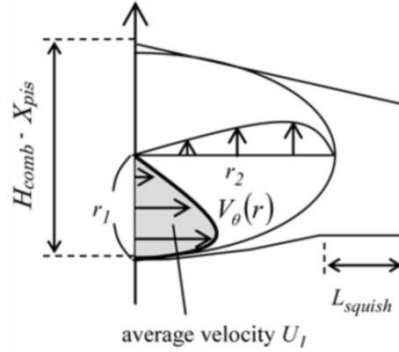


Figure 12. Ellipsoidal velocity distribution of in-cylinder tumble flow defined in [14].

If the term for the production of turbulent kinetic energy defined by [14] is compared with the one defined in equation (2.36), it is evident that the 0-D turbulence model presented by equations (2.36) and (2.37) neglects the shear effects on the production of turbulent kinetic energy. The turbulence model of Watanabe et al. has 6 constants that have to be calibrated for the considered engine. Two of them are related to the intake, two constants are used for the definition of integral length scale, one for the production and one for the turbulence dissipation term. Although the turbulence model presented by equations (2.36) and (2.37) assumes zero-velocity gradient and neglects the shear effects, it represents simple and more general 0-D description of in-cylinder turbulence which can be used for arbitrary flow structure in the cylinder, and uses only 3 tuning turbulence constants:

- $S_{in}$  - the intake  $k$  production constant;
- $C_{in}$  - the intake  $\varepsilon$  production constant;
- $C_\varepsilon$  - the dissipation constant of the high pressure cycle.

The first constant influences the turbulence production during the intake process, while the remaining two constants are dissipation constants that define the dissipation of turbulent kinetic energy during the intake process and high pressure cycle, respectively. These constants are calibrated within the fifth chapter where the 0-D results of in-cylinder turbulence are compared with the available 3-D CFD data.

### 3. Fundamentals of spark ignition and modeling

The combustion process of SI engines is an extremely complex combination of phenomena including the arc discharge, the fuel oxidation chemistry, heat losses in a complex geometry, and the role of turbulence over a wide range of length and time scales. The combustion process of SI engine is initiated by electric spark discharge that occurs between the spark plug electrodes. The electric spark life is generally divided into three phases: breakdown, arc and glow phase. The breakdown phase lasts a few nanoseconds during which the spark current rises to a first current maximum of several hundred amperes. After that, the voltage between the electrodes drops to very low values of around 100 V and this phase is known as arc phase. The discharge of electric energy accumulated in the coil and high voltage cable occurs during the time of 1  $\mu$ s. Finally, after the breakdown and arc phase, the glow phase occurs delivering the largest portion of the originally stored electrical energy into the electric spark. The duration of this phase depends on the engine ignition system and on the electric energy available in the secondary circuit. In the case of TCI (Transistorized Coil Ignition) system the glow phase lasts for about 2 ms. The glow phase of electric spark corresponds to the visible spark observed in experiments [28] and it lasts as long as the energy in the secondary electric circuit is larger than zero.

The size of the spark-generated flame kernel formed during the glow phase depends on the breakdown energy that the ignition system delivers to the surrounding gas. The local gas temperatures between the spark plug electrodes can reach extremely large values of order 60000 K resulting with the rapid heat transfer to the electrodes [54]. Therefore, the early flame kernel growth is non adiabatic process. A number of experimental studies have shown that the initial flame kernel formed within the few microseconds after the spark onset is about 1 mm in diameter [13, 54].



Figure 13. Visualization of the early flame kernel growth from the experiment [55] indicating the effects of local bulk flow and turbulence in the vicinity of the spark plug.

As the flame kernel grows, a gradual transition to the turbulent flame occurs due to the effects of local flow that increases the distortion of a very thin laminar-like reaction zone. On the other hand, the local bulk flow at the spark plug location convects the kernel center away

from the spark plug electrodes. The mentioned effects on the early flame kernel growth can be seen in Figure 13.

### 3.1. Ignition modeling in multidimensional models

Two more recent developments in terms of modeling of ignition phenomena in 3-D CFD simulations are Discrete Particle Ignition Kernel (DPIK) and Arc and Kernel Tracking Ignition Model (AKTIM) [56]. In quasi-dimensional combustion models ignition phenomena and early flame kernel growth are usually not considered. It is assumed that such process of flame initiation lasts for about 0.2 ms and the flame front is approximated as fully spherical with about 2 mm in radius.

Discrete Particle Ignition Kernel model represents the single flame kernel model and was developed by Reitz et al. [57-61]. It tracks the early flame propagation using the *G-equation* formulation. At the prescribed time of ignition, a single spherical flame kernel with radius 0.5 mm is formed at the center between the spark plug electrodes. The flame kernel growth rate is function of burned and unburned density, turbulent burning velocity and plasma expansion speed. Once the flame kernel exceeds the radius related to the integral length scale, the ignition model switches to the combustion model. The DPIK model is usually coupled to the *G-equation level-set* combustion model and is based on several simplifications:

- A criterion for successful ignition is not taken into account.
- The modeling of electric arc is omitted.
- The effects of spark-channel elongation and re-strikes on the position of flame kernel and its growth are not considered.
- The flame kernel is not shifted due to local flow velocity and remains in spherical shape.

The AKTIM is also used for the description of flame kernel process in 3-D CFD simulations. It is based on the four sub-models to describe different stages of the flame kernel development. The spark plug geometry is taken into account by using the marker particles and a drag force is induced onto the flow field. The electric arc is described by the Lagrangian particles whose position is defined with the local flow field in the vicinity of the spark plug taking into account the spark energy deposition into the arc. Compared to the DPIK, the AKTIM introduces several thousand particles (~ 4000) representing the gravity center of possible flame kernels. The flame kernels are shifted due to local flow velocity and receive the energy from the electric spark. When the critical energy is reached, ignition occurs, and the flame kernel is allowed to expand. The AKTIM does not apply flame extinction criteria

and neglects the fundamental effects leading to successful ignition or flame front propagation. The AKTIM is active as long as the specific portion of in-cylinder mass is burned. After that, the combustion process is usually described by the Coherent Flame Model.

### 3.2. Background of Quasi-Dimensional Ignition Model

It is already mentioned that the detail ignition phenomena and early flame kernel growth were not considered with the previous quasi-dimensional combustion model. It is assumed that the ignition period lasts about 0.2 ms and that the flame reaches the radius of about 2 mm. Such simplification of ignition delay modeling is not fully promising because the burning speed of the flame kernel depends on the energy released by the ignition system, heat losses from kernel to the spark plug electrodes, local fluid flow and mixture state. In order to include more comprehensive and detailed description of ignition phenomena and early flame kernel growth, the new quasi-dimensional ignition model (QDIM) is developed. The model is based on the AKTIM model that consists of four main sub-models: the electric circuit sub-model, early flame kernel growth sub-model, electric spark sub-model, and spark plug geometry sub-model. More details about each sub-model are given in the following sections.

### 3.3. The electric circuit sub-model

The simplified electric scheme of the engine ignition system is shown in Figure 14. At the prescribed time of ignition the switch is opened and about 60 % of electric energy stored in the primary inductance  $L_p$  (H) is transferred to the spark plug. The rest of electric energy is dissipated by the secondary inductance  $L_s$  (H). In order to simplify the model, only the secondary electric circuit is considered [62] and its initial energy at the time of ignition is given as an input parameter of the ignition sub-model.

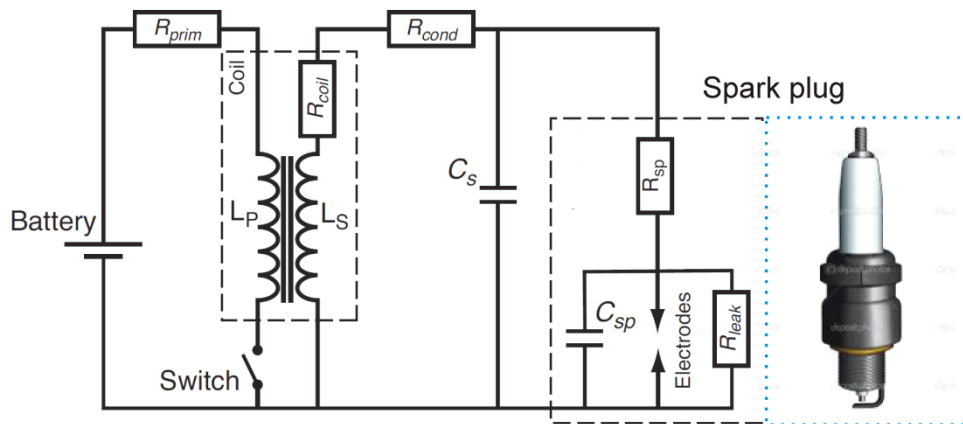


Figure 14. Simplified electric scheme of an engine ignition system with the spark plug.

A few microseconds after the prescribed time of ignition, the spark is formed between the electrodes. The spark life is generally divided into three phases: breakdown, arc and glow phase. The first two phases last a few  $\mu\text{s}$  and therefore are not modeled within the presented ignition model, but they are efficient in transmitting energy to the fresh gases. The breakdown voltage  $V_{\text{bd}}$  (kV) between the electrodes is calculated as [63]:

$$V_{\text{bd}} = 4.3 + 13.6 \cdot \frac{p}{T} + 324 \cdot \frac{p}{T} \cdot d \quad (3.1)$$

where  $p$  (bar) is instantaneous in-cylinder pressure,  $T$  (K) is in-cylinder temperature and  $d$  (mm) is gap distance. The equation (3.1) is analyzed over different in-cylinder pressures that ranges from 1 bar to 20 bars and over different temperatures from 300 K to 1000 K. The breakdown voltage  $V_{\text{bd}}$  as a function of in-cylinder pressure and temperature for the different gap distances is shown as 3-D plots in Figure 15.

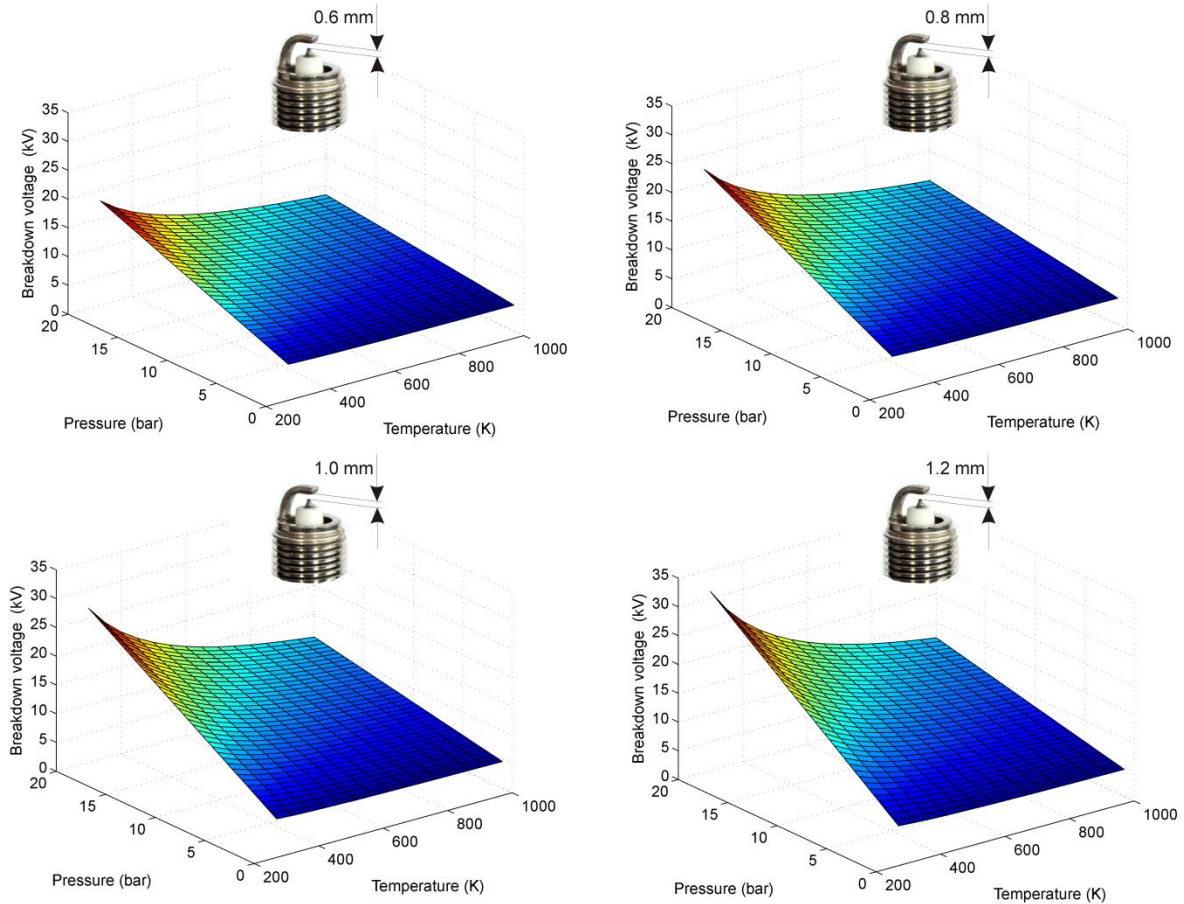


Figure 15. Breakdown voltage as a function of in-cylinder pressure and temperature for different gap distances ( $d = 0.6 - 1.2$  mm).

The breakdown energy  $E_{\text{bd}}$  (J) is approximately given by relation:



$$E_{bd} = \frac{V_{bd}^2}{C_{bd}^2 d} \quad (3.2)$$

where  $C_{bd}$  ( $V/\sqrt{J \cdot mm}$ ) is breakdown constant. The voltage between electrodes during the glow phase that corresponds to the visible electric spark observed in experiments is given by the relation:

$$V_{ie}(t) = V_{cf} + V_{af} + V_{cg} \quad (3.3)$$

where  $V_{cf}$  (V) and  $V_{af}$  (V) are cathode and anode voltage fall defined as input parameters. The voltage between the electrodes  $V_{cg}$  (V) depends on the spark length  $l_{spk}$  (mm), the electric current in the secondary circuit  $i_s$  (A) and on the in-cylinder pressure  $p$  (bar):

$$V_{cg} = C_{cg} \cdot l_{spk} \cdot i_s^{-0.32} p^{0.51} \quad (3.4)$$

where  $C_{cg}$  (-) is the voltage constant defined by the user.

The electric current of the secondary electric circuit is given by the relation:

$$i_s = \sqrt{\frac{2E_s}{L_s}} \quad (3.5)$$

where  $L_s$  (H) is secondary circuit inductance. The electric energy of secondary electric circuit  $E_s$  (J) is calculated by the following differential equation:

$$\frac{dE_s(t)}{dt} = -R_s i_s^2(t) - V_{ie} i_s(t) \quad (3.6)$$

where  $R_s$  ( $\Omega$ ) is the resistance of the secondary electric circuit. The differential equation (3.6) defines the duration of the visible spark; when the electric energy of the secondary circuit falls to 0 the electric spark disappears. The initial electric energy of the secondary circuit  $E_s(0)$  is defined as an input data.

### 3.4. Early flame kernel growth

After ignition, the progress of flame kernel is determined by the progress of the excess energy of kernel  $E_k$  (J) and the burned mass in kernel  $m_k$  (kg):

$$\frac{dE_k}{dt} = Q_E - Q_W \quad (3.7)$$

$$\frac{dm_k}{dt} = \rho_{UZ} \cdot S_K \cdot U_{L,eff} \quad (3.8)$$

where  $Q_E$  (W) is the supplied electric power,  $Q_W$  (W) is the kernel heat loss,  $\rho_{uz}$  (kg/m<sup>3</sup>) is unburned zone density,  $S_K$  (m<sup>2</sup>) is the free flame kernel surface area and  $U_{L,eff}$  (m/s) is the effective laminar flame speed. The initial kernel excess of energy is  $E_k(0) = 0.6 \cdot E_{bd}$  as the estimation of the energy that is received from the breakdown and arc phase. This means that only 60 % of the breakdown electric energy is transferred to the flame kernel [64]. The initial flame kernel radius is set to 0.5 mm as it is proposed in [65, 66]. The supplied electric power and the kernel heat loss are calculated as:

$$Q_E = V_{cg} \cdot i_s \quad (3.9)$$

$$Q_W = k_w \cdot S_e \cdot (T_K - T_{SP}) \quad (3.10)$$

where  $k_w$  (W/(m<sup>2</sup>K)) is heat transfer coefficient,  $S_e$  (m<sup>2</sup>) is the instantaneously entrained spark plug surface area by the flame kernel,  $T_K$  (K) is the flame kernel temperature and  $T_{SP}$  (K) is the spark plug temperature. The heat transfer coefficient and the spark plug temperature are defined by the user as input parameters of the ignition sub-model.

The free flame kernel surface  $S_K$  (m<sup>2</sup>) is given by the relation:

$$S_K = 4\pi \cdot \left( \frac{3m_k}{4\pi\rho_k} \right)^{\frac{2}{3}} \cdot F_{str} \quad (3.11)$$

with the flame kernel density  $\rho_k$  (kg/m<sup>3</sup>) calculated as:

$$\rho_k = \rho_{BZ} \cdot \left( 1 + \frac{E_k}{m_k c_{p,BZ} T_{BZ}} \right)^{-1} \quad (3.12)$$

where  $c_{p,BZ}$  (J/(kgK)) is the specific heat capacity of burned gases. The kernel density depends on the burned gas density and kernel excess of energy. When the kernel excess of energy is negative (heat transfer is higher than supplied electric power), the flame kernel temperature is lower than the burned gas temperature. The flame kernel temperature  $T_K$  is calculated from the state equation of ideal gas with the flame kernel density defined from equation (3.12):

$$T_K = \frac{p}{\rho_k \cdot R_{BZ}} \quad (3.13)$$

where  $R_{BZ}$  (J/kgK) is the individual gas constant of the burned zone.

The distortion factor  $F_{str}$  (-) of the flame kernel free surface is defined by the ratio between the instantaneous spark length  $l_{spk}$  (mm) and the gap distance  $d$  (mm) between the electrodes:

$$F_{str} = \left( \frac{l_{spk}}{d} \right)^{\frac{1}{3}} \quad (3.14)$$

The effective laminar flame kernel speed  $U_{L,eff}$  is calculated by the expression proposed and used in [25, 67]:

$$U_{L,eff} = S_L \cdot \left( \frac{T_K - T_q}{T_{ad} - T_q} \right) \quad (3.15)$$

where  $S_L$  (m/s) is the laminar flame speed [68] used in the previous fractal combustion model,  $T_q$  (K) is the flame quenching temperature (user-defined parameter) and  $T_{ad}$  (K) is the adiabatic flame temperature [25].

The calculation of the flame kernel growth lasts as long as the burned mass of the kernel does not reach the critical value defined by the following relation:

$$m_{k,crit} = 4\pi \cdot d \cdot r_0^2 \quad (3.16)$$

where  $r_0$  (m) is the assumed radius of the flame kernel that is large enough for the wrinkling of its surface to become significant and to be considered as turbulent flame. This is adjustable model parameter that has to be calibrated for the certain engine geometry. In some 3-D CFD simulation models of SI engine combustion the early flame kernel growth is calculated as long as the flame kernel radius is lower than the critical radius which is related to the integral length scale of the flow field as it is described in [69].

If the calculation of the flame kernel growth (ignition delay) is longer than the period for which the electric spark exists, the distortion factor  $F_{str}$  of the flame kernel surface is defined according to the fractal theory:

$$F_{str} = \left( \frac{L_I}{l_k} \right)^{D_3 - 2} \quad (3.17)$$

where  $L_I$  (m) and  $l_k$  (m) are the maximum and minimum integral length scales of the turbulent eddies defined by the applied  $k-\varepsilon$  turbulence model, respectively. The fractal dimension  $D_3$  (-) is fixed to 2.05 to reproduce the wrinkling of the flame front due to the effects of different turbulent eddies.

### 3.5. Modeling of electric spark and spark gap flow

Modeling of spark length is very important because it influences the voltage between the electrodes (see equation (3.4)) and the strain rate of the free kernel surface [28]. In the proposed quasi-dimensional ignition model the electric spark is modeled by spark marker points whose positions are defined by the velocity profile between the spark plug electrodes, shown in Figure 16.

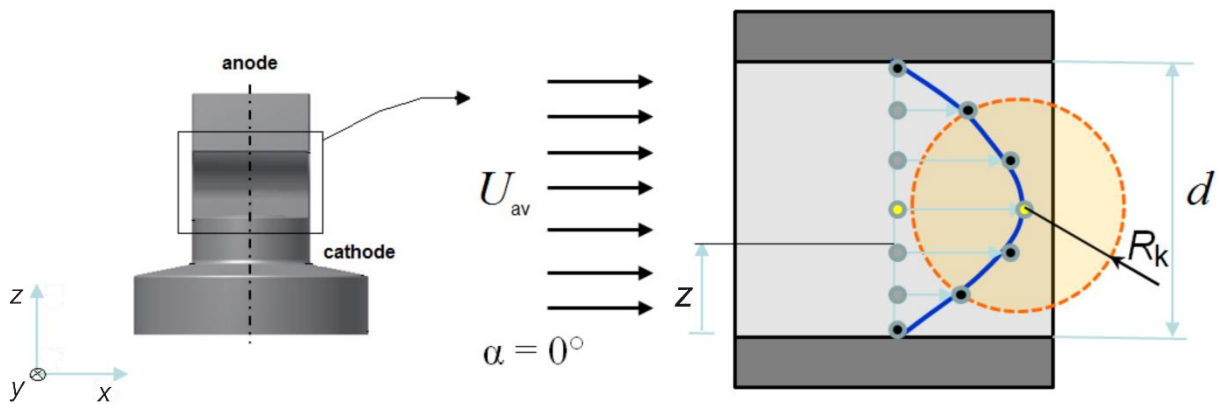


Figure 16. The spark cross flow and the electric spark represented by Lagrangian particles.

The velocity profile  $U(z)$  between the electrodes can be approximately given with the Hagen - Poiseuille flow [70]:

$$U(z) = -\frac{1}{2\mu} \cdot \frac{dp}{dx} \cdot d^2 \cdot \frac{z}{d} \cdot \left(1 - \frac{z}{d}\right) \quad (3.18)$$

where  $\mu$  (Pa·s) is dynamic fluid viscosity and  $z$  (m) is the arbitrary distance from one electrode to the other ( $0 \leq z \leq d$ ). The pressure drop  $dp/dx$  is calculated as:

$$\frac{dp}{dx} = \frac{12 \cdot \mu}{d^2} \cdot U_{av} \quad (3.19)$$

where  $U_{av}$  (m/s) is mean (macroscopic) velocity between the electrodes (cross-flow velocity). For a definition of the mean velocity in the spark gap region two options are available:

1. From the kinetic energy of the mean flow:  $U_{av} = \frac{1}{2} \cdot \sqrt{K}$  . This option requires the calculation of kinetic energy of the mean flow, which means that  $K$  differential equation have to be solved ( $K$ - $k$  turbulence model) and two turbulence model constants have to be specified.
2. From the turbulent kinetic energy  $k$  by directly correlating the local mean velocity  $U_{av}$  to the turbulence intensity  $u'$ :  $U_{av} = u' = \frac{2}{3} \cdot \sqrt{k}$  .

The second option is easier and simpler due to the fact that the  $k$ - $\varepsilon$  turbulence model can be directly used and validated with the 3-D CFD results. Therefore, it was applied in the presented ignition model. The direct correlation of the local mean velocity  $U_{av}$  to the turbulence intensity  $u'$  is reasonable because the spark plug is located near the wall of the cylinder head where the presence of boundary layer exists. The cross-flow velocities significantly depend on the combustion chamber geometry, the location of the spark plug and on the engine speed. They are usually in the range 0 – 20 m/s [35, 57-59].

In order to calculate the spark length from assumed velocity profile, it is necessary to define the discretization in  $z$  – direction. At the time of ignition, the initial spark markers are uniformly distributed along the shortest path between the electrodes, shown in Figure 16. The proposed quasi-dimensional ignition model has  $N_{SM} = 11$  spark marker points; an odd number is chosen so that the single flame kernel center can be placed in the mid-point. By applying the velocity operator defined by equation (3.17) on the particular spark marker point, each of

the points is shifted from the previous position in the direction that is defined by the flow angle  $\alpha$  ( $^\circ$ ). The flow angle is the required input parameter and is defined as the angle in  $x$ - $y$  plane where the zero value of  $\alpha$  corresponds to the positive direction of  $x$  - axis shown in Figure 16. Since the velocity profile is defined as planar velocity profile in the arbitrary plane that is coincident with the  $z$  - axis, the  $x$  - and  $y$  - coordinates of spark marker points can be calculated as functions of flow angle  $\alpha$ :

$$x(z) = v(z) \cdot \cos(\alpha) \cdot \Delta t \quad (3.20)$$

$$y(z) = v(z) \cdot \sin(\alpha) \cdot \Delta t \quad (3.21)$$

where  $\Delta t$  (s) is the calculation step size. Finally, the spark length is calculated by summing the shortest distances between particular Lagrangian marker points:

$$l_{\text{spk}} = \sum_{i=1}^{N_{\text{SM}}-1} \sqrt{(x_{i+1} - x_i)^2 + (y_{i+1} - y_i)^2 + (z_{i+1} - z_i)^2} \quad (3.22)$$

The effect of the cross-flow velocity on the spark length and early flame kernel growth has been analyzed in several experimental studies [71-73]. It has been shown that cross-flow velocity significantly influences the spark elongation as it is shown in Figure 17. Shichida et al. [71] have performed the experimental and numerical analysis of ignitability limits of the spark plug. It has been described that higher cross-flow velocities significantly increase the length of the spark, shown on the left side of Figure 17. Since the spark length influences the voltage between the electrodes (see equation (3.4)), the operating condition with the higher cross-flow velocity has shorter spark duration (the spark burn time). This phenomenon occurs because the available electric energy stored in the coil of the ignition system decreases faster which should be captured by the developed quasi-dimensional ignition model. In extreme conditions, when the cross-flow velocity is higher than 10 m/s, it is possible that the spark is discharged along the isolator surface (surface discharge) [72]. Although in these extreme operating conditions misfire usually occurs, it can not be captured by the presented approach for modeling of the electric spark length.

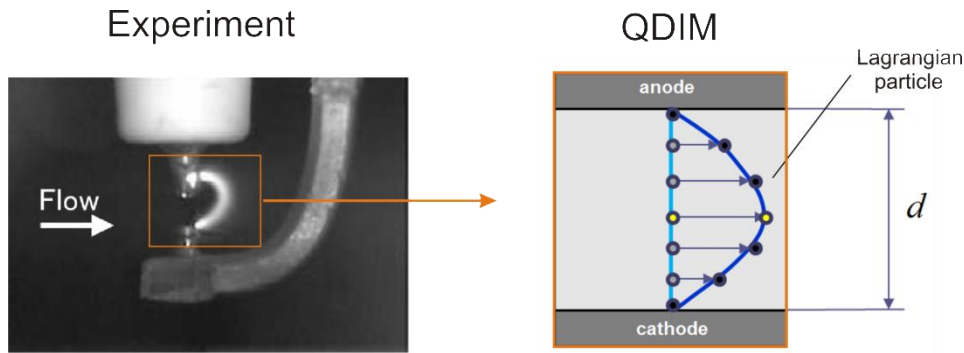


Figure 17. Elongation of electric spark due to the flow velocity: photograph of curved spark channel [71] at flow velocity 7.7 m/s (left), description of spark length by the set of Lagrangian particles.

In the presented quasi-dimensional ignition model the electric spark is always modelled as the parabolic profile defined by the set of Lagrangian particles whose movement is defined by the cross-flow velocity vector and with the velocity profile between the electrodes that is approximated with the Hagen - Poiseuille flow. Therefore, the mentioned surface discharge that occurs in extreme in-cylinder flows at the breakdown phase, cannot be predicted by the model. Although this phenomenon cannot be captured by the ignition model, the developed QDIM is able to capture the multiple breakdowns that may occur at the late part of the glow phase at operating conditions with higher engine speeds [28]. At higher engine speeds the cross-flow velocity is about 10 m/s and elongation of the curved spark is significant. The electric spark elongation increases the voltage between the electrodes which during the late part of the glow phase can reach the breakdown voltage. If this occurs, a new set of Lagrangian particles along the shortest distance between the electrodes is initiated representing the electric spark re-strike. It is shown under the validation of cycle-simulation results that the multiple breakdowns occur when the electric spark length is many times longer than distance between the electrodes.

### 3.6. Modeling of spark plug geometry

Modeling of the overall spark plug geometry is very challenging task for 0-D approach because the classic spatial discretisation is not considered. In order to calculate the instantaneous heat transfer between the flame kernel and the spark plug electrodes it is necessary to model the spark plug surface that is instantaneously entrained by the flame kernel. The surfaces of the spark plug electrodes are represented by the uniformly distributed points over the spark plug surfaces as shown in Figure 18. The similar approach has been

used in [9, 74] where the flame front area was defined by the uniformly distributed marker points on the smooth flame front with the defined mean flame radius.

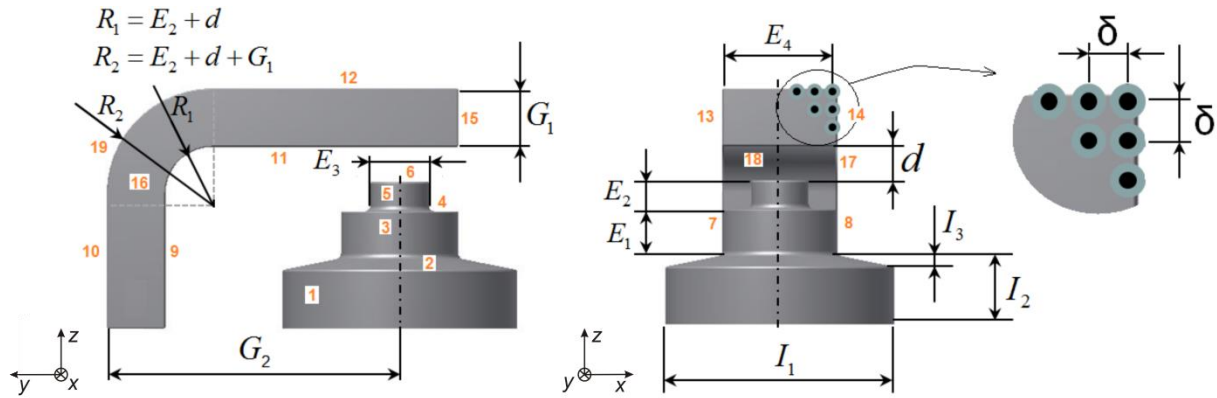


Figure 18. Description of the spark plug geometry in 0-D approach.

The increment  $\delta$  represents the distance between the points in  $x$ ,  $y$  or  $z$  - direction for the rectangular surfaces as shown in Figure 19 a). In the case of circular surfaces (e.g. central spark electrode) presented in Figure 19 b) the increment  $\delta$  represents the length of circular arc in the circular direction and the distance between the two neighboring radii in the radial direction. In general, each marker point represents the incremental surface areas of  $\Delta S$  that is also shown in Figure 19. The spark plug geometry is defined by the set of geometrical parameters:  $G_1$ ,  $G_2$ ,  $I_1$ ,  $I_2$ ,  $I_3$ ,  $E_1$ ,  $E_2$ ,  $E_3$ ,  $E_4$  and  $d$  (mm) that are defined by the user. The overall spark plug geometry is described by 19 surfaces shown in Figure 18 and each surface is marked with the specific number. If the central thin electrode shown in Figure 18 should not be considered the user has to set the geometrical parameter  $E_3$  to zero. By the proposed approach for the description of spark plug geometry in 0-D, modeling of different spark plug geometries (different gap distance  $d$ , with or without the central thin electrode defined by  $E_2$  and  $E_3$ , etc.), is enabled.

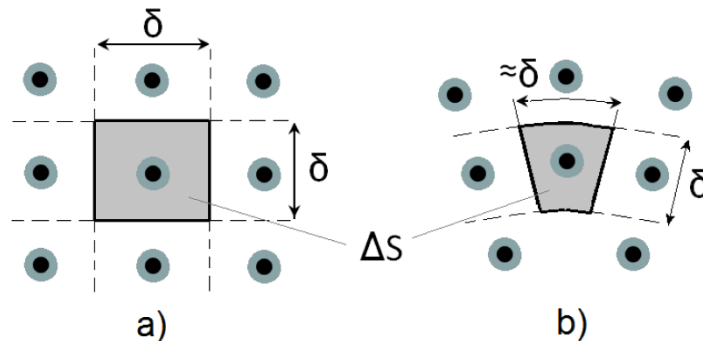


Figure 19. Illustration of incremental rectangular (a) and circular (b) surface area of the spark plug.



The total spark plug surface area  $S_{\text{tot}}$  ( $\text{m}^2$ ) can be calculated as the sum of particular surface areas  $S_i$  ( $\text{m}^2$ ):

$$S_{\text{tot}} = \sum_{i=1}^{19} S_i \quad (3.23)$$

Therefore, the particular surface areas depend on the input of geometrical parameters as follows:

$$S_1 = I_1 \cdot \pi \cdot (I_2 - I_3) \quad (3.24)$$

$$S_2 = \left( \frac{I_1^2}{4} - \frac{E_4^2}{4} \right) \cdot \pi \cdot \frac{1}{\sin \left( \arctan \left( \frac{I_1 - E_4}{2I_3} \right) \right)} \quad (3.25)$$

$$S_3 = (E_4 \cdot \pi) \cdot E_1 \quad (3.26)$$

$$S_4 = \left( \frac{E_4^2}{4} - \frac{E_3^2}{4} \right) \cdot \pi \quad (3.27)$$

$$S_5 = (E_3 \cdot \pi) \cdot E_2 \quad (3.28)$$

$$S_6 = \frac{E_3^2}{4} \cdot \pi \quad (3.29)$$

$$S_7 = S_8 = S_9 = S_{10} = G_1 \cdot (I_2 + E_1 + E_2) \quad (3.30)$$

$$S_{11} = S_{12} = E_4 \cdot \left( \frac{E_4}{2} + (G_2 - G_1 - d) \right) \quad (3.31)$$

$$S_{13} = S_{14} = G_1 \cdot \left( \frac{E_4}{2} + (G_2 - G_1 - d) \right) \quad (3.32)$$

$$S_{15} = G_1 \cdot E_4 \quad (3.33)$$

$$S_{16} = S_{17} = \frac{\pi}{4} \cdot [(d + G_1)^2 - d^2] \quad (3.34)$$

$$S_{18} = \frac{1}{2} \cdot d \cdot \pi \cdot E_4 \quad (3.35)$$

$$S_{19} = \frac{1}{2} \cdot (d + G_1) \cdot \pi \cdot E_4 \quad (3.36)$$

The instantaneous flame kernel center  $K_c$  shown in Figure 20 is defined by the coordinates  $x_k$ ,  $y_k$  and  $z_k$  which is calculated by the model for the electric spark, while the particular marker point  $T_i$  of the spark plug geometry is defined by the coordinates  $x_i$ ,  $y_i$  and  $z_i$ . Since the mean flame kernel radius  $R_k$  is defined at each time step, the value of distance  $D$  between the flame kernel center  $K_c$  and the particular marker point  $T_i$  defines whether the marker point is inside or outside of the flame kernel with radius  $R_k$ .

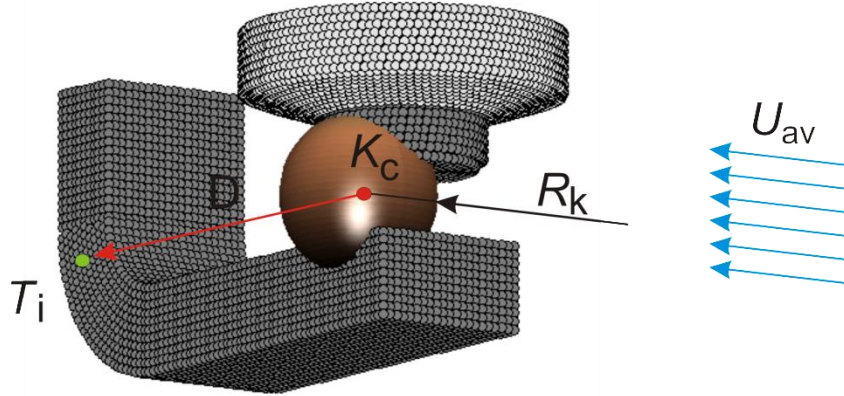


Figure 20. Illustration of early flame kernel growth; the kernel center is moved from its initial position due to the cross-flow velocity  $U_{av}$ .

The instantaneously entrained surface area  $S_e$  of the spark plug can be calculated as follows:

$$S_e = S_{tot} \cdot \frac{N_e}{N_{tot}} \quad (3.37)$$

where  $N_{tot}$  (-) is the total number of marker points that represent the spark plug geometry, and  $N_e$  (-) is the number of instantaneously entrained marker points by the flame kernel. The decision whether the marker point is inside or outside the flame kernel is made by checking the distance  $D$  between the flame kernel center  $K_C$  and particular marker point  $T_i$ . The

distance between the flame kernel center  $K_C (x_k, y_k, z_k)$  and particular marker point  $T_i (x_i, y_i, z_i)$  is calculated as:

$$D = \sqrt{(x_i - x_k)^2 + (y_i - y_k)^2 + (z_i - z_k)^2} \quad (3.38)$$

If the distance  $D$  is lower than the flame kernel radius  $R_k$  the particular marker point is entrained by the flame kernel, otherwise it is considered to be outside of the flame kernel, as it is illustrated in Figure 20. Due to the simplicity of the model, the entrained spark plug surface area is calculated with the assumption that the flame kernel has fully spherical shape with radius  $R_k$ . On the other hand, the real kernel burning rate incorporates the effect of free surface distortion of the kernel due to convective fluid motion and turbulence. In the presented ignition model, the distortion factor of the free kernel surface that entrains the fresh mixture is proportional to the ratio between the instantaneous spark length and distance between the electrodes – see equations (3.8), (3.11) and (3.14). The presented ignition model also neglects the local interaction between the flame kernel and the spark plug electrodes which, in real operating conditions, limits the flame kernel expansion close to the electrodes.

The effect of the spark plug electrode design on the early flame kernel growth was investigated experimentally in [57-59, 75-78]. The experimental Schlieren images of the early flame kernel growth [71] are shown in Figure 21. The experiment was performed in static field with stoichiometric mixture and initial pressure of 1.6 bar. On the left hand side of the Figure 21 the flame kernel is shown for the DFE-type of electrodes while on the right side of this figure for the standard Ni-type of electrode. Both Schlieren images are captured 3 ms after the spark discharge with the same ignition energy enabling the study of spark plug design on the early flame kernel growth. It is evident from Schlieren photographs that faster flame expansion was observed in the DFE-type of spark plug than in the Ni-type. This can be explained by the effects of heat losses from the hot kernel to the spark plug electrodes. During the early phase of development (glow phase) kernel radius is in the order of gap distance and its center is close to the midpoint between the electrodes. As the flame kernel grows, its volume expands and entrains the spark plug electrodes that have significantly lower temperature than the flame kernel. The heat loss that occurs between the flame kernel and spark plug electrodes is directly proportional to the instantaneously entrained spark plug surface area by the flame kernel. Hence, in the case of DFE-type of spark plug the initial spark plug surface entrained by the flame kernel is lower, resulting in the lower heat transfer and with faster kernel growth.

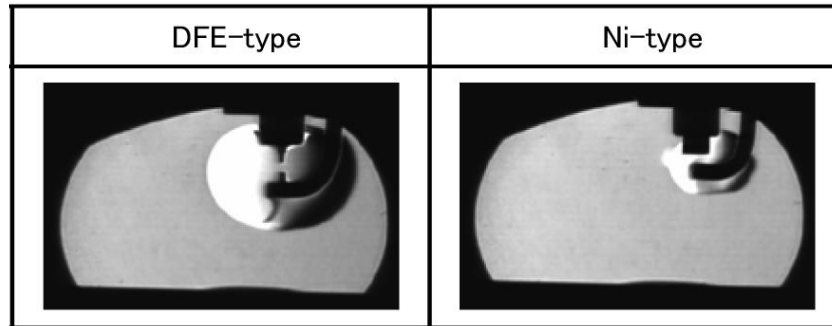


Figure 21. Effects of the spark plug geometry on the flame kernel development in the static field - Schlieren photographs at 3 ms after spark discharge; initial pressure is 1.6 bar and  $\lambda=1$  [71].

In terms of duration of the early flame kernel growth and ignition delay, the spark plug designs with thin central electrode are more favorable because the ignitability limits are higher. On the other hand, such spark plug electrodes have to be produced from the materials that are resistant to wear and to the higher thermal stresses (higher melting point). Therefore, they are usually produced from metals such as iridium, tungsten, palladium, platinum, silver or gold, that significantly increase the production costs and are usually applied in racing SI engines.

In order to simulate the above mentioned effects of heat losses for different spark plug designs with the developed quasi-dimensional ignition model, the model is prepared in the manner that the user has to change only two input parameters ( $E_2$  and  $E_3$ ) related to the definition of the spark plug geometry described in Figure 18.

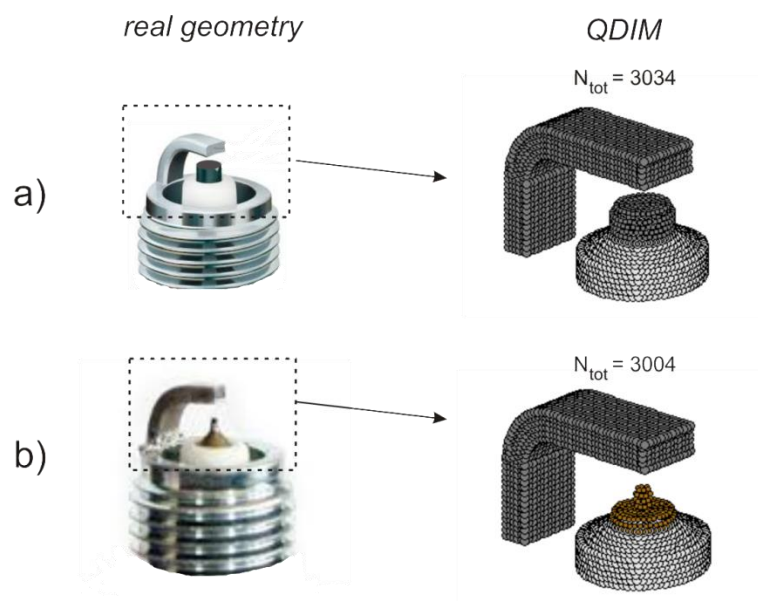


Figure 22. Examples of the spark plug designs that can be considered with the developed quasi-dimensional ignition model: a) the standard spark plug design with single side electrode; b) spark plug with the central thin electrode.

On the left hand side of Figure 22 two typical spark plug designs are shown as well as their representation by the geometrical points in QDIM that are uniformly distributed over the surfaces. In order to consider the spark plug design with the central thin electrode, shown in Figure 22 b), it is necessary to change two input parameters  $E_2$  and  $E_3$ , marked in Figure 18, that represent the height and width of the central electrode, respectively.

### 3.7. Features of the developed quasi-dimensional ignition model

Several main features of the developed quasi-dimensional ignition model may be specified:

- Ignition delay period and early flame kernel growth depend on large number of physical properties, such as spark plug geometry, cross-flow velocity, heat transfer effects, energy of the secondary electric circuit, etc.
- The misfire conditions can be captured: if there is a large heat transfer and low kernel energy received from the electric spark the flame kernel will not be able to grow enough and the misfire will occur.
- The QDIM is capable of handling multiple electrical breakdowns that may occur at high cross-flow velocities: when the voltage between the electrodes  $V_{ie}$  reaches the breakdown voltage  $V_{bd}$  the new breakdown is triggered and the new spark is formed increasing the kernel expansion speed.
- The possibility to simulate cycle-to-cycle variations in combustion; oscillations of ignition delay period by the oscillations of cross-flow velocity and/or by the oscillations of flow angle at the vicinity of the spark plug.

Possible drawbacks of the developed ignition model:

- There is no local interaction between the flame kernel and the spark plug surfaces in terms of its limitation for expansion.
- The flame kernel shape is approximated as fully spherical, although it is highly distorted due to convective and turbulent movement of fluid at the vicinity of the spark plug.
- The cross-flow is considered as 2-D flow in the plane defined by the flow angle.
- The cross-flow velocity that influences the electric spark length and convective movement of the flame center is independent on the spark plug position in the cylinder.
- The surface discharge of the spark during the breakdown phase at high cross-flow velocity that usually results with the misfire cannot be predicted.

## 4. Fundamentals of combustion in SI engines and modeling

The combustion process of SI engine is an extremely complex combination of phenomena which involve an arc discharge, the fuel oxidation chemistry, heat losses in a complex geometry and the role of turbulence over a wide range of time and length scales. In general, combustion is a very important part of the engine operating cycle where the chemical energy of the fuel is transformed into the internal energy of burned gases that expand and transfer work to the piston. It is initiated by the discharge of electric spark that occurs between the spark plug electrodes at the prescribed spark time. Due to the presence of a turbulent flow field inside the cylinder, the combustion process of SI engines is always turbulent. The turbulent flames can be classified into two main groups: premixed and non-premixed turbulent flames. The premixed turbulent flames are typical for the combustion in SI engines where a very thin flame wrinkled by turbulence effects propagates through the combustion chamber. The mass burning rate of the SI engine depends on several primary factors such as: geometry of the flame front and its interaction with the wall of combustion chamber, unburned zone state and composition, and flow field effects [54].

The combustion process of SI engine can be divided into three main phases (Figure 23):

- early flame kernel growth,
- main turbulent combustion,
- end of combustion ("wall combustion").

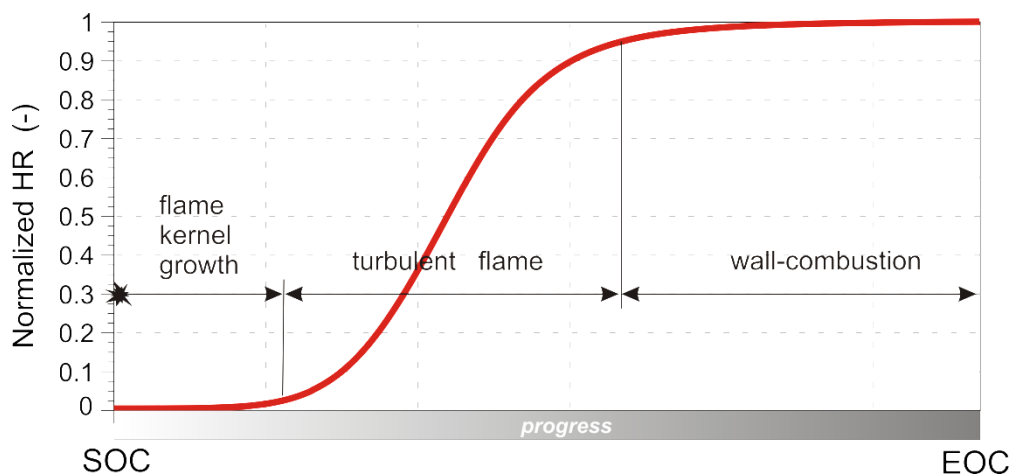


Figure 23. Description of three phases of combustion process on normalized heat release curve (SOC – start of combustion, EOC – end of combustion).

The early flame kernel growth is the initial phase of combustion, usually called ignition delay, when a very small portion of heat is released. This initial combustion phase is already described under the Chapter 3.

As the flame grows beyond the 10 mm radius, the convection of kernel center becomes insignificant because the burned mass is then too large to be transported by local flow velocity. The local turbulence at different length scales has enough time to influence the flame front which grows and becomes increasingly wrinkled and distorted. It can be concluded that both local flow and turbulence affect the flame development process inside the combustion chamber of SI engines [54].

Under normal operating conditions of SI engine, the flame front propagates radially in an approximately spherical manner from its center. As the flame grows, the wrinkles of flame front come near the chamber walls which causes the restriction of the turbulent flame propagation and local flame quenching. The remaining parts of the flame front that are close to the cylinder wall, but are not in the contact with the wall, burn out and only successive smaller scales of turbulence are available to affect the flame. Therefore, the final stage of the combustion process in SI engines may be slower than what would occur in the stage of fully developed turbulent flame, when the maximum rate of heat release is achieved. The described effect of influence of combustion chamber walls on the deceleration of combustion process can be seen in Figure 23.

#### **4.1. Background of quasi-dimensional fractal combustion model**

The real flame front of SI engines is very thin and highly wrinkled surface that propagates throughout the combustion chamber. There are two physical mechanisms that produce the flame front wrinkling in SI engines:

- A variation of the local in-cylinder temperature and mixture composition that affects the local burning velocity and a flame deformation.
- Turbulent eddies of different length scales influence the convective flame wrinkling that is partly compensated by the local laminar burning process.

The partial effects of the above phenomena depend on engine operating conditions. At high engine speeds the deformation of the flame front can be so strong that it produces a multiple connected flame front with "islands" and "peninsulas" of unburned zone trapped within the burned zone [79]. However, it is generally accepted that, in a wide range of combustion conditions occurring in an SI engines, the flame front is single connected contour wrinkled by the convective effects of the turbulent flow field. For the description of the real geometry of the flame front in SI engine that has irregular shape and is illustrated in Figure 24, the conventional methods of Euclidian geometry cannot be used.

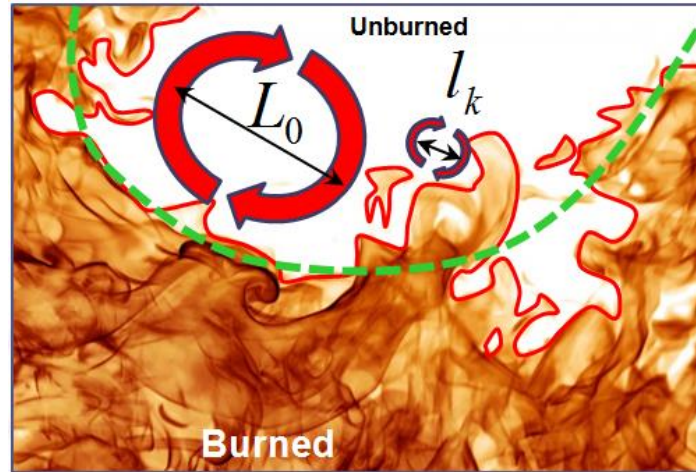


Figure 24. Illustration of the wrinkled flame front segment of SI engine as a very thin layer that separates burned and unburned zone.

The most common approach to describe the combustion process of SI engine in the cycle-simulations is based on a two zone modeling approach where the cylinder mixture is divided into the burned and unburned zone. The specific sub-group of two zone combustion models is quasi-dimensional combustion models. The quasi-dimensional combustion models consider the real flame front propagation across the combustion chamber and its interactions with walls are taken into account. General differential equations of two zone combustion model are specified and described in the Appendix.

There are two quasi-dimensional combustion models that are usually used to evaluate the key engine parameters on its performance: turbulent entrainment model (known also as BK model) [1, 9, 21, 80] and fractal combustion model [19, 34, 81]. The turbulent entrainment model considers the fully spherical flame front and the fresh mixture crosses this front with a characteristic velocity scale caused by the turbulent convection [79]. The fresh mixture entrained by the flame front burns with combustion structure sizes that are typical for the laminar combustion process. The use of fractal geometry to model the effects of turbulence on the combustion process in SI engines is a promising technique for the application to both quasi-dimensional and multi-dimensional engine codes. The fractal combustion model considers the wrinkled flame front that develops across the combustion chamber and propagates by the laminar flame speed. The effect of turbulence wrinkles the flame front and increases the flame front area, and consequently increases the combustion rate and stretches the flame. The flame surface area of the wrinkled flame front is calculated by a concept of fractal geometry. The fundamental behavior of fractal geometry is the self-similarity between scales of different sizes which manifests itself in the power-law scaling between measured size and measurement scale. This is for the case of turbulent flame surface illustrated in



Figure 25 where the measured flame contour is plotted versus measurement scale  $\varepsilon$  (caliper length) with the logarithmic  $x$ -axis. In the caliper technique to determine the fractal dimension, the length of a curve on a plane is estimated by counting how many caliper lengths it takes to cover the whole length of the curve [18]. The most physical geometries, however, can be expected to have a smallest and a largest scale, beyond which the measured size does not change. These scales are the inner and outer cutoffs,  $\varepsilon_i$  and  $\varepsilon_0$ , that are also illustrated in Figure 25. It has been proposed, for the case of turbulent flames, that the outer cutoff is the integral length scale of the turbulence  $L_1$ , while the Kolmogorov length scale  $l_k$  has been proposed as the appropriate inner cutoff [17, 82].

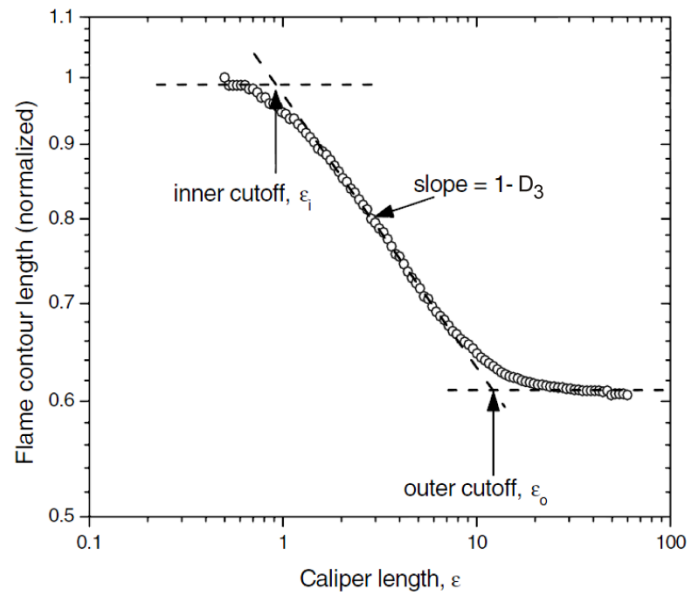


Figure 25. Example of typical Richardson plot to evaluate the fractal dimension  $D_3$  [18].

Using the description of the turbulent flame structure represented by the Figure 25 it is possible to write the following expression (first introduced by Damköhler in 1940):

$$\frac{S_T}{S_L} = \frac{A_T}{A_L} = \left( \frac{\varepsilon_0}{\varepsilon_i} \right)^{D_3-2} \quad (4.1)$$

where the Kolmogorov  $l_k$  (m) and integral length scales  $L_1$  (m) are taken to be the inner  $\varepsilon_i$  (m) and outer cutoffs  $\varepsilon_0$  (m), respectively,  $S_T$  (m/s) is the turbulent flame speed,  $S_L$  (m/s) is the laminar flame speed,  $A_T$  (m<sup>2</sup>) is the turbulent (wrinkled) flame surface area and  $A_L$  (m<sup>2</sup>) is the laminar (smooth) flame surface area. Therefore, modeling and prediction of the turbulence quantities is a key step for the correct prediction of the turbulent flame surface area  $A_T$  which is responsible for the increase in turbulent burning rate with respect to the laminar case. In a

number of comprehensive experimental studies about turbulent flames [17, 82] it has been found that the value of fractal dimension  $D_3$  is a function of non-dimensional turbulent velocity fluctuation,  $u'/S_L$  (ratio of turbulent velocity fluctuation to the laminar burning velocity). These studies asserted that the fractal dimension  $D_3$  of the flame countour approaches the value of 2.37 as the ratio  $u'/S_L$  increases.

Santavicca et al. [83] proposed the calculation of the fractal dimension for the turbulent flames as follows:

$$D_3 = D_{3,\min} \frac{S_L}{u'+S_L} + D_{3,\max} \frac{u'}{u'+S_L} \quad (4.2)$$

where the maximum value of fractal dimension  $D_{3,\max}$  was set to 2.35 while the minimum value  $D_{3,\min}$  is adopted as 2.05 at which burning speed is close to the laminar one. The turbulent velocity  $u'$  (m/s), usually called turbulence intensity, is defined from in-cylinder turbulent kinetic energy assuming the isotropic turbulent flow field.

In the fractal combustion model previously integrated into the cycle-simulation model of AVL BOOST, the minimum value  $D_{3,\min}$  is set as 2.05 which determines the initial burning speed which is close to the laminar one, while the maximum value  $D_{3,\max}$  was not set as a fixed value. In order to simulate the smooth transition from the laminar to fully developed turbulent flame, the maximum value of fractal dimension is defined as:

$$D_{3,\max} = D_{3,\min} \cdot (1 - I_f) + f_{D3,\max} \cdot I_f \quad (4.3)$$

$$I_f = 1 - e^{-\gamma_{wr}} \quad (4.4)$$

$$\gamma_{wr} = \frac{r_f}{r_{f,\text{ref}}} \cdot \frac{n}{n_{\text{ref}}} \quad (4.5)$$

where  $I_f(-)$  is an under-relaxation function,  $\gamma_{wr}(-)$  is proposed for the non-dimensional flame wrinkling rate,  $r_f$  (m) is the mean flame front radius,  $r_{f,\text{ref}}$  (m) is the (tunable) reference flame radius of 10 mm,  $n$  (rpm) represent the engine speed and  $n_{\text{ref}}$  (rpm) represent the reference engine speed fixed to 1000 rpm. The parameter  $f_{D3,\max}(-)$  is set to

2.35 and generally represents the maximum value of fractal dimension  $D_{3, \max}$  when the under-relaxation function  $I_f$  is equal to one.

When the fractal dimension  $D_3$  of the turbulent flame and the laminar flame speed  $S_L$  are defined, the mass burning rate is calculated:

$$\left( \frac{dm_{BZ}}{dt} \right)_{\text{fractals}} = \rho_{UZ} \left( \frac{L_T}{l_k} \right)^{D_3-2} A_L S_L \quad (4.6)$$

The laminar flame speed  $S_L$  is calculated by a correlation proposed in [84] and is a function of fuel characteristics, in-cylinder pressure, unburned gas temperature, air-fuel ratio and mass fraction of trapped burned gas products. The equation (4.6) for the mass burning rate is valid for the transition from laminar to fully developed turbulent flame as well as for the freely expanding turbulent flame. During the termination of combustion process, when the flame front is close to the cylinder walls, an additional correction term is required.

When the flame front reaches the combustion chamber walls the described fractal mechanism of the flame propagation is no longer valid. The termination of combustion is under the effect of the flame reaching wall and slowing down the burning process, also known as "wall combustion". The wall limits all flows, constrains gas expansion and forms a boundary layer with relatively low temperature that cools down the gas. All mentioned factors change the fundamental behavior of the combustion, compared to that of a flame propagating freely across the combustion chamber [19]. About 30 - 40 % of the unburned mixture burns in the wall combustion mode. Wall combustion burning rate can simply be described by an exponential decay, as follows [85]:

$$\left( \frac{dm_{BZ}}{dt} \right)_{\text{wall-combustion}} = \frac{m - m_{BZ}}{\tau} \quad (4.7)$$

where  $m$  (kg) is total in-cylinder mass,  $m_{BZ}$  (kg) is burned mass and  $\tau$  (s) is the characteristic time scale of wall combustion phenomena. The characteristic time scale is computed assuming that wall combustion burning rate equals to the one derived from the fractal model:

$$\tau = \frac{(m - m_{BZ})}{(\rho_{UZ} A_T S_L)} \quad (4.8)$$

The overall burning rate can be consequently defined as a weighted mean of the two described combustion rates:

$$\left(\frac{dm_{BZ}}{dt}\right)_{\text{overall}} = (1-w)\left(\frac{dm_{BZ}}{dt}\right)_{\text{fractals}} + w\left(\frac{dm_{BZ}}{dt}\right)_{\text{wall-combustion}} \quad (4.9)$$

where  $w$  (-) is the weight factor that linearly increases with time, depending on the instantaneous mass of the unburned zone:

$$w = 1 - \frac{m - m_{BZ}}{(m - m_{BZ})_{tr}} \quad (4.10)$$

With this type of calculation a smooth transition between the two modes is easily achieved. There are two ways to define the time when the wall combustion mode is activated:

- by identifying the first flame plume arrival to the cylinder wall;
- by the user-defined constant named "*Mass Fraction Burned at Wall Combustion Start*" that represents the mass fraction burned when the wall combustion phase is started.

In the presented study, the second option is used because it enables more freedom for tuning the model in which the cycle-simulation results of combustion are compared with the available 3-D CFD data. In Chapter 5 it is demonstrated that the wall combustion mode can be fully omitted when the two zone turbulence model is applied.

### Specification of chamber geometry

The specification of combustion chamber geometry is very important because the free flame surface area, which is presented as the surface of sphere, depends on the flame center, instantaneous mean flame radius and on the actual piston position, as it is illustrated in Figure 26.

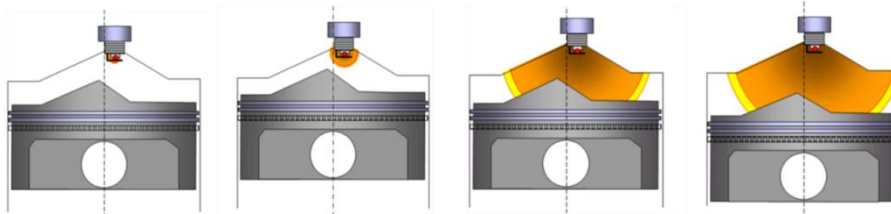


Figure 26. Illustration of the free flame front surface propagation with respect to the crank angle, for the pent roof cylinder head and piston geometry [21].

For simple geometries in AVL BOOST, the table of free flame surface areas is generated during the preprocessing. For that the selection of chamber geometry in terms of cylinder head and piston as well as the specification of main dimensions depending on the considered cylinder design has to be made. The simplified shapes of the cylinder head and piston for which the above mentioned tables can be made during preprocessing of AVL BOOST, are shown in Figure 27.

Alternatively, for more complex cylinder geometries the table of free flame surface areas can be generated externally and can be loaded through the input file. Due to the simplicity of the cycle-simulation model, the considered cylinder geometries that have been modelled in 3-D CFD were approximated by the pent roof cylinder head and flat piston design. Within Chapter 6, the experimental results of the CFR engine were used and analyzed. The cycle-simulation of this engine was performed with fully flat geometry of the cylinder head and piston since the design of the head and piston of the CFR engine is very close to flat shape (Figure 27).

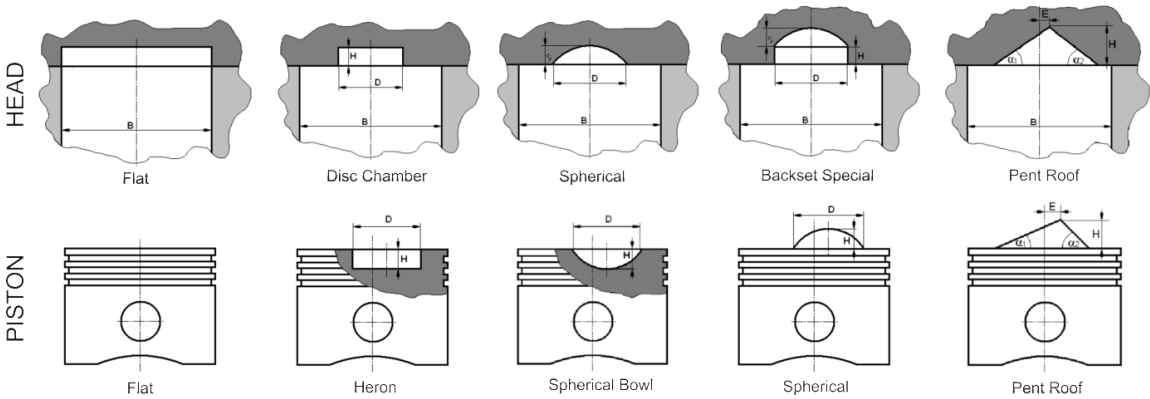


Figure 27. Simplified geometries of the cylinder head and piston designs that can be calculated directly by AVL BOOST [86].

**4.2. Modification and extension of the quasi-dimensional fractal combustion model**

The original fractal combustion model, described in section 4.1 is extended and modified. The developed quasi-dimensional ignition model (shown in section 3) is integrated with the combustion model and can be used for the calculation of ignition phenomena and early flame kernel growth. Furthermore, a new definition of wrinkling delay time is proposed and applied to the fractal combustion model. The application of the newly developed two zone  $k-\varepsilon$  turbulence model enables the extension of combustion calculation in a more physical context because the flame wrinkling and burning rate depends on the unburned zone

turbulence. All modifications and extensions of the fractal combustion model are described in the following text.

#### 4.2.1. Ignition delay and early flame kernel growth

In the original version of the fractal combustion model the ignition process and early flame kernel growth are not considered. The kernel initiation process ends 200  $\mu\text{s}$  after the prescribed ignition time where the flame is stable and spherically shaped of 2 mm radius. The kernel initiation time is tunable with the ignition-formation time multiplier  $c_{\text{ign}}(-)$  :

$$\alpha_{\text{id}} = 2 \cdot 10^{-4} \cdot c_{\text{ign}} \cdot \omega \quad (4.11)$$

The duration of the ignition process and early flame kernel growth depend on a large number of parameters such as: pressure, temperature, mixture composition, cross-flow velocity, spark plug geometry and design, ignition system properties, etc. If one wants to correctly predict the combustion process of SI engine by using the assumption of ignition delay time with equation (4.11) a tuning of the ignition-formation time multiplier for each operating point has to be performed. The original fractal combustion model also assumes that the position of the flame center is equal to the center of the spark plug electrode defined by the user. In the real conditions of SI engine, the location of the flame center does not correspond to the spark plug location. As it is described in the previous chapter, the flame kernel center is shifted from its initial position between the electrodes due to the effects of cross-flow velocity that causes the convective movement of the flame.

When the newly developed ignition model is applied, the calculation of the combustion process starts with the quasi-dimensional ignition model. When the specific portion of the spark-ignition related in-cylinder mass is burned, the fractal combustion model is employed. Therefore, the ignition delay time is defined by controlling the burned mass. At the prescribed time of ignition, the initial electric spark and the flame kernel are formed. The kernel center is set to the midpoint between the spark plug electrodes, while the initial kernel radius is 0.5 mm [65, 66]. The flame kernel receives the electric energy from the electric spark and expands with the defined expansion speed. As the flame kernel becomes larger and larger, it entrains the spark plug electrodes that cool the flame kernel reducing its expansion speed. The shifting of the flame center from its initial position is defined by the maximum value of the cross-flow velocity in the spark gap region. The flame center can be shifted away in any direction with the shifting distance that may reach the value equal to the 20 % of the engine bore.

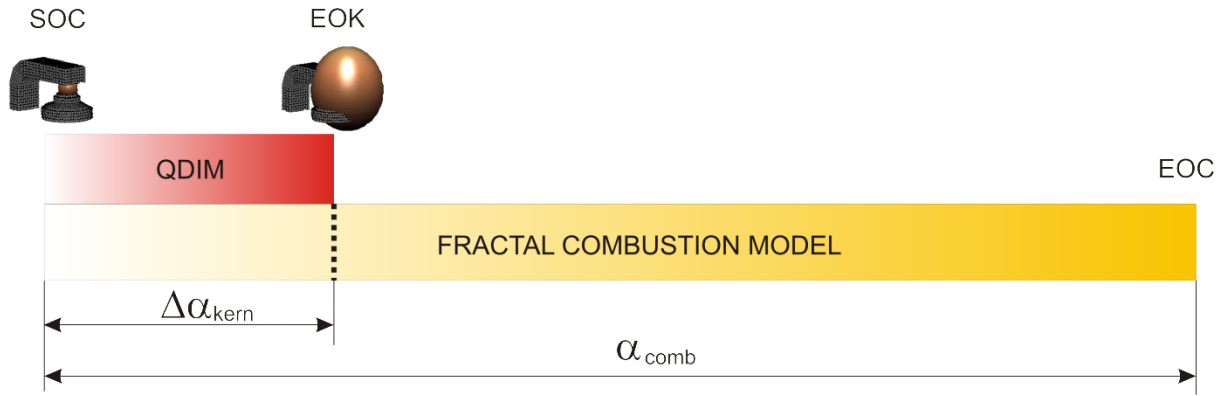


Figure 28. Integration of the newly developed QDIM with the quasi-dimensional fractal combustion model; SOC - start of combustion, EOK - end of kernel, EOC - end of combustion.

When the burned mass calculated by the QDIM is equal to the one defined by equation (3.16), the calculation of the early flame kernel growth and shifting of the flame kernel are finished. Since the flame kernel center is shifted from its initial position between the spark plug electrodes and due to the fact that the free flame surface area depends on the flame center position and the combustion chamber geometry, the recalculation of the free flame surface areas (as spherical surfaces) with the new flame center at the end of the kernel calculation has to be performed. The remaining part of the combustion period, i.e. the combustion process, is performed by the modified fractal combustion model, as it is illustrated in Figure 28.

#### 4.2.2. Transition of laminar to turbulent flame

In the original fractal combustion model, the transition from laminar to fully developed turbulent flame is modeled by using the equations (4.3) – (4.5). In equation (4.5) the  $r_f$  (m) represents the actual (mean) flame front radius that continuously grows starting as fully spherical shape of 2 mm in radius. It is previously mentioned that  $r_{f, \text{ref}}$  (m) is a user-defined constant representing the assumed flame front radius when the maximum wrinkling of flame front will occur. Such definition of transition time, usually called wrinkling delay time [22], is very unfavorable from the user point of view, especially if the  $r_{f, \text{ref}}$  constant has to be tuned for each operating point. The qualitative progress of under-relaxation function  $I_f$  is given in Figure 29.

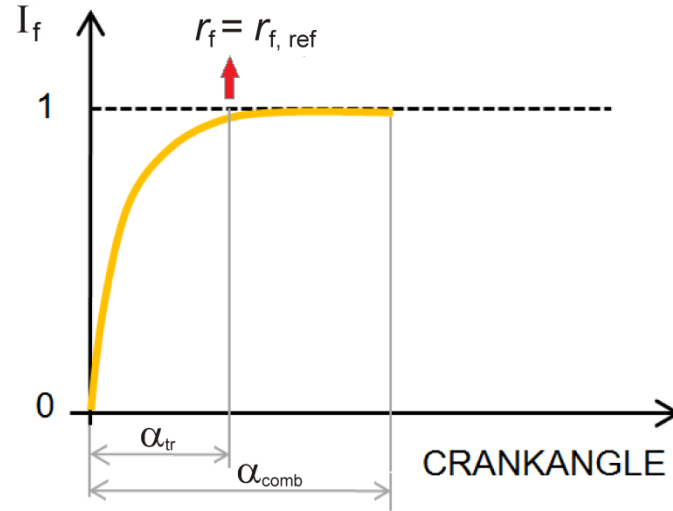


Figure 29. Qualitative progress of under-relaxation function for the simulation of transition time.

The wrinkling delay time that represents the transition time from the laminar to the fully developed turbulent flame can be approximated as the time necessary for the turnover of turbulent eddies that wrinkle the flame front [1, 22]. Therefore, the following expression for eddy turnover time can be written [5, 39]:

$$\Delta t = 0.55 \cdot C_{\tau} \cdot \frac{L_1}{u'} \quad (4.12)$$

where  $L_1$  (m) is the turbulent integral length scale and  $u'$  (m/s) is the turbulence intensity at the start of combustion that are defined by the applied  $k-\varepsilon$  turbulence model. The constant  $C_{\tau}(-)$  is the new user-defined constant which has to be calibrated for the certain engine geometry. In order to transform the transition period from time scale to the crank angle domain, the equation (4.12) has to be multiplied by the angular velocity  $\omega$  (rad/s) :

$$\alpha_{tr} = \frac{180}{\pi} \cdot \omega \cdot \Delta t = \frac{180}{\pi} \cdot \omega \cdot \left( 0.55 \cdot C_{\tau} \cdot \frac{L_1}{u'} \right) \quad (4.13)$$

Now instead of using equations (4.4) and (4.5), the under-relaxation function  $I_f$  can be calculated by using equation (4.13) and:

$$I_f = 1 - e^{-\left( \frac{\alpha}{\alpha_{tr}} \cdot \frac{n}{n_{ref}} \right)} \quad (4.14)$$



where  $\alpha$  ( $^{\circ}$  CA) is the relative instantaneous crank angle (crank angle from the beginning of combustion). During the validation process shown in Chapter 5, the cycle-simulations are performed with the original definition of transition time where the reference flame radius  $r_{f, \text{ref}}$  was tuned for each individual operating point of the engine. After that, the new calculation of transition time based on the turbulence quantities was employed showing that a single value of the user-defined constant  $C_{\tau}$  can be applied for one engine geometry.

#### 4.2.3. Combustion process with single and two zone turbulence model

The procedure of combustion process calculation is already described with the description of fractal combustion model, but the details about the turbulence effects are not specified. The turbulent integral length scale  $L_1$  represents the diameter of the turbulent eddies that have most of the kinetic energy in the turbulent energy spectrum, shown in Figure 6. In the original fractal combustion model that uses the  $K$ - $k$  turbulence model, the turbulent integral length scale was assumed to be proportional to the instantaneous clearance height  $H$  (m) inside the cylinder:

$$L_1 = c_1 \cdot H \quad (4.15)$$

where  $c_1$  (–) is the user-defined constant ( $c_1 = 0.2 - 0.8$ ).

With the assumption of isotropic and homogeneous turbulence [5, 39] inside the cylinder, during the combustion, it is possible to estimate the Kolmogorov length scale:

$$l_k = \frac{L_1}{\text{Re}_t^{3/4}} \quad (4.16)$$

where  $\text{Re}_t$  (–) is the Reynolds number calculated as a function of turbulence intensity  $u'$ , integral length scale  $L_1$  and kinematic viscosity of the unburned zone  $\nu_{\text{UZ}}$ :

$$\text{Re}_t = \frac{u' \cdot L_1}{\nu_{\text{UZ}}}. \quad (4.17)$$

In the case of  $k$ - $\varepsilon$  turbulence model the turbulent integral length scale can be expressed as the function of turbulent kinetic energy and its dissipation rate [1, 39]:

$$L_1 = \frac{\sqrt[3]{k}}{\varepsilon} \quad (4.18)$$

When a two zone turbulence model is applied, the turbulent kinetic energy  $k_{UZ}$  and dissipation rate  $\varepsilon_{UZ}$  of the unburned zone, defined by the  $k$ - $\varepsilon$  turbulence model, are used for the definition of integral length scales:

$$L_1 = \frac{\sqrt[3]{k_{UZ}}}{\varepsilon_{UZ}} \quad (4.19)$$

$$\text{Re}_t = \frac{u'_{UZ} \cdot L_1}{\nu_{UZ}} \quad (4.20)$$

$$u'_{UZ} = \sqrt{\frac{2}{3}k_{UZ}} \quad (4.21)$$

If isotropic and homogeneous turbulence is assumed, the Kolmogorov length scale  $l_k$  can be expressed by the equation (4.16). This change in calculation of minimum and maximum integral length scale changes the ratio of integral length scales used in equation (4.6) that defines the fractal burning rate.

The ratio of maximum to minimum integral length scales during the combustion process is shown in Figure 30. The first profile (dashed gray line) is based on the mean (total) turbulent quantities that are calculated when the single zone  $k$ - $\varepsilon$  turbulence model is used. The second profile (solid red line) is the profile obtained when the unburned zone turbulent quantities are used, which is made possible by the application of two zone  $k$ - $\varepsilon$  turbulence model. Since the turbulent kinetic energy and the volume of the unburned zone rapidly decrease during combustion, it is logical that the maximum length scale (characteristic for large scale eddies) decreases and that the ratio of integral length scales decreases. As the combustion process comes to an end, the turbulence intensity of the unburned zone at the late part of combustion is very low. Therefore, the fractal dimension also comes close to the minimum value resulting with the turbulent flame surface area at the late part of combustion close to the laminar one.

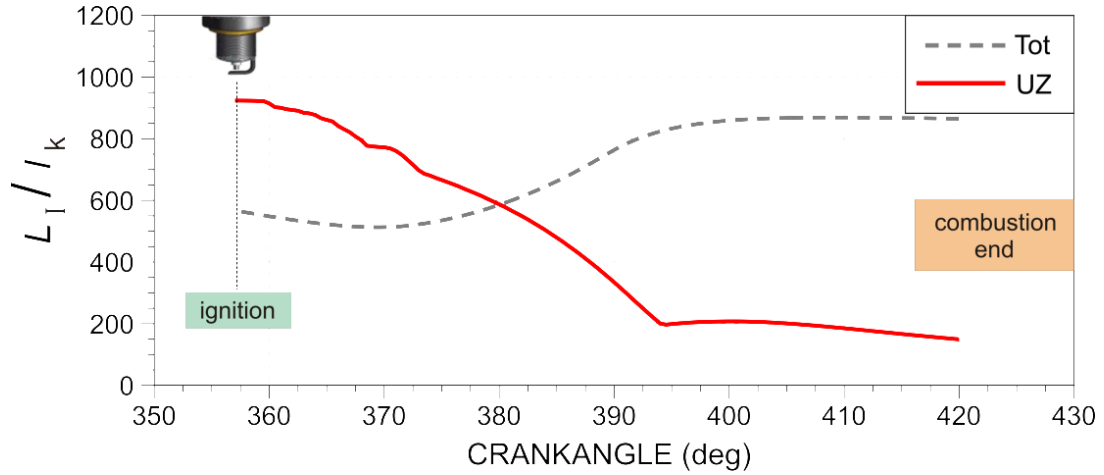


Figure 30. An example of calculated ratios of maximum to minimum integral length scale during the combustion (dashed gray line is calculated using the total in-cylinder turbulence, red solid line is defined using the unburned zone turbulence).

When turbulent quantities of the unburned zone are used in the calculation of combustion, the slowing down of the combustion process at the later stages is correctly predicted by the fractal combustion model, which makes the wall combustion part of the calculation unnecessary. Therefore, when a two zone turbulence model is applied, the overall burning rate is equal to the fractal burning rate:

$$\left(\frac{dm_{BZ}}{dt}\right)_{\text{overall}} = \left(\frac{dm_{BZ}}{dt}\right)_{\text{fractals}} = \rho_{UZ} \left(\frac{L_1}{l_k}\right)^{D_3-2} A_L S_L \quad (4.22)$$

As previously mentioned, the application of the two zone turbulence model represents physically more accurate prediction of the combustion process because the turbulent eddies in front of the flame are responsible for wrinkling of the flame front wrinkling and consequently for the burning rate of the SI engine. An influence of the two zone turbulence model on the prediction of combustion process and comparison with the combustion results obtained with the single zone turbulence model is demonstrated in Chapter 5.

## 5. Validation of cycle-simulation results with 3-D CFD data

The validation of the developed sub-models integrated into the cycle-simulation model of AVL BOOST was performed by the comparison of specific cycle-simulation results with the available 3-D CFD data from AVL FIRE. After that, the cycle-simulation model of the experimental engine was made and the combustion results were compared directly to the experimental data at several operating points. The validation of the developed sub-models with the 3-D CFD results was performed on several SI engines at different engine speeds and loads. The general engine data are shown in Table 1. All considered SI engines have pent roof design of the cylinder head and flat geometry of the piston top. The first three considered engines have the standard valve strategy (opening/closing angles are specified in Table 1) while the last engine has the VVA (variable valve actuator) strategy. The valve profiles for the considered engines are plotted in Figure 31. Furthermore, the last engine (Engine 4) utilizes direct injection of the fuel into the cylinder that can produce intensive mixture stratification compared to engines with port fuel injection. All considered engines were fueled by gasoline.

Table 1. Main data of considered SI engines

Engine name	Engine 1	Engine 2	Engine 3	Engine 4
Head geometry	pent roof			
Piston geometry	flat			
Fuel	gasoline			
Bore (mm)	86	79	84	86
Stroke (mm)	94.6	81.4	88.6	96
Displacement (cm <sup>3</sup> )	603.9	400	492.6	558
Compression ratio (-)	11.1:1	11.1:1	9.5:1	10.8:1
Con-rod length (mm)	146.7	137	160	143
Number of valves (-)	4 (2 intake, 2 exhaust)			
Intake valves open (° CA BTDC)	24	4	22	variable
Intake valves close (° CA BTDC)	133	134	108	variable
Exhaust valves open (° CA BBDC)	39	42	64	variable
Exhaust valves close (° CA ATDC)	9	18	46	variable
Intake valve seat diameter (mm)	30	27.4	33	33
Exhaust valve seat diameter (mm)	27	22.3	27	29
Mixture preparation	port injection	port injection	port injection	direct injection
Nbr. of operating. points (-)	3	4	3	5

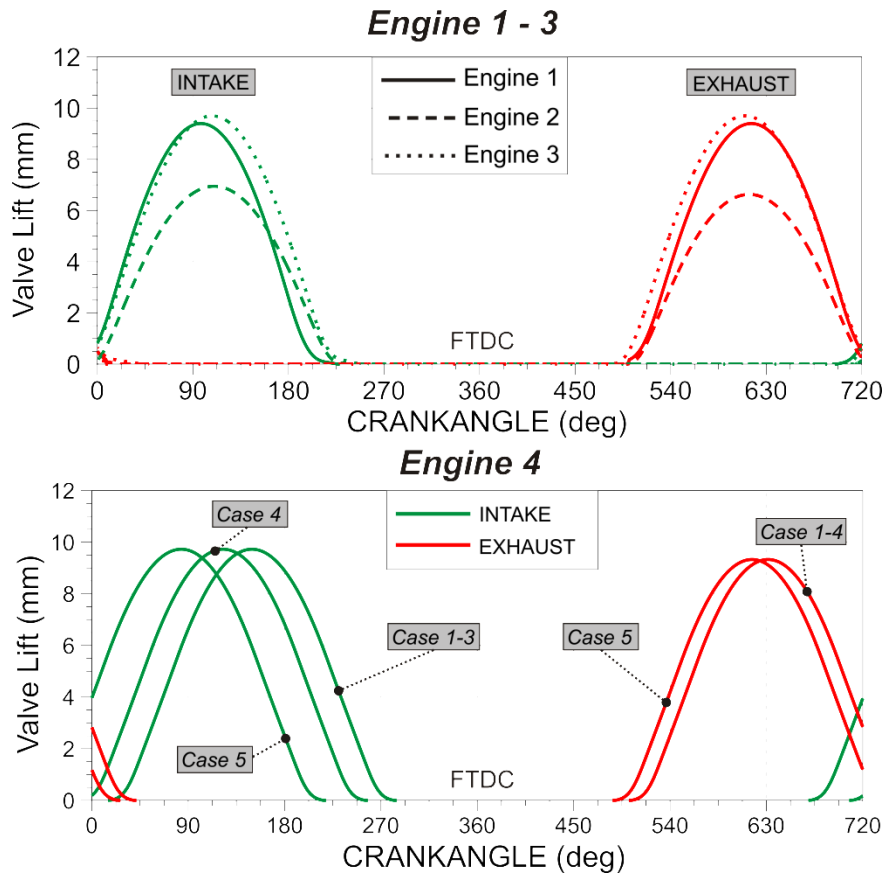


Figure 31. Intake and exhaust valve lift profiles of Engine 1 - 4.

The computational meshes of considered SI engines that are captured at TDC are shown in Figure 32. Unstructured moving meshes were used with different numbers of computational cells at the top and bottom dead center. At TDC the computational meshes have around 70000 cells, while at the BDC the number is around 1200000 cells. Detailed modeling of the intake and the exhaust system was not performed because the boundary conditions of pressure, temperature and mass flows are available from the experiment. The 3-D CFD simulations were performed as RANS simulations in AVL FIRE using the  $k-\varepsilon$  turbulence model and Three Zone-Extended Coherent Flame Model (3Z-ECFM) [87, 88] for the modeling of combustion associated phenomena.

The cycle-simulation models of considered engines in AVL BOOST are reduced models that consist of the intake system boundary (SB1), intake pipe (1), cylinder (C1), exhaust pipe (2) and exhaust system boundary (SB2) as it is already shown in Figure 2. Different engine geometries within the cycle-simulation model are defined by the specification of main geometry parameters such as intake pipe length and diameter, bore, stroke, compression ratio, etc.

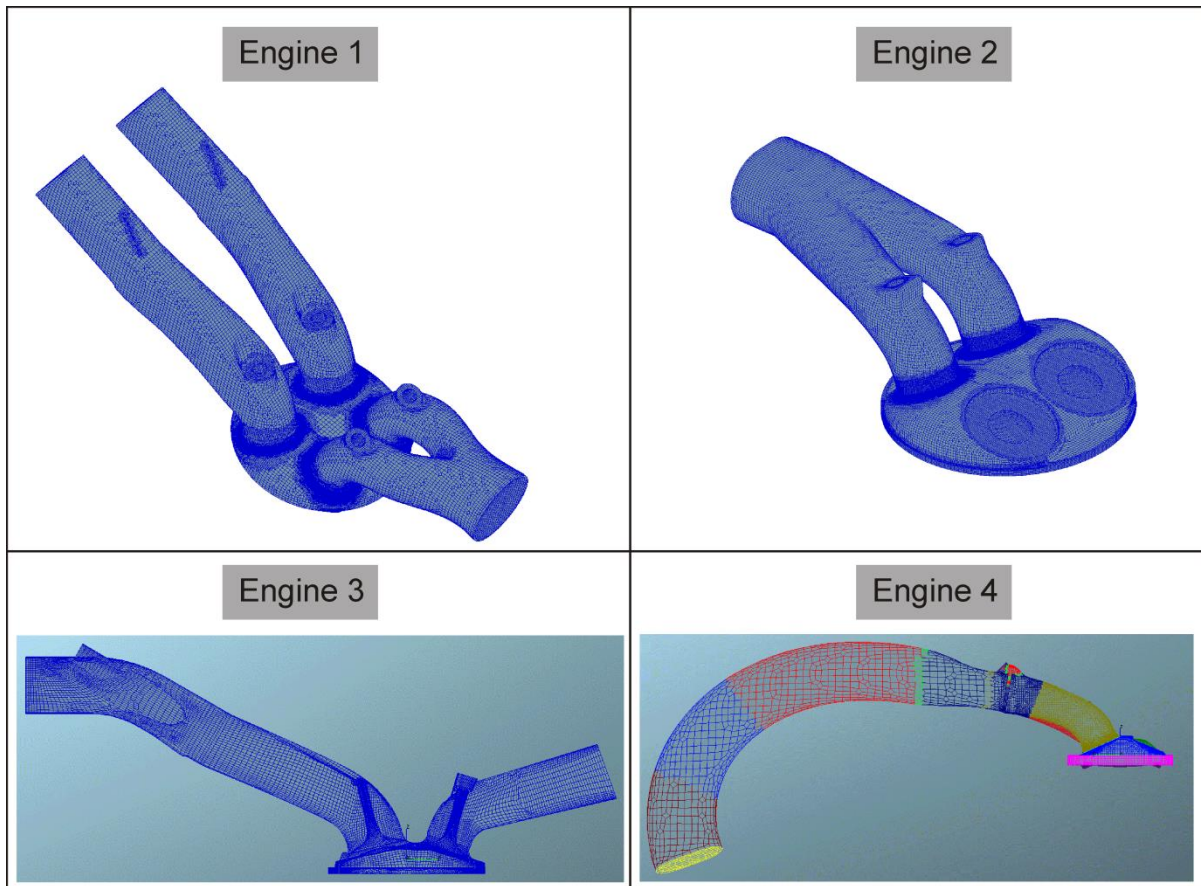


Figure 32. Geometries of the considered SI engines; computational meshes are captured at TDC.

The validation process of the cycle-simulation model is divided into six parts. In the first part, the developed single and two zone  $k-\varepsilon$  turbulence model were applied and its influence on the prediction of the combustion process was studied and analyzed. After that, the turbulence model was extended to the modeling of in-cylinder turbulence during the gas exchange phase and the cycle-simulation results of in-cylinder turbulence level were compared with the available 3-D CFD data from AVL FIRE during the intake and high pressure cycle. Within the third part the developed quasi-dimensional ignition model and modified transition from laminar to turbulent flame were applied, reducing the number of user-defined parameters that should be calibrated for each operating point. An analysis of turbulence and combustion model parameters that were tuned for each operating point of the engine resulted in a proposed parameterization of the turbulence and combustion constants which is described in fourth part. In order to obtain a single set of parameters for the turbulence sub-model for one engine geometry that will give cycle-simulation results of in-cylinder turbulence at a satisfactory level, the optimization of turbulence model constants was performed and described within the fifth part. At the end, the single set of constants related to

the combustion and turbulence models were applied and the cycle-simulation results were compared to the 3-D CFD data.

### 5.1. Validation of single and two zone $k$ - $\varepsilon$ turbulence model

The single zone  $k$ - $\varepsilon$  turbulence model was first developed as the turbulence model that can be applied during the high pressure cycle with the initial conditions of turbulent kinetic energy and its dissipation rate at the beginning of high pressure cycle specified from 3-D CFD results. Differential equations for the total in-cylinder turbulent kinetic energy (2.21) and its dissipation rate (2.22) and the new user-defined constant  $C_\varepsilon$  are described in Chapter 2.1.

The developed two zone  $k$ - $\varepsilon$  turbulence model is based on the simplified approach that uses previously defined single zone model. Instead of setting the model that will calculate the changes of turbulent kinetic energy and its dissipation rate for the burned and unburned zone [11], the developed two zone turbulence model calculates the total in-cylinder turbulent kinetic energy and the turbulent kinetic energy of the unburned zone. The turbulence values of the burned zone are then explicitly calculated from the total turbulence level and from the values obtained in the unburned zone. The two zone turbulence model is used during the combustion process when the cylinder mixture is divided into the burned and unburned zone. The initial turbulence values of the unburned zone are equal to the total in-cylinder turbulence values at the defined spark time because at that time the unburned zone is spread across the entire combustion chamber volume. Differential equations (2.31) and (2.33) of two zone turbulence model and the new user-defined constant  $C_\varepsilon^{UZ}$  are given and described in Chapter 2.2.

For each considered operating point of Engines 1 – 4, the newly introduced user-defined constants,  $C_\varepsilon$  and  $C_\varepsilon^{UZ}$ , were calibrated so that a best agreement of the cycle-simulation results with the 3-D CFD results of the turbulent kinetic energy is achieved. In order to analyze the influence of single and two zone turbulence model on the prediction of the combustion process, the normalized heat release (HR) and in-cylinder temperature for single and two zone turbulence model, are also shown and compared with the 3-D CFD results.

#### *Engine 1*

For the first considered engine geometry (Engine 1), the results of three operating points were analyzed. The specifications of considered operating points are listed in Table 2.

Table 2. Values of constants of single and two zone  $k-\varepsilon$  turbulence model and fractal combustion model – Engine 1

Case Name	<i>Case 1</i>	<i>Case 2</i>	<i>Case 3</i>
Engine speed (rpm)	2000	2000	5500
Load	Part (BMEP = 2.9 bar)	100 %	100 %
Spark Timing (° CA BTDC)	34	4	24
Excess Air Ratio (-)	1.0		
<b>Single zone turbulence model</b>			
$C_2$ (-)	1.92		
$C_\varepsilon$ (-)	2.35	2.35	2.48
<b>Two zone turbulence model</b>			
$C_2$ (-)	1.92		
$C_\varepsilon^{uz}$ (-)	3.00	7.50	4.70
<b>Fractal combustion model</b>			
$f_{D3,max}$ (-)	2.39 (1z) 2.37 (2z)	2.45 (1z) 2.43 (2z)	2.41 (1z) 2.40 (2z)
$c_{ign}$ (-)	4.00	0.40	1.80
$r_{f,ref}$ (m)	0.015	0.022	0.020
$x_B$ - mass fraction burned at wall comb. start (-)	0.50 (1z) - (2z)	0.45 (1z) - (2z)	0.20 (1z) - (2z)

The first operating point named *Case 1* represents relatively low engine speed and part load condition while the second operating point, *Case 2*, has the same engine speed but full load condition. The last operating point, *Case 3*, represents the full load condition and relatively high engine speed. The simulation of the combustion process for each operating point was performed first with the single zone turbulence model and after that with the two zone turbulence model. In Table 2 the parameters of the single and two zone turbulence models as well as the parameters of the fractal combustion model for both turbulence cases are specified.

The cycle-simulation results of the total in-cylinder turbulence and of the turbulence of the unburned zone are shown in Figure 33 and compared with the 3-D CFD results. Since the 3-D CFD simulation model consists of thousands of computational cells where each cell has certain value of some physical property, the 3-D CFD results used for the validation are mass-averaged results over the entire cylinder domain. In order to obtain the mass-averaged physical properties of the unburned zone from the 3-D CFD results, it is necessary to separate computational cells on the burned and unburned cells. The separation of cells on the burned and unburned is made by controlling the number of mass fraction burned at each cell. The computational cells which have mass fraction burned below 0.5 are selected as unburned cells while the cells where the mass fraction burned is above the value of 0.5 are considered as



burned cells. This enables the possibility to directly compare the cycle-simulation results with the available 3-D CFD data.

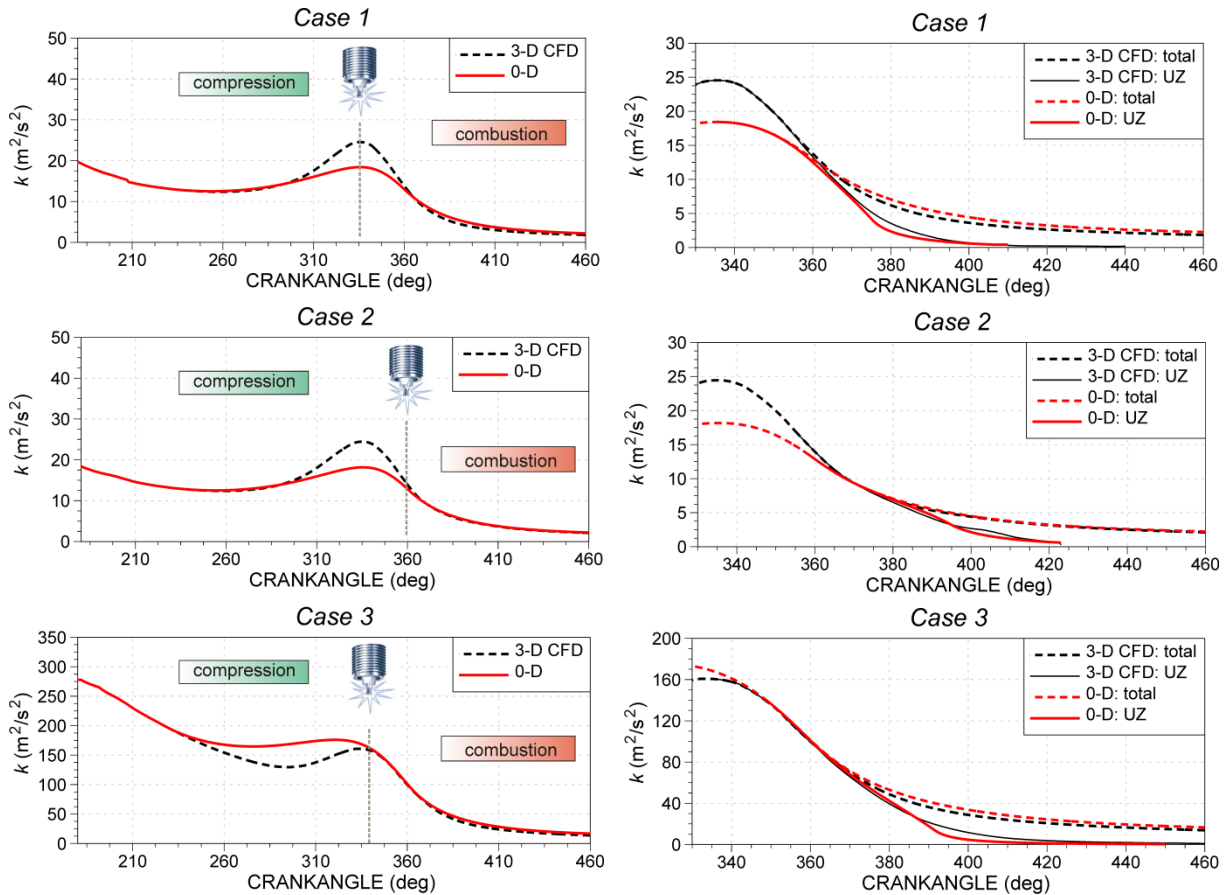


Figure 33. Comparison of total turbulent kinetic energy of the single zone model during the HPC (left) and results of total and unburned zone turbulent kinetic energy of the two zone model during the combustion (right); Engine 1.

On the left hand side of Figure 33 the total in-cylinder turbulent kinetic energies during the high pressure cycle are compared with the 3-D CFD results. The initial values of turbulent kinetic energy at the beginning of the high pressure cycle are the same because the 3-D CFD results were used as the input data. During the early part of compression stroke, 0-D simulation results of the turbulent kinetic energy are very close to the profiles calculated with multi-dimensional  $k-\varepsilon$  turbulence model in AVL FIRE. As the piston moves to the top position, the large scale flow structures in the cylinder are dissipated into the smaller ones resulting in an increase of the turbulence level that can be observed close to the TDC in both, 3-D CFD and 0-D simulation. Moreover, it is stated in [51] that during the rapid compression of gases, characteristic for the compression in IC engines, small scale structures in the turbulent flow field interacts more rapidly with the large scale structures than it interacts with itself. This non-linear interactions between the turbulent eddies are neglected in the presented 0-D model.

The new user-defined constant  $C_\epsilon$  is calibrated for each operating point so that a very good agreement of 0-D results with the 3-D CFD results are achieved during the combustion period, when the turbulence has a very strong impact on the combustion process. In *Case 1* and *Case 2* it can be seen that the peak values of in-cylinder turbulence around TDC are slightly lower in the 0-D simulation. There are three possible reasons for such results:

- 1) Turbulent flow field is non-homogeneous and anisotropic.
- 2) The viscous (shear) effects are so high (low Reynolds number) that they produce significant change in the turbulent kinetic energy.
- 3) A complex 3-D interaction of turbulent eddies.

Bearing in mind that the 0-D turbulence model is based on a significantly simplified approach, neglecting the complex 3-D effects that can occur in the cylinder, the obtained 0-D results of the total in-cylinder turbulence are in a very good agreement with the 3-D CFD results. During the combustion period, when the turbulent eddies wrinkle the flame front and increase the combustion rate, the cylinder mixture is divided into the burned and unburned zone. Therefore, the turbulent kinetic energy of the unburned zone can also be calculated if the two zone turbulence model is activated. Otherwise, the turbulence of the unburned zone is equal to the total in-cylinder turbulence level. The 0-D results of the total in-cylinder turbulence and the turbulent kinetic energy of the unburned zone during the combustion period are shown on the right hand side of Figure 33 and the results are compared with the 3-D CFD data. The solid lines are related to the unburned zone turbulence while the dashed lines represent the total in-cylinder turbulent kinetic energy. By tuning the new user-defined constant  $C_\epsilon^{UZ}$ , that influences the dissipation rate of the unburned zone, at each operating point, the progress of unburned zone turbulence is very close to the one obtained by the 3-D CFD model. Besides tuning of this constant, the combustion process is also responsible for the progress of turbulent kinetic energy of the unburned zone. Faster combustion results in the faster decrease of the unburned zone turbulence and vice versa. As the combustion process advances, the unburned zone turbulent kinetic energy decreases because its volume becomes smaller and the turbulent eddies of larger integral length scales that are dominant in energy spectrum cannot exist any more.

In order to analyze the influence of single and two zone turbulence model formulations on the combustion process, the normalized heat release (HR) and in-cylinder temperature are compared with the 3-D CFD solution in Figure 34. The 0-D simulation results that were calculated with the single zone turbulence model are shown with the solid grey line

while the results obtained with the two zone turbulence model are presented with the solid red line. In both cases, the parameters of fractal combustion model were calibrated so that a very good agreement between the 0-D and 3-D CFD results of the combustion progress is achieved. The constants of the fractal combustion model in both cases, single and two zone turbulence model, are specified in Table 2.

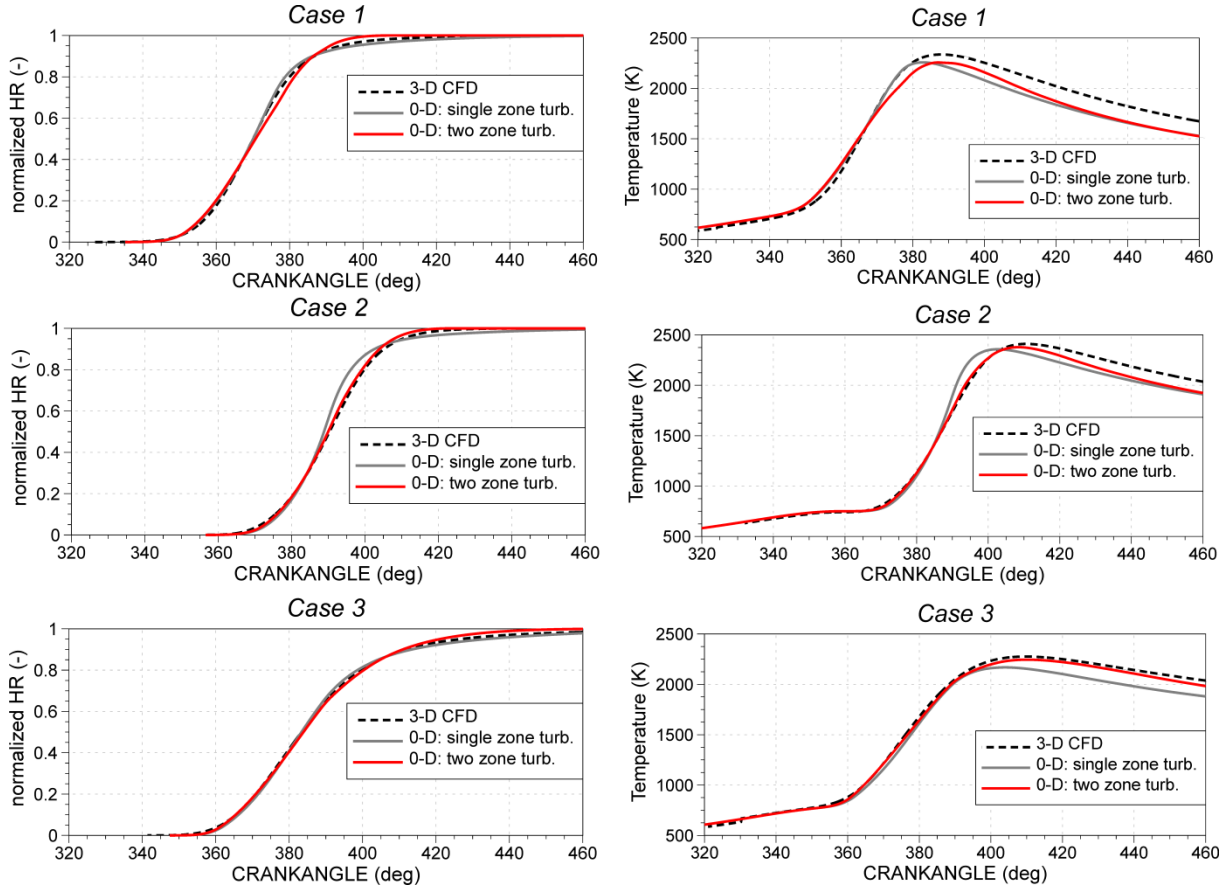


Figure 34. Normalized heat release (left) and in-cylinder temperature (right) of Engine 1: single and two zone turbulence model.

The fractal combustion model calculates the turbulent burning rate on the assumption that the wrinkled flame front  $A_T$  propagates through the unburned zone at the laminar flame speed  $S_L$  [83]. When the single zone turbulence model is applied, the unburned zone turbulence is equal to the total in-cylinder turbulence level. In this case, the overall burning rate is calculated as a weighted mean of the fractal and wall combustion rate as already described by equation (4.9). Therefore, for each operating point it was necessary to define the mass fraction burned when the wall combustion is activated. This parameter is also specified in Table 2. Although the default value of the mentioned parameter is 0.2, as it was used in *Case 3*, for good agreement it should be calibrated for each individual operating point by comparing the

normalized HR with the reference (3-D CFD) result at the late part of combustion, when about 50 % of in-cylinder mass is already burned.

The remaining three parameters of the fractal combustion model specified in Table 2 are  $f_{D3,max}$ ,  $C_{ign}$  and  $r_{f,ref}$  representing the upper limit of fractal dimension, ignition formation time multiplier and the reference flame front radius when the maximum wrinkling will occur, respectively. An ignition formation time multiplier represents the tunable model parameter that multiplies the duration of ignition process (see equation (4.11)). It is defined by comparing the normalized HR with the 3-D CFD results during the early combustion process when the mass fraction burned is below 5 %. The reference flame front radius represents the average flame front radius when the maximum wrinkling of the flame front occurs. This does not mean necessarily that the maximum burning speed is achieved at this radius, because the burning speed depends also on the flame front surface area. The reference flame front radius can be used to tune the early part of combustion (up to 50 % of mass fraction burned) process during which the transition from laminar to fully developed turbulence flame occurs. For individual operating points the same values of the ignition delay multiplier  $C_{ign}$  and the reference flame front radius  $r_{f,ref}$  were used in the single and two zone turbulence model. The calibration of constant  $f_{D3,max}$  that represents the upper limit of fractal dimension was performed so that the prediction of the point when the 50 % of the mass is burned is in a good agreement with the 3-D CFD result.

When the two zone turbulence model is applied, the overall combustion rate is equal to the fractal combustion rate and the wall combustion mode is fully omitted, as it is presented by equation (4.22). In this case, the user-defined parameter "*Mass fraction burned at Wall Combustion Start*" does not have to be specified, but the dissipation constant  $C_{\epsilon}^{UZ}$  of the unburned zone has to be defined. When the results of the in-cylinder temperature calculated by the single and the two zone model are compared with the 3-D CFD results (Figure 34), it is evident that the results of the two zone turbulence model show better agreement with the 3-D CFD data. This is expected due to the fact that the unburned zone turbulence is used for the definition of flame front wrinkling and for its development across the combustion chamber. There are two main effects that influence the better prediction of combustion rate when the unburned zone turbulence is calculated:

- 1) The ratio of maximum to minimum integral length scale based on the unburned zone turbulence slows down the combustion rate because this ratio becomes

lower and lower as the combustion approaches to the end. An example of this effect is already shown in Figure 30.

- 2) Turbulence intensity of the unburned zone that defines the instantaneous value of the fractal dimension decreases the wrinkling ratio of the flame front.

## Engine 2

For the second engine geometry named Engine 2, four operating points were available. The main operating parameters, constants of turbulence and of combustion sub-model for Engine 2 are given in Table 3.

Table 3. Values of constants of single and two zone  $k-\varepsilon$  turbulence model and fractal combustion model – Engine 2

Case Name	Case 1	Case 2	Case 3	Case 4
Engine speed (rpm)	1500	1500	2000	5500
Load	Part (BMEP = 2.62 bar)	100 %	100 %	100 %
Spark Timing (° CA BTDC)	14	- 0.2	2.1	15.7
Excess Air Ratio (-)	1.0			
<b>Single zone turbulence model</b>				
$C_2$ (-)	1.92			
$C_\varepsilon$ (-)	2.30	2.35	2.23	2.30
<b>Two zone turbulence model</b>				
$C_2$ (-)	1.92			
$C_\varepsilon^{uz}$ (-)	4.00	6.50	6.50	5.00
<b>Fractal combustion model</b>				
$f_{D3,max}$ (-)	2.52 (1z) 2.48 (2z)	2.48 (1z) 2.48 (2z)	2.47 (1z) 2.43 (2z)	2.52 (1z) 2.49 (2z)
$c_{ign}$ (-)	0.30	0.01	0.01	0.80
$r_{f,ref}$ (m)	0.015	0.010	0.015	0.036
$x_B$ - mass fraction burned at wall comb. start (-)	0.35 (1z) - (2z)	0.45 (1z) - (2z)	0.25 (1z) - (2z)	0.35 (1z) - (2z)

The first two operating points, *Case 1* and *Case 2*, represent low engine speed conditions with different loads. The third operating point, *Case 3*, has slightly increased engine speed of 2000 rpm and full load. The last operating point, *Case 4*, represents high engine speed and full load condition. All considered operating points are operated at stoichiometric gasoline/air mixtures.

The results of the in-cylinder turbulent kinetic energies during the high pressure cycle and during the combustion period are shown below in Figure 35. On the left hand side of Figure 35 the progress of total in-cylinder turbulent kinetic energy during the high pressure

cycle calculated using the single zone model is shown and the 0-D results (red solid lines) are compared with the 3-D CFD results (black dashed lines). On the right side of Figure 35 the turbulent kinetic energies (total and unburned zone) calculated using the two zone model during the combustion period are shown and compared with the 3-D CFD results.

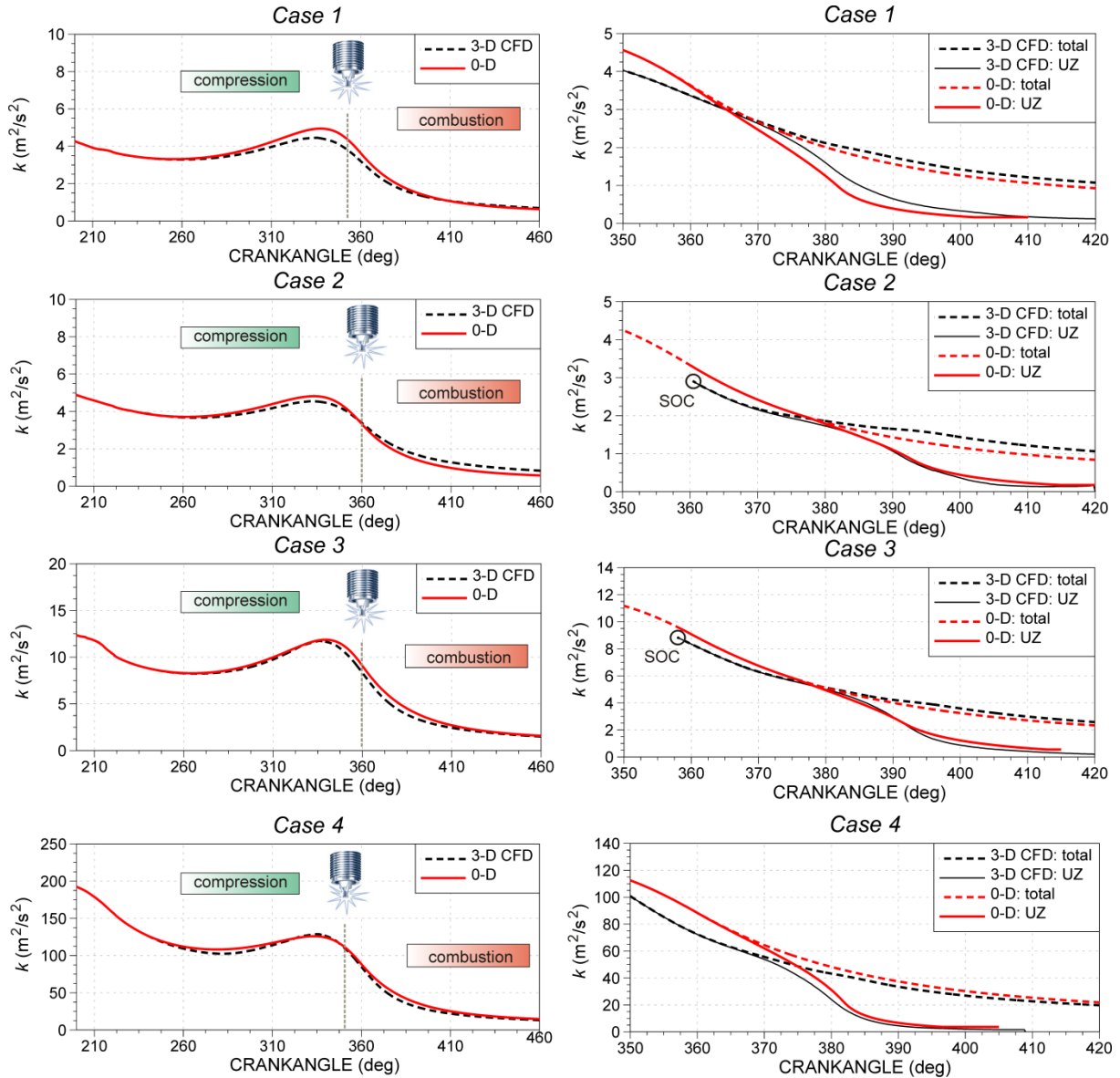


Figure 35. Comparison of total turbulent kinetic energy of the single zone model during the HPC (left) and results of total and unburned zone turbulent kinetic energy of the two zone model during the combustion (right); Engine 2.

It can be seen that by fine tuning of new user-defined constant  $C_e$  a very good agreement of prediction of total in-cylinder turbulence level at different operating conditions during the high pressure cycle can be achieved. In terms of predictions of peak values that occur around TDC, the developed 0-D turbulence model shows better behavior on Engine 2. This may be explained by more homogeneous and isotropic turbulent flow field that occurs

during the high pressure cycle. Since the 0-D turbulence model is based on this assumption, the predicted progress of total in-cylinder turbulence is significantly better.

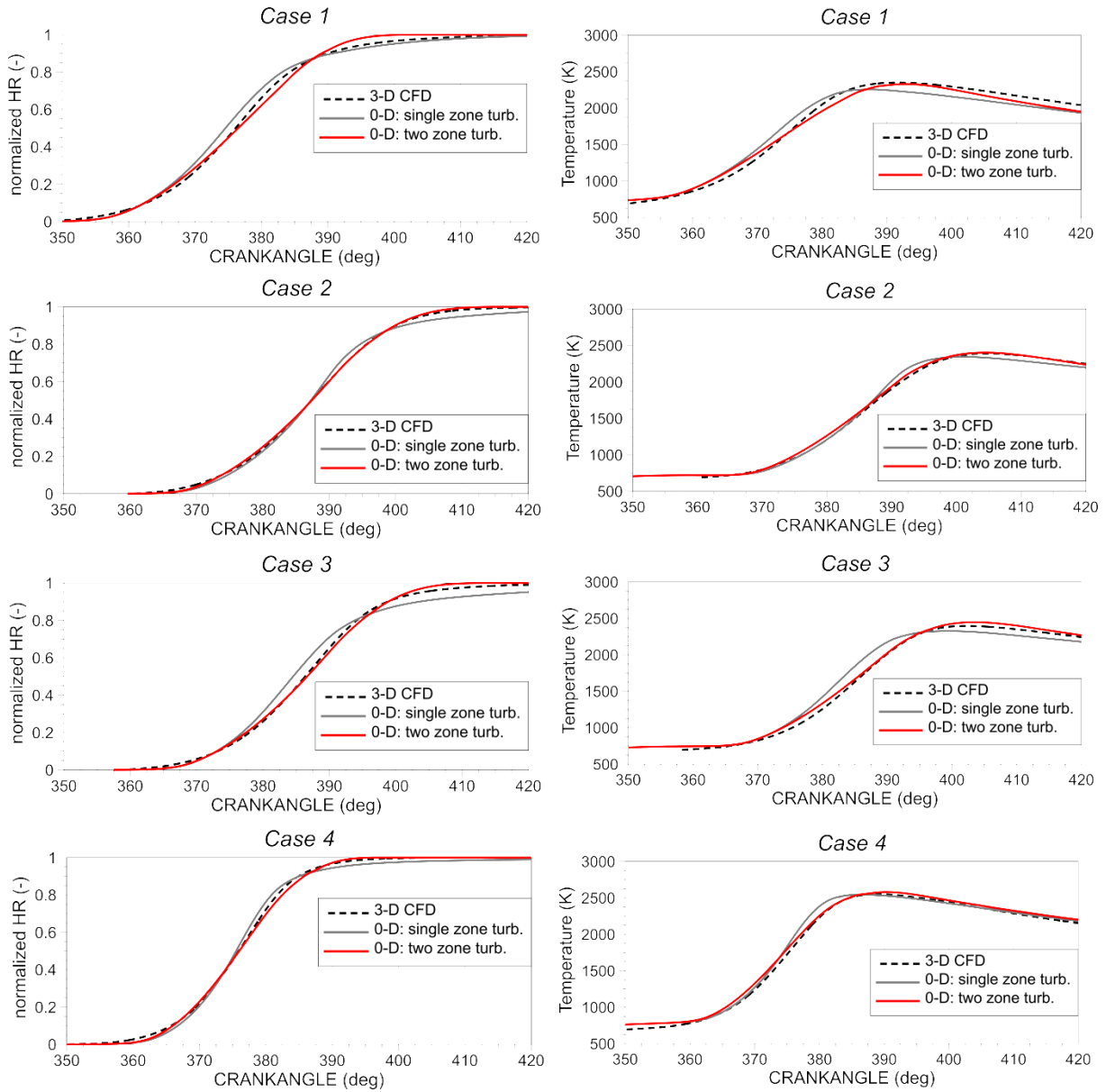


Figure 36. Normalized heat release (left) and in-cylinder temperature (right) of Engine 2: single and two zone turbulence model.

The normalized HR and in-cylinder temperatures are shown and compared with the 3-D CFD results for all considered operating points of Engine 2 in Figure 36. As it can be seen from Figure 36, the two zone turbulence model once again shows better prediction of the combustion progress as well as the in-cylinder temperature. Although the exhaust gas emissions are not considered within this study, the better prediction of in-cylinder temperature and its peak values creates significantly better conditions for the calculation of exhaust gas emissions in terms of nitric oxides ( $\text{NO}_x$ ), carbon monoxide (CO) and unburned hydrocarbons (HC).

### Engine 3

For the third engine geometry named Engine 3, three operating points were available. The main operating parameters, constants of turbulence and of combustion sub-model for Engine 3 are given in Table 4.

Table 4. Values of constants of single and two zone  $k$ - $\varepsilon$  turbulence model and fractal combustion model – Engine 3

Case Name	Case 1	Case 2	Case 3
Engine speed (rpm)	1500	1500	3000
Load	Part (BMEP = 2.0 bar)	Part (BMEP = 1.8 bar)	100 %
Spark Timing (° CA BTDC)	30	15	21
Excess Air Ratio (-)	1.0		
<b>Single zone turbulence model</b>			
$C_2$ (-)	1.92		
$C_\varepsilon$ (-)	2.00	2.23	2.48
<b>Two zone turbulence model</b>			
$C_2$ (-)	1.92		
$C_\varepsilon^{uz}$ (-)	4.00	3.00	3.00
<b>Fractal combustion model</b>			
$f_{D3,max}$ (-)	2.56 (1z) 2.52 (2z)	2.58 (1z) 2.58 (2z)	2.48 (1z) 2.48 (1z)
$c_{ign}$ (-)	2.00	0.01	1.00
$r_{f,ref}$ (m)	0.020	0.010	0.018
$x_B$ - mass fraction burned at wall comb. start (-)	0.60 (1z) - (2z)	0.65 - (2z)	0.50 - (2z)

The first two operating points of Engine 3, *Case 1* and *Case 2*, are analyzed at low engine speed and at part load conditions with different spark timings. The last operating point named *Case 3* represents the middle engine speed and full load condition.

The results of in-cylinder turbulent kinetic energies during the high pressure cycle and during the combustion period are shown in Figure 37. By tuning the dissipation constant  $C_\varepsilon$  of turbulent kinetic energy it is possible to achieve the progress of total in-cylinder turbulence that is very close to the 3-D CFD profile, especially during the combustion period when the turbulent eddies influence the flame wrinkling and flame front deformation. On the right side of Figure 37 the turbulent kinetic energies (total and unburned zone) during the combustion period are shown and compared with the 3-D CFD results. The progress of unburned zone turbulent kinetic energy calculated by the 0-D turbulence model (red solid lines in Figure 37 right) is close to the 3-D CFD solution. For *Case 2* and *Case 3*, it can be seen that the curves



of unburned zone turbulence from 0-D simulation are terminated before the 3-D CFD results for about  $10^\circ - 15^\circ$  of crank angle because the combustion duration is lower.

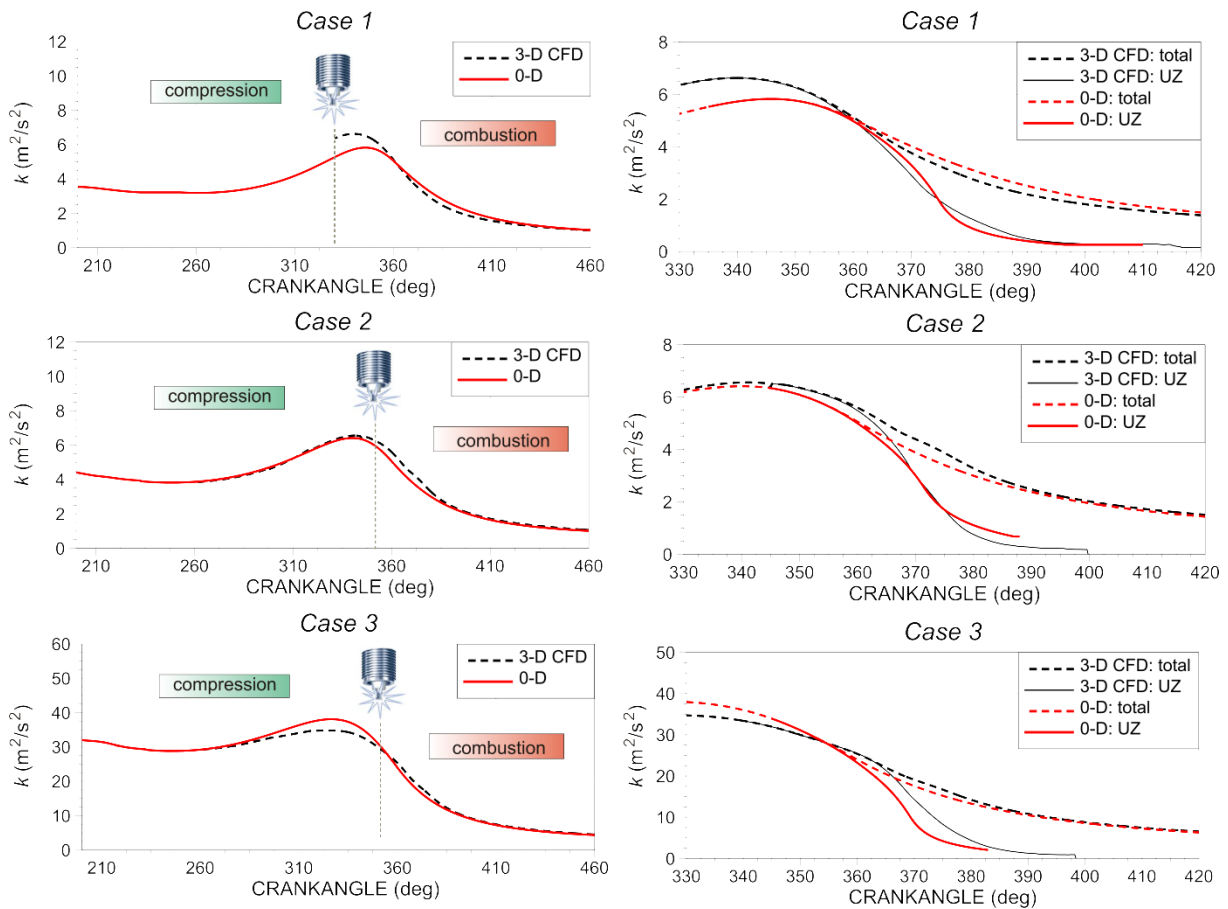


Figure 37. Comparison of total turbulent kinetic energy of the single zone model during the HPC (left) and results of total and unburned zone turbulent kinetic energy of the two zone model during the combustion (right); Engine 3.

The normalized HR and in-cylinder temperatures are shown and compared with the 3-D CFD results for the three operating points of Engine 3 in Figure 38. The reference results of 3-D CFD simulation are shown with the black dashed lines, while the results of single and two zone turbulence model are presented with the gray and red solid line, respectively. It can be observed that the 0-D simulation results of the in-cylinder temperature do not fully match the profiles calculated by 3-D CFD although the in-cylinder turbulence level is predicted correctly. The mentioned difference of in-cylinder temperature is more pronounced at the second operating point *Case 2* where the 0-D simulation results of peak temperature are significantly under-predicted. Such difference can be caused by the different air equivalence ratio of the in-cylinder mixture (higher energy that can be released) because the normalized HR in both single and two zone turbulence models are close to the 3-D CFD results, but the peak temperatures are significantly lower. Moreover, the trends of temperature profile are

very similar to the 3-D CFD results indicating that the turbulence and combustion parameters are correctly defined.

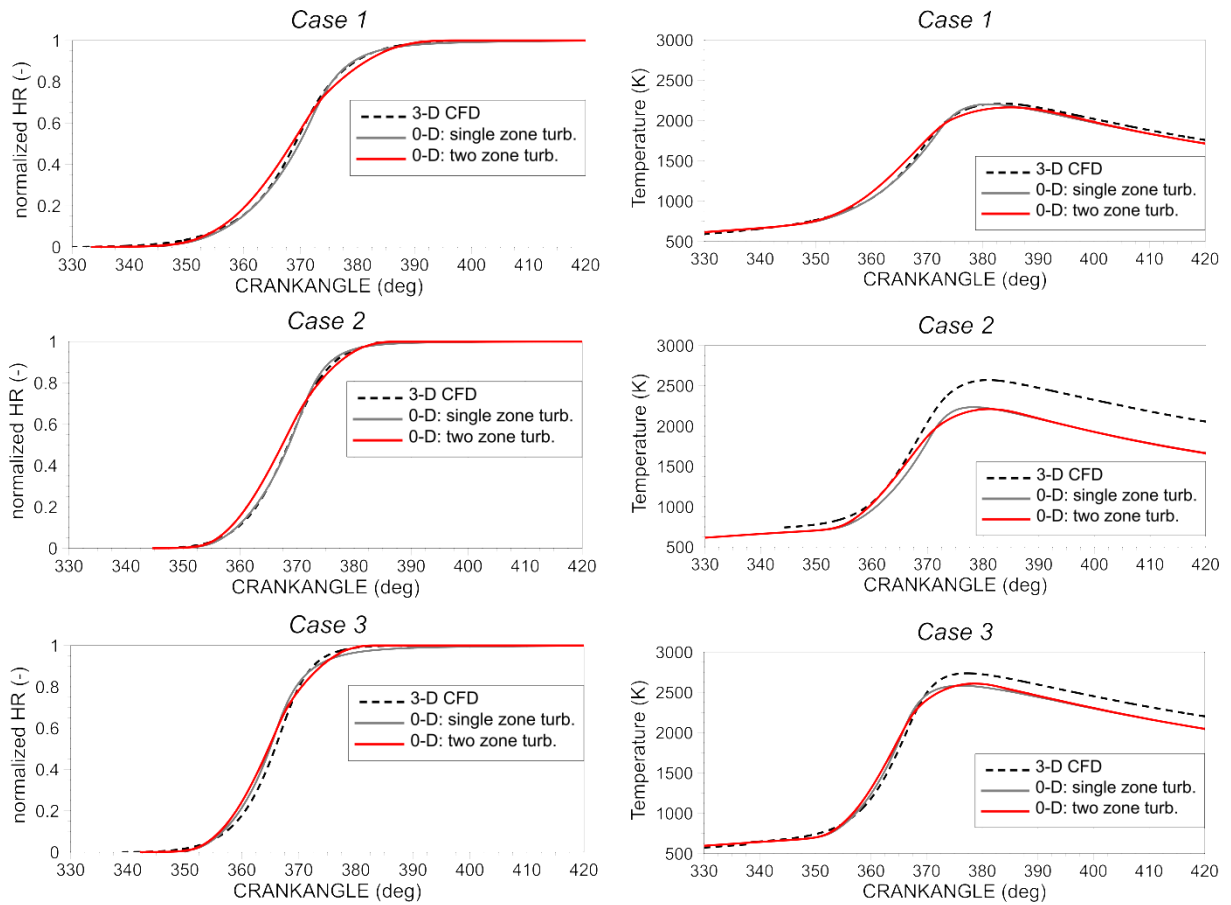


Figure 38. Normalized heat release (left) and in-cylinder temperature (right) of Engine 3: single and two zone turbulence model.

### Engine 4

The last considered engine geometry (Engine 4) within this study has five operating points that were analyzed. It is already shown in Figure 31 that this engine has variable valve timing at the intake and exhaust. The first three operating points named *Case 1*, *Case 2* and *Case 3* represent part load conditions with engine speed set at 1000, 2000 and 3000 rpm, respectively. The remaining two operating points, *Case 4* and *Case 5*, represent the full load conditions at middle and high engine speed when the maximum engine torque and the output power are achieved. The main operating parameters, constants of the turbulence and of the combustion sub-model for Engine 4 are given in Table 5.

Table 5. Values of constants of single and two zone  $k-\varepsilon$  turbulence model and fractal combustion model – Engine 4

Case Name	Case 1	Case 2	Case 3	Case 4	Case 5
Engine speed (rpm)	1000	2000	3000	2845	6215
Load	Part (BMEP = 1 bar)	Part (BMEP = 2 bar)	Part (BMEP = 3 bar)	100 % (max. torque)	100 % (max. power)
Spark Timing (° CA BTDC)	35	36	25.5	22.5	22.5
Excess Air Ratio (-)	1.0				
<b>Single zone turbulence model</b>					
$C_2$ (-)	1.92				
$C_\varepsilon$ (-)	2.05	2.32	2.55	2.20	2.35
<b>Two zone turbulence model</b>					
$C_2$ (-)	1.92				
$C_\varepsilon^{uz}$ (-)	3.00	5.00	3.00	5.00	4.00
<b>Fractal combustion model</b>					
$f_{D3,max}$ (-)	2.49 (1z) 2.46 (2z)	2.46 (1z) 2.44 (2z)	2.45 (1z) 2.44 (2z)	2.45 (1z) 2.43 (2z)	2.48 (1z) 2.46 (2z)
$c_{ign}$ (-)	9.00	7.00	2.50	1.80	1.00
$r_{f,ref}$ (m)	0.010	0.016	0.015	0.024	0.038
$x_B$ - mass fraction burned at wall comb. start (-)	0.50 (1z) - (2z)	0.40 (1z) - (2z)	0.55 (1z) - (2z)	0.40 (1z) - (2z)	0.30 (1z) - (2z)

The results of the in-cylinder turbulent kinetic energies during the high pressure cycle and during the combustion period are shown in Figure 39. On the left side of Figure 39 the progress of total in-cylinder turbulent kinetic energy during the high pressure cycle is shown and the 0-D results are compared with the 3-D CFD results. The initial conditions for the unburned zone turbulent kinetic energy are predicted correctly because the total in-cylinder turbulence level is captured well. The progress of total and unburned zone turbulent kinetic energy during the combustion period obtained by the two zone model is shown on the right side of Figure 39. It can be seen that the 0-D results of the unburned zone turbulent kinetic energy are in a very good agreement with the 3-D CFD results if the new user-defined constant  $C_\varepsilon^{UZ}$  as well as the parameters of the fractal combustion model are tuned correctly.

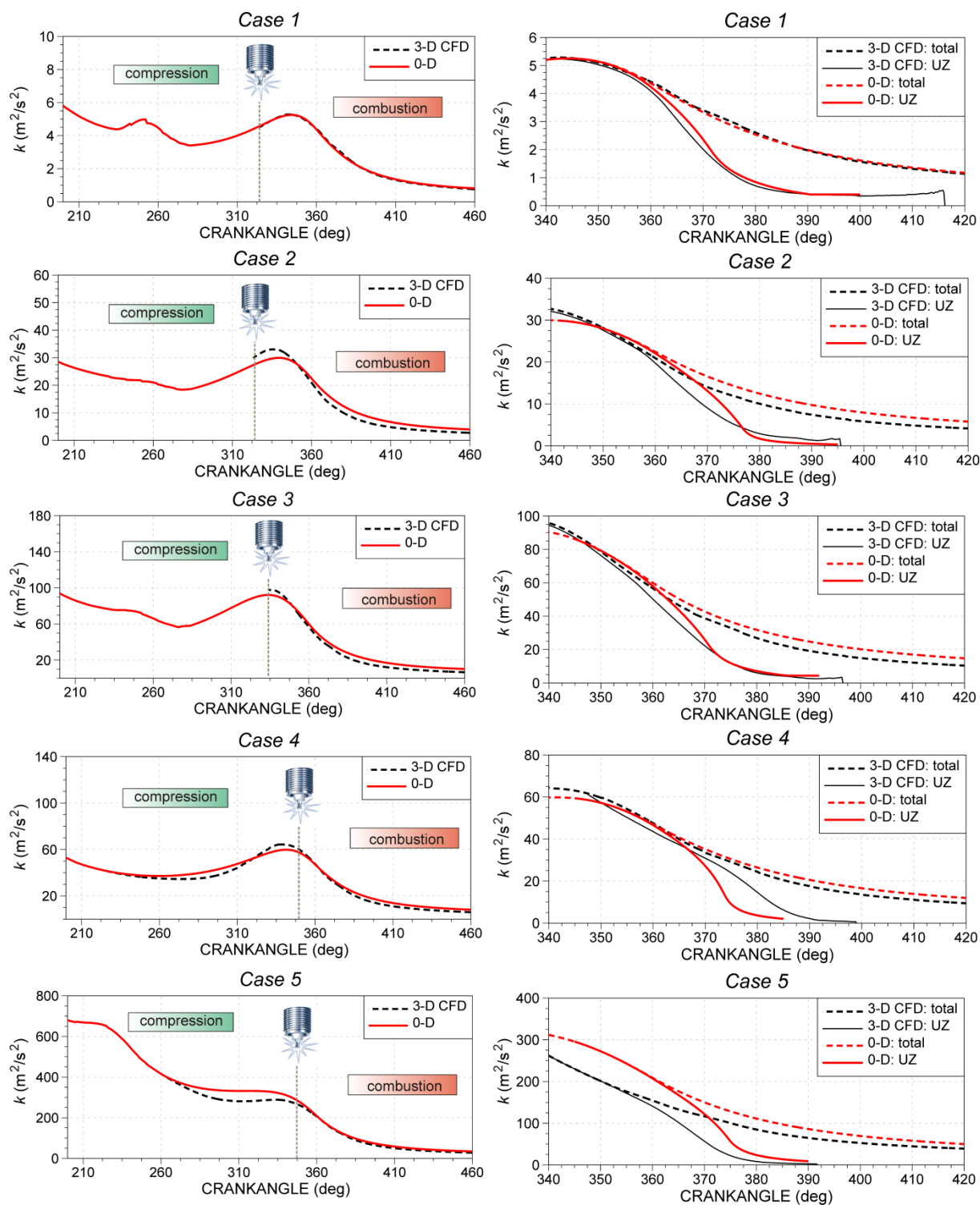


Figure 39. Comparison of total turbulent kinetic energy of the single zone model during the HPC (left) and results of total and unburned zone turbulent kinetic energy of the two zone model during the combustion (right); Engine 4.

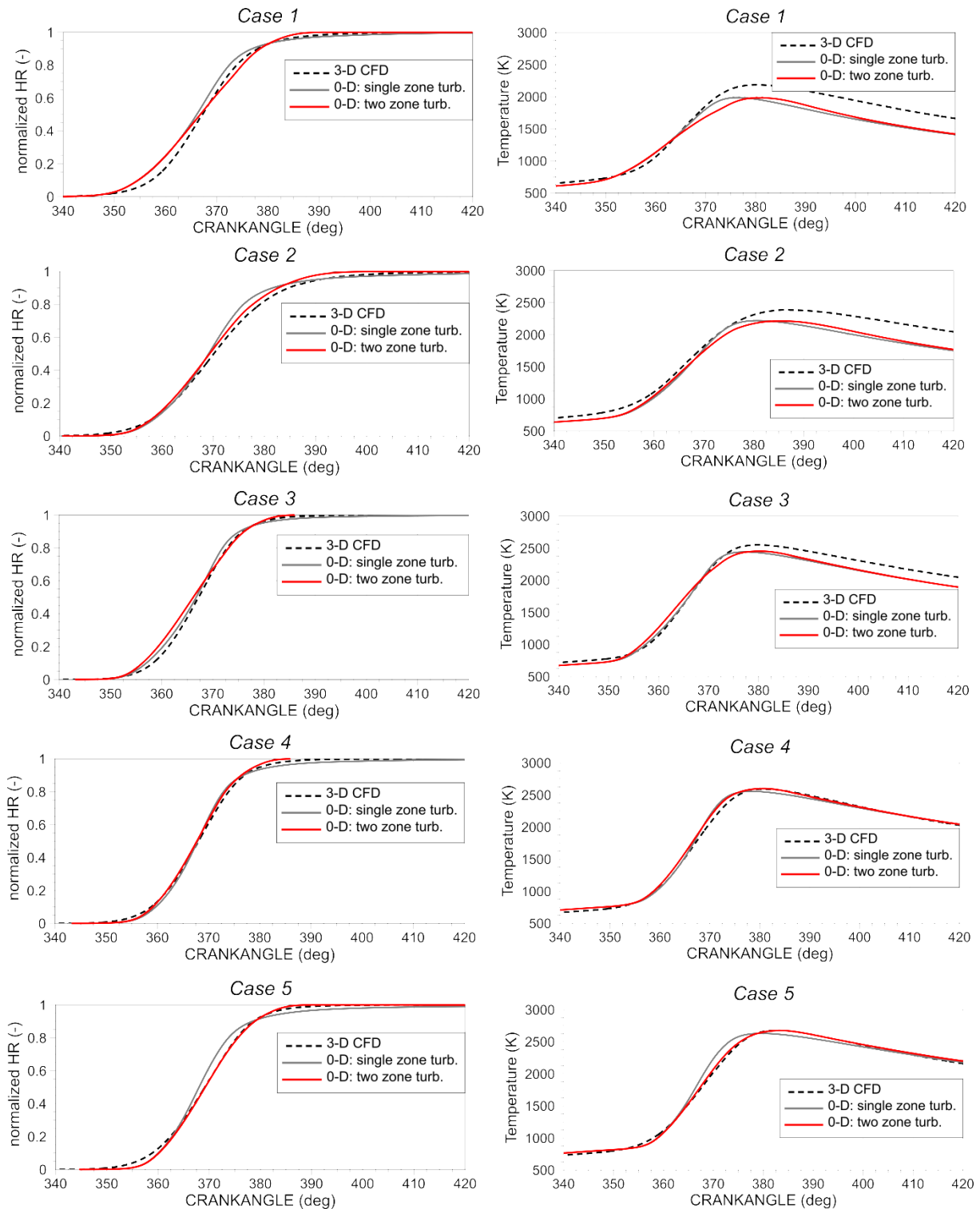


Figure 40. Normalized heat release (left) and in-cylinder temperature (right) of Engine 4: single and two zone turbulence model.

The normalized HR and the in-cylinder temperatures are shown and compared with the 3-D CFD results for all operating points of Engine 4 in Figure 40. Once again, it is shown that the two zone turbulence model gives the better prediction of the combustion process than the single zone turbulence model with the same number of user-defined constants. The results of

the combustion progress obtained by the two zone turbulence model are much closer to the 3-D CFD results, especially during the late part of combustion, when the unburned zone turbulence defines the overall burning rate ("wall combustion" sub-model is fully omitted). The better prediction of the combustion process obtained by two zone turbulence model is observable at all cases of Engine 4 because the profile of in-cylinder temperature as well as the peak in-cylinder temperatures are closer to the 3-D CFD results than the results calculated by single zone turbulence model.

## 5.2. Validation of full cycle $k$ - $\varepsilon$ turbulence model

In the previous chapter the single and two zone turbulence models were used and validated by comparing the 0-D results with the available 3-D CFD results. The initial condition of the in-cylinder turbulent kinetic energy at the beginning of the high pressure cycle was specified from 3-D CFD simulations for each operating point of the engine. In order to eliminate the model dependency on external initial conditions, the full single zone  $k$ - $\varepsilon$  turbulence model was developed and applied to the considered operating points of Engine 1 – 4. From differential equations of the turbulent kinetic energy (2.36) and its dissipation rate (2.37) it can be seen that 3 user-defined constants have to be specified:  $S_{in}$ ,  $C_{in}$  and  $C_\varepsilon$ . The first user-defined constant  $S_{in}$  is the intake  $k$  production constant and  $C_{in}$  is the intake  $\varepsilon$  production constant. These constants have to be calibrated by comparison of the 0-D simulation results of turbulent kinetic energy to the 3-D CFD results during the entire engine cycle. The dissipation rate constant  $C_\varepsilon$  which is dominant during the high pressure cycle is already calibrated in the previous chapter, but the values of  $C_\varepsilon$  are different at different operating points (it varies in the range from 2.0 to 2.48). In order to avoid the calibration of this constant at each operating point of the engine, in the application of full  $k$ - $\varepsilon$  turbulence model the new user-defined constant  $C_\varepsilon$  is fixed to a single value of 2.40, while the intake  $k$  and  $\varepsilon$  production constants are tuned so that a good agreement of the turbulent kinetic energy during the engine cycle is achieved, particularly during the combustion process when the values of the turbulent kinetic energy are very important. For the modeling of the combustion process, the two zone turbulence model was used and the applied constants of two zone model are specified in Table 2 - Table 5.

## Engine 1

For the first engine geometry the parameters of full  $k-\varepsilon$  turbulence model are specified in Table 6. The two user-defined constants ( $S_{in}$  and  $C_{in}$ ) were calibrated for each operating point influencing the production terms of the turbulent kinetic energy and its dissipation rate during the intake process. For the modeling of combustion, the two zone turbulence model is applied.

Table 6. Values of constants of full  $k-\varepsilon$  turbulence model – Engine 1

Case Name	Case 1	Case 2	Case 3
Engine speed (rpm)	2000	2000	5500
Load	Part (BMEP = 2.9 bar)	100 %	100 %
$C_2$ (-)	1.92		
$C_\varepsilon$ (-)	2.40		
$S_{in}$ (-)	$4.8 \cdot 10^{-4}$	$4.8 \cdot 10^{-4}$	$2.5 \cdot 10^{-3}$
$C_{in}$ (-)	2.80	1.53	2.25

The progress of the in-cylinder turbulent kinetic energy during the entire engine cycle for three operating points of Engine 1 are shown in Figure 41 and the 0-D simulation results are compared with the 3-D CFD results. Two user-defined constants  $S_{in}$  and  $C_{in}$  are manually set at each operating point to reproduce the level of turbulent kinetic energy during the combustion period close to the profile of 3-D CFD shown with the black dashed line. Unfortunately, the 3-D CFD results of in-cylinder turbulent kinetic energy during the exhaust were not available, but this does not prevent the validation of the developed turbulence sub-model at the remaining part of the engine cycle.

When the mass of fresh mixture or fresh air from the intake pipe flows into the cylinder, it increases both, mean flow and turbulent kinetic energy. During this phase usually the peak value of in-cylinder turbulence occurs, as it can be observed in Figure 41 in the crank angle range from  $0^\circ$  to  $180^\circ$ . According to the energy cascade phenomenon, the large coherent flow structures that represent the mean flow kinetic energy are dissipated into the continuously smaller and smaller turbulent eddies. This means that the mean flow kinetic energy influence the production of turbulent kinetic energy. Although the proposed  $k-\varepsilon$  turbulence model for the entire engine cycle does not include the calculation of mean flow kinetic energy, this effect is included with the first term on the right hand side of equation (2.36) that is multiplied by the new user-defined constant  $S_{in}$ .

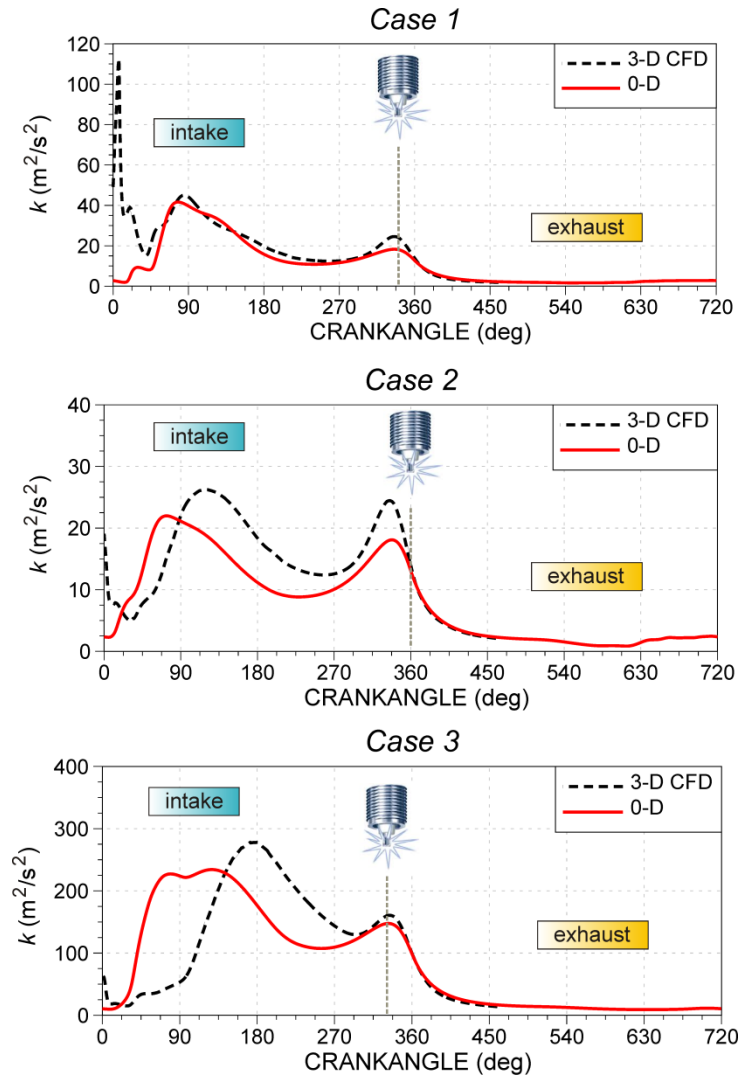


Figure 41. Total in-cylinder turbulent kinetic energy during the entire cycle of Engine 1 calculated by the full cycle turbulence model.

In Figure 41 the prediction of phasing of intake peak value of the turbulent kinetic energy compared with 3-D CFD data is not fully correct, especially at operating conditions with high engine speed (*Case 3*). At high engine speed ( $n = 5500$  rpm) the intake peak value in 0-D simulation occurs about  $90^\circ$  of crank angle earlier than in the 3-D CFD result. The mentioned difference in phasing of peak values occurs because the 0-D differential equations (2.36) and (2.37) consider the instantaneous transformation of mean kinetic energy (at the intake valve cross section) into the turbulent kinetic energy. In real flows over the intake valve, the transformation of mean kinetic energy to the turbulent kinetic energy takes certain amount of time so that the large scale flow structures are dissipated into the progressively smaller ones, as already described by energy cascade in Figure 6. Although the differences in the turbulent kinetic energy during the intake are significant, it does not represent an obstacle because the



turbulent kinetic energy during this period is not used for the calculation of any other in-cylinder property.

The geometry of the intake system and the intake valve design influence the progress of in-cylinder turbulent kinetic energy during the intake process. In [10] it has been shown that the shrouded design of intake valves produce higher turbulence level during the intake than the un-shrouded design. Since the 0-D simulation approach does not include the detail spatial discretization of the cylinder domain and intake ports, such local geometrical effects on the production of turbulence level during the intake cannot be predicted. But, the new user-defined constants  $S_{in}$  and  $C_{in}$  can be tuned so that the overall effects of the local geometries are taken into account.

## Engine 2

The constants of full  $k-\varepsilon$  turbulence model that were applied in the calculation of in-cylinder turbulence of four operating points of Engine 2 are shown in Table 7. As it was already mentioned, the  $C_\varepsilon$  constant was fixed to 2.40 for all considered operating points, while the remaining two user-defined constants  $S_{in}$  and  $C_{in}$  were tuned manually to produce the in-cylinder turbulence level during combustion at the satisfactory level.

Table 7. Values of constants of full  $k-\varepsilon$  turbulence model – Engine 2

Case Name	Case 1	Case 2	Case 3	Case 4
Engine speed (rpm)	1500	1500	2000	5500
Load	Part (BMEP = 2.62 bar)	100 %	100 %	100 %
$C_2$ (-)	1.92			
$C_\varepsilon$ (-)	2.40			
$S_{in}$ (-)	$1.0 \cdot 10^{-4}$	$1.2 \cdot 10^{-4}$	$1.8 \cdot 10^{-4}$	$1.3 \cdot 10^{-3}$
$C_{in}$ (-)	2.30	1.60	1.65	2.25

The progress of in-cylinder turbulent kinetic energy during the entire engine cycle for all operating points of Engine 2 is shown in Figure 42 and the 0-D simulation results are compared with the 3-D CFD results. It can be seen that by tuning two intake constants ( $S_{in}$  and  $C_{in}$ ) the intake peak values and trends of the turbulent kinetic energy close to the 3-D CFD results can be obtained at low engine speed cases.

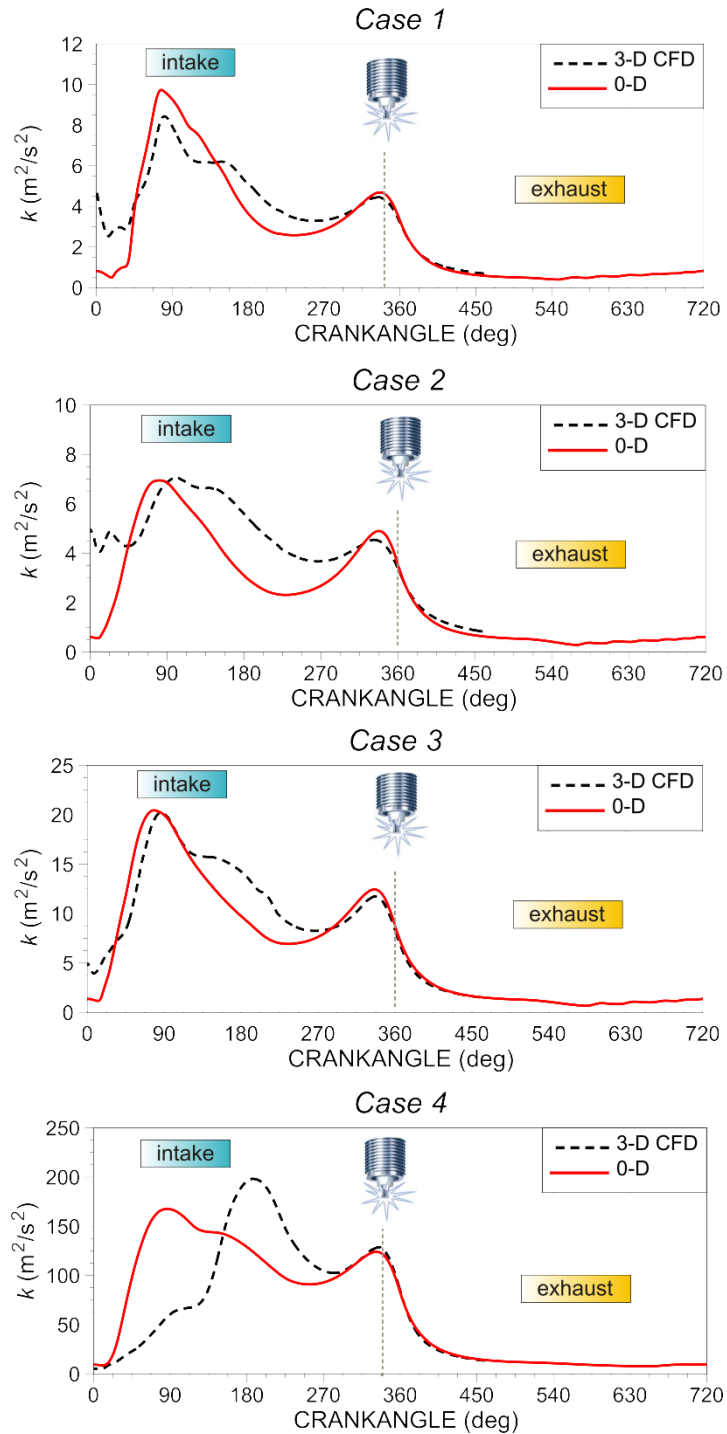


Figure 42. Total in-cylinder turbulent kinetic energy during the entire cycle of Engine 2 calculated by the full cycle turbulence model.

At the *Case 4* that represents the high engine speed operating point the 0-D simulation result of the in-cylinder turbulence does not match fully the profile of 3-D CFD result during the intake. The intake peak value of 0-D model is slightly lower and occurs at the point of maximum intake mass flow at the intake valve cross section that represents the boundary of cylinder control volume. When the maximum intake mass flow is reached, the volume flow is

also at the maximum value and the mean flow velocity at the intake valve cross-section is maximal. Hence, the peak value of the turbulent kinetic energy calculated with the 0-D turbulence model during the intake occurs when the maximum kinetic energy enters into the cylinder. It is obvious that in the 3-D CFD solution, the peak intake value of turbulent kinetic energy occurs later due to the fact that the turbulent kinetic energy is produced from kinetic energy of the mean flow according to the energy cascade which is not instantaneously. The process of dissipation of large scale eddies that are generated within the combustion chamber during the intake to progressively smaller eddies takes certain amount of time. Therefore, at operating conditions with high engine speed the difference of timing of the peak intake turbulent kinetic energy between the 0-D and 3-D CFD simulation results becomes noticeable in the crank angle scale. The same effect can be seen on the operating points with high engine speed of other engines (see Figure 41 and Figure 44).

### Engine 3

The constants of full  $k-\varepsilon$  turbulence model that were applied in the calculation of in-cylinder turbulence of three operating points of Engine 3 are shown in Table 8. The first two operating points (*Case 1* and *Case 2*) of Engine 3 differs in spark timing specified in Table 4.

Table 8. Values of constants of full  $k-\varepsilon$  turbulence model – Engine 3

Case Name	<i>Case 1</i>	<i>Case 2</i>	<i>Case 3</i>
Engine speed (rpm)	1500	1500	3000
Load	Part (BMEP = 2.0 bar)	Part (BMEP = 1.8 bar)	100 %
$C_2$ (-)	1.92		
$C_\varepsilon$ (-)	2.40		
$S_{in}$ (-)	$1.1 \cdot 10^{-3}$	$1.1 \cdot 10^{-3}$	$1.3 \cdot 10^{-3}$
$C_{in}$ (-)	3.17	3.25	1.95

The progress of in-cylinder turbulent kinetic energy during the entire cycle of Engine 3 for all three considered operating points is shown in Figure 43 and the 0-D simulation results are compared with the 3-D CFD solutions. Although the 0-D simulation results of the in-cylinder turbulence do not fully match the 3-D CFD results during the intake and early compression, it is in a very good agreement during the combustion period when the turbulence quantities define the flame front propagation and combustion burning rate. The mentioned differences during the intake and compression are acceptable because the turbulent kinetic energy is not used for the calculation of any other physical property outside the combustion period.

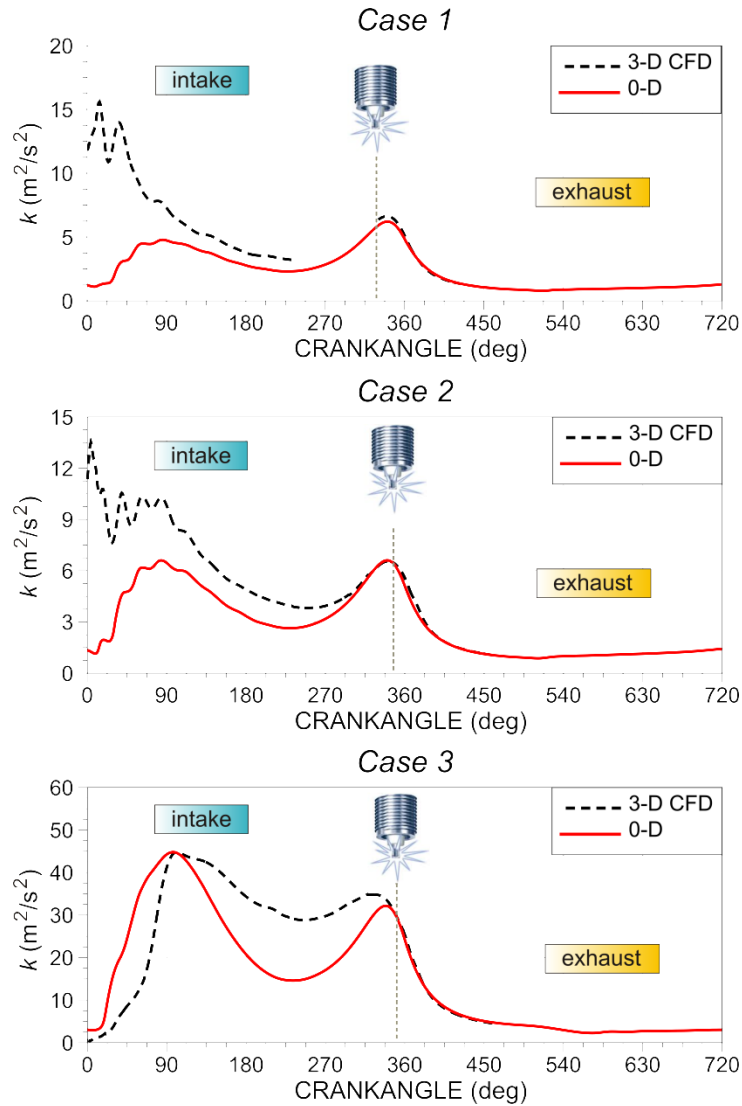


Figure 43. Total in-cylinder turbulent kinetic energy during the entire cycle of Engine 3 calculated by the full cycle turbulence model.

### Engine 4

For the last engine geometry (Engine 4) the constants of full  $k$ - $\varepsilon$  turbulence model are specified in Table 9. At the previous engine geometries, the intake  $k$  production constant  $S_{in}$  have to be higher as the engine speed is higher. This indicates that at higher engine speeds the turbulence intensity is higher because the larger amount of mean kinetic energy is transferred to the turbulent kinetic energy. The engine load in the presented cycle-simulation model is defined with the imposed intake boundary condition of pressure/mass flow and temperature. The intake  $\varepsilon$  production constant has the highest value at the first operating point *Case 1* that represents the low engine speed and part load condition. As the engine load is increased, the value of this constant have to be lower which means that the dissipation rate of the turbulent kinetic energy at higher intake pressure is lower (see equation (2.37)).

Table 9. Values of constants of full  $k$ - $\varepsilon$  turbulence model – Engine 4

Case Name	<i>Case 1</i>	<i>Case 2</i>	<i>Case 3</i>	<i>Case 4</i>	<i>Case 5</i>
Engine speed (rpm)	1000	2000	3000	2845	6215
Load	Part (BMEP = 1 bar)	Part (BMEP = 2 bar)	Part (BMEP = 3 bar)	100 % (max. torque)	100 % (max. power)
$C_2$ (-)	1.92				
$C_\varepsilon$ (-)	2.40				
$S_{in}$ (-)	$1.5 \cdot 10^{-3}$	$2.4 \cdot 10^{-3}$	$2.8 \cdot 10^{-3}$	$4.5 \cdot 10^{-3}$	$6.0 \cdot 10^{-3}$
$C_{in}$ (-)	5.40	4.70	3.90	2.65	2.70

The progress of in-cylinder turbulent kinetic energy during the entire cycle of Engine 4 for all five considered operating points is shown in Figure 44 and the 0-D simulation results are compared with the 3-D CFD solutions. If the progress of in-cylinder turbulent kinetic energy for all operating points of Engine 4 is compared with the results of other engines, it can be observed that the Engine 4 geometry has significant higher intake peak values of turbulent kinetic energy. This confirms that the engine geometry, including the design of intake plenum and valves, has a strong impact on the progress of turbulent kinetic energy during the intake, influencing the initial conditions for the high pressure cycle. Although the proposed full  $k$ - $\varepsilon$  turbulence model does not take into account the geometry of intake plenums and intake valves, the correct calibration of intake turbulence model constants can reproduce the effects of geometry on the progress of turbulent kinetic energy, but some reference results have to be available for tuning purposes (in this case the 3-D CFD results were used as the reference results).

The brief analysis of intake constants specified in tables 6 – 9 indicates that the values of intake  $k$  production constant  $S_{in}$  show certain rising trend with the increase of engine speed, while the intake  $\varepsilon$  production constant  $C_{in}$  shows the opposite trend (decline) with the increase of engine load. This behavior of intake turbulence constants is analyzed in more details within the Chapter 5.4 of this thesis where the specific linear correlations are proposed and applied to the  $k$ - $\varepsilon$  turbulence model.

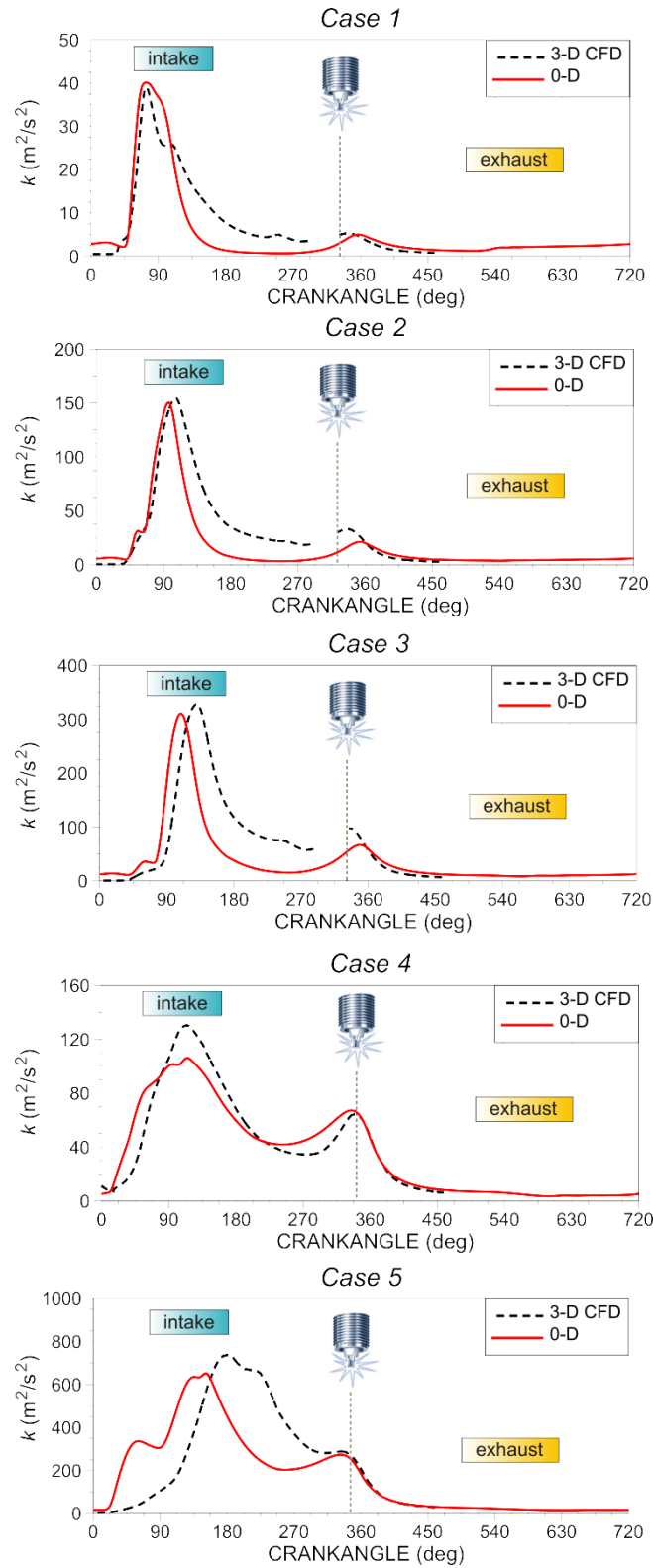


Figure 44. Total in-cylinder turbulent kinetic energy during the entire cycle of Engine 4 calculated by the full cycle turbulence model.

### 5.3. Validation of developed QDIM and modified transition time from laminar to fully developed turbulent flame

In the Chapter 5.1 the single and two zone turbulence models were validated with the 3-D CFD results. In these calculations, the initial conditions of in-cylinder turbulence at the beginning of the high pressure cycle were defined from 3-D CFD solutions. It was shown in Table 2 – 5 that in both models, single and two zone turbulence model, the 5 user-defined constants related to the turbulence and combustion sub-models have to be specified. In that validation the application of two zone turbulence sub-model showed a better prediction of combustion process than the single zone turbulence model.

In order to avoid the model dependency on the initial conditions of in-cylinder turbulence at the beginning of high pressure cycle, the full  $k-\varepsilon$  turbulence model was employed and validated in the Chapter 5.2. It was shown that the calibration of two intake turbulence model constants ( $S_{in}$  and  $C_{in}$ ) for different engines and operating conditions is necessary to achieve the 0-D results that are comparable with the 3-D CFD results. Moreover, for the correct prediction of the combustion process by using the two zone turbulence model applied in Chapters 5.1 and 5.2, two user-defined constants,  $c_{ign}$  and  $r_{f,ref}$ , have to be calibrated for each operating point of the engine.

For the reduction of the number of user-defined constants that have to be specified and tuned for each operating point and in order to achieve the correspondence of 0-D results of combustion with the 3-D CFD results, the new quasi-dimensional ignition sub-model was developed (Chapter 3) together with the modified transition from laminar to fully developed turbulent flame (Chapter 4.2.2).

The developed quasi-dimensional ignition model has the set of parameters that can be classified into two main groups:

- 1) Geometrical parameters related to spark plug design,
- 2) Operating parameters of ignition model and early flame kernel growth.

The considered spark plug design for the simulations of ignition phenomenon of Engines 1 – 4 is shown in Figure 45 where the main dimensions are expressed in millimeters. The considered spark plug design and specified dimensions are close to the standard type of spark plug with 12 mm of shell diameter (e.g. NGK DR8ES) shown in Figure 45 c).

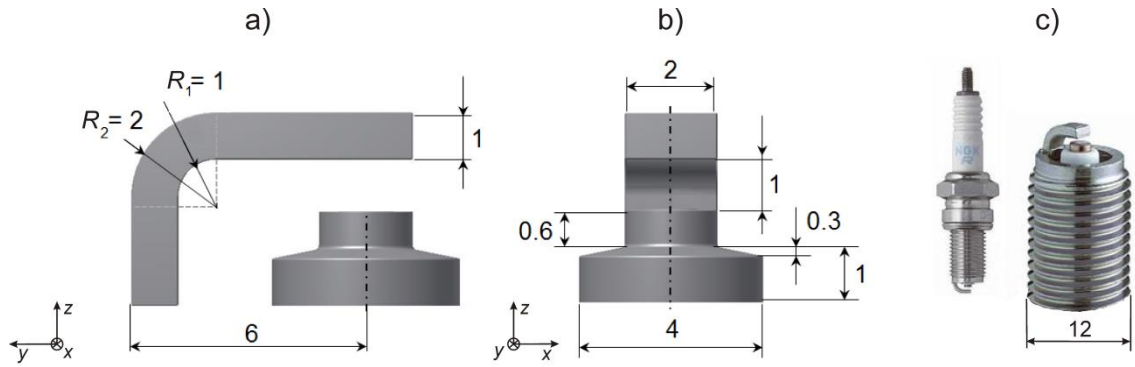


Figure 45. Geometry of the considered standard type of spark plug – marked dimensions are expressed in mm; figure a)  $y$ - $z$  view, figure b)  $x$ - $z$  view, figure c) NGK (DR8ES) standard type of the spark plug with 12 mm of shell diameter.

The spark plug geometry is in 0-D approach presented with the uniformly distributed geometrical points with the incremental distance  $\delta$  between the points set to 0.1 mm. Hence, the considered spark plug geometry in 0-D environment is presented with the set of 3034 geometrical points and each of these points present the incremental spark plug surface area of  $\Delta S$ .

The operating parameters of the ignition model and early flame kernel growth are specified in Table 10. The parameters listed in Table 10 are applied for all engines (Engine 1 – 4) and operating points as the single set of constants. Two additional user-defined constants of developed QDIM,  $r_0$  (radius of the flame kernel when it can be considered as turbulent flame) and  $T_{SP}$  (spark plug temperature), were individually defined for each geometry to achieve the 0-D combustion results close to the 3-D CFD solutions.

Table 10. Uniform operating parameters of the ignition model applied to all engines

Symbol	Value (Unit)	Description
$\delta$	0.1 mm	distance between geom. points
$\alpha$	0°	flow angle at spark plug
$T_q$	1200 K	quenching temperature
$k_w$	2000 W/(m <sup>2</sup> K)	heat transfer coefficient
$E_S(0)$	60 mJ	initial el. energy of secondary circuit
$L_S$	20 H	inductance of secondary circuit
$R_S$	20 k $\Omega$	resistance of secondary circuit
$C_{cg}$	40.46 -	voltage constant
$V_{af}$	18.75 V	anode voltage fall
$V_{cf}$	252 V	cathode voltage fall
$C_{bd}$	$1 \cdot 10^5 \text{ V}/\sqrt{\text{J} \cdot \text{mm}}$	breakdown constant



In order to eliminate the tuning of the reference flame front radius  $r_{f, \text{ref}}$  when the maximum wrinkling occurs for each operating point of the engine, the modification of transition time from laminar to fully developed turbulent flame is proposed. It is assumed that the maximum wrinkling ratio of the flame front will occur when the turbulent eddy, described with the integral length scale  $L_1$ , is dissipated. In other words, the transition time is equal to the turbulent eddy turn-over time represented by equation (4.12). The proposed calculation of transition time requires the correct prediction of in-cylinder turbulence intensity  $u'$  and the integral length scale  $L_1$  at the start of combustion (SOC). Since the 0-D results of integral length scale are not compared with the 3-D CFD results, for the calculation of transition time the absolute value of integral length scale was assumed to be proportional to the instantaneous cylinder height as it was already used in the  $K-k$  turbulence model [5]. It was previously described that the calculation of the combustion process in the case of two zone turbulence model is equal to the fractal burning rate represented by equation (4.6). In the mentioned equation the integral length scales (Kolmogorov and Taylor micro scale) are calculated from the calculated values of turbulent kinetic energy  $k_{\text{UZ}}$  and its dissipation rate  $\varepsilon_{\text{UZ}}$ , as can be seen in equations (4.16), (4.19) and (4.20). This is acceptable without the additional validation of the absolute values of integral length scales because the ratio of integral length scales is used in the equation (4.6). The tuning of transition time when the laminar to fully developed turbulent flame occurs is possible with the user-defined constant  $C_\tau$ . In the previous quasi-dimensional fractal combustion model whose results are shown in Chapter 5.1 the tuning of  $r_{f, \text{ref}}$  parameter for each operating point of the engine was performed. The modified calculation of the transition time from laminar to fully developed turbulent flame will enable the application of single value of  $C_\tau$  constant for each engine. For the modeling of total in-cylinder turbulent kinetic energy the full cycle turbulence model which is validated in Chapter 5.2 was used. The dissipation constant of high pressure cycle  $C_\varepsilon$  was set to 2.40 for all considered engines as specified in Table 6 – 9.

In the following text, the terminology "*modified fractal combustion model*" includes the following modifications:

- 1) ignition sub-model (QDIM),
- 2) modified transition from laminar to fully developed turbulent flame,
- 3) two zone turbulence model.

## Engine 1

The constants of the two zone turbulence model and the parameters of the modified fractal combustion model for Engine 1 are specified in Table 11.

Table 11. Values of constants of two zone  $k-\varepsilon$  model and modified fractal combustion model – Engine 1

Case Name	Case 1	Case 2	Case 3
Engine speed (rpm)	2000	2000	5500
Load	Part (BMEP = 2.9 bar)	100 %	100 %
Spark Timing (° CA BTDC)	34	4	24
Excess Air Ratio (-)	1.0		
	<b>Two zone turbulence model</b>		
$C_2$ (-)	1.92		
$C_\varepsilon^{UZ}$ (-)	3.00		
	<b>Ignition model (QDIM)</b>		
$r_0$ (m)	0.008		
$T_{SP}$ (K)	470		
	<b>Fractal combustion model</b>		
$C_\tau$ (-)	0.70		
$f_{D3,max}$ (-)	2.37	2.46	2.41

Modeling of turbulence during the gas exchange and during the compression was performed by the full cycle  $k-\varepsilon$  turbulence model. The intake production constants  $S_{in}$  and  $C_{in}$  are equal to the values specified in Table 6 and they are calibrated for each operating point of the engine. The dissipation rate constant of the unburned zone  $C_\varepsilon^{UZ}$  is set to a single value. In terms of the fractal combustion sub-model, only the upper limit of fractal dimension  $f_{D3,max}$  was tuned for each operating point. From Table 6 and 11 that show the constants of the simulation model it is evident that the 3 user-defined constants have to be tuned for each operating point; two of them are related to the turbulence sub-model and one is the parameter of the fractal combustion sub-model.

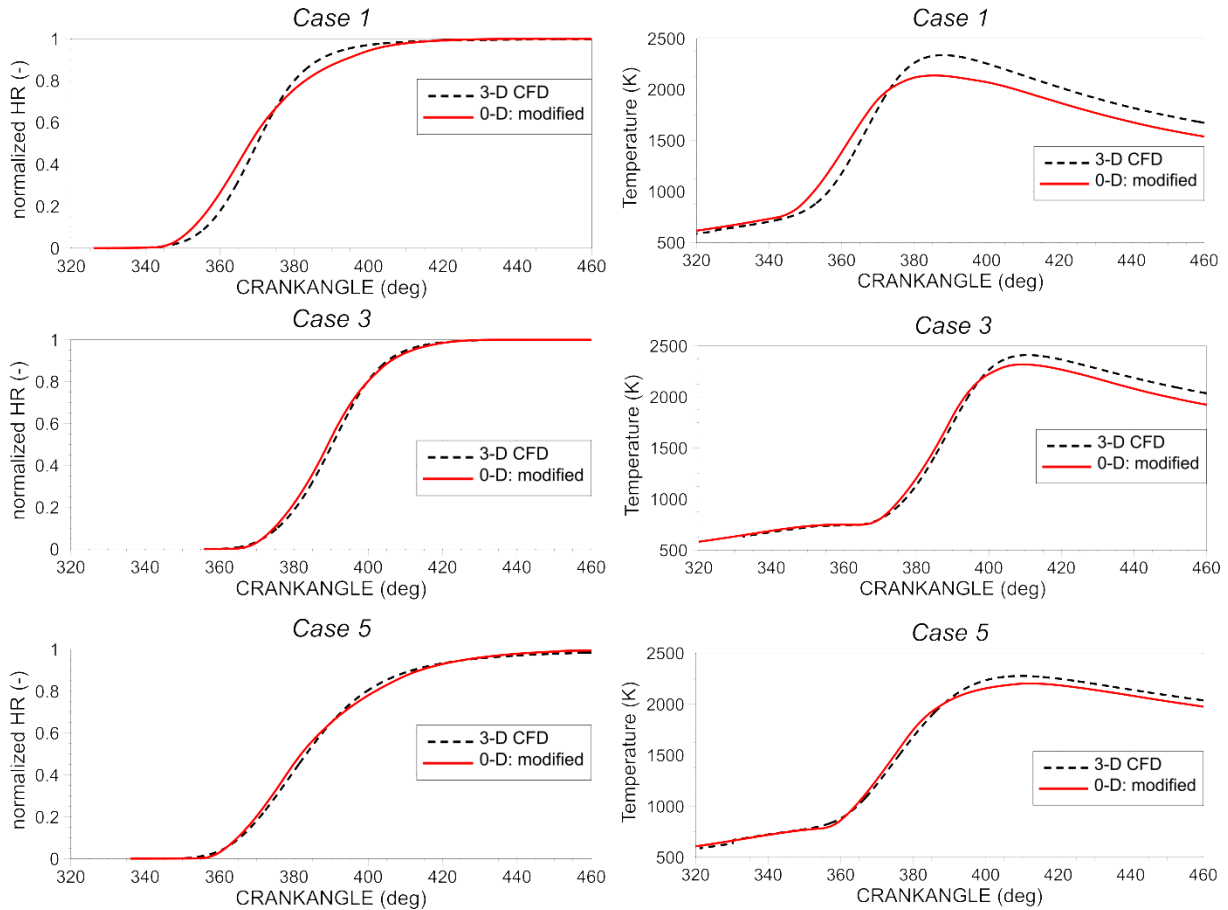


Figure 46. Normalized heat release (left) and in-cylinder temperature (right) of Engine 1: modified fractal combustion model.

The profiles of normalized HR and of the in-cylinder temperature for the considered operating points of Engine 1 are shown in Figure 46. The comparison of the combustion progress calculated by the 0-D model of AVL BOOST with the 3-D CFD results shows that the 0-D results match well the desired profiles. It can be noticed that in the first operating point *Case 1* the combustion is slightly faster at the early combustion phase. This is caused by the shorter ignition delay and early flame kernel growth period and by the faster transition time from the laminar-like flame front to the fully developed turbulent flame with highly wrinkled surface. Bearing in mind that this model is independent of any CFD results (as it was in Chapter 5.1) and that the number of user-defined constants that have to be tuned for each operating point is reduced from 5 to 3, it can be concluded that the proposed simulation model is significantly improved and simplified.

## Engine 2

The constants of the two zone turbulence model and the parameters of the modified fractal combustion model applied on the second engine geometry are specified in Table 12.

Table 12. Values of constants of two zone  $k-\varepsilon$  model and modified fractal combustion model – Engine 2

Case Name	Case 1	Case 2	Case 3	Case 4
Engine speed (rpm)	1500	1500	2000	5500
Load	Part (BMEP = 2.62 bar)	100 %	100 %	100 %
Spark Timing (° CA BTDC)	14	-0.2	2.1	15.7
Excess Air Ratio (-)	1.0			
	<b>Two zone turbulence model</b>			
$C_2$ (-)	1.92			
$C_\varepsilon^{UZ}$ (-)	2.00			
	<b>Ignition model (QDIM)</b>			
$r_0$ (m)	0.005			
$T_{SP}$ (K)	470			
	<b>Fractal combustion model</b>			
$C_\tau$ (-)	0.40			
$f_{D3,max}$ (-)	2.51	2.58	2.44	2.45

Once again, the intake constants of  $k-\varepsilon$  turbulence model for each operating point of Engine 2 were the same as in the previous chapter where the 0-D simulation results of in-cylinder turbulent kinetic energy were compared with the 3-D CFD results (Table 7). The dissipation rate constant  $C_\varepsilon$  (specified in Table 7) that defines the overall dissipation rate of the cylinder mixture during the high pressure cycle as well as the unburned zone dissipation constant  $C_\varepsilon^{UZ}$  were fixed to single values for all considered operating points of Engine 2.

The normalized HR and the in-cylinder temperature profiles calculated with the 0-D simulation model are shown and compared with the 3-D CFD results in Figure 47. The ignition and combustion model constants ( $r_0$ ,  $C_\varepsilon^{UZ}$ ,  $C_\tau$  and  $f_{D3,max}$ ) were tuned manually so that the prediction of combustion progress at different engine operating conditions is in a good agreement with the 3-D CFD results. For the last case (*Case 4*) of Engine 4 the combustion progress is predicted slightly earlier within the period from 0 % to 50 % of burned mass, while the remaining part of combustion progress is under-predicted, compared with the 3-D CFD result. Earlier combustion progress within the period from 0 % to 50 % of burned mass is caused by the faster transition from laminar to fully developed turbulent flame calculated by equation (4.13). The better agreement of combustion progress with the 3-D CFD result of *Case 4* could be achieved with the fine tuning of  $C_\tau$  constant in equation (4.13), but the intention is to apply the single value of  $C_\tau$  for each engine.

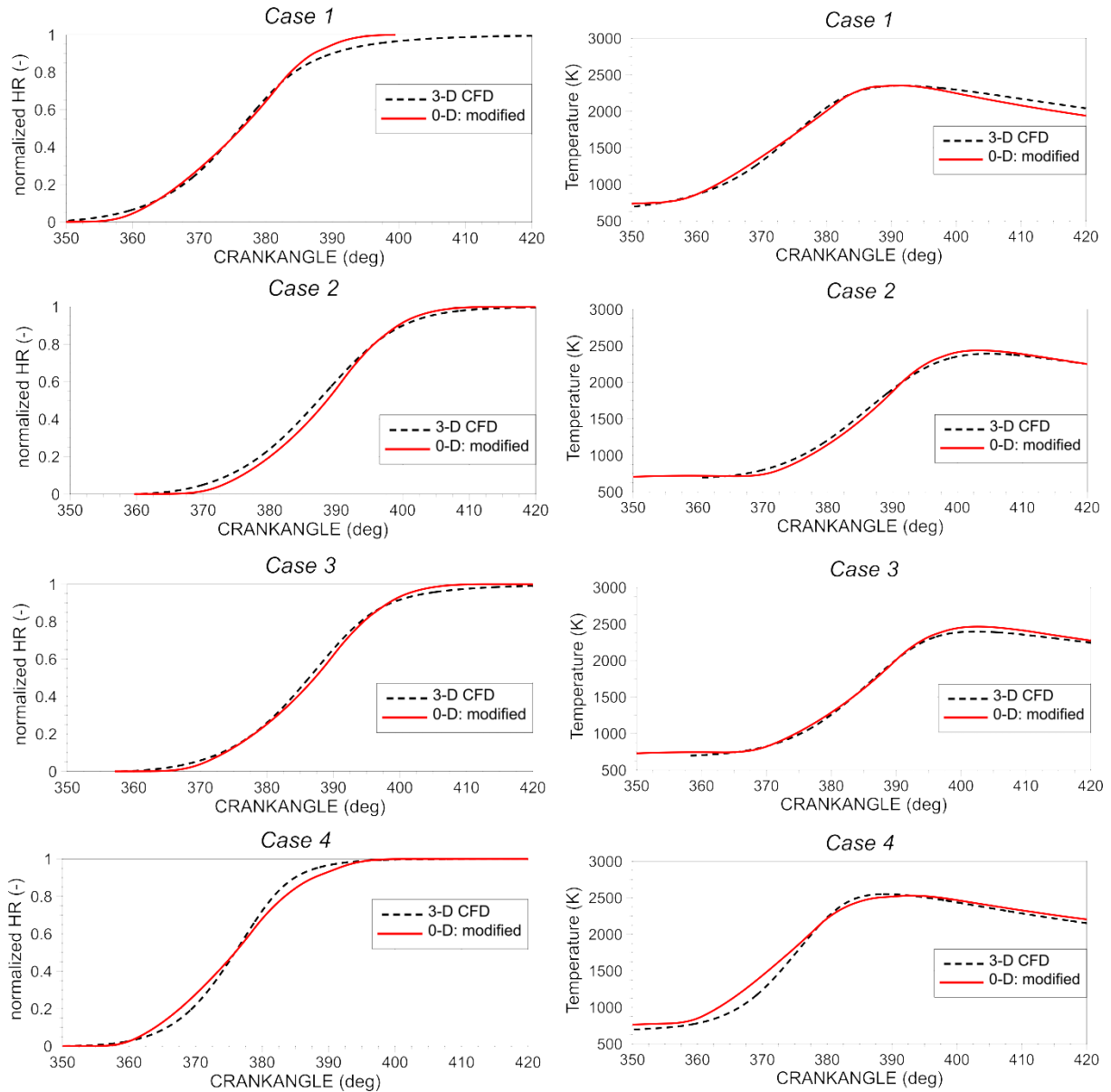


Figure 47. Normalized heat release (left) and in-cylinder temperature (right) of Engine 2: modified fractal combustion model.

### Engine 3

For the third engine geometry that was analyzed within this study, the constants of the two zone turbulence model and the constants of the modified fractal combustion model are specified in Table 13. The intake constants of full  $k-\varepsilon$  turbulence model that were used for modeling of the total in-cylinder turbulence level (single zone model) are specified in Table 8. In order to achieve the 0-D results of the combustion progress that match well the 3-D CFD results the same approach as on the previous engines (Engine 1 and Engine 2) was used, where the dissipation constants  $C_\varepsilon$  and  $C_\varepsilon^{UZ}$ , and the new  $C_\tau$  constant are fixed to single values for the considered engine. In terms of combustion sub-model constants calibration,

only the upper limit of fractal dimension  $f_{D3,max}$  was tuned for each operating point of the engine.

Table 13. Values of constants of two zone  $k-\varepsilon$  model and modified fractal combustion model – Engine 3

Case Name	Case 1	Case 2	Case 3
Engine speed (rpm)	1500	1500	3000
Load	Part (BMEP = 2.0 bar)	Part (BMEP = 1.8 bar)	100 %
Spark Timing (° CA BTDC)	30	15	21
Excess Air Ratio (-)	1.0		
	<b>Two zone turbulence model</b>		
$C_2$ (-)	1.92		
$C_\varepsilon^{UZ}$ (-)	2.00 (additionally tuned to 1.50 for Case 1)		
	<b>Ignition model (QDIM)</b>		
$r_0$ (m)	0.002		
$T_{SP}$ (K)	450		
	<b>Fractal combustion model</b>		
$C_\tau$ (-)	0.50 (additionally tuned to 1.40 for Case 1)		
$f_{D3,max}$ (-)	2.39 (2.52)	2.71	2.44

The normalized HR and the in-cylinder temperature profiles calculated with the 0-D modified simulation model for Engine 3 are plotted and compared with the 3-D CFD results in Figure 48. If the 0-D combustion results are compared with the 0-D combustion results shown in Figure 38 where the constants related to ignition, unburned zone turbulence, laminar-turbulent flame transition and fractal dimension are manually tuned for each operating point, it could be concluded that the application of modified fractal combustion model shows slightly worse results. But, although the 0-D simulation results of combustion do not fully match the 3-D CFD results, the application of modified fractal combustion model is acceptable because the number of user-defined constants that have to be tuned for each operating point is reduced. In order to show the possibility to achieve the combustion progress by the modified fractal combustion model close to the 3-D CFD result, the additional tuning of  $C_\varepsilon^{UZ}$ ,  $C_\tau$  and  $f_{D3,max}$  constants on Case 1 was performed. The values of mentioned constants for Case 1 are specified in the brackets in Table 13. The normalized HR and the in-cylinder temperature profile calculated with the 0-D modified fractal combustion model and with the additionally tuned constants ( $C_\varepsilon^{UZ}$ ,  $C_\tau$  and  $f_{D3,max}$ ) on Case 1 are shown with the blue solid line in Figure 48. It can be seen that the additional tuning of previously mentioned constants on Case 1 of

Engine 3, with the application of modified fractal combustion model, resulted with the better agreement of 0-D and 3-D CFD combustion progress results. The 0-D results calculated with the modified fractal combustion model and with the additional tuning of model constants ( $C_{\varepsilon}^{UZ}$ ,  $C_{\tau}$  and  $f_{D3,max}$ ) are very close to the 0-D results calculated with the 0-D fractal combustion model whose results are shown in Figure 38. Since the constants of the ignition sub-model (QDIM) did not have to be additionally tuned for the *Case 1*, the modified transition from laminar to fully developed turbulent flame is the obvious reason for differences in the combustion progress between the 0-D and 3-D CFD results when the modified fractal combustion model is applied.

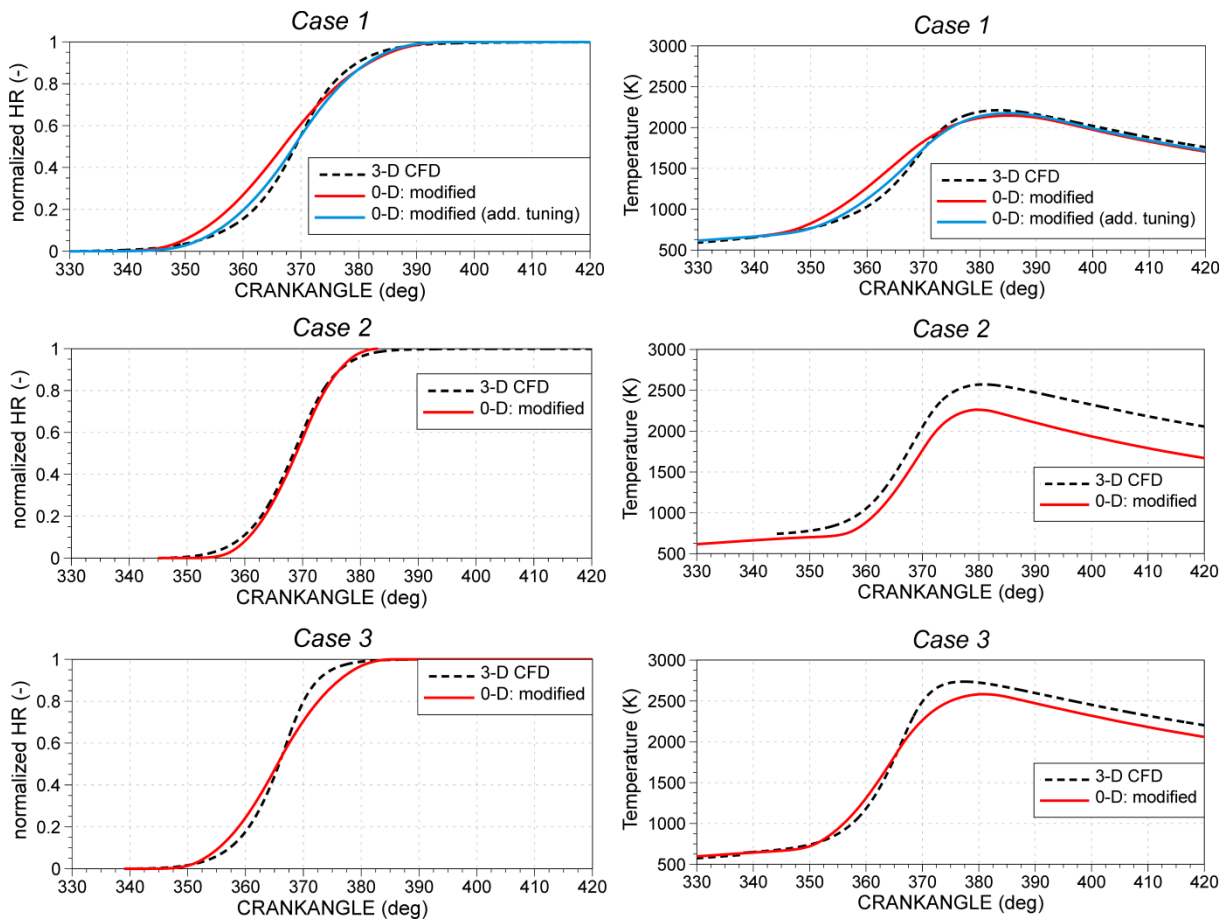


Figure 48. Normalized heat release (left) and in-cylinder temperature (right) of Engine 3: two zone turbulence model and extended fractal combustion model.

#### Engine 4

For the last engine geometry that was analyzed within this study, the constants of the two zone turbulence model and the constants of the modified fractal combustion model are specified in Table 14.

Table 14. Values of constants of two zone  $k-\varepsilon$  model and modified fractal combustion model – Engine 4

Case Name	Case 1	Case 2	Case 3	Case 4	Case 5
Engine speed (rpm)	1000	2000	3000	2845	6215
Load	Part (BMEP = 1 bar)	Part (BMEP = 2 bar)	Part (BMEP = 3 bar)	100 % (max. torque)	100 % (max. power)
Spark Timing (° CA BTDC)	35	36	25.5	22.5	22.5
Excess Air Ratio (-)	1.0				
<b>Two zone turbulence model</b>					
$C_2$ (-)	1.92				
$C_\varepsilon^{UZ}$ (-)	2.00				
<b>Ignition model (QDIM)</b>					
$r_0$ (m)	0.006				
$T_{SP}$ (K)	650				
<b>Fractal combustion model</b>					
$C_\tau$ (-)	1.30				
$f_{D3,max}$ (-)	2.58	2.39	2.43	2.41	2.45

Modeling of overall in-cylinder turbulence is performed using the full cycle  $k-\varepsilon$  turbulence model whose parameters ( $S_{in}$ ,  $C_{in}$ ,  $C_\varepsilon$ ) are specified in Table 9. The same approach, as used on the previous engines (Engine 1, Engine 2 and Engine 3), was applied where the constants  $C_\varepsilon^{UZ}$  and  $C_\tau$  as well as the ignition model parameters are fixed to single values so that a good agreement of combustion progress between the 0-D and 3-D CFD results is achieved.



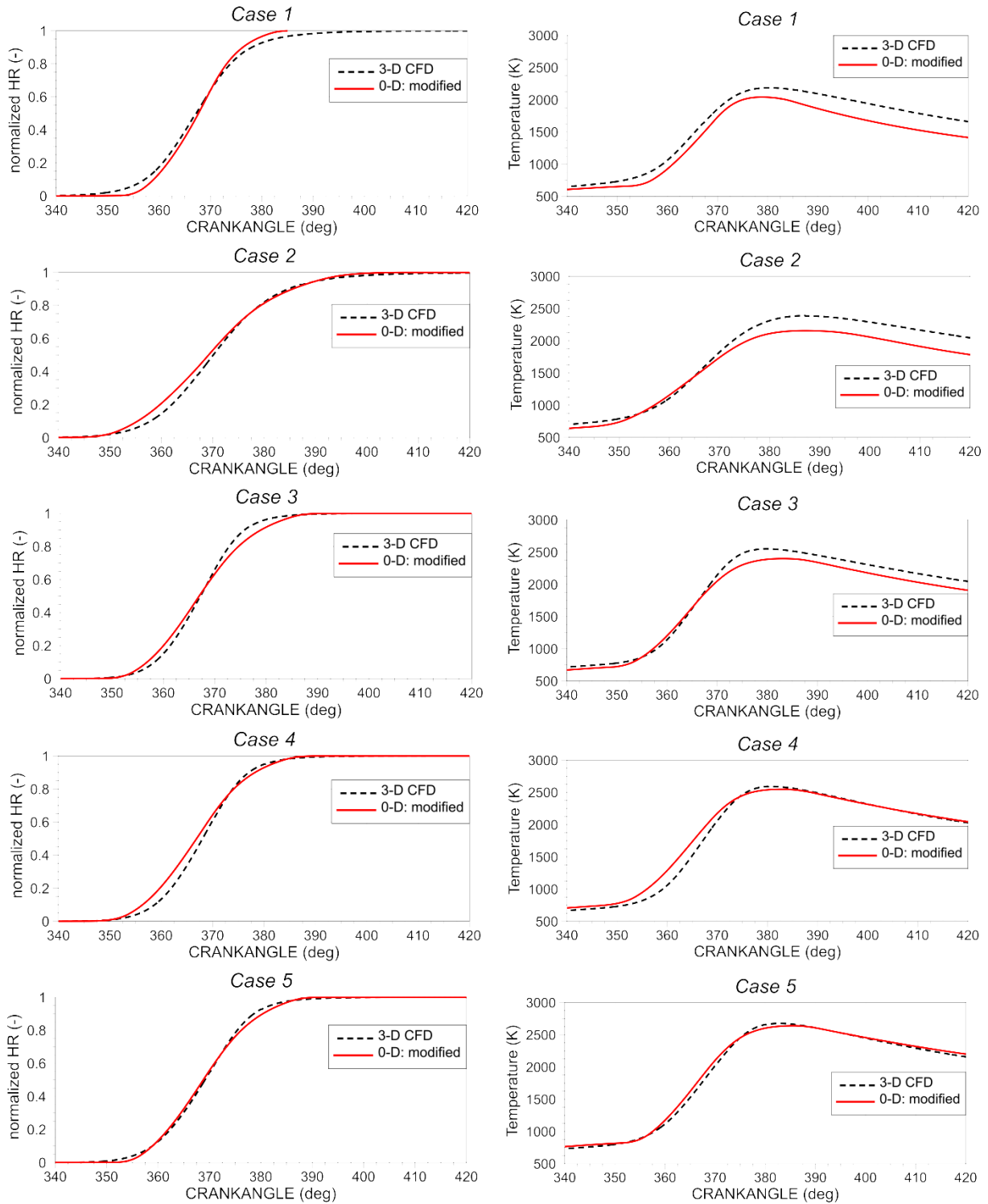


Figure 49. Normalized heat release (left) and in-cylinder temperature (right) of Engine 4: modified fractal combustion model.

The normalized HR and the in-cylinder temperature profiles calculated with the 0-D simulation model for Engine 4 are plotted and compared with the 3-D CFD results in Figure 49. The combustion results of Engine 4 calculated with the 0-D approach are in a good agreement with the 3-D CFD data at all considered operating conditions.

### 5.3.1. Quantitative analysis of the early combustion phase

For the quantitative analysis of the early combustion phase in a case when the calculation of combustion is performed by using the modified fractal combustion model, the crank angles at which the specific values of mass fraction burned are compared to the 3-D CFD results. The relative crank angle  $\Delta\alpha_{0.1}$ , as the crank angle between the 0 % to the 0.1 % mass fraction burned, for all considered engines is shown in Figure 50 (0 % of mass fraction burned corresponds to spark timing).

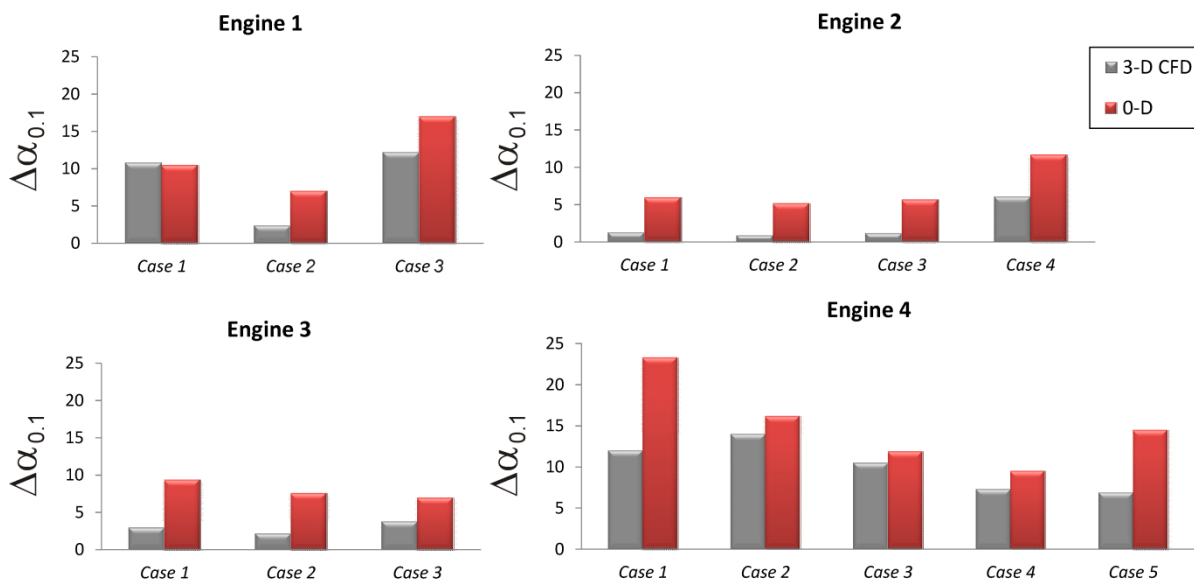


Figure 50. Prediction of relative crank angle  $\Delta\alpha_{0.1}$  at which the 0.1 % of mass is burned – comparison of 3-D CFD and 0-D simulation results.

The 3-D CFD results in Figure 50 are shown with the gray columns, while the red ones relate to the 0-D simulation results. It can be seen that for all operating points of all considered engines, except the *Case 1* of Engine 1, the predicted crank angles at 0.1 % mass fraction burned are longer than in the 3-D CFD result. This is caused by the longer ignition delay period that is defined by the applied quasi-dimensional ignition model. Due to the unavailability of 3-D CFD results regarding the exact values of ignition delay, the mentioned reason for the difference between the 3-D CFD and 0-D results cannot be confirmed. Moreover, at several operating points (*Case 1* and *3* of Engine 3; *Case 1* and *2* of Engine 4) the trends in the prediction of  $\Delta\alpha_{0.1}$  are different compared with 3-D CFD results. It will be shown in the following section that the manual tuning of ignition energy and flow angle at the spark plug can significantly improve the prediction of early combustion phase. The values of 0.1 % mass fraction burned represents the early stage of combustion process when there is no significant heat released, and the influence of combustion cannot be observed in the pressure

or in the temperature trace. It can be seen that the second engine geometry has very short periods of this early combustion phase even at the high engine speed (*Case 4*). This behavior could be achieved by applying the higher ignition energy, suitable spark plug design, different local in-cylinder conditions at the vicinity of the spark plug and different flow angle that accelerate the flame kernel expansion speed. In the presented QDIM the initial energy of the secondary electric circuit was set to 60 mJ as a default value of AKTIM model. An influence of higher ignition energy (longer electric spark duration) in the developed QDIM can be considered by increasing the initial electric energy of the secondary electric circuit to higher values. The effect of spark plug design on the early flame kernel growth can also be taken into account with the presented ignition model as it is shown in Figure 22. The 0-D simulation results of the combustion process are performed with the assumption that all considered engines were equipped with the same spark plug geometry whose design and dimensions are given in Figure 45. In terms of local in-cylinder conditions at the vicinity of the spark plug only the stratification of mixture composition (fuel and combustion products) can be considered [81], while the local burned/unburned temperatures and flow velocity are the same in the entire cylinder volume because the 0-D approach neglects the spatial discretization of the calculation domain. Although the mixture stratification can be studied, this model feature was not used in the presented 0-D simulations and only the homogeneous mixtures were simulated. Moreover, the angle of the flow velocity  $\alpha$  can have a strong influence on the early flame kernel growth because it influences the heat transfer between the hot kernel and spark plug electrodes. Due to the simplicity of the model and unavailability of the detail 3-D CFD or experimental data regarding the flame kernel growth, for the considered operating conditions of Engines 1 – 4 the flow angle was set to  $0^\circ$  as a default value. In the following section and for the Engine 1, the parametric analysis of ignition energy and flow angle was performed.

The relative crank angles at which the 5 % of the mixture is burned (5 % mass fraction burned point)  $\Delta\alpha_5$  for all operating points of all considered engine geometries are shown in Figure 51 and the 0-D results (orange columns) are compared with the 3-D CFD results. The 5 % mass fraction burned was selected because after this phase the fully developed turbulent flame should occur and the maximum burning rate should be achieved. Before the fully developed turbulent flame is obtained, the transition of laminar to fully developed turbulent flame occurs. Since the calculation of transition time is changed in the modified fractal combustion model, the 0-D results of crank angle at 5 % mass fraction burned are compared

with the 3-D CFD solutions. Although the predictions of early stage of combustion process (when only 0.1 % mass fraction burned) do not fully match the 3-D CFD data, the remaining part of the early flame kernel growth shows a very good agreement with the reference results at different operating conditions and engine geometries shown in Figure 51. Such behavior of 0-D simulation model is achieved by the correct prediction of total in-cylinder turbulence level and by the tuning of  $C_r$  constant that can be fixed for one engine geometry. Since the prediction of  $\Delta\alpha_5$  also depends on the ignition model parameters, the tuning of certain ignition parameters for each operating point can contribute to the better prediction of the early combustion phase. For the detailed calibration of the ignition model constants, the experimental or some 3-D CFD results of early flame kernel growth should be available. It was demonstrated within the parametric analysis described in the following text that the individual tuning of ignition energy and/or flow angle can significantly improve the prediction of  $\Delta\alpha_5$ .

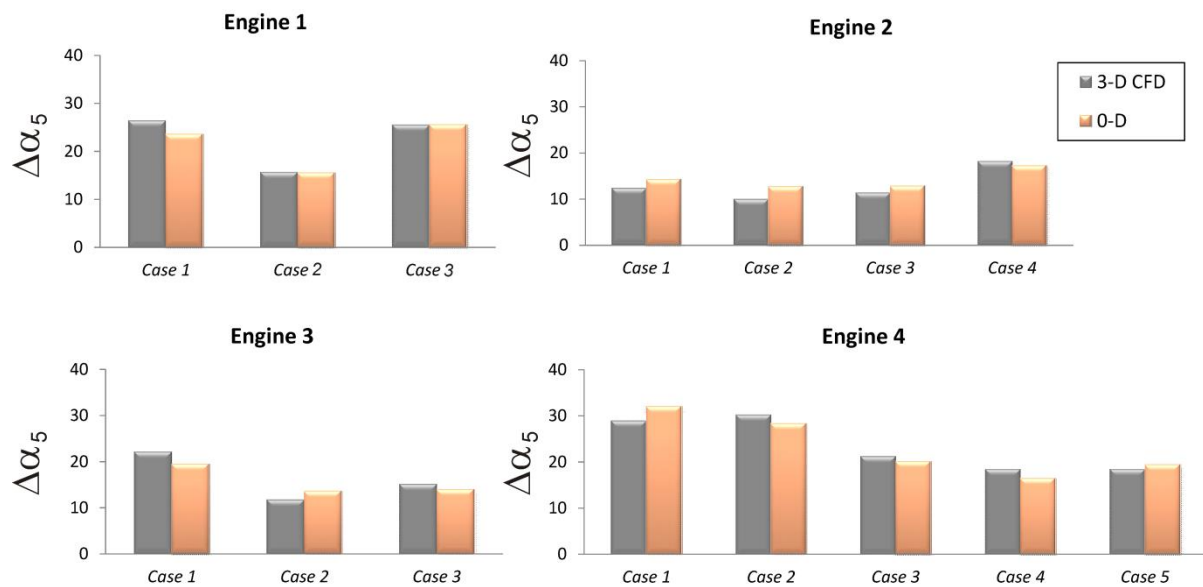


Figure 51. Prediction of relative crank angle  $\Delta\alpha_5$  at which the 5 % of mass is burned – comparison of 3-D CFD and 0-D simulation results.

### *Parametric analysis of ignition energy and flow angle on the early combustion phase*

To investigate the influence of ignition energy and flow angle on the early combustion phase, the parametric analysis of initial electric energy available at the secondary circuit  $E_s(0)$  and the flow angle  $\alpha$  at the spark plug location was made.

The parametric analysis is performed at all considered operating points of Engine 1. As the basic values regarding the initial electric energy available at the secondary circuit and flow angle were chosen the values already used in Chapter 5.3 and specified in Table 10. This includes that the initial electric energy available at the secondary circuit  $E_s(0)$  is considered as 60 mJ, while the flow angle  $\alpha$  is set to  $0^\circ$ . First, the initial electric energy available at the secondary circuit was set to 30 mJ and 120 mJ so that the effects of two times lower and two times larger ignition energy can be considered with the flow angle  $\alpha = 0^\circ$ . After that, the initial electric energy available at the secondary circuit was set to 60 mJ and the flow angle was changed to  $30^\circ$  and  $60^\circ$ . The simulation results of relative crank angle  $\Delta\alpha_5$ , when the 5 % of mass fraction burned, obtained by the variation of ignition energy and flow angle are shown and compared with the 3-D CFD results in Figure 52.

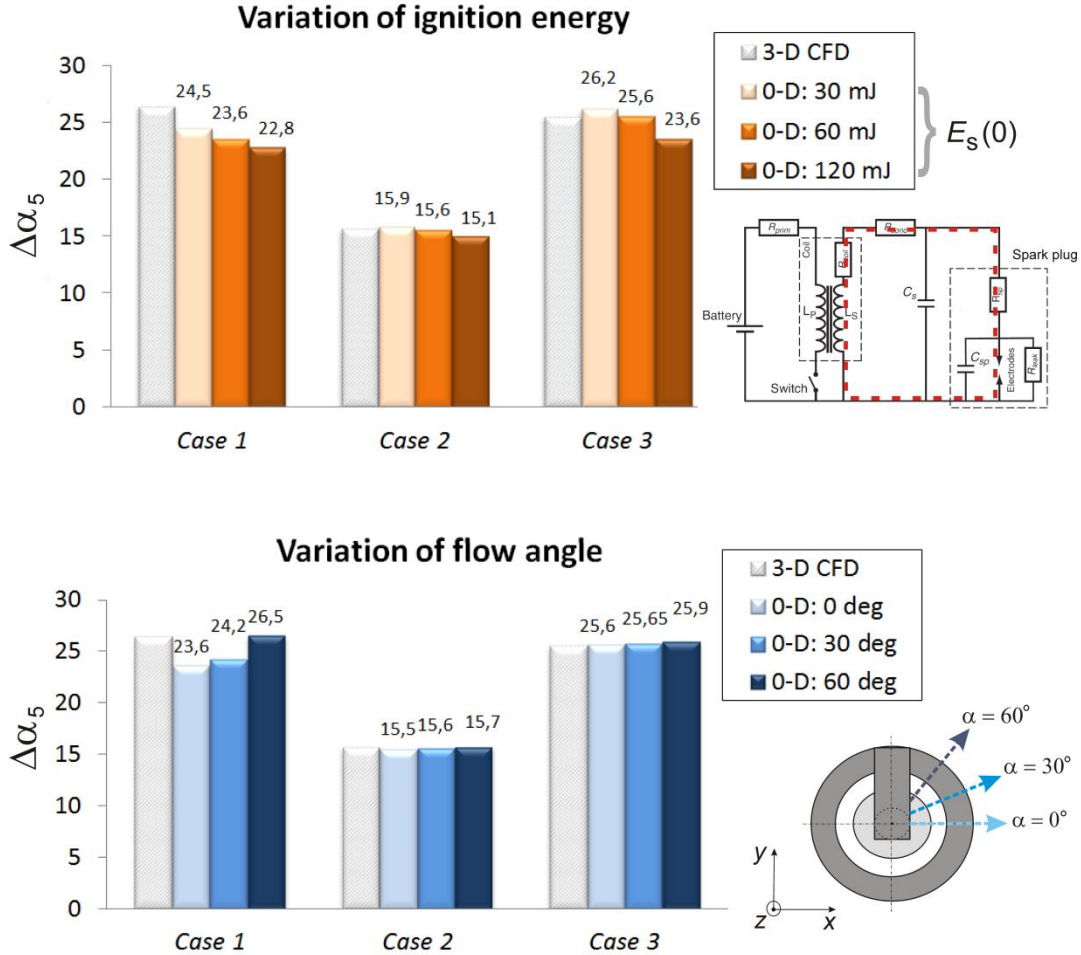


Figure 52. Prediction of relative crank angle  $\Delta\alpha_5$  at which the 5 % of mass is burned – the influence of ignition energy (top) and the flow angle at the spark plug (bottom) of Engine 1.

In top diagram of Figure 52 it can be seen that the developed QDIM shows logical behavior. When the initial electric energy available in the secondary circuit is two times lower

the relative crank angle  $\Delta\alpha_5$  is longer. The larger ignition energy resulted in the faster progress of early combustion phase for all considered operating points of Engine 1. The simulation results are the most sensitive on the ignition energy at operating point with the high engine speed and 100 % load (*Case 3*), while the minimum effect can be observed at low engine speed and 100 % of engine load. Four times higher ignition energy resulted with the approximately 10 % shorter early combustion phase described by the relative crank angle  $\Delta\alpha_5$  at *Case 3*. At high engine speed conditions, the cross-flow velocity is higher and the spark length is longer. Since the electric energy transferred to the flame kernel depends on the voltage between the electrodes  $V_{cg}$  and electric current of secondary circuit  $i_s$  (see equation (3.9)), the effect of increased ignition energy on the early combustion phase becomes significant at high engine speed conditions. At part load and low engine speed condition (*Case 1*), the higher ignition energy extends the duration of glow phase (visible electric spark) that increases the kernel excess of energy and kernel expansion speed.

In bottom diagram of Figure 52 the effect of different flow angles on the early combustion phase is shown. As the flow angle  $\alpha$  is increased, the duration of early combustion phase described by the relative crank angle  $\Delta\alpha_5$  is longer. The effect of flow angle increase is significant at part load and low engine speed condition (*Case 1*). When the flow angle is changed from  $0^\circ$  to  $60^\circ$ , the relative crank angle  $\Delta\alpha_5$  is longer about 12 %. The longer early combustion phase at flow angle set to  $60^\circ$  is achieved because the flame kernel is closer to the ground electrode and the heat losses become significant compared to the received electric energy, decreasing the kernel expansion speed.

It can be seen that the individual tuning of ignition energy and flow angle for each operating point of the engine could contribute to the better agreement of relative crank angle  $\Delta\alpha_5$  with the 3-D CFD data. For example, to achieve the better agreement of cycle-simulation results of  $\Delta\alpha_5$  for *Case 1* of Engine 1 with the 3-D CFD result, the ignition energy should be lower and/or the flow angle should be increased. Since the ignition energy and flow angle at spark plug were not available from the 3-D CFD nor from the experimental data, the uniform set of operating parameters for Engines 1 – 4 specified in Table 10 was applied.

### 5.3.2. Specific results of developed QDIM

In order to check the validity of developed ignition sub-model, the specific results for the considered operating points of Engine 1 were analyzed. Since the early flame kernel growth depends on the electric spark length and heat losses (flame kernel – spark plug

electrodes), the electric spark length, the mean flame kernel radius and instantaneously entrained spark plug surface area are studied and the discussion about the obtained results for Engine 1 are given in the following text.

The excess of the flame kernel energy depends on the balance between the electric power delivered to the flame kernel and heat losses that occur between the flame kernel and spark plug electrodes. The electric power  $Q_E$  delivered to the flame kernel is the linear function of the electric spark length  $l_{spk}$  as can be seen in equations (3.4) and (3.9), while the heat transfer  $Q_W$  depends on the instantaneously entrained surface area  $S_e$  of the spark plug electrodes by the flame kernel.

The electric spark lengths for the three operating points of Engine 1 are plotted in Figure 53. At the defined spark time the instantaneous breakdown between the electrodes occurs and the initial electric spark is formed along the shortest distance between the electrodes which is equal to the spark plug gap. Hence, the initial spark length at the breakdown phase is equal to gap distance set to 1 mm. It was already described in Chapter 3 that the electric spark length is described and tracked by Lagrangian particles. Their movement in the  $x$ ,  $y$  and  $z$  coordinate system depends on the flow angle defined by the user and on the velocity profile described by the Hagen-Poiseuille flow. By summing the shortest distances between the neighboring Lagrangian particles the instantaneous spark length is approximated. Due to the influence of the cross-flow velocity that is correlated to the overall in-cylinder turbulence intensity the Lagrangian particles are convected and the electric spark is elongated as can be observed in Figure 53. As the electric spark is elongated the voltage between the electrodes increases and in extreme conditions its value may reach the value of the breakdown voltage. In this case, the Lagrangian particles are suppressed and a new set of particles corresponding to a new spark is initiated.

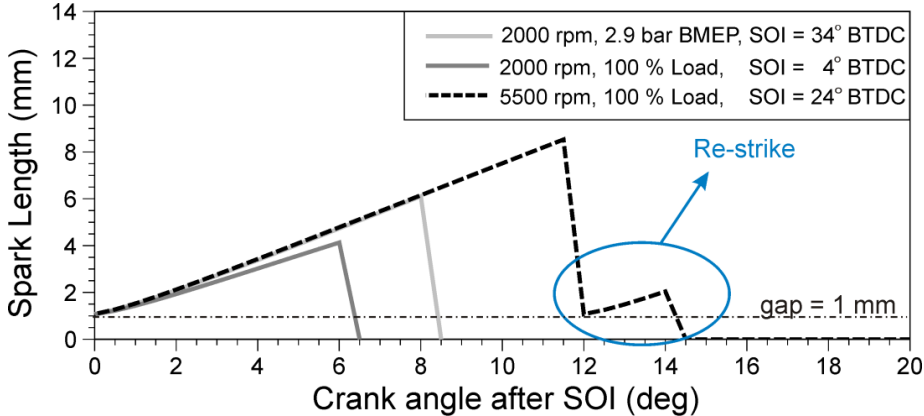


Figure 53. Cycle-simulation result of electric spark length for considered operating points of Engine 1; SOI – start of ignition.

The new breakdown of electric spark occurred at the last operating point of Engine 1 where the engine speed is high. This behavior is expected because at high engine speed the cross-flow velocity is high and the convective movement of Lagrangian particles significantly increases the spark length and enhances the ignition process. The duration of the electric spark, usually called glow phase, is defined by the available electric energy in the secondary electric circuit. When the available electric energy in the secondary electric circuit falls to zero, the electric spark vanishes. When the results of the spark length are compared with the 3-D CFD results reported in [28], it will be seen that the presented QDIM predicts the new breakdown in terms of spark length very close to the 3-D CFD results presented in [28]. In the study presented in [28] the new breakdown occurred at the spark length of 7.6 mm with the mean cross-flow velocity at ignition time equal to 10 m/s. As it can be seen in Figure 53 the developed QDIM predicts the new breakdown in the last operating point at spark length of 8.5 mm with the cross-flow velocity at ignition time equal to 9.62 m/s. The small difference of electric spark length at the new breakdown point is caused by the uniform temperature distribution of the burned zone in 0-D approach. Once the spark is formed, the breakdown voltage is calculated by the equation (3.1) with the temperature in the equation set to the burned zone temperature. This is reasonable because the flame kernel always stays in a connection with the spark plug electrodes [25, 89, 90]. Due to the calculation of temperature stratification in the burned zone, in the 3-D CFD simulation the local temperature around the electrodes is higher. Therefore, the new breakdown voltage is lower leading to a slightly shorter spark length when the re-strike occurs.

The visualization of the electric spark progress during the glow phase, for the considered operating points of Engine 1, is shown in Figure 54. The electric sparks are visualized with the blue solid lines, while the new sparks, formed after the new breakdown, at the last operating point are plotted with the green solid lines. When the new breakdown is occurred, the center of flame kernel remains in the mid-plane and position that is defined with the previous electric spark, while the new spark is formed along the shortest distance between the electrodes. After the re-strike occurrence, the flame kernel also receives the electric energy from the electric spark, which assumes that the contact between the flame kernel and electric spark is realized, although it has not to be in contact in the simulation case. This assumption imposes that the calculation of kernel excess of energy takes into account the fact that the flame kernel always stays in contact with the spark plug electrodes [25, 89, 90]. Since the flow angle for all operating points was set to  $0^\circ$  representing the flow in positive direction of  $x$ -axis, the spark elongation occurred in  $x$ - $z$  plane.



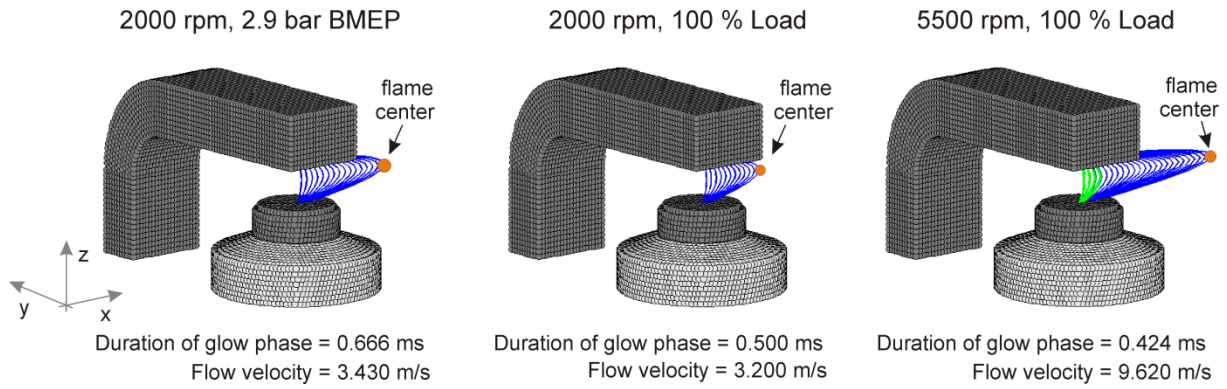


Figure 54. Visualization of the electric spark history of glow phase for Engine 1; green color of electric spark at 5500 rpm represents the sparks formed after new breakdown. Time between the electric spark profiles is 0.5 crank angle degrees.

The glow phase, which corresponds to the visible electric spark, lasts as long as the energy of secondary electric circuit is higher than 0. The duration of the glow phase expressed in time scale is specified in Figure 54. It is evident that the electric spark duration in the time domain is longer at the first operating point and it becomes shorter as the engine speed and load are increased. This behavior of the ignition model is expected and reasonable because the electric energy available in the secondary electric circuit decreases more rapidly when the voltage between the electrodes is higher. The higher level of voltage  $V_{ie}$  is caused by the larger cross-flow velocities that increase the spark length as well as with the larger in-cylinder pressure according to equation (3.4). The cross-flow velocities specified in Figure 54 are calculated from the total in-cylinder turbulent kinetic energy  $k$  at the defined spark timing assuming that the total turbulence intensity  $u'$  is equal to the local mean flow velocity  $U_{av}$  at the vicinity of the spark plug, as it is already described in Chapter 3. The QDIM is developed so that the single flame kernel center always occurs at the center between the spark plug electrodes and it moves with the flame center displacement velocity as it is illustrated in Figure 54. The flame kernel center is located in the mid-plane (already defined in Chapter 3) between the electrodes assuming that this zone represents the potential ignition location due to the higher local temperature that occurs during the gas ionization. The local gas particles closer to the spark plug electrodes have lower temperatures and therefore the ignition process will never be initiated in these locations [91-93].

For the detailed analysis of the early flame kernel growth, the flame kernel radius and the entrained spark plug surface area by the flame kernel for the three operating points of Engine 1 are plotted in Figure 55. The visualization of the flame kernel at  $6^\circ$  crank angle after the ignition is also shown. The duration of the early flame kernel growth that is calculated by

the developed QDIM is defined by the equation (3.16) representing the critical burned mass at which the flame kernel can be considered as turbulent flame and when the wrinkling of flame front becomes significant. It can be seen that the flame kernel radius at the end of the flame kernel calculation reaches the radius of 4 – 6 mm. Although the user-defined constant  $r_0$  for Engine 1 is set to 8 mm, the flame kernel did not reach this radius because the transition from early flame kernel growth to turbulent flame is defined by the controll of burned mass. Due to the lower in-cylinder pressure at part load conditions, the flame kernel radius at the end of the kernel calculation is larger (about 6 mm). Therefore, the equation (3.16) imposes that the ignition delay period and the early flame kernel growth is longer at part load engine conditions.

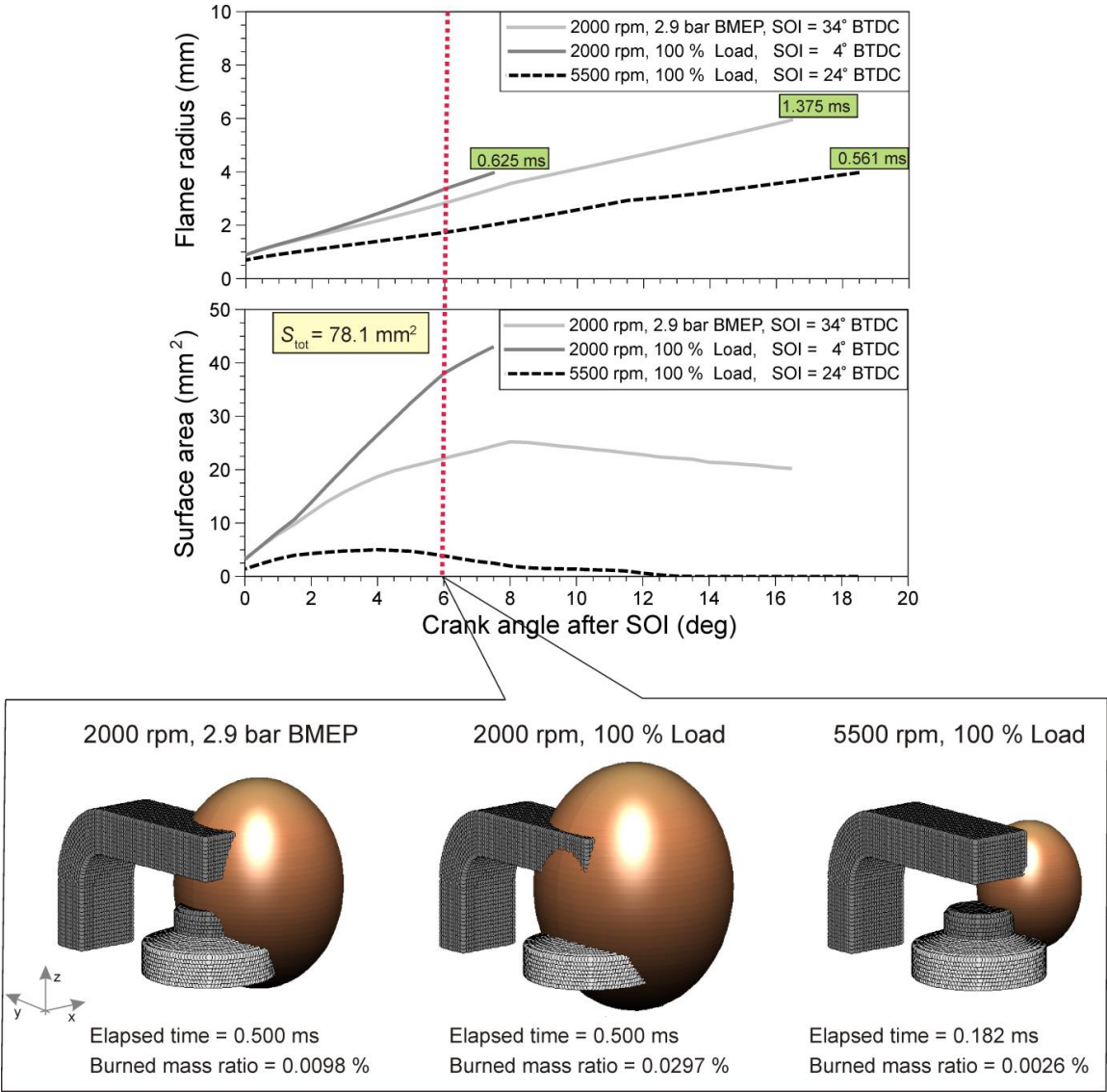


Figure 55. Cycle-simulation result of the flame kernel radius  $R_k$ , entrained spark plug surface area  $S_e$  and visualization of the flame kernel at 6° CA after SOI for all considered operating points of Engine 1.

Experimental studies of flame kernel growth show that, once the flame kernel has grown to more than about 5 mm in radius, it can be approximately described as a turbulent flame [94]. This means that the calibration constants of quasi-dimensional ignition model are correctly specified and that the global effects of ignition phenomena and early flame kernel growth are taken into account.

The entrained spark plug surface area by the flame kernel is also plotted in Figure 55. The largest entrained surface area of the spark plug electrodes is achieved in the second operating condition because the expansion speed of the kernel is high (full load condition) while the displacement of its center from the initial position is weak due to the low cross-flow velocity (specified in Figure 54). At such operating conditions, the flame kernel is able to entrain approximately 50 % of the total spark plug surface area increasing the heat transfer and reducing the flame kernel growth. Of course, in the real operating conditions of the SI engine the flame kernel growth is bounded locally by the electrodes and hence its shape has irregular form that may significantly change the heat transfer. These geometrical effects cannot be captured with the presented QDIM in terms of heat transfer prediction, but the influence of flame kernel distortion on the burning rate is taken into account by calculating the flame distortion factor (see equation (3.14)). Since the flame kernel growth is a time dependent process, at operating conditions with the high engine speed the duration of flame kernel development in crank angle scale is longer compared to the full load conditions at low engine speed. Also, it can be seen that at high engine speed the entrained spark plug surface area after the 5 degrees of crank angle decreases continuously to a very small values and after about 12 degrees of crank angle the flame kernel loses contact with the electrodes. This behavior is not fully physical because the experimental studies regarding the flame kernel development have shown that the flame kernel always stays in contact with the electrodes [25, 89, 90]. The proposed QDIM can be improved so that the mentioned effect at high cross-flow velocity is conserved, but without some experimental or detail 3-D CFD results regarding the flame kernel development this is not feasible.

In order to analyze the flame kernel growth over time for all considered operating points of Engine 1, the flame kernel positions are visualized and approximated by the fully spherical shape with the mean kernel radius  $r_k$  as it is shown in Figure 56. The flame kernel is shown at specific times: 0.02, 0.06, 0.1, 0.2 and 0.3 ms after spark onset. The same time sequences were used in the experimental studies of Heywood [54].


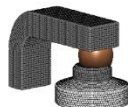
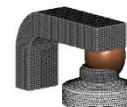
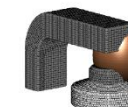

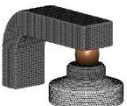
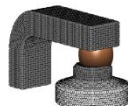
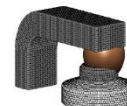
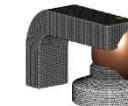
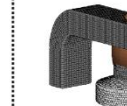

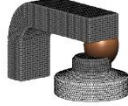

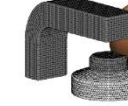
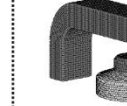
	0.02 ms	0.06 ms	0.10 ms	0.20 ms	0.30 ms
2000 rpm 2.9 bar BMEP	 $R_k = 0.69$ mm	 $R_k = 0.98$ mm	 $R_k = 1.16$ mm	 $R_k = 1.54$ mm	 $R_k = 1.90$ mm
2000 rpm 100 % Load	 $R_k = 0.69$ mm	 $R_k = 0.99$ mm	 $R_k = 1.18$ mm	 $R_k = 1.60$ mm	 $R_k = 2.06$ mm
5500 rpm 100 % Load	 $R_k = 0.73$ mm	 $r_k = 1.00$ mm	 $R_k = 1.21$ mm	 $R_k = 1.75$ mm	 $R_k = 2.44$ mm

Figure 56. Illustration of the flame kernel growth for all operating points of Engine 1 at specific times after spark onset.

At 0.02 ms after spark onset, the flame kernel radius is close to the initial value of 0.5 mm. Since the flame kernel receives the energy from the electric spark, it starts to grow rapidly. On the other hand, as the flame kernel radius becomes larger it entrains the larger surface area of the electrodes that contributes to the heat transfer and decreases the flame expansion speed. At the time of 0.20 ms after spark onset the flame kernel radius is about 1.60 mm. As it was already described, the previous fractal combustion model did not include modeling of the ignition process and early flame kernel growth. It was assumed that this process lasts for about 0.20 ms and that the flame front reaches the radius of about 2 mm. This assumption was adopted according to the experimental studies of North and Santavicca [83]. On Engine 1 (Figure 56) this radius is reached at approximately 0.30 ms after spark onset indicating that the model predictions are close to the experimental data published in the literature [25, 65, 83, 94, 95].

The mean flame kernel radius at time of 0.20 ms after spark onset is lower than 2 mm (see Figure 56), as it is assumed by the original fractal combustion model. Different values of the flame kernel radii at 0.20 ms after spark onset for all considered operating points of Engine 1 are calculated because the early flame kernel growth depends on the actual in-cylinder conditions that are different between the considered operating points. Therefore, the developed QDIM is able to predict the early flame kernel growth physically and more accurate than the previous fractal combustion model. It can be concluded that the calculation of early flame kernel growth described by the QDIM depends on the in-cylinder conditions

(pressure, temperature and mixture composition), cross-flow velocity that displaces the kernel center from its initial position between the electrodes and on the spark plug design.

The detailed simulation results obtained by the QDIM showed that the developed ignition model integrated into the cycle-simulation is able to capture the main effects that affect the early combustion phase of SI engine. This feature gives the possibility to analyze the influence of newly introduced parameters (e.g. spark plug design, gap distance, ignition energy, flow angle, etc.) on the SI engine output performances. Moreover, the early flame kernel growth can be responsible up to 50 % of CCV in combustion. Since the QDIM depends on the in-cylinder conditions and cross-flow velocity, the QDIM is well promising sub-model to capture the part of CCV in combustion caused by the variations in early flame kernel growth, as described in Chapter 6.

#### **5.4. Parameterization of turbulence and combustion model constants**

In the previous section the developed quasi-dimensional ignition model and the modified transition laminar-turbulent flame were applied and the 0-D simulation results were analyzed and compared with the available 3-D CFD data. It was demonstrated that the single set of parameters related to QDIM and to the transition of flame from laminar to fully developed turbulent can be applied for one engine geometry. On the other hand, for each operating point of the engine the intake  $k$  production constant  $S_{in}$  and the intake  $\varepsilon$  production constant  $C_{in}$  were manually tuned so that the 0-D results of the total in-cylinder turbulent kinetic energy matched well the 3-D CFD results during the combustion period. Furthermore, the combustion constant that defines the upper limit of fractal dimension  $f_{D3,max}$  was also manually set for each individual operating point in order to achieve the 0-D combustion rate close to the 3-D CFD results. Tuning of two turbulence and one combustion model constant for each operating point does not represent the user friendly approach because the user of the cycle-simulation model cannot define the model that can be used for calculation of wide operating area of the engine without first calibrating the engine model for that same operating area.

In order to reduce the number of user-defined constants that have to be tuned for each operating point of the engine, the analysis of the intake constants of  $k$ - $\varepsilon$  turbulence model and the analysis of upper limit of fractal dimension are performed. After that, the parameterization of the turbulence model constants and of upper limit of fractal dimension are proposed and applied to the considered engines.

### 5.4.1. Parameterization of turbulence model constants

The intake  $k$  production constant  $S_{in}$  and the intake  $\varepsilon$  production constant  $C_{in}$  were manually tuned for each operating point within the validation of the full  $k-\varepsilon$  turbulence model in Chapter 5.2, achieving a turbulence level during the combustion period close to the 3-D CFD results. By analyzing the values of two newly introduced constants, the dependency of the mentioned constants on certain physical properties were noticed. The dependence of intake  $k$  production constant  $S_{in}$  on the engine speed, for all considered engine geometries and all operating points is shown in Figure 57.

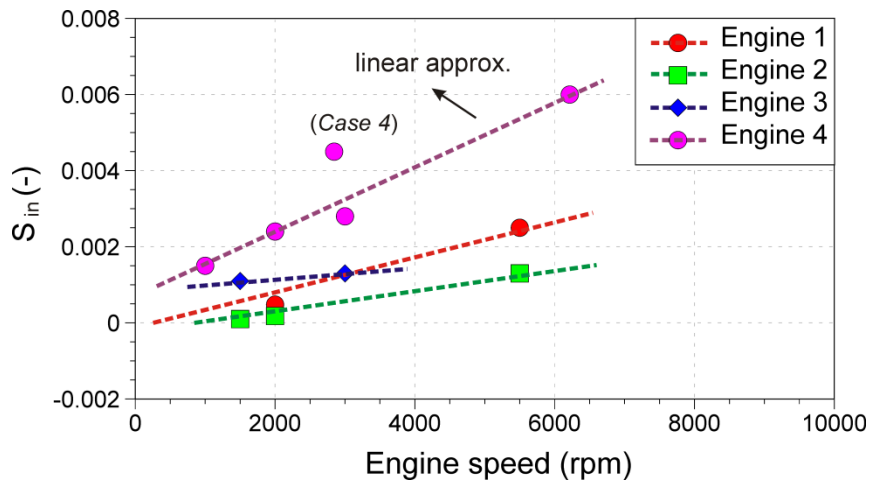


Figure 57. The influence of intake  $k$  production constant  $S_{in}$  on engine speed.

Figure 57 shows that the intake  $k$  production constant  $S_{in}$  is increased as the engine speed increases. In order to achieve the correct air delivery ratio at high engine speed with the same intake valve timing and lift, the volume flow  $q_v$  ( $m^3/s$ ) has to be increased. Therefore, the higher peak value of the mean velocity at the intake valve cross section occurs at the higher engine speed. The larger intake production constant of the turbulent kinetic energy at high engine speed means that the transformation of mean flow kinetic energy that enters into the cylinder is more intensive at operating conditions with the high engine speed, i.e. with larger velocity at the intake valve cross section. For each engine, the linear dependence of the intake  $k$  production constant  $S_{in}$  on the engine speed can be observed. By assuming that the mean flow velocity at the intake valve cross section  $U_{ivcs}$  linearly increases with the higher engine speed, the intake  $k$  production constant  $S_{in}$  can be expressed as a linear function of mean flow velocity at the intake valve cross section:

$$S_{in} = S_{00} + S_{10} \cdot U_{ivcs} \quad (5.1)$$

where  $S_{00}$  (–) and  $S_{10}$  (s/m) are the new user-defined constants. If the proposed linear function (5.2) is applied to the differential equation of the total in-cylinder turbulent kinetic energy (2.36) the following equation can be written:

$$\frac{dk}{dt} = (S_{00} + S_{10} \cdot U_{ivcs}) \cdot \left( \frac{q_m^{in}}{m_c} U_{ivcs}^2 \right) + \frac{2}{3} \frac{k}{\rho} \frac{d\rho}{dt} - \frac{2}{3} \frac{k}{v} \frac{dv}{dt} - \varepsilon \quad (5.2)$$

If the values of the intake  $\varepsilon$  production constant  $C_{in}$  specified in Tables 6 – 9 are analyzed, it can be observed that the higher values of this constant are used at part load conditions are used, while at the full load conditions the  $C_{in}$  constant is lower. This indicates that the dissipation of the turbulent kinetic energy is more intense at low pressure and vice versa. Therefore, the intake  $\varepsilon$  production constant  $C_{in}$  is plotted as a function of in-cylinder pressure at the start of high pressure  $p_{SHP}$  and shown in Figure 58.

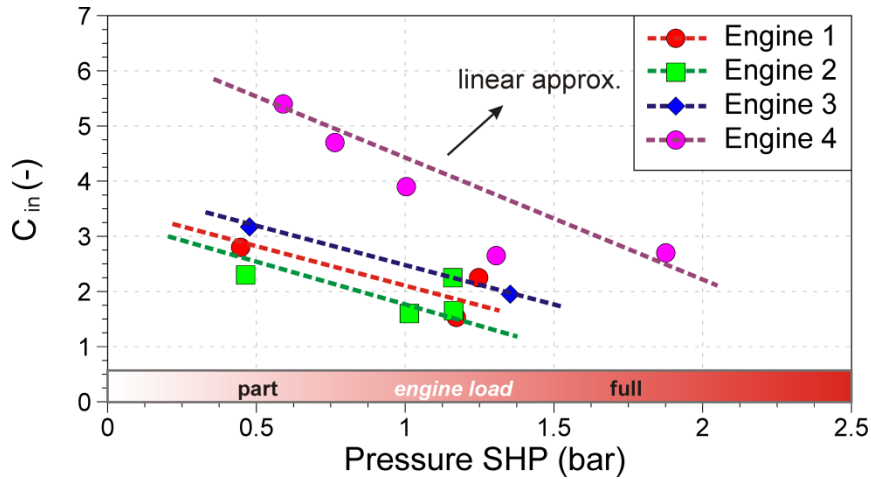


Figure 58. The influence of intake  $\varepsilon$  production constant  $C_{in}$  on in-cylinder pressure at SHP - start of high pressure.

Assuming that the intake  $\varepsilon$  production constant  $C_{in}$  linearly decreases with the increase of in-cylinder pressure, as the measure of engine load, the following correlation may be drawn:

$$C_{in} = C_{00} + C_{10} \cdot p_c \quad (5.3)$$

where  $C_{00}$  (–) and  $C_{10}$  ( $\text{bar}^{-1}$ ) are the new user-defined constants, while  $p_c$  (bar) represents instantaneous in-cylinder pressure. If the proposed correlation (5.3) is inserted into the differential equation of the dissipation rate (2.37), the following form is obtained:



$$\frac{d\varepsilon}{dt} = (C_{00} + C_{10} \cdot p_c) \left( \frac{4}{3} \frac{q_m^{\text{in}}}{m_c} \varepsilon \right) + C_\varepsilon \left( \frac{4}{3} \frac{\varepsilon}{\rho} \frac{d\rho}{dt} \right) + \frac{5}{12} \frac{\varepsilon}{\nu} \frac{d\nu}{dt} - C_2 \frac{\varepsilon^2}{k} \quad (5.4)$$

The proposed differential equations (5.2) and (5.4) for the calculation of turbulent kinetic energy and its dissipation rate over the entire engine cycle represent the parameterized turbulence model that includes 5 user-defined constants. Four constants ( $S_{00}$ ,  $S_{10}$ ,  $C_{00}$  and  $C_{10}$ ) are related to the turbulence generation during the intake process, while the  $C_\varepsilon$  constant influences the dissipation rate during the high pressure cycle when the rapid distortion theory is applied. If the new user-defined constants  $S_{10}$  and  $C_{10}$  are set to 0, the proposed differential equations (5.2) and (5.4) are equal to the basic differential equations (2.36) and (2.37) where  $S_{00} = S_{\text{in}}$  and  $C_{00} = C_{\text{in}}$ . If all user-defined constants related to the intake process are used, the first bracket on the right hand side of equation (5.2) represents the intake parameter of the turbulent kinetic energy whose value will change as the mean flow velocity at the intake valve cross section changes over the time, during the intake process. Furthermore, the first bracket on the right hand side of equation (5.4) represents the intake parameter of dissipation rate that changes during the intake process as the in-cylinder pressure is changed.

The four intake constants of the proposed differential equations (5.2) and (5.4) for the calculation of turbulent kinetic energy and its dissipation rate have to be optimized for each engine geometry with the objective that the total in-cylinder turbulence level during the combustion process is close to the 3-D CFD results at multiple operating points. This will enable the use of a single set of turbulence model constants on a single engine at different operating conditions. The optimization model and the optimization results of the turbulence model constants are described in Chapter 5.5.

#### 5.4.2. Parameterization of upper limit of fractal dimension

In order to achieve the combustion process that is comparable with the 3-D CFD results  $f_{D_3, \text{max}}$  combustion constant was manually tuned for each operating point. Since the combustion model is very sensitive to the value of the fractal dimension  $D_3$  defined by the constant  $f_{D_3, \text{max}}$ , the tuning of this constant for each operating point is not user friendly. Therefore, a detailed analysis of the fractal dimension was made.



The profiles of fractal dimension  $D_3$  during the combustion period for all operating points of Engine 2 are plotted in Figure 59. Due to the influence of the under-relaxation function shown with equation (4.14), the maximum values of fractal dimension are reached after the specific crank angle interval  $\alpha_{tr}$  defined by expression (4.13). In addition, the under-relaxation function that is used to simulate the smooth transition from laminar to fully developed turbulent flame does not allow that the maximum values specified by  $f_{D_3, \max}$  constant are reached. Therefore, the maximum fractal dimensions  $D_{3, \max}$ , which are also marked in Figure 59 are below the specified values of  $f_{D_3, \max}$  constant, which does not represent the real maximum value of the fractal dimension that will be reached during the developed turbulent flame when the flame front wrinkling is at the maximum level. For example, for the *Case 1*, represented by the red solid line, the constant  $f_{D_3, \max}$  is set to 2.51, while the maximum value of  $D_{3, \max}$  during the combustion is 2.28. The same behavior can be observed at other operating points of Engine 2 as well as for the other engines.

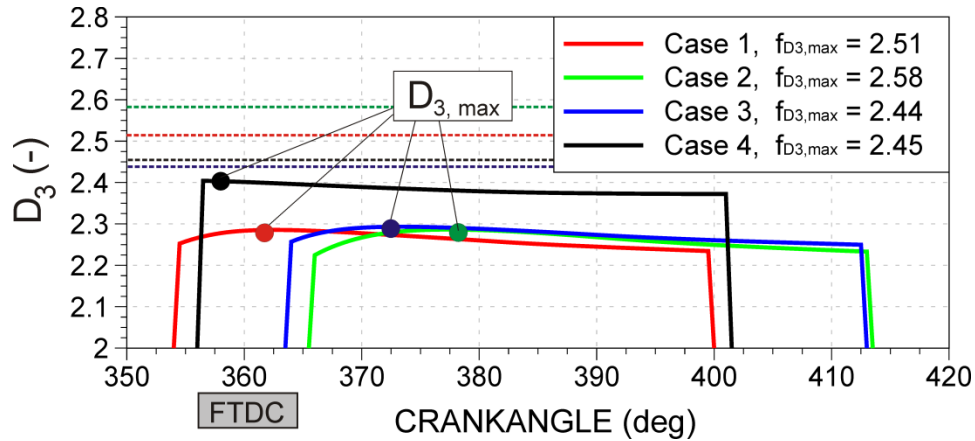


Figure 59. The values of fractal dimension during the combustion period of Engine 2.

The fractal nature of the premixed turbulent flame structures has been experimentally investigated over a range of turbulent Reynolds numbers from 50 to 1500 [82, 96]. It was found that the fractal dimension increases as the ratio of turbulence intensity  $u'$  to laminar flame speed  $S_L$  increases, as shown in Figure 60. The maximum values of fractal dimensions at high Reynolds numbers before flame extinction has been predicted to have a value between 2.37 and 2.41 [83].

In Figure 60 the results of the maximum fractal dimension  $D_{3, \max}$  that are reached during the combustion for all considered operating points of all engines are also plotted. Since the turbulence intensity and the laminar flame speed change during the combustion, the

turbulence intensity to laminar flame speed ratio  $u'/S_L$  for Engines 1- 4 was defined at the time when the maximum fractal dimension  $D_{3, \max}$  is reached.

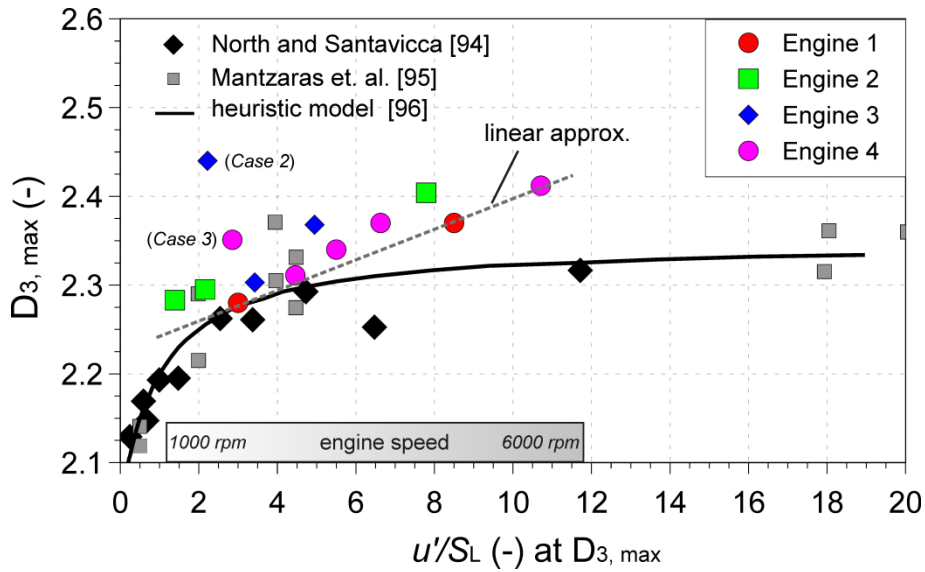


Figure 60. Maximum values of the fractal dimension as a function of the ratio of turbulence intensity and laminar flame speed.

Figure 60 shows that at low and medium engine speeds (1000 – 3000 rpm), that correspond to the ratio of turbulence intensity to laminar flame speed lower than 5, the maximum fractal dimension  $D_{3, \max}$  obtained in the 0-D simulations are close to the experimental results [82, 96], while at high engine speed these values are above the ones observed in experiment. It was already mentioned that the  $f_{D_{3, \max}}$  constant that defines the maximum fractal dimension  $D_{3, \max}$  was tuned for each operating point so that a good agreement of 0-D and 3-D CFD results of the combustion process is achieved. The manual tuning of this constant assumes that the calculation of laminar flame speed proposed by Metghalchi and Keck [84] is correct. There are two operating points (*Case 2* of the Engine 3 and *Case 3* of the Engine 4) whose maximum fractal dimensions are significantly higher than the expected values for the corresponding turbulence intensity to laminar flame speed ratio. These differences can be caused by the incompatibility of 0-D and 3-D CFD results (it is already mentioned for *Case 2* of Engine 3 in Chapter 5.1), by the incorrect calculation of laminar flame speed due to mixture stratification, or by the complex 3-D interaction of turbulent structures and the flame front that cannot be predicted with the quasi-dimensional combustion models. Since the turbulence model constants were manually tuned for each operating point, the turbulence intensity during the combustion period is very close to the 3-D CFD results, as it is shown in the Chapter 5. Therefore, the mentioned effects that can cause different combustion progress and are not, or cannot be, predicted with the presented quasi-dimensional combustion model

are compensated by the tuning of upper limit of fractal dimension. If the two operating points (*Case 2* of the Engine 3 and *Case 3* of the Engine 4) are neglected, the maximum value of fractal dimension  $D_{3, \max}$  shows almost linear increase with the increase of the ratio of turbulence intensity to laminar flame speed within the considered range of engine speed.

Therefore, the linear function for the approximation of  $D_{3, \max}$  value is proposed:

$$D_{3, \max} = C_3 \cdot \left[ 2.20 + 1.8 \cdot 10^{-2} \cdot \left( \frac{u'}{S_L} \right) \right] \quad (5.5)$$

where  $C_3$  (-) is new user-defined constant that can change the slope of the approximation function (shown in Figure 60 with the dashed line) as well as its minimum value when the ratio of turbulence intensity and laminar flame speed is zero. The linear function of maximum fractal dimension (5.5) predicts the maximum value that should be reached during the combustion period. In order to incorporate this information into the quasi-dimensional combustion model it is necessary to define the constant  $f_{D3, \max}$  that will lead to calculating the desired maximum value  $D_{3, \max}$ . From equations (4.2) and (4.3) the constant  $f_{D3, \max}$  can be expressed as:

$$f_{D3, \max} = \frac{D_{3, \max} \cdot (u'_{D3, \max} + S_L) - 2.05 \cdot (u'_{D3, \max} \cdot (1 - I_f) + S_L)}{I_f \cdot u'_{D3, \max}} \quad (5.6)$$

When the maximum value of fractal dimension is reached, the under-relaxation function should be close to 1, while the laminar flame speed is about 1 m/s for gasoline. If such values are taken into account the equation (5.6) can be reduced to the following form:

$$f_{D3, \max} = \frac{D_{3, \max} \cdot (u'_{D3, \max} + 1) - 2.05}{u'_{D3, \max}} \quad (5.7)$$

The remaining unknown in expression (5.7) is the turbulence intensity  $u'_{D3, \max}$  when the maximum value of fractal dimension occurs. If the 3-D CFD results of the total in-cylinder turbulent kinetic energy during the late compression and expansion are analyzed, in non-dimensional domain, it is very interesting to notice, in Figure 61, that the obtained profile of non-dimensional turbulent kinetic energy for all considered operating points of all engines

follow the same profile presented with the black circle markers. The non-dimensional turbulent kinetic energy  $k^*(-)$  at each crank angle degree is calculated so that the corresponding turbulent kinetic energy is divided by the maximum value of turbulent kinetic energy that occurs before TDC. The obtained profile of non-dimensional turbulent kinetic energy from 3-D CFD results during the interval of  $140^\circ$  of crank angle can be fitted with the polynomial function:

$$k^*(\alpha) = c_1 \cdot \alpha^{10} + c_2 \cdot \alpha^9 + c_3 \cdot \alpha^8 + c_4 \cdot \alpha^7 + c_5 \cdot \alpha^6 + c_6 \cdot \alpha^5 + \dots \quad (5.8)$$

$$\dots + c_7 \cdot \alpha^4 + c_8 \cdot \alpha^3 + c_9 \cdot \alpha^2 + c_{10} \cdot \alpha + c_{11}$$

where  $\alpha$  ( $^\circ$ ) represents the relative crank angle (zero crank angle corresponds to  $40^\circ$  CA before FTDC), while the polynomial coefficients are defined as follows:

$$c_1 = -1.132 \cdot 10^{-18} \quad (\text{deg}^{-10}), \quad c_2 = 8.147 \cdot 10^{-16} \quad (\text{deg}^{-9}), \quad c_3 = -2.486 \cdot 10^{-13} \quad (\text{deg}^{-8})$$

$$c_4 = 4.17 \cdot 10^{-11} \quad (\text{deg}^{-7}), \quad c_5 = -4.159 \cdot 10^{-9} \quad (\text{deg}^{-6}), \quad c_6 = 2.481 \cdot 10^{-7} \quad (\text{deg}^{-5})$$

$$c_7 = -8.386 \cdot 10^{-6} \quad (\text{deg}^{-4}), \quad c_8 = 1.433 \cdot 10^{-4} \quad (\text{deg}^{-3}), \quad c_9 = -1.341 \cdot 10^{-3} \quad (\text{deg}^{-2})$$

$$c_{10} = 1.133 \cdot 10^{-2} \quad (\text{deg}^{-1}) \quad \text{and} \quad c_{11} = 0.9281 \quad (-)$$

The crank angle at which the maximum fractal dimension is achieved can be estimated by equation (4.13) and by the correct prediction of turbulence quantities (integral length scale  $L_1$  and turbulence intensity  $u'$ ) at the time when the burned mass is equal to the critical one defined by equation (3.16). By using the polynomial function (5.8), the equation (4.13) that defines the transition period when the maximum fractal dimension is reached and by the correct prediction of in-cylinder turbulent kinetic energy at SOC, it is possible to estimate the turbulence intensity  $u'_{D3, \max}$  at the time when the maximum wrinkling of the flame front is achieved:

$$u'_{D3, \max} = u'_{\text{SOC}} \cdot \frac{k^*(\alpha_{\text{tr}})}{k^*(\alpha_{\text{SOC}})} \quad (5.9)$$

where  $\alpha_{\text{SOC}}$  ( $^\circ\text{CA}$ ) and  $\alpha_{\text{tr}}$  ( $^\circ\text{CA}$ ) represent the relative crank angles at the start of combustion and at the point where the maximum fractal dimension is achieved, respectively. The start of combustion corresponds to the spark time when the QDIM is applied.

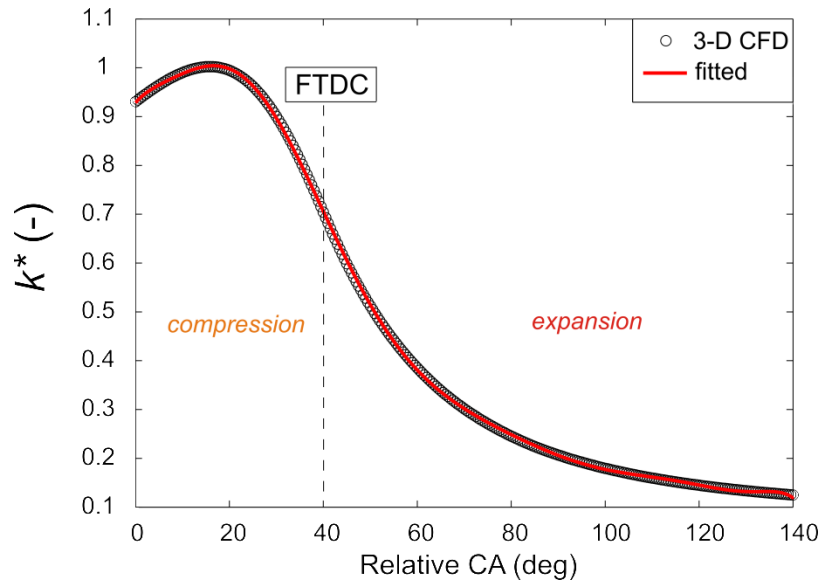


Figure 61. The parameterization of non-dimensional turbulent kinetic energy during the combustion period; the profile of non-dimensional turbulent kinetic energy is the same for all operating points of all engines.

The application of equations (5.5) – (5.9) including the specification of new user-defined constant  $C_3$  enables that the fractal dimension  $D_3$  can be correctly predicted at different engine operating conditions. In other words, the proposed equations represent the parameterization model of the upper limit of fractal dimension that requires the tuning of  $C_3$  constant for one engine. The proposed parameterization model is defined for the engines fueled with gasoline and for the range of engine speeds from 1000 rpm to 6215 rpm (*Case 5* of Engine 4). In the following chapters first the optimization of the turbulence model constants ( $S_{00}$ ,  $S_{10}$ ,  $C_{00}$  and  $C_{10}$ ) for each engine will be made and afterwards the proposed parameterization of the upper limit of fractal dimension will be applied.

## 5.5. Optimization of turbulence model constants towards the single set of constants

The quasi-dimensional combustion models are very sensitive to the values of input parameters particularly related to the turbulence and combustion sub-models. The sensitivity analysis of the two turbulence model parameters was performed and shown in [21]. It was concluded that the calibration of only two constants and the possible adjustments of the free flame surface area are sufficient to provide a predictive SI engine simulation using a 0-D approach.

In order to find the single set of constants related to the  $k-\varepsilon$  turbulence sub-model of the cycle-simulation model for one engine geometry, the optimization process of four intake

turbulence constants, described in Chapter 5.4, ( $S_{00}$ ,  $S_{10}$ ,  $C_{00}$  and  $C_{10}$ ), was performed. The main information about the applied optimization algorithm, specification of objective function as well as the optimization results are given in the following text.

### 5.5.1. Optimization algorithm and definition of objective function

The optimization process of turbulence constants was performed by the genetic algorithm. The genetic algorithm is a global search method based on the analogy of natural biological evolution. At each generation a new population of design points is defined with the genetic modifications like crossover and mutation. The selection of individual design points is performed according to their level of fitness, which measures the performance of the individual member based on the defined objective function. The initial population is generated randomly within the project space and the optimization process terminates when a termination criterion is met, which is usually defined by the number of generations. For the optimization of turbulence model constants the population size was set to 30 with 10 generations. The other parameters of applied genetic algorithm, i.e. the crossover and mutation probability as well as their distributions, were used as default values [99].

For each operating point of the engine, the objective function is defined as the area between the 3-D CFD and the 0-D result of the turbulent kinetic energy during the first 90° of crank angle from firing top dead center when the maximum burning rate is achieved. The illustration of the objective function of each operating point is given in Figure 62.

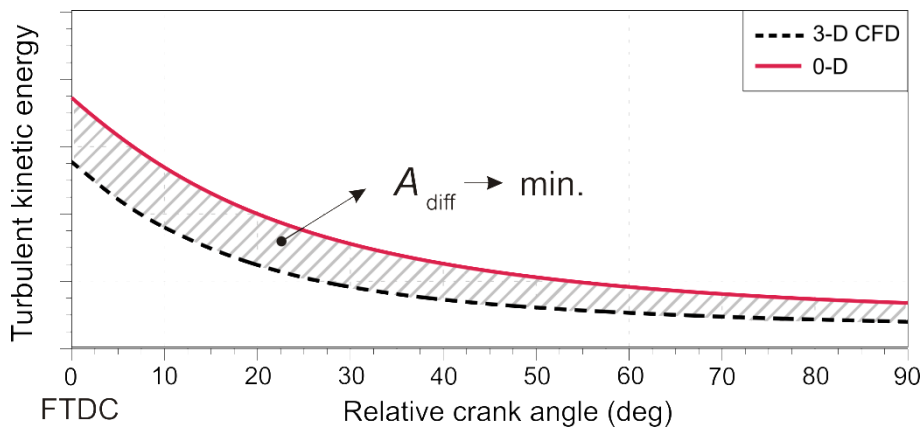


Figure 62. Illustration of the objective function for optimization of turbulence model constants.

Therefore, the individual objective function is calculated as:

$$f_{\text{case}} = A_{\text{diff}} = \int_{0^{\circ}}^{90^{\circ}} (k^{3-D\text{CFD}} - k^{0-D}) d\alpha \quad (5.10)$$

The overall objective function of one engine is obtained by the weighted sum of the individual objective functions defined by equation (5.10) for each operating point:

$$f_{\text{engine}} = \sum_{i=1}^N w_i \cdot f_{\text{case},i} \quad (5.11)$$

where  $w_i$  (-) represents the weight of each operating point of the engine. The weight of a particular operating point of the engine is defined with respect to the level of turbulent kinetic energy of that operating point, so that in the overall sum each operating point has the same importance. This means that the optimization problem of one engine has one objective function  $f_{\text{engine}}$  and four project variables,  $S_{00}$ ,  $S_{10}$ ,  $C_{00}$  and  $C_{10}$ . During the optimization process, the objective function  $f_{\text{engine}}$  was minimized and the optimization results are shown below.

### 5.5.2. Optimization results

In order to increase the calculation speed of the optimization process for one engine geometry, the combustion process was simulated with the single zone turbulence model, without the application of quasi-dimensional ignition model. This is acceptable because the effect of the combustion process on the progress of total in-cylinder turbulence level is minimal (the kinematic viscosity does not include increase of in-cylinder temperature caused by combustion) and the application of the ignition model only affects the initial part of combustion process. The constants of the fractal combustion model, when the single zone turbulence model is used, are already specified in Tables 2 – 5. The simulation of each operating point of the engine was performed for 15 cycles, to achieve a converged solution. This means that for one run (one set of constants that are optimized) during the optimization of Engine 2, 60 cycles have to be calculated (4 operating points with 15 cycles). The number of runs that are necessary to find the optimum result depends on the applied optimization algorithm and its setup. In this case approximately 300 runs were required to find the solution for  $S_{00}$ ,  $S_{10}$ ,  $C_{00}$  and  $C_{10}$  that gives the total in-cylinder turbulence during the expansion close to the 3-D CFD data. The total calculation time was about 5 hours for one engine. The optimized constants of the proposed  $k$ - $\varepsilon$  turbulence model for the considered engines are specified in Table 15.

Table 15. Overview of single set of constants for the single zone  $k$ - $\varepsilon$  turbulence model: optimization results for Engines 1 – 4

Engine Name	<i>Engine 1</i>	<i>Engine 2</i>	<i>Engine 3</i>	<i>Engine 4</i>
$C_2$ (-)	1.92			
$C_\varepsilon$ (-)	2.40			
$S_{00}$ (-)	0	0	0	$3.5 \cdot 10^{-2}$
$S_{10}$ (s/m)	$3.92 \cdot 10^{-6}$	$2.65 \cdot 10^{-6}$	$1.5 \cdot 10^{-5}$	$9.8 \cdot 10^{-5}$
$C_{00}$ (-)	3.10	3.40	3.80	9.80
$C_{10}$ ( $\text{bar}^{-1}$ )	- 1.90	- 2.17	- 2.10	- 5.20

The optimized value of constant  $S_{00}$  is zero for all engines except for the Engine 4. The remaining values of optimized constants are as expected due to the previously described behavior of the intake  $k$  production constant  $S_{in}$  and the intake  $\varepsilon$  production constant  $C_{in}$  shown in Figure 57 and Figure 58. The last considered engine has significantly different values of optimized constants compared to the Engines 1 – 3 indicating that some geometrical effects of intake plenum, pipe, intake valve or combustion chamber geometry influence the total in-cylinder turbulence level during the intake and consequently the remaining part of the engine cycle. The mentioned geometrical effects cannot be predicted by the proposed turbulence model, but they can be compensated by the correct tuning of intake constants.

The overall objective functions of Engines 1 and 2 are defined by taking into account all individual objective functions of each particular operating point of the engine, as it is described by equations (5.10) and (5.11). The results of the total in-cylinder turbulent kinetic energy during the first  $100^\circ$  crank angles of expansion, obtained by using optimized turbulence model constants for all operating points of Engine 1 and 2 are shown in Figure 63 and the 0-D results are compared with the 3-D CFD data and with the previous 0-D results (gray solid lines) where the intake turbulence model constants ( $S_{in}$  and  $C_{in}$ ) are manually tuned for each operating point of the engine (see Chapter 5.2).



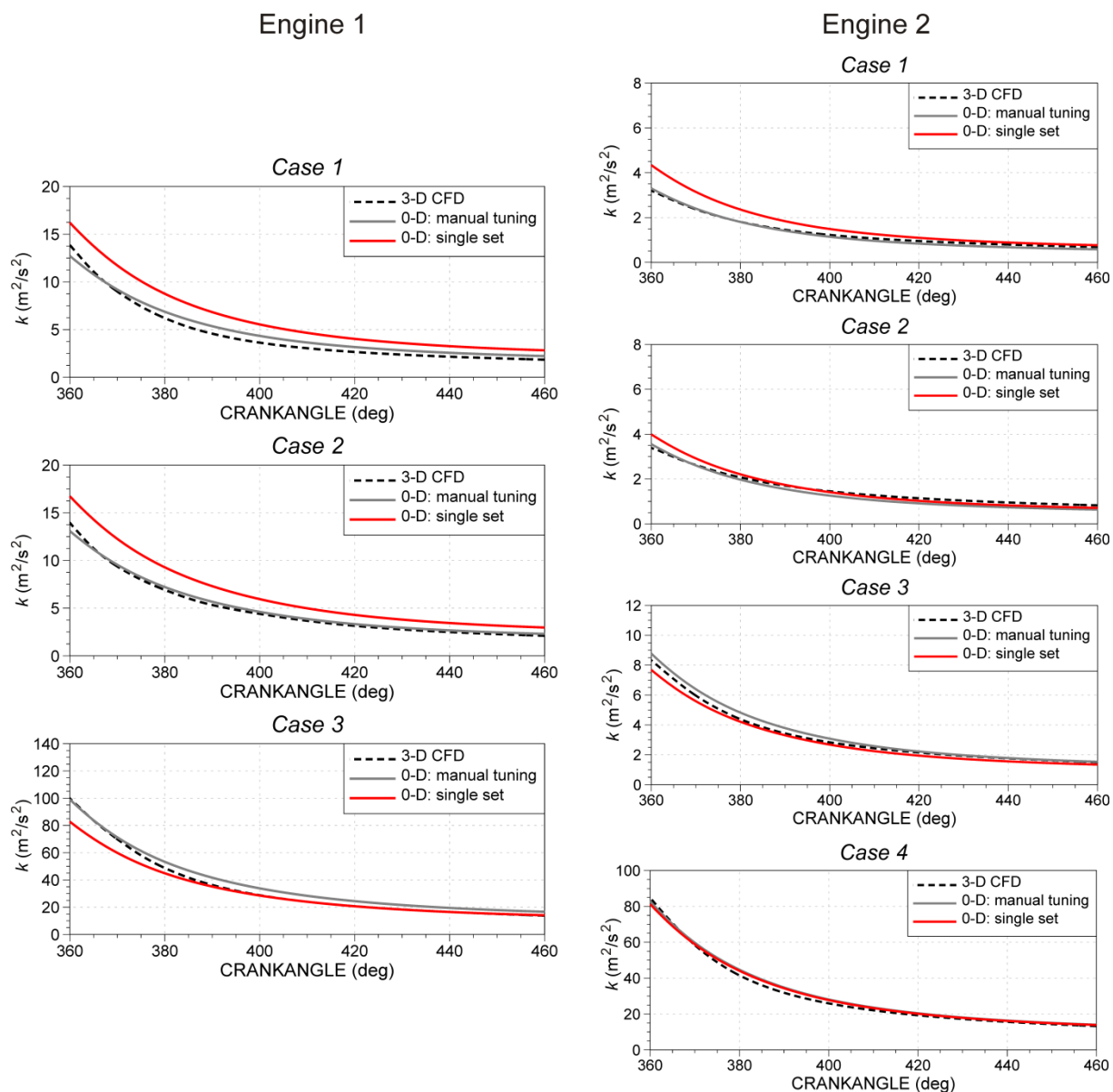


Figure 63. Turbulent kinetic energy during the expansion calculated by a single zone model that uses optimized turbulence model constants, for Engine 1 (left) and Engine 2 (right).

The predicted progress of total in-cylinder turbulent kinetic energy during the expansion match well the 3-D CFD results. At the first two operating points (*Case 1* and *Case 2*) of Engine 1 and first operating point (*Case 1*) of Engine 2 the values of in-cylinder turbulence levels are slightly overpredicted, by approximately 15 % at TDC. These differences are caused by the introduction of linear approximations for the intake turbulence constants  $S_{in}$  and  $C_{in}$  shown in Figure 57 and Figure 58. Since the quasi-dimensional combustion model is sensitive to the turbulence level, the slightly overpredicted turbulent kinetic energy can be compensated by the combustion model constants, for example by the proposed parameterization of the upper limit of fractal dimension. The applied linear approximations

for the intake turbulence constants and the performed optimization process of the turbulent kinetic energy during the expansion resulted with the single set of turbulence model constants ( $S_{00}$ ,  $S_{10}$ ,  $C_{00}$  and  $C_{10}$ ) for each engine where the in-cylinder turbulence level for different operating conditions during the turbulent combustion matched well the 3-D CFD results.

Due to different boundary conditions that were available for operating points of Engine 3, the overall objective function of that engine included only two individual objective functions of *Case 1* and *Case 3*. After the optimization of intake constants of  $k$ - $\varepsilon$  turbulence model at *Cases 1* and *3*, the optimized turbulence model constants are applied on the remaining operating point (*Case 2*). The optimization results of all operating points of Engine 3 obtained by the application of an optimized set of turbulence model constants are shown on the left side of Figure 64. It can be seen that the optimization process performed on two different operating points resulted in a set of turbulence model constants that predict the in-cylinder turbulence level during the expansion correctly even when they are applied on other operating points. For the *Case 2* operating point of Engine 3, which was not used in the optimization of turbulence model constants, the progress of total in-cylinder turbulent kinetic energy is slightly overpredicted. If the 3-D CFD results are not available for more than 2 different operating points, at least 2 different operating points of the considered engine may be taken into account in the optimization process of turbulence model constants. The first operating point should represent relatively low engine speed and part load condition, while the second one should represent higher engine speed and full load (100 %) condition. This enables the correct definition of the linear approximations of intake coefficients  $S_{in}$  and  $C_{in}$ .

The optimization process of intake constants by genetic algorithm on Engine 4 was again performed with individual objective functions for all considered operating points and the optimization results are shown on the right side of Figure 64. At part load condition and low engine speed the level of in-cylinder turbulence is overpredicted by about 50 % at TDC and during the expansion compared to the 3-D CFD data and 0-D results when the intake turbulence constants are manually tuned (gray solid curves). Although the turbulence level of *Case 3* of Engine 4 during the early part of expansion is underpredicted for about 40 %, it is acceptable because the turbulence effects on the combustion process becomes significant only when the highly wrinkled turbulent flame is developed. The application of a single set of turbulence model constants obviously reduced the accuracy of results of turbulent kinetic energy during the expansion at several operating points, but the presented  $k$ - $\varepsilon$  turbulence

model becomes predictive for the entire operating range of SI engine once the model constants are calibrated correctly.

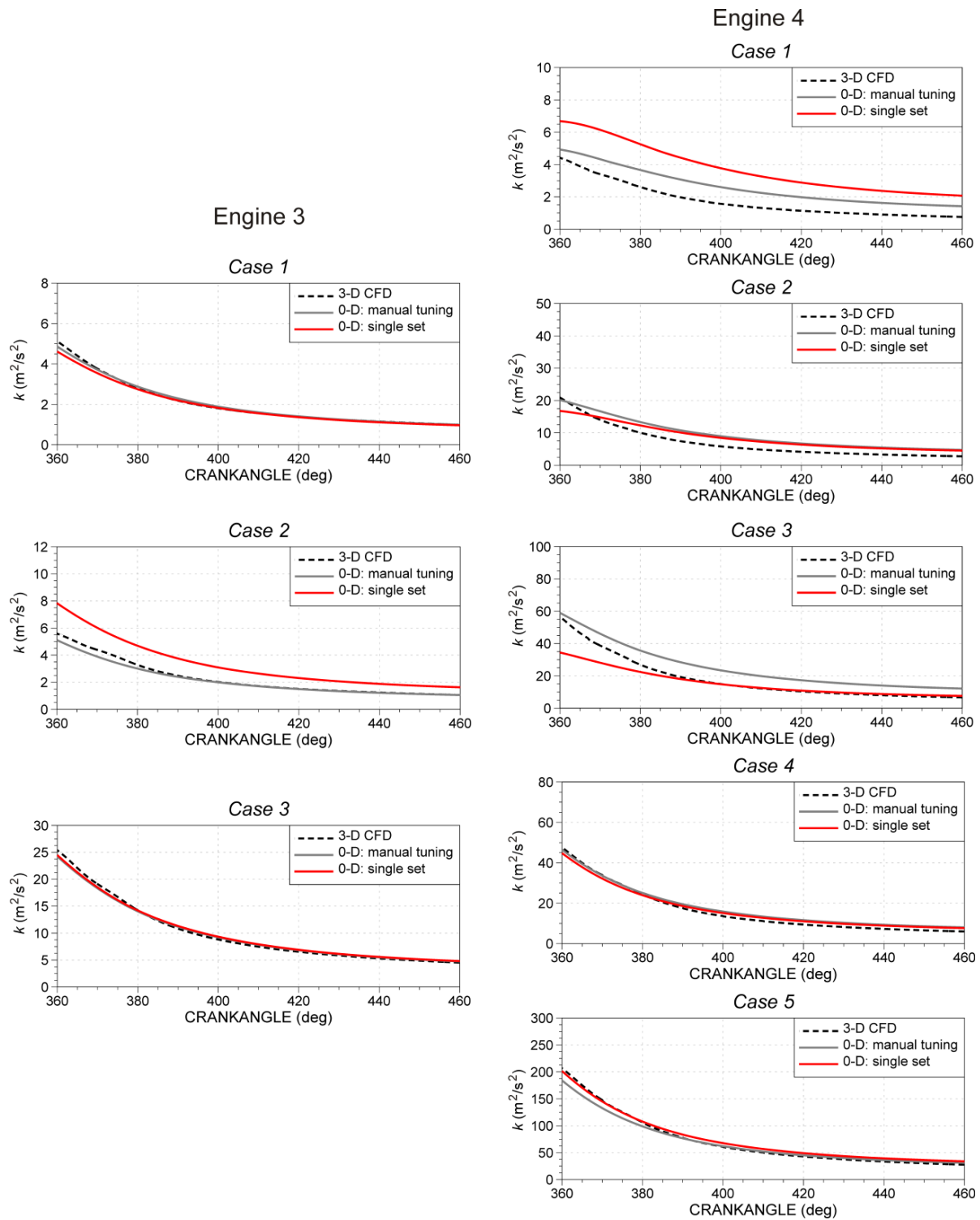


Figure 64. Turbulent kinetic energy during the expansion calculated by a single zone model that uses optimized turbulence model constants, for Engine 3 (left) and Engine 4 (right).

## 5.6. Application of single sets of constants

In the previous section the proposed parameterization of the turbulence model constants was optimized so that a single set of turbulence model constants is obtained for one engine. The optimized results of in-cylinder turbulent kinetic energy during the expansion are shown in Figure 63 and Figure 64, and the results are compared with the 3-D CFD data. In section 5.4.2 there is also the proposal for the parameterization model of maximum fractal dimension  $D_{3,\max}$  that requires the tuning of new user-defined constant  $C_3$ .

In order to demonstrate the possibility of the proposed parameterization models of turbulence and combustion sub-models to predict the combustion process at the different operating conditions with the single set of constants, the simulation of combustion of all considered engines and conditions is performed. The single sets of constants related to turbulence, ignition and combustion sub-models are specified in Table 16.

Table 16. Overview of single set of constants for turbulence, ignition and combustion used in simulation of Engines 1 – 4

Engine Name	<i>Engine 1</i>	<i>Engine 2</i>	<i>Engine 3</i>	<i>Engine 4</i>
	<b>Two zone turbulence model</b>			
$C_2$ (-)	1.92			
$C_e^{UZ}$ (-)	3.00	2.00	2.00	2.50
	<b>Ignition model (QDIM)</b>			
$r_0$ (m)	0.008	0.005	0.002	0.0065
$T_{SP}$ (K)	470	450	450	650
	<b>Fractal combustion model</b>			
$C_\tau$ (-)	0.70	0.40	1.20	1.70
$C_3$ (-)	1.005	1.026	1.035	1.003

The optimized constants of  $k-\varepsilon$  turbulence model are already specified in previous chapter, Table 15. Therefore, only the dissipation rate constant of the unburned zone  $C_e^{UZ}$  is listed in Table 16. In terms of the developed ignition sub-model, two constants were tuned to achieve the prediction of the combustion process close to the 3-D CFD results. The first constant  $r_0$  represents the constant that defines the burned mass when the tracking of combustion can be performed with the fractal combustion model. The second constant of ignition model represents the spark plug temperature. It was defined as the temperature that is slightly higher (about 50 K) than the cylinder head temperature. Since the cylinder head temperature for Engine 4 defined from 3-D CFD simulation is set to 585 K, the spark plug temperature is set

to 650 K. The last two constants in Table 16 are related to the fractal combustion sub-model. The first constant  $C_\tau$  defines the transition time from the laminar to fully developed turbulent flame, while the last  $C_3$  constant defines the maximum value of fractal dimension according to the proposed equation (5.5). The described combustion model constants as well as the dissipation constant of the unburned zone, specified in Table 16, are manually tuned so that the predictions of combustion process at different operating conditions of the engine are close to the 3-D CFD results.

The results of the normalized heat release and in-cylinder temperature for all considered operating points of Engines 1 – 4 are plotted and the results are compared with the 3-D CFD results in Figure 65 - Figure 68.

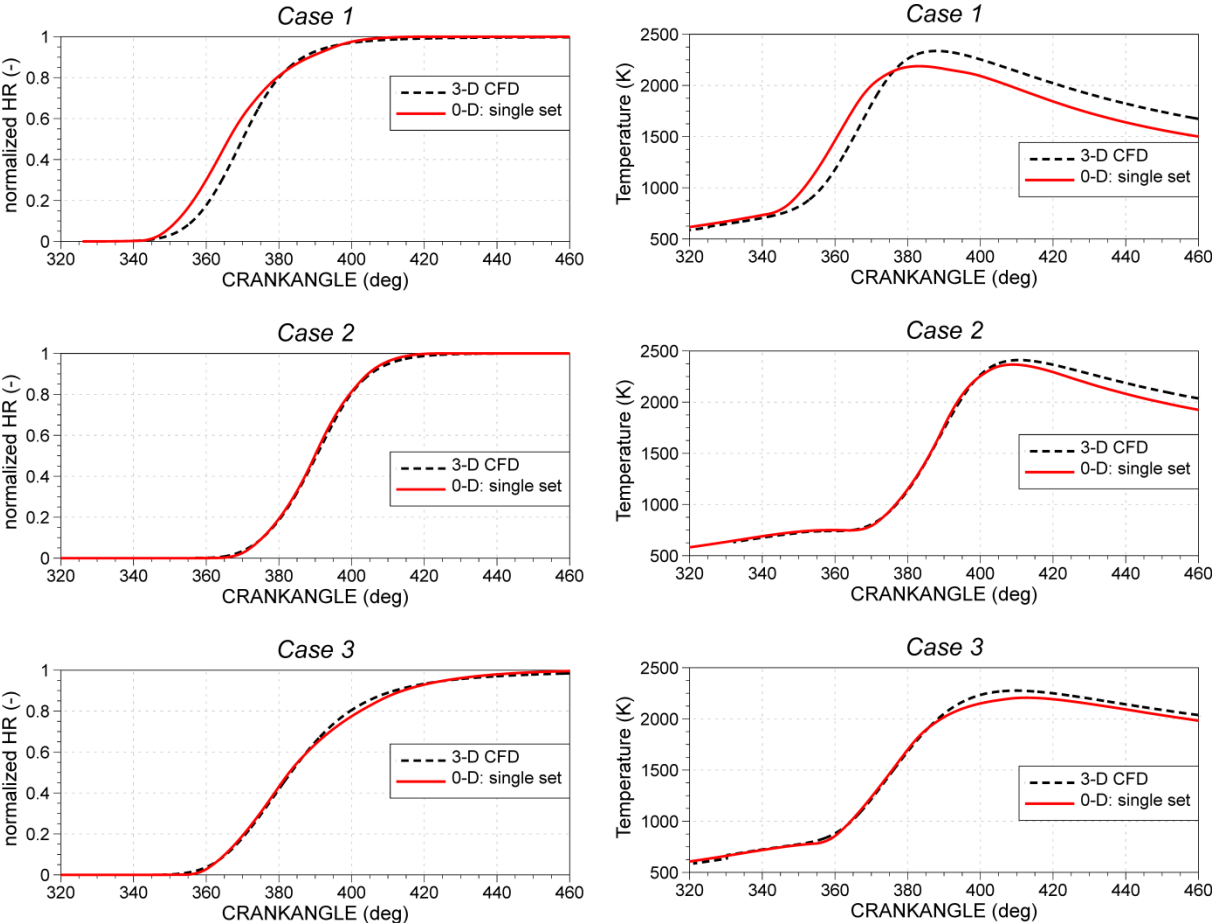


Figure 65. Normalized heat release (left) and in-cylinder temperature (right) of Engine 1 obtained by application of single set of constants.

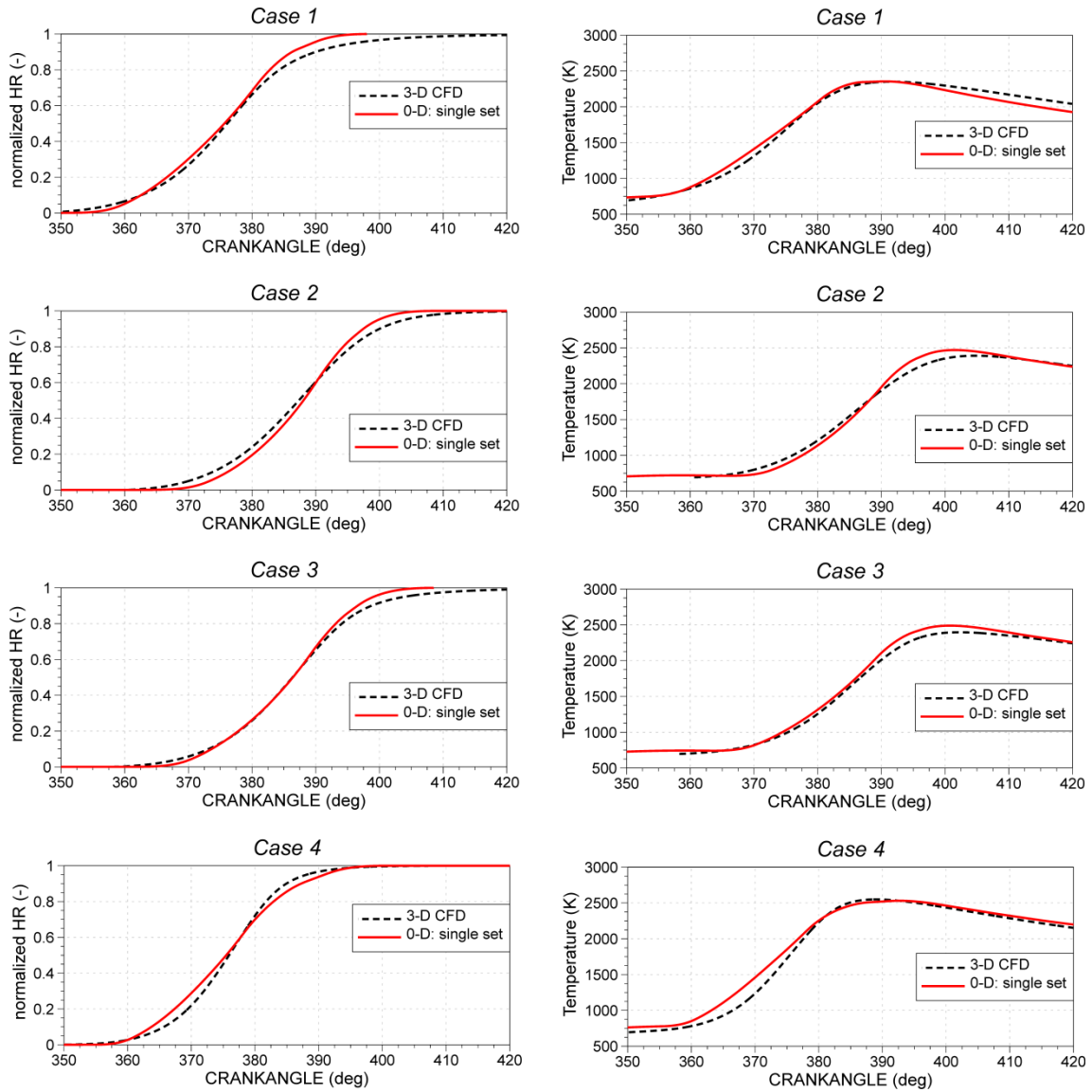


Figure 66. Normalized heat release (left) and in-cylinder temperature (right) of Engine 2 obtained by application of single set of constants.

The obtained profiles of normalized heat release and in-cylinder temperature by applying the single set of constants for different operating conditions of Engine 1 and Engine 2 are very close to the 3-D CFD results. If the results of the in-cylinder temperature shown in Figure 46 and Figure 47, where the turbulence constants  $S_{in}$  and  $C_{in}$  as well as the upper limit of fractal dimension  $f_{D3, max}$  are manually set for each operating point, are compared with the results where the single set of constants is applied, a very small difference can be noticed which means that still a very good agreement with the 3-D CFD results is achieved.

The results of normalized heat release and in-cylinder temperature obtained by applying the single set of constants for considered operating points of Engine 3 are shown in Figure 67. The prediction of combustion progress for *Case 2* of Engine 3 calculated by the

application of 0-D model and single set of constants does not match correctly the 3-D CFD result. Although the overall in-cylinder turbulence level for this case, shown in Figure 64, is slightly higher compared to the one obtained with the manual tuning of turbulence model constants, the combustion progress is very slow compared with the 3-D CFD result. The value of maximum fractal dimension  $D_{3, \max}$  shown in Figure 60 that was manually set to achieve the correct prediction of combustion progress, required unusual high value of fractal dimension that cannot be predicted with the proposed linear approximation (see equation (5.5)).

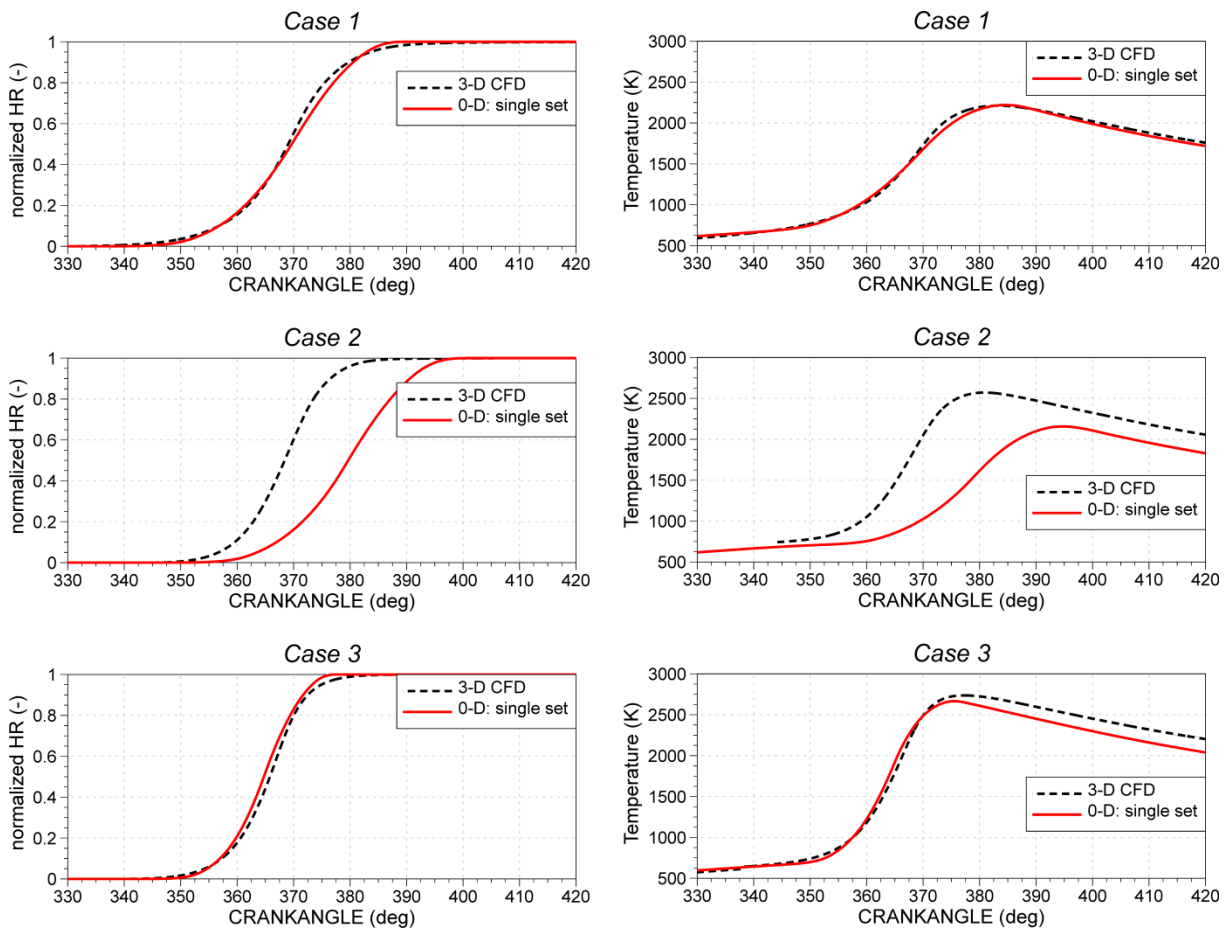


Figure 67. Normalized heat release (left) and in-cylinder temperature (right) of Engine 3 obtained by application of single set of constants.

Even when the upper limit of fractal dimension was manually set and when the normalized HR was close to the 3-D CFD result for *Case 2* of Engine 3, it was shown in Figure 48 that the in-cylinder temperature profile calculated with the 0-D model was significantly lower than the 3-D CFD result. This indicates that there is a disagreement in boundary conditions in terms of air delivery ratio and air equivalence ratio between the cycle-simulation and 3-D CFD model. Therefore, this operating point cannot be very reliable for the comparison of normalized HR and in-cylinder temperature. For other operating points (*Case 1* and *Case 3*)



of Engine 3 the application of the single set of constants of the 0-D model resulted in good agreement of combustion progress and in-cylinder temperature with the 3-D CFD results.

The obtained profiles of normalized heat release and in-cylinder temperature by applying the single set of constants for different operating conditions of Engine 4 are shown in Figure 68.

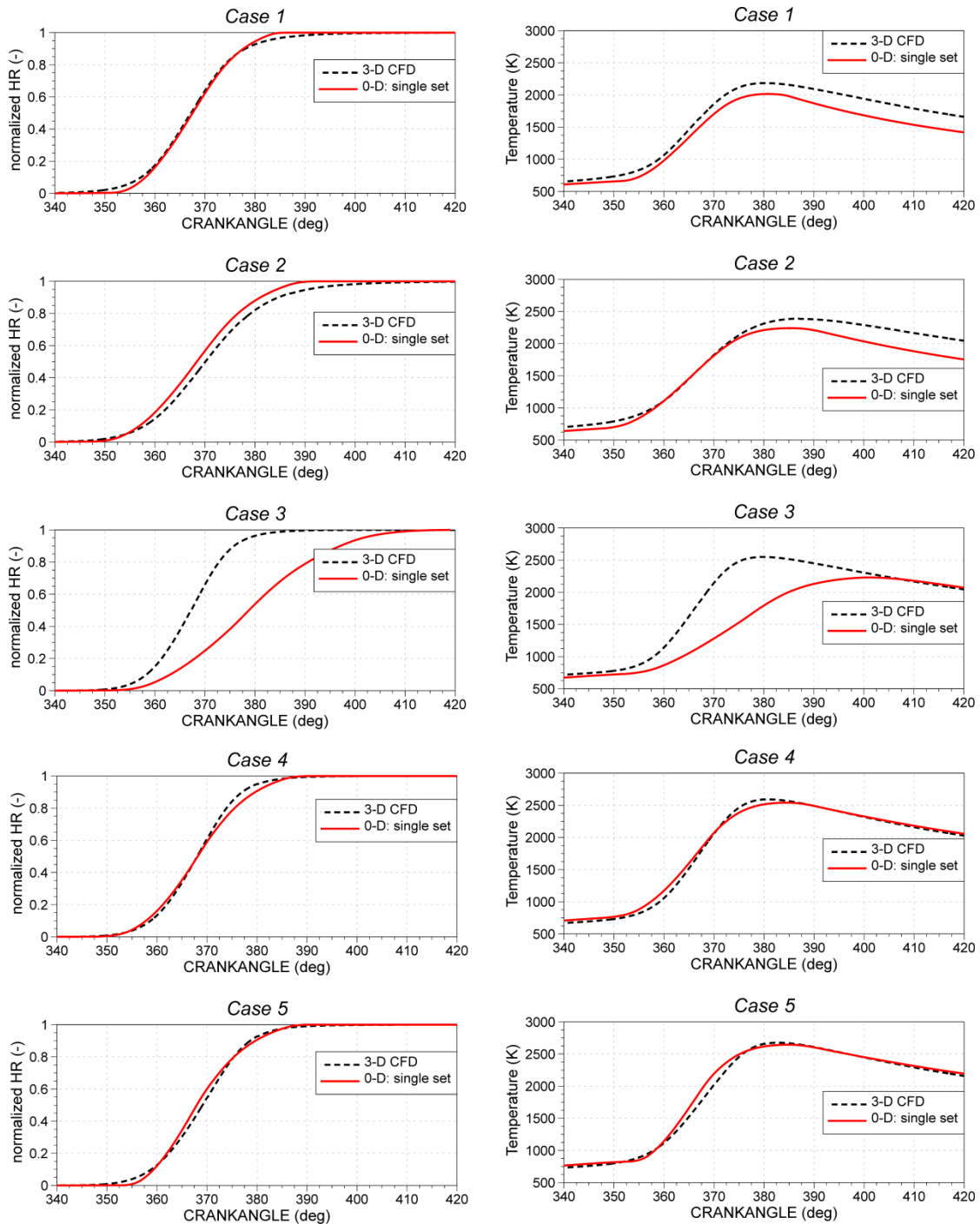


Figure 68. Normalized heat release (left) and in-cylinder temperature (right) of Engine 4 obtained by application of single set of constants.



The application of the single set of constants to Engine 4 shows that the achieved results are very close to the 3-D CFD results if the results of *Case 3* are not considered. The slow combustion progress and lower in-cylinder temperature in *Case 3* of Engine 4 that can be observed in Figure 68 are caused by the slightly lower initial turbulent kinetic energy (see Figure 64) and by the introduction of a linear function that approximates the upper limit of fractal dimension. As can be seen in Figure 60, to achieve the combustion progress of this operating point that is close to the 3-D CFD result, the upper limit of fractal dimension had to be significantly higher than the linear profile defined by the proposed equation (5.5).

In order to estimate the prediction of combustion phasing with the application of the single set of constants, the relative crank angle (after SOI) when the 50 % of in-cylinder mass is burned is plotted and the 0-D results are compared with the 3-D CFD data in Figure 69. If the previously mentioned operating points (*Case 2* of Engine 3 and *Case 3* of Engine 4) are neglected, the combustion phasings obtained by 0-D simulation are in a very good agreement with the reference 3-D CFD results.

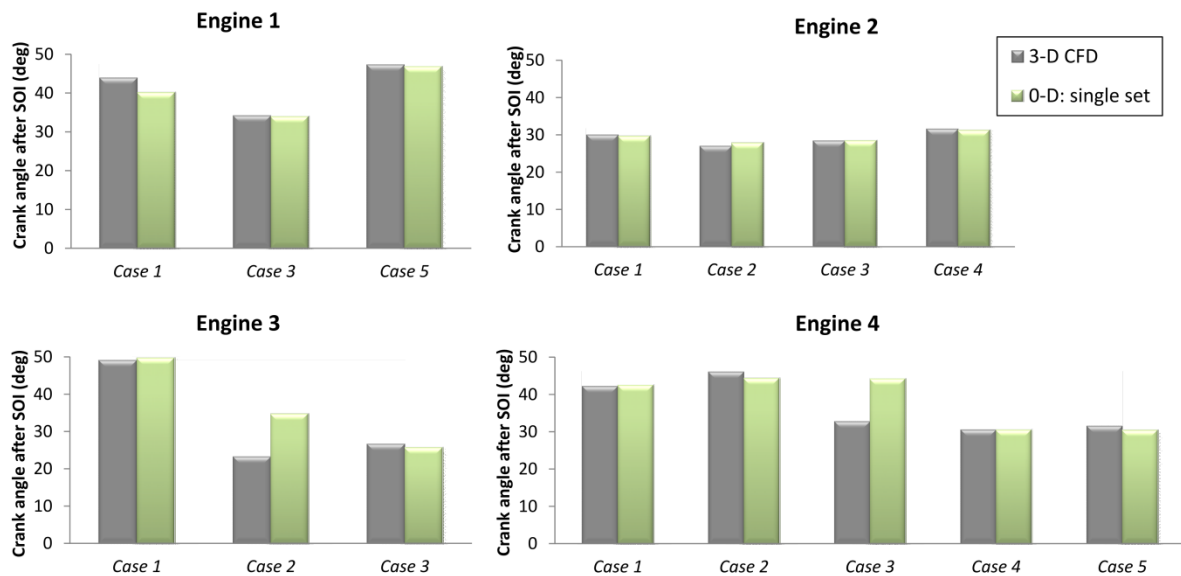


Figure 69. Relative crank angle position after start of ignition (SOI) at which the 50 % of in-cylinder mass is burned (CA50); comparison of 3-D CFD results and 0-D simulation results with the single set of constants.

## 5.7. Overview of validation with 3-D CFD results

In this chapter, the validation of the developed sub-models for modeling of turbulence, ignition and combustion phenomena was performed in which the 0-D simulation results were compared with the available 3-D CFD data. First, the developed single and two zone  $k-\varepsilon$  turbulence models were validated during the high pressure cycle and during the combustion

with the initial conditions of turbulent kinetic energy at IVC specified from 3-D CFD results. The two user-defined turbulence constants, the dissipation constant of the high pressure cycle  $C_\varepsilon$  and the dissipation constant of unburned zone  $C_\varepsilon^{UZ}$ , were manually tuned to achieve the 0-D results of (total and unburned zone) turbulent kinetic energy close to the 3-D CFD results. In order to achieve the combustion progress that matches well the 3-D CFD data, the combustion model constants ( $f_{D3,max}$ ,  $c_{ign}$  and  $r_{f,ref}$ ) were manually calibrated for each operating point of the engine. It was shown that the two zone turbulence model better predicts the profiles of in-cylinder temperature where the wall combustion mode of burning rate can be fully omitted. After that, the full cycle  $k-\varepsilon$  turbulence model was applied in order to eliminate the model dependence on the initial conditions that have to be specified at IVC. The 0-D simulation results were validated with the 3-D CFD results during the entire cycle and two user-defined constants, the intake  $k$  production constant  $S_{in}$  and the intake  $\varepsilon$  production constant  $C_{in}$ , were calibrated for each operating point of the engine. In order to reduce the number of user-defined constants that have to be tuned for each operating point, the modified fractal combustion model, that includes the quasi-dimensional ignition model, modified transition from laminar to fully developed turbulent flame and two zone turbulence model, was applied. After that, the analysis of turbulence and combustion model constants that were manually tuned for each operating point was performed and the parameterization of turbulence model constants and of the upper limit of fractal dimension were proposed. The optimization process of turbulence model constants resulted in the single set of constants that can produce the in-cylinder turbulence level during the expansion close to the 3-D CFD results at different operating conditions of an engine. The proposed linear function for the approximation of the upper limit of fractal dimension represented by equation (5.5) was applied and the achieved results with the single set of combustion constants are compared with the 3-D CFD results showing a very good agreement with 3-D CFD results.

Due to the robustness and low computational time of the presented cycle-simulation model, the analysis of certain operating parameter (e.g. ignition energy, spark plug design, intake pressure, temperature, etc.) can be performed for the entire operating range of the engine with the single set of constants regarding the turbulence, ignition and combustion sub-models.

## **6. Validation of cycle-simulation model with the experimental data**

The validation of the cycle-simulation model with the 3-D CFD results ensures that the constants of particular sub-models can be correctly specified and that particular sub-models give correct predictions of specific physical quantity. On the other hand, such procedure requires that a 3-D CFD model of the considered engine is made and that the simulation of the combustion process for defined operating points is performed. From the user point of view, building of a 3-D CFD model and of a cycle-simulation model of the considered engine is very complex and takes a lot of time.

In order to show the direct application of the cycle-simulation model using the developed sub-models without any 3-D CFD data, the experimental results of Waukesha CFR F4 for several operating points were analyzed and used for the validation. The constants of developed sub-models were specified according to the previous experience where the cycle-simulation results were compared to the 3-D CFD data of four SI engines at different operating conditions.

In real operating conditions of SI engine, the stochastic nature of the in-cylinder flow and turbulence causes the oscillations of individual engine cycle. This behavior is known as cycle-to-cycle variation (CCV) and significantly influences the engine performance and exhaust gas emissions. In order to simulate this phenomenon, the specific approach is proposed and the obtained cycle-simulation results are compared to the experimental data at several operating points of the experimental CFR engine fueled by gasoline.

### **6.1. Cycle-to-cycle variations, background and modeling**

In the real SI engine, even with imposed constant boundary conditions, the instantaneous combustion rate of the individual engine cycle shows non-repeatable behavior known as cycle-to-cycle variation (CCV) in combustion. The cyclic dispersion of the combustion process is usually described by the coefficient of variation (CoV) of indicated mean effective pressure (IMEP). For the cases where the CoV of IMEP exceeds 5 % individual cycles are significantly different than the statistically-averaged mean cycle. Particular cycles presented by higher IMEP than the mean value may reach extreme conditions with the occurrence of knock while the cycles with lower IMEP may reach misfire condition [100]. The upper and lower conditions usually presented by knock and misfire cycles have significant influence on the fuel consumption and exhaust emissions. On the other

hand, the current trend in legislation towards the reduction in fuel consumption and CO<sub>2</sub> emissions leads to increased use of new SI engine technologies, such as downsizing, charging, direct-injection etc. In order to exploit the full potential of these technologies simulation tools are increasingly used in their development and optimization. Since the new SI engine technologies influence the combustion process, modeling of the CCV in combustion is required.

The SI engines are affected by the effect of CCV in combustion because the combustion process is strongly dependent on the in-cylinder fluid motion and turbulence that oscillate from cycle-to-cycle. In general, the main sources of CCV have been identified by the number of physical factors: the stochastic nature of the in-cylinder fluid motion, variation of in-cylinder turbulence level and mixing of fuel, air and residual gases [29]. Variations of these factors are shown in the initial kernel growth rate, in shifting of the flame center from the spark plug location and in the turbulent burning rate. For the correct prediction of CCV in combustion all mentioned effects should be taken into account. Although the cycle-to-cycle variations have been investigated for many years, the available information regarding the causes for CCV is relatively limited and detailed overview of many CCV related issues is given in [101]. The work presented in [30-32] demonstrates that the oscillations in the mixture composition are not the dominant factor that causes the CCV in combustion. The main conclusion of the work presented in [31, 32] is that the oscillations in the in-cylinder turbulence between individual cycles is the most influencing factor responsible for CCV in combustion. The variations in the burning rates observed in [102] have been entirely attributed to the variations in the in-cylinder turbulence whose distribution is approximately Gaussian. For higher in-cylinder turbulence levels and for non-stoichiometric mixtures the oscillations of the burning rate were found to increase. The initial flame kernel growth as well as the fully developed turbulent flame highly depends on the turbulence properties. It is stated in [103, 104] that the initial flame kernel growth is responsible for up to 50 % of total CCV. In the early 1950's during the experiment conducted in the wind tunnel it was observed that the distribution of burning rate of a free turbulent flame is approximately Gaussian [102]. For stronger turbulence and non-stoichiometric mixtures the variance of combustion was found to increase. Moreover, from the analysis of experimental results presented in [74, 105] it can be concluded that the distribution of burning rates at specific time as well as the turbulence intensity in the vicinity of the spark location are very close to the Gaussian. It has been concluded [74, 105] that the variations in turbulence intensity have a dominant factor on the combustion variations.

Nowadays, the researchers all over the world are investing a great effort in development of cycle-simulation models with more and more details included into the models, such as gas exchange, turbulence, combustion, wall heat transfer, emissions, knock, etc. The cycle-simulation models are usually based on 1-D finite volume method for the calculation of flow through the pipes, while the 0-D approach is applied to the engine cylinder. Therefore, the cycle-simulation models are often called 0-D/1-D [2, 3] models and are used for rapid and robust evaluation of key engine parameters. The most popular combustion models within the cycle-simulations are well known quasi-dimensional combustion models [30-32, 103] that take into account the flame front propagation across the combustion chamber typical for combustion process in SI engines. The cycle-simulation models enable fast and low demanding simulations with limited details of flow and combustion, especially compared to the 3-D CFD solutions. By introduction of more comprehensive sub-models into the cycle-simulations the analysis and simulation of detailed physical phenomena becomes possible with reasonable computational effort. A common practice in 3-D CFD modeling is to use the RANS approach based on time averaging of the flow data, which is not suitable when one tries to model CCV caused by stochastic nature of the in-cylinder flow. As the computer power is getting more and more increased, the application of more detailed modeling with 3-D CFD is becoming possible. The Large Eddy Simulation (LES) approach can resolve the large scales of turbulence and the related non-linear interaction between the turbulent eddies. Therefore, LES is suitable for calculating individual engine cycles and for improving the understanding of the CCV phenomena [36, 106, 107]. The most commonly used approach for modeling of CCV within the cycle-simulations models is based on imposing the perturbations of certain model parameters from cycle-to-cycle. The perturbations of certain model parameters are defined by analyzing the experimental pressure traces or 3-D CFD simulation results. This is mainly done by specifying perturbations of turbulence and/or combustion model constants from cycle-to-cycle [30-32, 36, 108, 109]. Modeling of CCV by using the cycle-simulation presented in [2] was performed by perturbations of one turbulent and two combustion model constants. The perturbations of model constants were set so that the best match of individual pressure traces is achieved. After that, the specific cross-correlations between the turbulence and combustion parameters were derived and analyzed.

## **6.2. Modeling of CCV using cycle-simulation model**

The numerical analysis of the CCV phenomena presented in this chapter is performed by using the cycle-simulation of AVL BOOST. For modeling of the in-cylinder turbulence the

newly developed  $k$ - $\varepsilon$  turbulence model presented in Chapter 2 is employed, while the combustion process is simulated by the modified fractal combustion model that includes the ignition sub-model, modified transition from laminar to turbulent flame and two zone turbulence sub-models (Chapter 5.3). The early flame kernel growth is modeled by the new quasi-dimensional ignition model (QDIM) that is integrated into the fractal combustion model and is based on the AKTIM ignition model [28] commonly used in 3-D CFD simulations. The CCV in calculation of combustion will be produced by the predefined perturbation of one turbulence production constant and by the perturbation of flow angle at the spark plug from cycle-to-cycle. The perturbation of turbulence production constant follows the normal (Gaussian) distribution around the mean value, while oscillation of the flow angle follows a uniform distribution assuming that the flame kernel can be shifted in any direction in the cylinder, as analyzed in [103]. The experimental pressure traces will be used for tuning of combustion parameters as well as for the tuning of mean value and standard deviation of turbulence production constant. The statistical analysis of experimental and simulation results will be performed on the sample size of 300 cycles.

The study is performed on the Waukesha CFR F4 engine fueled by gasoline (91 octane rating taken from the gas station in California). In the analysis the operating points that have different spark timings capturing the effects of low and high CCV in combustion are used. Based on this engine the simulation model will be set up that uses the proposed approach in modeling of CCV. The statistical analysis of indicated mean effective pressure (IMEP) and normalized HR when the specific value of mass fraction burned is reached will be performed for both the experimental and the simulation cases, and the results will be compared. At the end, the different relative standard deviations of the turbulence production constant will be analyzed and the variation of flow angle from cycle to cycle will be introduced into the cycle-simulation model.

### 6.2.1. Experimental setup

The experimental results that have been considered and analyzed in the presented study were obtained on the single cylinder Waukesha CFR F4 engine whose experimental setup is shown in Figure 70. The engine is equipped with the fuel injector at the intake pipe producing the premixed mixture that is close to the homogeneous one. The air equivalence ratio of the mixture is measured by the lambda sensor in the exhaust pipe while the engine management (fuel injection and spark timing) is performed by a programmable *MOTEC M4* engine-control unit (ECU). The measurement of instantaneous in-cylinder and intake pressure

was performed using a piezoelectric *Kistler 6052B* pressure transducer (PT) with the recording resolution of  $0.1^\circ$  CA. The intake PT is located 110 mm upstream of the intake valve shown in Figure 70.

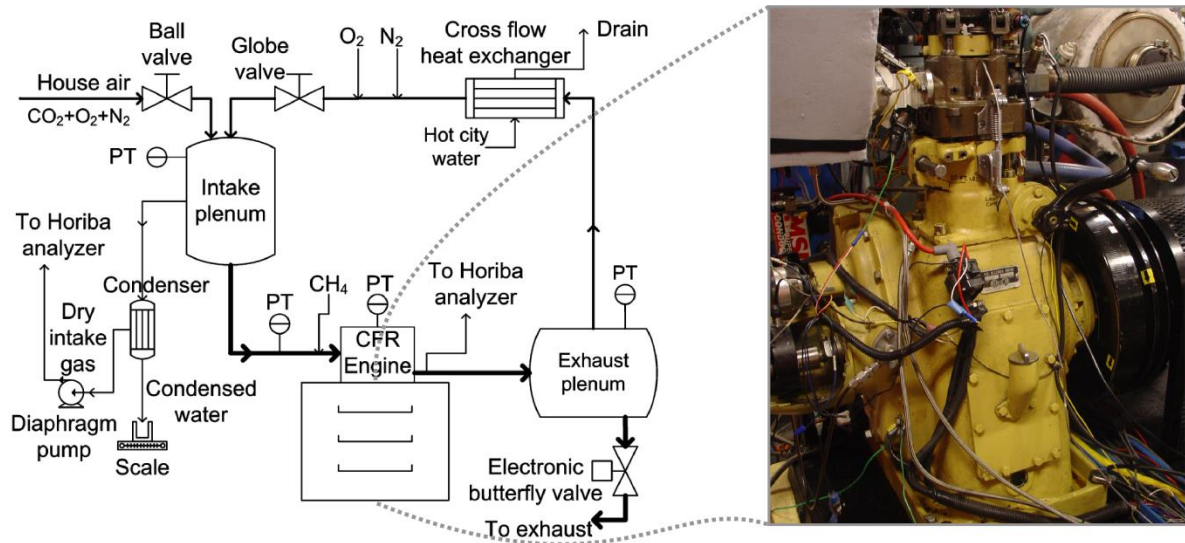


Figure 70. Layout of experimental setup (left) [110] of single-cylinder Waukesha CFR F4 engine (right) from Combustion analysis Laboratory of University of California - Berkeley.

The intake and exhaust plenums are used to damp pressure oscillations and to ensure homogeneous mixtures. For the measurement of intake temperature, the K-type thermocouples were used [110], while the fuel consumption was measured using the digital scale also shown in Figure 70. The entire management of the engine and data acquisition are performed using the *LabView* code. The experimental setup is also equipped with the *Horiba* analyzer for exhaust gases, but the analyzer was not used because the exhaust gas emissions were not the objective of presented study. The spark plug in Waukesha CFR F4 engine has been mounted close to the cylinder liner in order to obtain a long distance of flame front propagation across the combustion chamber, as a typical precondition for the occurrence of knock. The main engine parameters are summarized in Table 17.

Table 17. General specifications of the experimental Waukesha CFR F4 engine

Stroke	114.3 mm
Bore	82.65 mm
Connecting Rod Length	254 mm
Compression Ratio	4:1 to 17.5:1
Number of Valves	2
Exhaust Valve Opens	$50^\circ$ CA BBDC
Exhaust Valve Closes	$15^\circ$ CA ATDC
Intake Valve Opens	$15^\circ$ CA BTDC
Intake Valve Closes	$130^\circ$ CA BTDC

## 6.2.2. Engine operating conditions and data processing

The main objective of the presented study is the analysis and modeling of CCV in combustion using the significantly improved cycle-simulation model that includes the newly developed sub-models for modeling of turbulence, ignition and combustion phenomena. Therefore, four measured engine operating points, specified in Table 18, have been considered representing the spark sweep which captured low and high CCV in combustion. The first two letters of the operating point name denote "Spark Time", while the number behind the letters represents specified spark time expressed in the crank angle degrees BTDC. In order to avoid the knock combustion of high intensity, the adopted compression ratio is relatively low, while the intake pressure and temperature are set to the ambient conditions simulating the naturally aspirated engine fueled by gasoline. The stoichiometric mixtures have been considered as the most common mixtures in today's SI engines.

Table 18. Main parameters of considered engine operating points

<i>Name of Operating Point</i>	<b>ST5</b>	<b>ST10</b>	<b>ST15</b>	<b>ST20</b>
Spark Timing (° CA BTDC)	5	10	15	20
IMEP (bar)	6.52	7.31	7.87	8.15
Compression Ratio (-)	8			
Ave. Intake Pressure (bar)	1.013			
Intake Temperature (° C)	32			
Excess Air Ratio (-)	1.0			
Engine Speed (rpm)	900			

For each operating point the in-cylinder pressure traces of 300 cycles have been recorded with the resolution of  $0.1^\circ$  CA (sample rate of pressure sensor is 54 kHz at considered engine speed of 900 rpm). The offline application for the pressure data filtering (Savitzky-Golay filter) and calculation of rate of heat release was applied on the measured results. In order to calculate the rate of heat release for each individual cycle, the first law of thermodynamic is applied and the difference between instantaneous in-cylinder pressure and the measured one on the motored case has to be defined. In addition, the heat transfer is approximated with the Woschni correlation, while the gasoline composition is declared as consisting of isooctane, n-heptane and ethanol in the volume fractions in liquefied gasoline 79 %, 13 % and 8 %, respectively. For the statistical analysis of the combustion progress that will be shown in the following sections, the statistical results of CA5, CA10, CA50 and CA90 from the experimental data are defined.



Experimental results of the cycle-resolved in-cylinder pressures for all considered operating points are shown with the black lines, while the 300 cycles averaged pressures are shown with the red lines in Figure 71. The experimental results of the in-cylinder pressure show that IMEP increases with the advanced ignition timing, while the CoV of IMEP decreases.

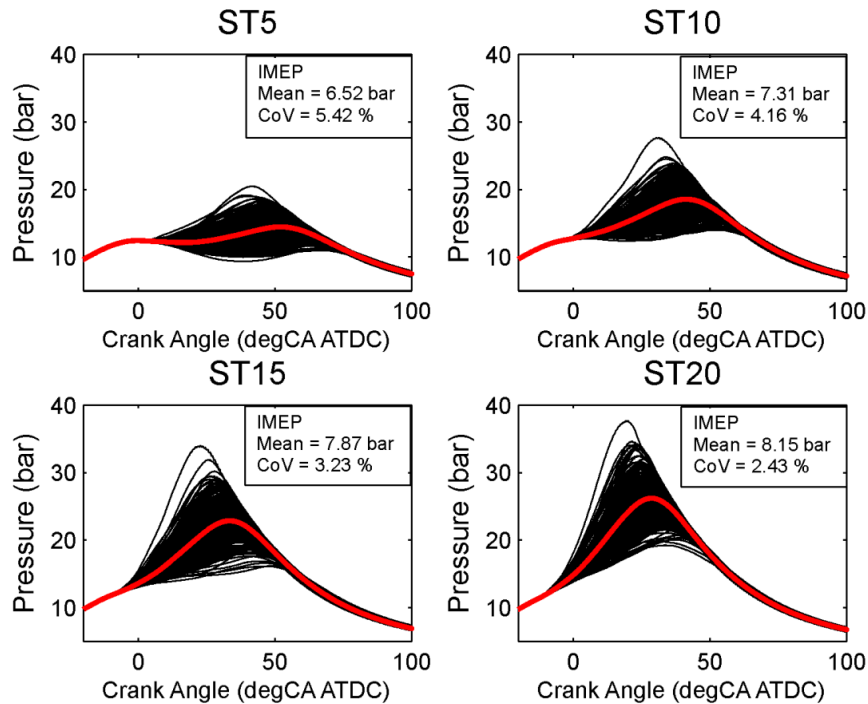


Figure 71. Experimental cylinder pressure traces for all considered operating points; black lines are individual cycle-resolved data, red lines represent averaged data (sample size = 300 cycles).

### 6.2.3. Cycle-simulation model

The cycle-simulation model of the experimental CFR single-cylinder engine made in AVL BOOST [111] is shown in Figure 72. It consists of intake (1) and exhaust pipe (2 and 3), cylinder (C1), intake (SB1) and exhaust system boundary (SB2), restrictor (R1) at the exhaust pipe and engine interface (EI1). Since the intake pressure profile is available from the experiment, the simulation model is significantly reduced with the intake system boundary (SB1) condition of pressure set from experimental data, as it is shown in Figure 72. Therefore, the length of the intake pipe within the simulation is set to 110 mm. That corresponds to the location of intake pressure transducer in the experiment (Figure 70). The majority of the engine parameters are specified in the cylinder data group including the engine geometry, combustion, heat transfer and valve port specifications.

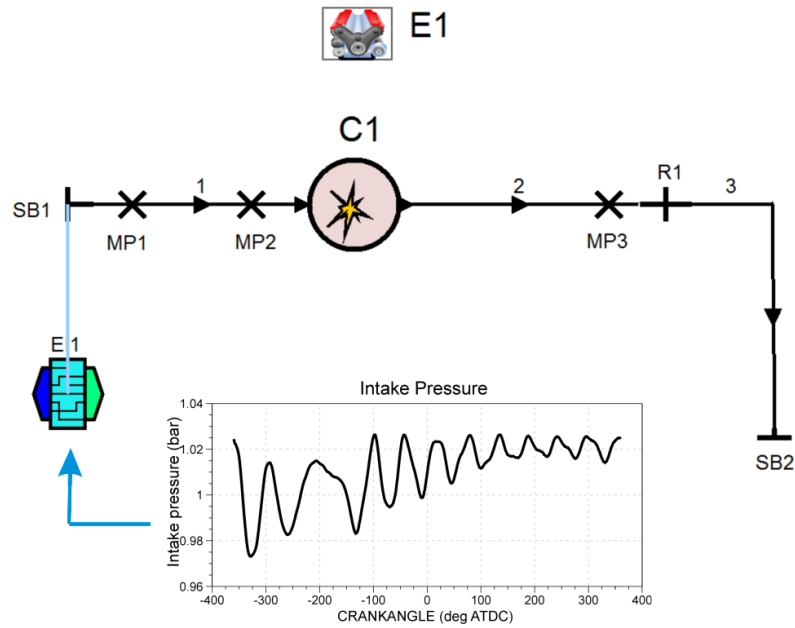


Figure 72. Reduced cycle-simulation model of CFR engine in AVL BOOST with the imposed intake pressure obtained by measurement.

In order to capture the effects of variability of the early flame kernel growth that lasts only a few crank angle degrees, the simulation step size is set to  $0.25^\circ$  of crank angle. The simulation interval is set to 320 cycles. The first 20 cycles are simulated with the constant value of turbulence production constant to achieve the converged solution, while the remaining 300 cycles take into account the perturbation of the turbulence production constant and only these cycles were used in the statistical analysis. By using this approach, numerical errors due to un-converged solutions were reduced to a minimum level.

A number of comprehensive studies [29, 74, 103, 112, 113] have attempted to model the cyclic variability in SI engines using separate sub-models for ignition, combustion and turbulence. Different input parameters such as air to fuel ratio, shifting of kernel center, turbulence, residual gas fraction, etc. have been varied as random variables, computed from the results obtained in previous cycles, or some combination of both methods is used. If the cycle-simulation model is detailed enough to correctly predict particular effects and their interaction (e.g. turbulence-combustion) the CCV of a certain input parameter may produce CCV in combustion, as it can be observed in the experiment. In the study presented in [2] perturbations of particular model parameters (turbulence and combustion) have been defined by the optimization process in which the best match of experimental pressure traces has been obtained. In the conclusion of [2] it is stated that such detailed method is time demanding, especially for the large number of simulated cycles, whereas the tendency is to reduce the number of variables and speed up the whole simulation process.

### 6.3. Cycle-averaged results

Before the simulations of CCV in combustion are performed, it was necessary to adjust the model constants for the prediction of heat transfer and blow-by flow so that the best agreement of simulated and the experimental in-cylinder pressure in the motored case is achieved. The experimental pressure trace of the motored engine that was used for calibration of the model constants was defined as cycle-averaged result over 300 motored cycles because CCV in the in-cylinder pressure occurs even under the motored conditions [105]. After that four operating points have been analyzed (Table 18) and simulations of 300 cycles with CCV in combustion have been performed. The sample size of 300 cycles for the statistical analysis and for the cycle-averaging was chosen according to the recommendations given in [37]. The procedure contained the processing of the cycle-averaged results and comparison of cycle-simulation results with the available experimental data. After that, the comparison of cycle-resolved results and statistical analysis of both experimental and simulation results were performed.

A number of different parameters can be used as the measure of cyclic variability in an engine, where the most commonly used parameters are [32, 39, 114]:

- Indicated mean effective pressure (IMEP);
- Maximum in-cylinder pressure or the pressure taken at specific crank angle;
- The crank angle at which the maximum or specific pressure occurs;
- The pressure rise rate;
- The time at which the flame arrives at specific point inside the cylinder;
- Ignition delay period;
- The crank angle at which the certain portion of in-cylinder mass is burned.

For any of these parameters an appropriate standard deviation (StD) and coefficient of variation (CoV) can be defined. Within the present study, the indicated mean effective pressure, the maximum in-cylinder pressure, the crank angle position of maximum in-cylinder pressure and the crank angle when the 5 %, 50 % and 90 % mass is burned (CA5, CA50 and CA90) were used as the parameters in the validation of cycle-simulation results with the experimental data.

The first step in modeling of CCV in combustion was to determine the adjustable constants of ignition, turbulence and combustion model so that the simulated pressure curve and normalized HR (heat release) matched well the experimental ones on the averaged cycle,

in all considered operating points. The comparisons of simulated and measured in-cylinder pressures and normalized HR are shown in Figure 73.

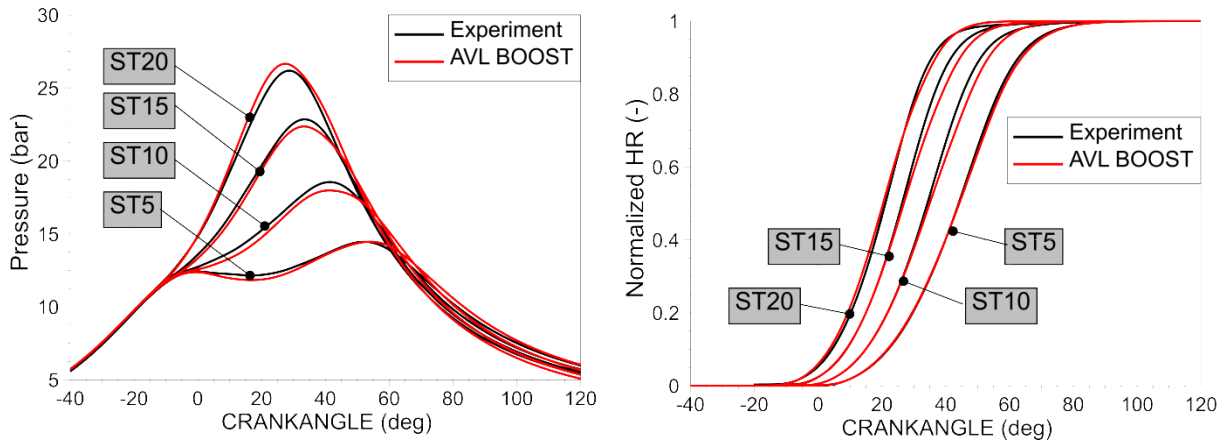


Figure 73. Comparison of experimental and simulation results of averaged cycle for all considered operating points. The left diagram shows the in-cylinder pressure, while the right diagram shows normalized HR.

Figure 73 shows that the simulated cycle-averaged data match well the experimental data even with the single set of adjustable model constants for all operating points. The only difference in model input constants between these four points is in a definition of spark timing. Since the experimental results of the in-cylinder turbulence and flow were not available, the adjustable turbulence model constants were defined according to the previous experience [52, 115], while the adjustable constants of the flame kernel and the combustion model were set so that the simulation results of pressure and normalized HR match well the experimental cycle-averaged data.

Table 19. The peak pressure and corresponding crank angle in experiment and cycle-simulation

		$p_{MAX}$ -mean (bar)	$p_{MAX}$ -position ( $^{\circ}$ CA)
<b>ST5</b>	Experiment	14.46	52.2
	AVL BOOST	14.46	54.0
<b>ST10</b>	Experiment	18.55	41.4
	AVL BOOST	17.98	41.0
<b>ST15</b>	Experiment	22.85	33.4
	AVL BOOST	22.36	33.0
<b>ST20</b>	Experiment	26.19	28.9
	AVL BOOST	26.66	27.0

The values of peak pressure and the corresponding crank angle that are defined from the calculated cycle-averaged pressure (shown in Figure 73) are compared with the experimental

data in Table 19. The predictions of both, peak pressure and its position, are very close to the experimental results at different spark timings. The simulation results shown in Figure 73 and Table 19 present the capability of the cycle-simulation model to capture the effects of different spark timing on the averaged-cycle level, by the application of single set of model parameters. The calibration of model parameters was a necessary step before the perturbations of turbulence production constant were imposed on the model, simulating the CCV in combustion. The overview of the adjusted ignition, turbulence and combustion model constants is given in Table 20.

Table 20. Overview of the cycle-simulation model constants

Operating Point	ST5	ST10	ST15	ST20
	<i>Ignition Model (QDIM)</i>			
$\delta$ (mm)	0.15			
$r_0$ (m)	0.008			
$k_w$ (W/m <sup>2</sup> K); $T_{SP}$ (K)	2000; 500			
	<i>k-ε Turbulence Model</i>			
$S_{00}$ (-); $S_{10}$ (s/m)	0; $1 \cdot 10^{-6}$			
$C_{00}$ ; $C_{10}$ (bar <sup>-1</sup> )	3.50; - 1.80			
$C_\epsilon$ ; $C_\epsilon^{UZ}$ ; $C_2$ (-)	2.30; 6.00; 1.92			
	<i>Fractal Combustion Model</i>			
$C_3$ (-)	1.034			
$C_\tau$ (-)	1.00			

#### 6.4. Cycle-resolved results

As it is mentioned earlier, the CCV in combustion was modeled by the perturbation of the intake turbulence production constant  $S_{10}$  that affects the progress of turbulent kinetic energy during the intake process and consequently the remaining part of the engine cycle. For the simulation of 320 engine cycles the computational time was about 50 minutes per operating point on one processor (Intel Xeon E5-1620) of 3.6 GHz.

The simulation model was made so that the first 20 cycles were simulated with the constant (mean) value of intake turbulence production constant  $S_{10}$  in order to achieve converged solution and to avoid the numerical errors in the statistical analysis. The remaining 300 cycles were calculated by imposing the perturbation of intake turbulence production constant  $S_{10}$  around the mean value (shown in Table 20), by the user-defined relative standard deviation  $\sigma_{rel, S_{10}}$ , which was set to 0.14. The relative standard deviation  $\sigma_{rel, S_{10}}$  of turbulence

production constant  $S_{10}$  is defined as the ratio between the standard deviation ( $\sigma_{S_{10}}$ ) and mean value of the turbulence production constant ( $\bar{S}_{10}$ ). The distribution of intake turbulence production constant  $S_{10}$  around the mean value (specified by the user) is shown in Figure 74. In Figure 74 the variation of intake turbulence production constant  $S_{10}$  from cycle-to-cycle can be observed.

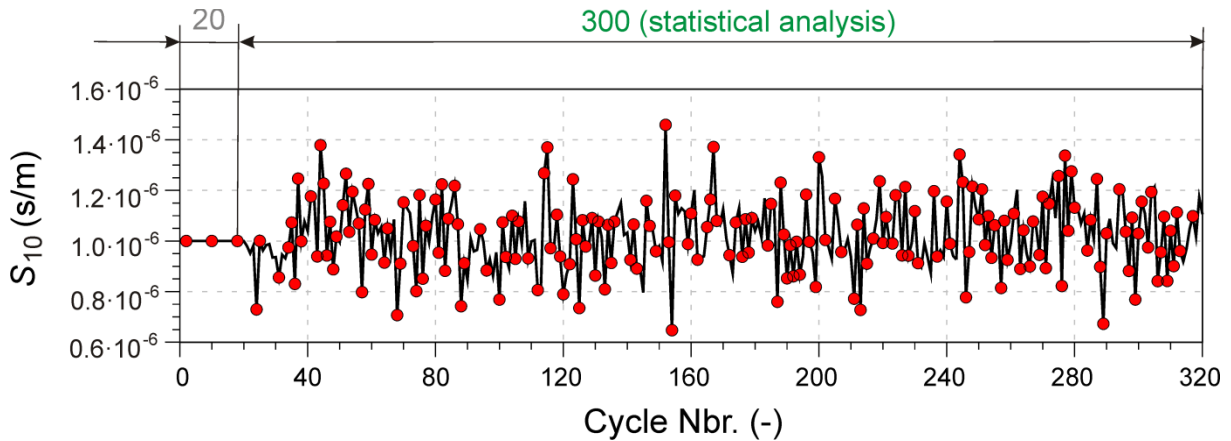


Figure 74. Variation of intake turbulence production constant  $S_{10}$  in calculation of operating point ST5 that reproduced cycle-to-cycle variations of in-cylinder turbulence.

When the value of  $S_{10}$  constant is lower the level of in-cylinder turbulence during the intake is also lower. This reduces the initial conditions of the turbulent kinetic energy and its dissipation rate at the start of high pressure cycle resulting in the lower in-cylinder turbulence intensity and lower integral length scales during the combustion. From equations (4.2) - (4.6) it is evident that in such case wrinkling of the flame front will be lower, reducing the overall burning rate. In terms of the flame kernel growth model, the lower in-cylinder turbulence will reduce the mean flow velocity in the vicinity of the spark plug. Therefore, the length of the electric spark between the electrodes will be decreased influencing the energy that kernel received from the secondary electric circuit of the ignition system. Furthermore, low mixture velocity in the vicinity of the spark plug is not able to shift the flame kernel away from the spark plug center and as a result higher heat loss will occur. This will finally result in the longer ignition delay period. It is obvious that the lower value of  $S_{10}$  increases the ignition delay period and slows down the turbulent combustion. When the value of  $S_{10}$  constant is higher there is an opposite effect; the ignition delay will be shortened and the main turbulent combustion will be faster.

### Statistical analysis of IMEP

The statistical results of the indicated mean effective pressure (IMEP) for the considered operating points, in both experiment and simulation, are summarized in Table 21. The changes of IMEP in the 300 cycle window for all operating points are plotted and compared with experiment in Figure 75. The comparison of the cycle-simulation and experimental results of IMEP shown in Figure 75 should not be performed for individual cycles, but the dispersion and statistics of simulated and experimental data should be considered. The mean value of IMEP obtained by the cycle-simulation model at all considered operating points is equal or slightly lower than in the experimental data. At operating points ST10, ST15 and ST20 the mean values of IMEP are under predicted for approximately 1 %. In terms of the prediction of IMEP standard deviation (StD) and coefficient of variation (CoV) the values for the ST5 and ST10 operating point are over predicted by 10 %, while the same values are equal or slightly under-predicted for the remaining two operating points (ST15 and ST20), as it can be seen in Table 21.

Table 21. Statistical results of IMEP in experiment and cycle-simulation made in AVL BOOST

		IMEP – Mean (bar)	IMEP - StD (bar)	IMEP - CoV (%)
<b>ST5</b>	Experiment	6.52	0.353	5.42
	AVL BOOST	6.51	0.387	5.95
<b>ST10</b>	Experiment	7.31	0.304	4.16
	AVL BOOST	7.24	0.338	4.68
<b>ST15</b>	Experiment	7.87	0.254	3.23
	AVL BOOST	7.76	0.254	3.27
<b>ST20</b>	Experiment	8.15	0.198	2.43
	AVL BOOST	8.09	0.149	1.84

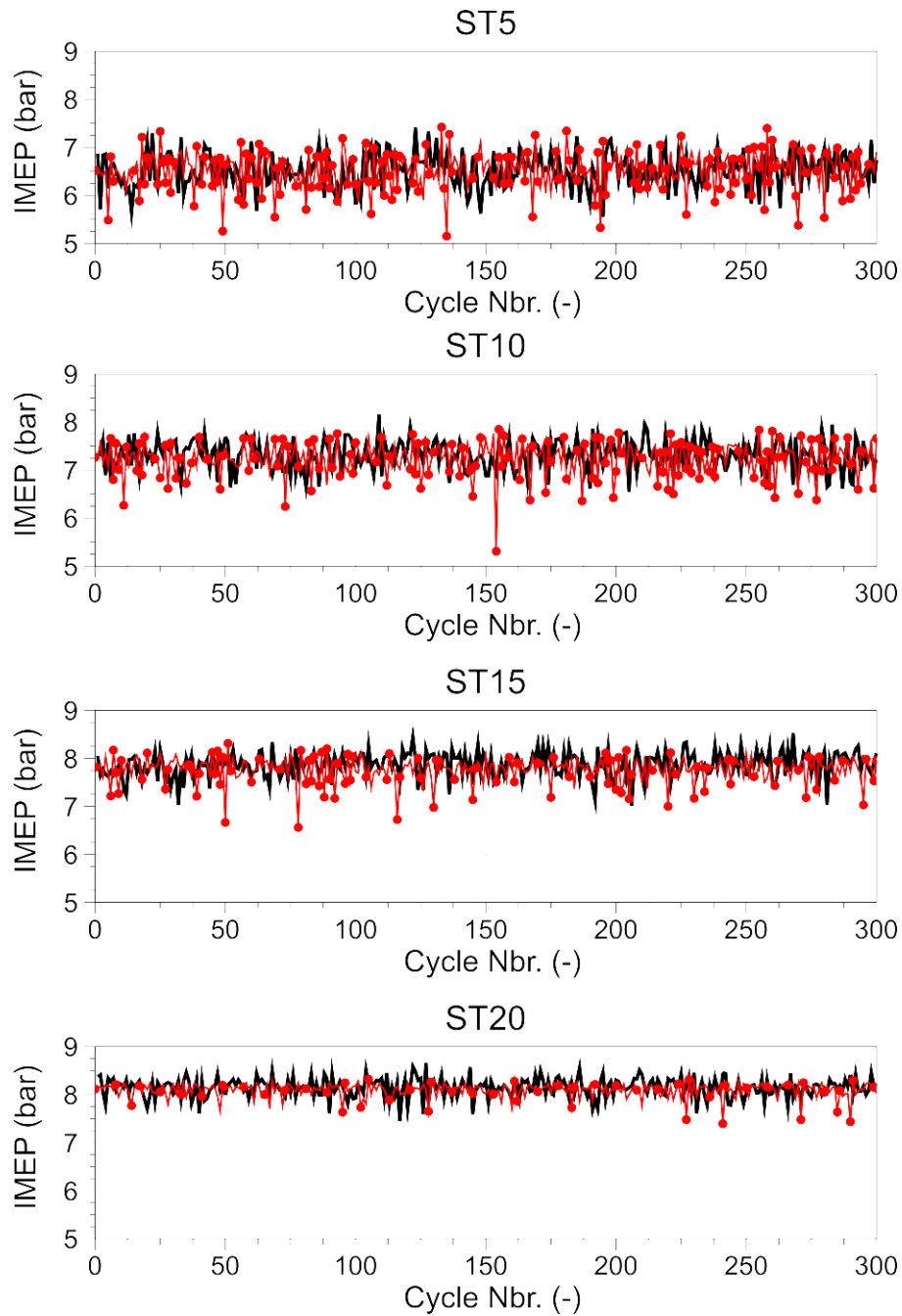


Figure 75. Comparison of simulation results (red line) with the experimental data (black line) of IMEP over the 300 cycles.

For the better analysis, the statistical results of IMEP specified in Table 21 are plotted in Figure 76. It seems that the overall trends in terms of statistical properties of IMEP are captured very well even though the cycle-simulation model parameters and standard deviation of the turbulence production constant  $S_{10}$  were kept constant for all operating points.



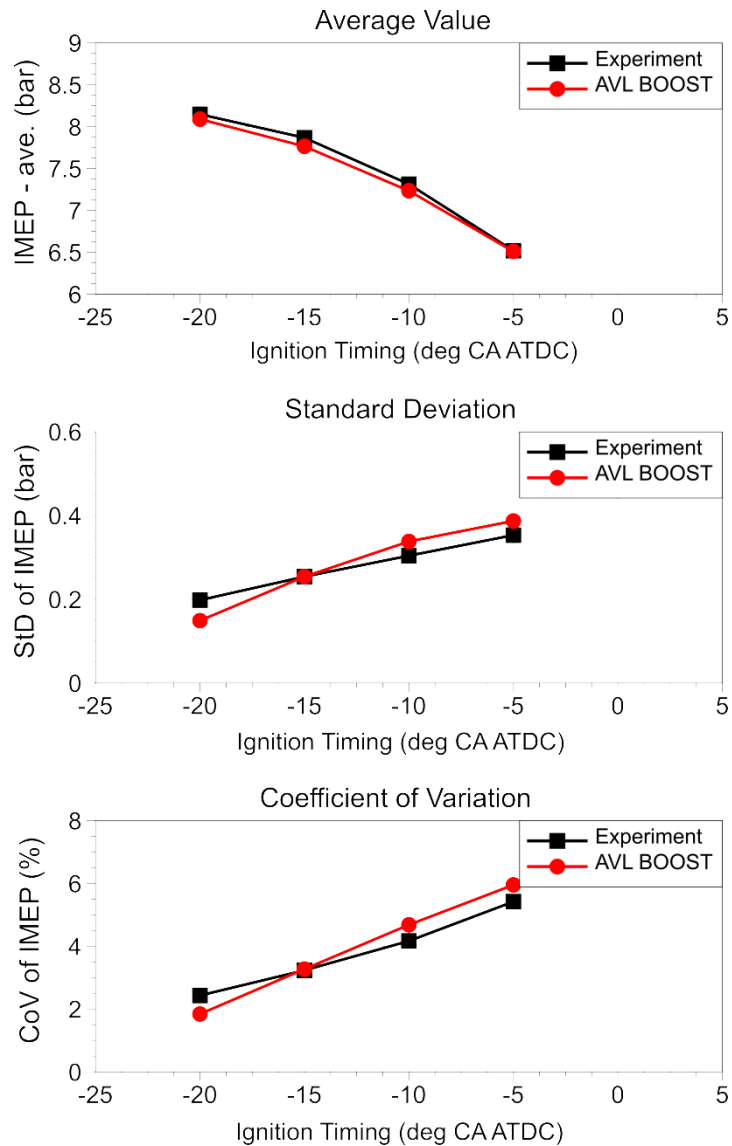


Figure 76. Comparison of experimental and cycle-simulation results of IMEP (average value), standard deviation (StD) and coefficient of variation (CoV) of IMEP.

### *Cycle-resolved results of in-cylinder pressure*

The cycle-resolved results of in-cylinder pressure obtained by experiment and simulation for 300 cycles are shown in Figure 77. The simulated pressure profiles at the late part of compression, prior to the ignition, matched well the measured in-cylinder pressure. This confirms that the model parameters for the calculation of gas exchange process, blow-by flow and heat transfer were defined correctly. The pressure profiles plotted in Figure 77 do not give the detailed information as the one obtained by the statistical analysis, but they give the general overview of the in-cylinder pressure dispersion at the considered operating points. In operating point ST10 it can be noticed that there is one simulated cycle whose pressure profile during expansion is significantly lower than the others and that such cycle is not

shown in the experiment. This is a result of dramatically reduced turbulence production constant that increased the period of flame kernel growth and slowed down the turbulent combustion. Beside that, the overall picture of the in-cylinder pressure oscillations shows very good fit with the experimental data; especially bearing in mind that the set of cycle-simulation model parameters and the standard deviation of the turbulence production constant were kept fixed for all considered operating points (Table 20).

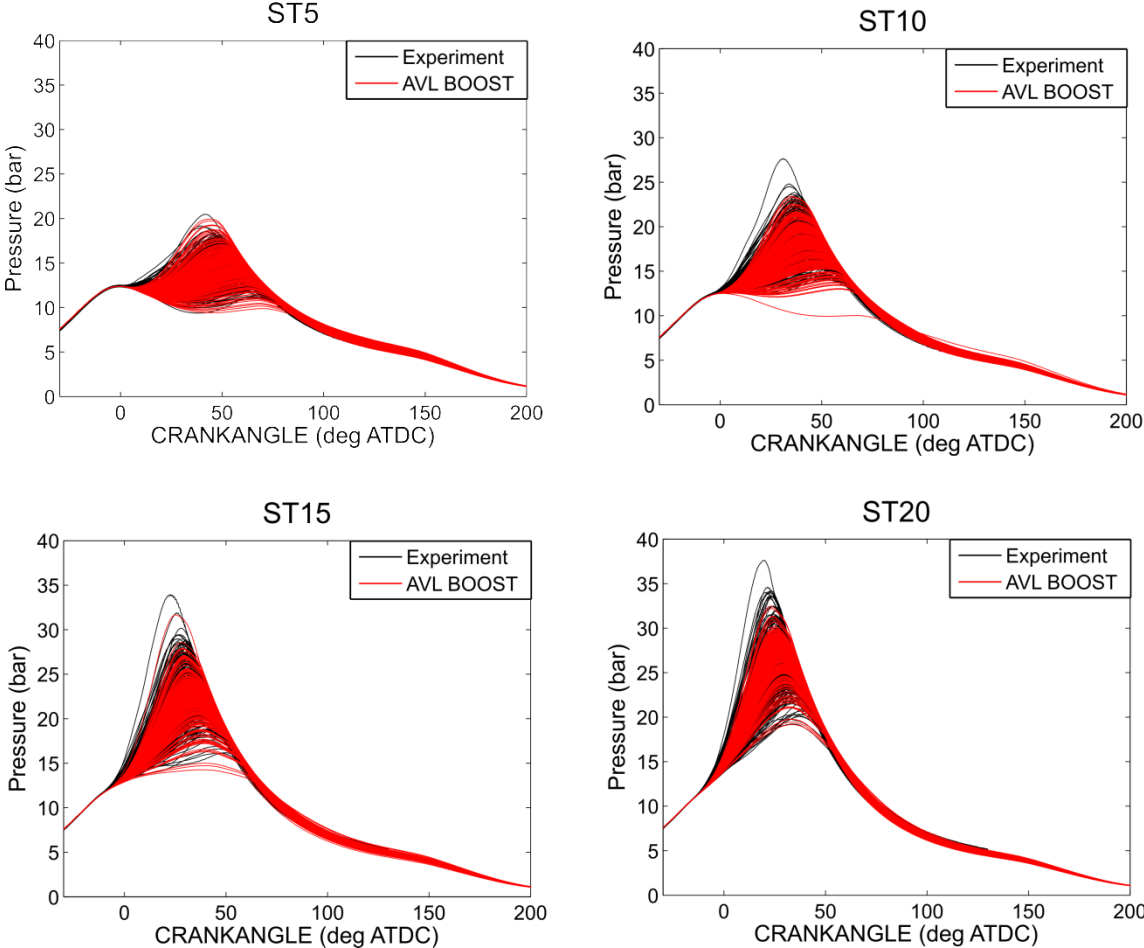


Figure 77. Comparison of experimental and simulation results of cycle-resolved in-cylinder pressure for all considered operating points and sample size of 300 cycles.

**Peak pressure positions**

More detailed results regarding the in-cylinder pressure are shown in Figure 78, where the value of peak pressure against its crank angle position is plotted for 300 simulated cycles and the results are compared with the experimental data. The cycle-simulation results are plotted with the red markers, while the experimental results are plotted with the black markers. From the experimental data of the operating point ST5 it can be seen that there are several cycles whose peak pressure positions are around the FTDC (firing top dead center). The oscillations of peak pressure around the FTDC observed in experiment, when the

combustion process is still negligible, can be described by the oscillations in the heat transfer during the compression stroke that are caused by the oscillations of in-cylinder temperature. Since the calculation of heat transfer used in the cycle-simulation model is based on the Woschni correlation [116] that is independent on the in-cylinder turbulence level, the mentioned oscillations of peak pressure around FTDC (caused by the oscillations of temperature) can not be captured. For all considered operating points the fronts generated by the plots of peak pressure against its crank angle, obtained by the cycle-simulation model, seem to follow the almost linear trend. In the case of experimental results a slight dispersion around the linear trend seems to be present. This effect could be explained by the presence of in-cylinder non-homogeneity in terms of mixture temperature, composition and turbulence including complex 3-D interactions between the flame and turbulent structures [117] that are not captured in the present cycle-simulation model. Modeling of the mixture stratification [81] in the cycle-simulation software AVL BOOST is possible, but it requires the input data that could be obtained either from 3-D CFD or by the assumption of mixture stratification. Due to simplicity of the cycle-simulation model and unavailability of the 3-D CFD results the mixture stratification was not considered in this study.

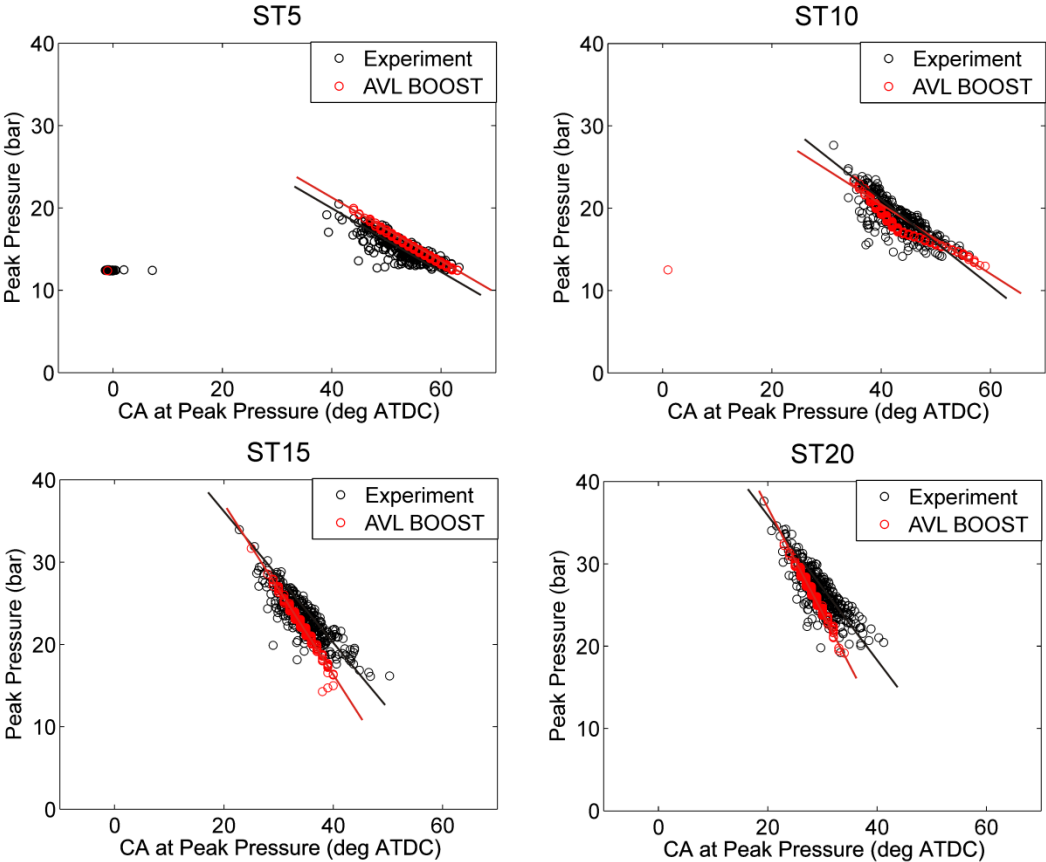


Figure 78. Experimental and cycle-simulation peak pressure plotted against crank angle at peak pressure (sample size = 300 cycles).

The trends of peak pressure position are also shown in Figure 78 with the black (experiment) and red (simulation) solid lines. It can be seen that the slope of experimental lines is larger as the spark is advanced and such behavior is captured with the cycle-simulation.

### *Cycle-resolved and statistical results of normalized HR*

In order to perform the analysis of the combustion process, the normalized HR has been considered. The black lines in Figure 79 represent the cycle-resolved experimental data obtained by processing the measured pressure traces, while the red lines are calculated cycle-resolved results of normalized HR, also known as mass fraction burned. Similarly to the cycle-resolved results of the in-cylinder pressure, the cycle-resolved results of normalized HR, shown for all considered operating points in Figure 79, give the qualitative picture about the CCV in combustion process.

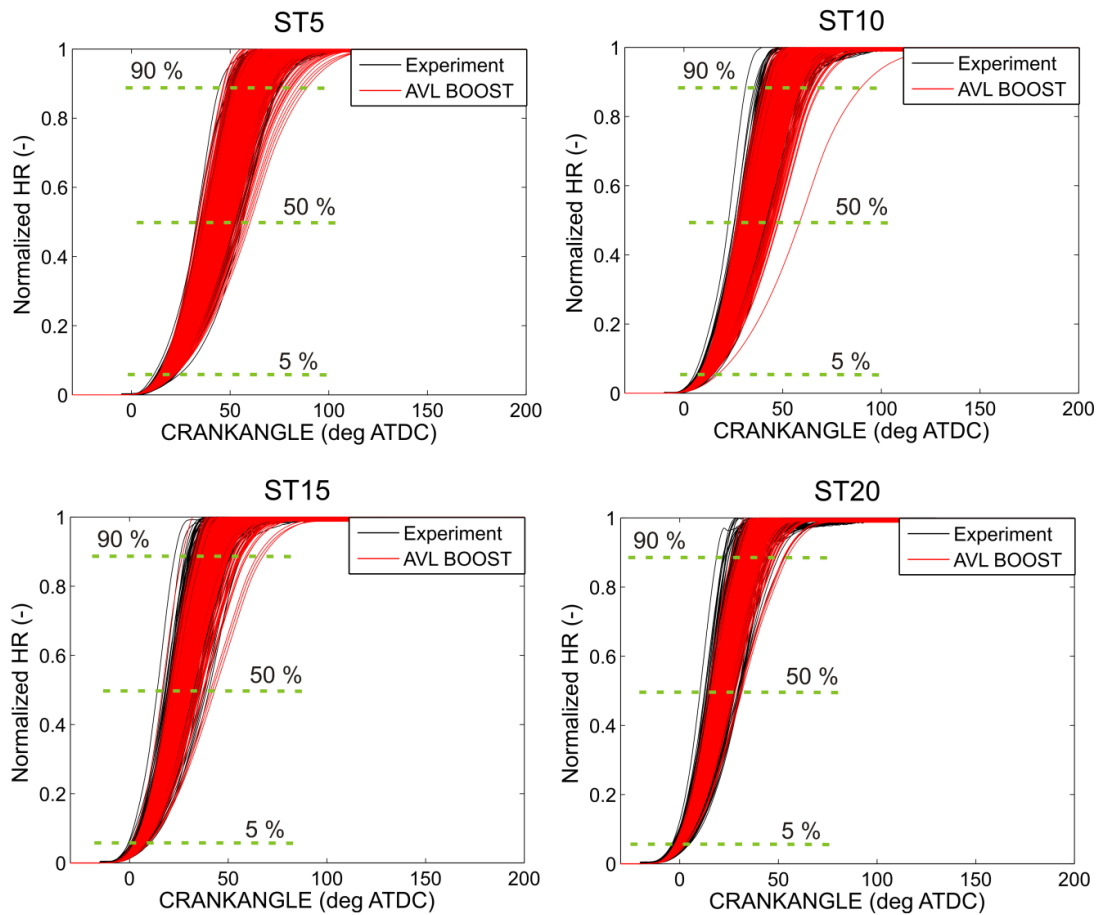


Figure 79. Comparison of experimental and simulation results of the cycle-resolved normalized HR for all considered operating points and sample size of 300 cycles.

To illustrate the dispersion of the combustion process and to obtain more detailed and quantitative results, the statistical analysis of the crank angle where the predefined mass fraction burned is reached was performed. As it is marked in the Figure 79, the statistical

analysis was made for the prescribed mass fractions burned of 5 %, 50 % and 90 % representing the early flame kernel growth, main turbulent combustion and termination of combustion, respectively. The statistical results of the experiment and simulation regarding the combustion process are shown and compared in Figure 80. The similar analysis of the combustion process has been performed in [9, 105], but only on the sample of several hundred cycles of experimental results. The  $x$ -axes in Figure 80 present the crank angle position ATDC, while the  $y$ -axes show the probability of occurrence. It can be observed from Figure 80 that for all considered operating points the early flame kernel growth follows narrow Gaussian distribution around the mean value. As the combustion develops, the dispersion around the mean value increases. For the statistical results when the 50 % of mass is burned the distribution around the mean value is wider and still nearly Gaussian-like, while for the statistical results when the 90 % of mass is burned show more randomly dispersed and wide distribution.

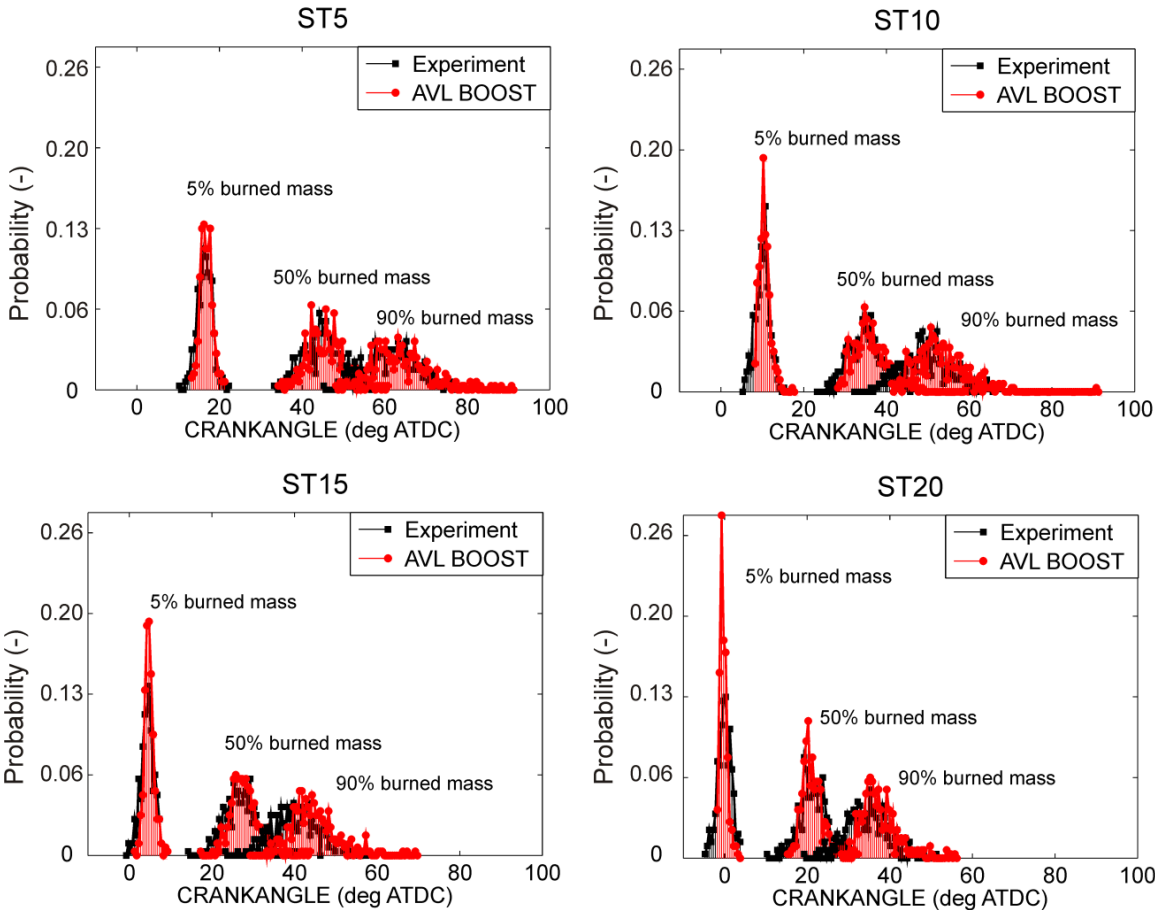


Figure 80. Comparison of experimental and cycle-simulation statistical distribution results of CA5, CA50 and CA90 for the considered operating points and sample size of 300 cycles.

From the results of the statistical analysis, presented in Figure 80, the prediction of combustion phasing can be quantified. The early flame kernel growth and the positions of 50

% of mass fraction burned are predicted very well in terms of mean values and dispersions, while the termination of combustion process, the position of 90 % of mass fraction burned is predicted on average about 3° CA later when compared to the experimental data. To quantify the prediction of mean values and dispersions of crank angle distribution at 5 %, 50 % and 90 % of mass fraction burned, the results of the mean values and standard deviations are summarized in Table 22. Generally, the predictions of mean values and standard deviations are very close to the experimental results. The dispersion of the early flame kernel growth described by the standard deviation of crank angle at 5 % of mass fraction burned is about 0.4° CA lower compared to the experimental data. Since the expansion speed of the flame kernel depends on the mixture composition and kernel temperature [84], the introduction of non-homogenous mixture composition would affect the early combustion phase and it is expected that the statistical result would be additionally improved. In order to confirm that fact a detailed 3-D CFD modeling is necessary. It was demonstrated in [107, 117] that even with homogeneous in-cylinder mixture the complex 3-D interactions between the flame and turbulent structures exist while such phenomenon is not predicted by the presented 0-D combustion and turbulence sub-model.

Table 22. Statistical results of CA5, CA50 and CA90 – experiment vs. cycle-simulation

			CA5 (° CA ATDC)	CA50 (° CA ATDC)	CA90 (° CA ATDC)
<b>ST5</b>	Experiment	Ave.	16.4	44.6	61.4
		StD.	1.82	4.51	6.25
	AVL BOOST	Ave.	16.8	45.5	63.7
		StD.	1.44	4.53	7.10
<b>ST10</b>	Experiment	Ave.	10.0	34.9	49.8
		StD.	1.74	4.09	6.13
	AVL BOOST	Ave.	10.5	36.3	53.1
		StD.	1.35	4.42	6.12
<b>ST15</b>	Experiment	Ave.	4.4	26.9	40.6
		StD.	1.77	4.02	5.88
	AVL BOOST	Ave.	4.8	28.0	44.6
		StD.	1.14	3.68	5.68
<b>ST20</b>	Experiment	Ave.	- 0.1	21.5	34.7
		StD.	1.64	3.51	5.33
	AVL BOOST	Ave.	- 0.3	21.3	37.4
		StD.	0.91	2.76	4.51

## Results of CA5 vs. CA10-90

To additionally analyze the capability of the cycle-simulation model to simulate the CCV in combustion with homogeneous mixture composition, the crank angle at 5 % of mass fraction burned is plotted against the corresponding crank angle period when 10 % – 90 % of mass is burned. The predicted results are compared with the experimental data and they are shown in Figure 81. The black markers are experimental and the red ones represent the cycle-simulation results.

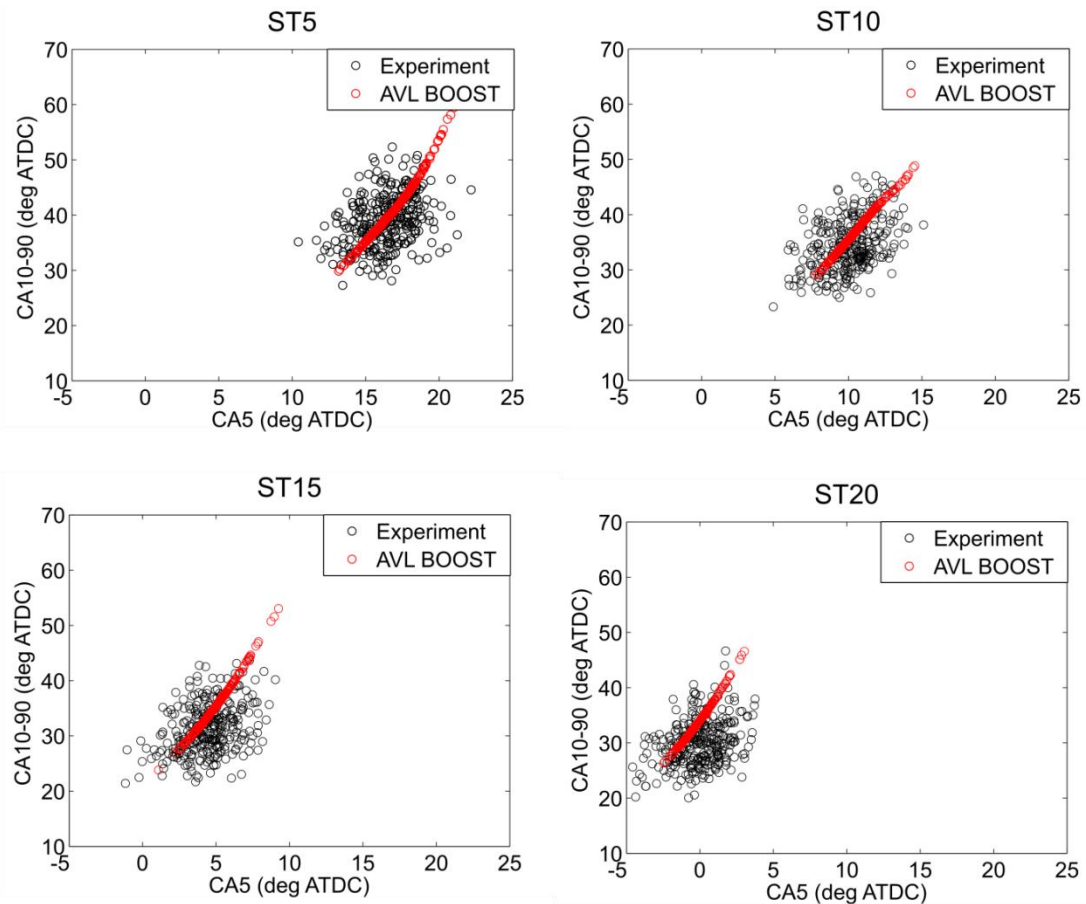


Figure 81. Comparison of experimental and cycle-simulation results of CA5 vs. CA10-90 for all considered operating points and sample size of 300 cycles.

The crank angle period between 10 – 90 % of mass fraction burned is marked with CA10-90 and can be considered as the combustion duration. On the other hand, the crank angle at 5 % of mass fraction burned (CA5) shows the period that is typical for the early flame kernel development when there is no significant heat released. Therefore, CA5 can be considered as the start of combustion. The experimental data in Figure 81 show that cycles with faster flame kernel development may have very slow main turbulent combustion and vice versa, indicating the presence of in-cylinder non-homogeneities as well as complex 3-D interactions between the flame and turbulent structures [117]. Therefore, the overall structure of the experimental

results shown in Figure 81 seems to follow ‘O’ shaped form with high dispersion in any direction. In the cycle-simulation results, the cycles that have faster flame kernel development have also faster main turbulent combustion and vice versa. Therefore, the cycle-simulation results presented in Figure 81 follow ‘I’ shaped front that may be described by the linear trend. Introduction of mixture stratification [81] into the presented cycle-simulation model could spread ‘I’ shaped front in the perpendicular direction approaching the ‘O’ shaped form, but it is not possible to present that conclusion without detailed 3-D CFD modeling.

**Distribution of cross-flow velocity at the spark plug**

Unfortunately, the experimental results of the in-cylinder flow around the spark plug were not available because the CFR engine is not equipped with the fiber-optic spark plug, as it was the case in [74, 105]. For the partial validation of the  $k-\epsilon$  turbulence model, used in the cycle-simulation, the statistical analysis of the turbulent velocity at the spark plug location was performed and results are shown in Figure 82.

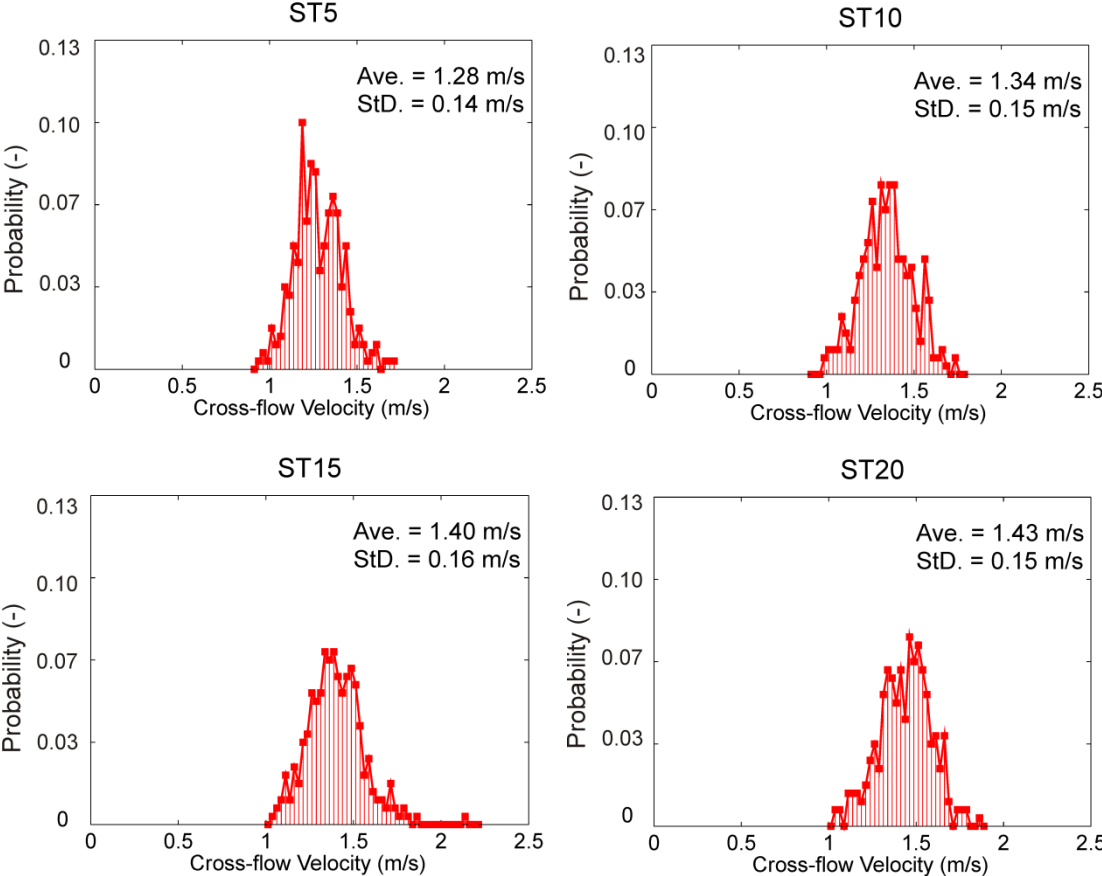


Figure 82. The statistical distribution of cross flow velocities at the spark timing, from analysis of cycle-simulation results of 300 cycles.

The statistical analysis of the cross-flow velocity at the spark plug location was for each operating point performed at the prescribed spark timing. The average result and the standard



deviation of cross-flow velocity are also specified in Figure 82. If the obtained results are compared to the results published in [74], it can be concluded that the mean values of the cross-flow velocity at the spark plug location are very similar. Direct comparison of results could not be performed because the experimental data presented in [74] was measured at different engine geometry, at the engine speed of 1500 rpm, at part load condition and with the spark timing of  $26^\circ$  CA BTDC. The average value of the flow velocity in the vicinity of the spark location, that was calculated over the 600 cycles, reported in [74], is 1.8 m/s with the standard deviation of 0.466 m/s. The predicted average values of cross-flow velocity at the spark plug location in the CFR engine are slightly lower because the engine speed is 40 % lower. It is also known that the turbulence effects on the combustion process in CFR engine are very low indicating the in-cylinder turbulence levels are low. Moreover, the simulated standard deviations of cross-flow velocity are 3 times lower compared with the experimental data reported in [74]. These differences can be explained by the lower mean values of cross-flow velocities and by the spark plug position which is close to the cylinder liner at considered CFR engine. The validation of turbulence model constants cannot be fully performed without the comprehensive experimental or 3-D CFD results. In terms of turbulent velocity distribution around the mean value, it seems that the distribution in all operating points is nearly Gaussian, depending largely on the distribution of turbulence production constant  $S_{10}$  defined by the user.

## 6.5. Influence of in-cylinder turbulence variation on CCV in combustion

An influence of different relative standard deviations that define the variation of in-cylinder turbulence level from cycle-to-cycle on the statistics of IMEP is shown in Figure 83 and the cycle-simulation results are compared to the experimental data.

The cycle-simulation results of AVL BOOST where the relative standard deviation of intake  $k$  production constant  $S_{10}$  is set to 0.12 are shown with the blue circle markers, while the statistical results of the cycle-simulation model when the relative standard deviation of intake  $k$  production constant  $S_{10}$  is set to 0.16 are presented with the green circle markers. When the relative standard deviation of  $S_{10}$  constant is set to 0.14 (red circle markers) the best agreement with the experimental data for the considered operating points is achieved (Chapter 6.3). The change of relative standard deviation of  $S_{10}$  constant for about  $\pm 15$  % does not change the average value of IMEP over the 300 cycles. This is expected because the variation of  $S_{10}$  constant is performed by the Gaussian distribution around the mean value that is fixed to  $1 \cdot 10^{-6}$ . The change of relative standard deviation of  $S_{10}$  constant influences the StD of

IMEP and CoV of IMEP. From Figure 83 it can be observed that the effect of in-cylinder turbulence oscillations becomes significant at operating points whose spark timing is retarded. With the 15 % increase in relative standard deviation of  $S_{10}$  constant, at the operating point ST5 the standard deviation of IMEP and its coefficient of variation are increased for about 45 %. The same trend of larger CoV of IMEP, with the stoichiometric mixture, when the spark timing is retarded has been observed in [103]. Such behavior is explained by the higher oscillations of in-cylinder pressure during the expansion period – see Figure 77. As the oscillation of in-cylinder turbulence becomes lower, with the lower relative standard deviation of  $S_{10}$  constant, the standard deviation and coefficient of variation of IMEP is lower.

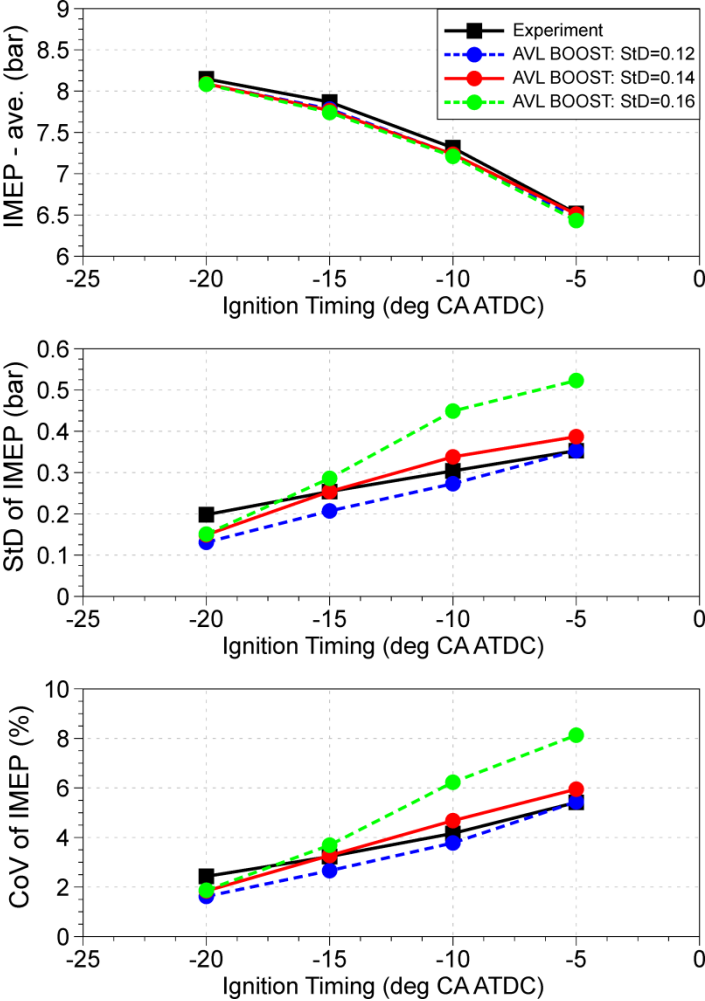


Figure 83. Influence of relative standard deviation of turbulence production constant on the statistical results of IMEP at all considered operating points ST5 – ST20.

From the statistical results shown in Figure 83 it can be seen that the statistical results of experimental IMEP was used to correctly tune the relative standard deviation of  $S_{10}$  constant at all considered operating points of the CFR engine. The simulation results (StD and CoV of IMEP) obtained by the relative standard deviation of intake  $k$  production constant  $S_{10}$  set to

0.14 are close to the experimental results in terms of absolute values, while the simulation case with the relative standard deviation of intake  $k$  production constant  $S_{10}$  set to 0.12 has better prediction of trends (slope) of StD and CoV of IMEP for the considered spark sweep and compared with the experimental data. The fine tuning or the optimization of relative standard deviation of intake  $k$  production constant  $S_{10}$  has to be made to achieve even better agreement with the experimental results.

## 6.6. The variation of cross-flow direction at the spark plug

The simulations of cycle-to-cycle variation in combustion whose results are shown in previous figures are performed with the variation of in-cylinder turbulence level from cycle-to-cycle where the flow angle  $\alpha$  was set to  $0^\circ$ . In a number of experimental and numerical studies [103, 117] it was shown that the oscillation of flow angle at the spark plug location also influences the variation of early flame kernel growth and the main turbulent combustion. The variation of early flame kernel growth, when the flow angle at the spark plug is changed, occurs because the kernel heat loss is changed and consequently its expansion speed is different. On the other hand, the variation of flow angle at the spark plug means that the flame kernel center is convected in different directions from its initial position between the electrodes. This can cause the differences in the free surface area of the flame entraining the fresh mixture from cycle-to-cycle, resulting in the variations of combustion burning rate. The different final positions of the flame centers, around the defined spark plug position, were studied numerically in [103] indicating the significant influence on the variation of combustion rate.

For the analysis of the influence of flow angle oscillations on the CCV in combustion, the presented cycle-simulation model was extended. The flow angle is defined randomly according to the uniform distribution, but not over the entire  $360^\circ$ . The possible flow angles are in Figure 84 marked as  $\alpha_1^*$  and  $\alpha_2^*$ . The model that includes the random oscillation of flow angle assumes that the ground (negative) electrode gives a certain drag force on the in-cylinder flow field, restricting the possible flow angles to the angles marked as  $\alpha_1^*$  and  $\alpha_2^*$ . Therefore, possible flow angles are function of ground electrode dimensions  $G_2$  and  $E_4$ :

$$\operatorname{tg}\beta = (E_4 / G_2) \quad (6.1)$$

$$\alpha_1^* = \left[ \left( -90^\circ + \frac{\beta}{2} \right), \left( 90^\circ - \frac{\beta}{2} \right) \right], \quad \alpha_2^* = \left[ \left( 90^\circ + \frac{\beta}{2} \right), \left( 270^\circ - \frac{\beta}{2} \right) \right] \quad (6.2)$$

The defined possible range of flow angles can only be used for the single-ground spark plugs, while for the spark plug design with the two- or three-ground electrodes, the possible flow angles should be defined in a different way.

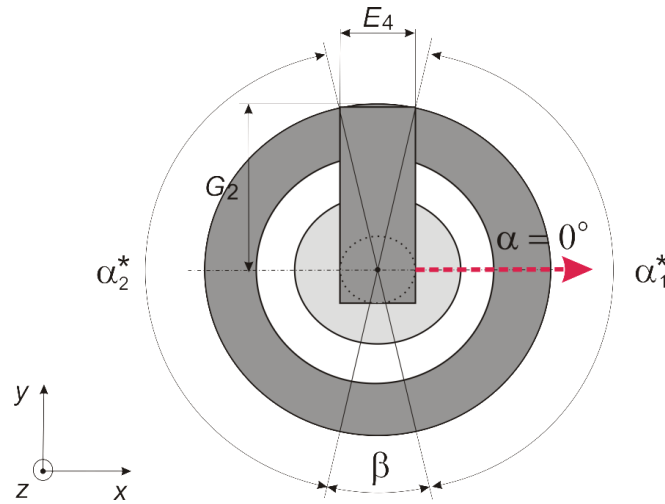


Figure 84. The possible cross-flow velocity directions at the spark plug (top view):  $\alpha_1^*$  and  $\alpha_2^*$  represent the possible angles of the velocity vector.

In order to analyze the influence of the flow angle variation on the CCV in combustion, the three cycle-simulations of all considered operating points of the CFR engine were performed and the statistical results of IMEP are shown in Figure 85. The first calculation shown with the red markers is already statistically analyzed and represents the variation only of in-cylinder turbulence from cycle-to-cycle, while the flow angle is set to  $0^\circ$  (parallel with the positive direction of  $x$  - axis). The second set of cycle-simulation results, presented with the gray circle markers, is obtained by the oscillation of only flow angle, while the in-cylinder turbulence was not oscillated. The last set of cycle-simulation results, shown with the cyan circle markers, is obtained by the variation of both, flow angle and in-cylinder turbulence level from cycle-to-cycle. The random and uniform distribution of the flow angle is fully independent on the variation of  $S_{10}$  constant that follows normal (Gaussian) distribution. This means that cycles with the higher in-cylinder turbulence level can have flow angles that increase the ignition delay and vice versa.

The variation of only flow angle without the variation of in-cylinder turbulence level gave the statistical results of IMEP that show weak oscillations. The different flow angle  $\alpha$  from cycle-to-cycle influences the early flame kernel growth as well as the free flame surfaces that define the turbulent combustion burning rate. But, the statistical results achieved with the variation of only flow angle are compared with the results obtained with the simultaneous variation of in-cylinder turbulence and flow angle, it can be seen that only approximately 10

% of the total in-cylinder variations (where all other effects that can cause CCV in combustion are neglected) can be attributed to the variation of flow angle at the spark plug. Since the considered experimental engine has fully symmetrical combustion chamber (flat cylinder head and piston top) and due to low engine speed ( $n = 900$  rpm) and full load conditions, the flow angle variations do not significantly contribute to the overall CCV in combustion. For the non-symmetric combustion chamber designs like the pent roof cylinder head, the free flame surface areas could change significantly with the different positions of the flame kernel, depending on the cross-flow velocity that shifts the flame kernel from its initial position. Moreover, at part load conditions the kernel excess of energy is lower and the early flame kernel growth becomes more sensitive on the variation of flow angle influencing the ignition delay period, as shown in Figure 52.

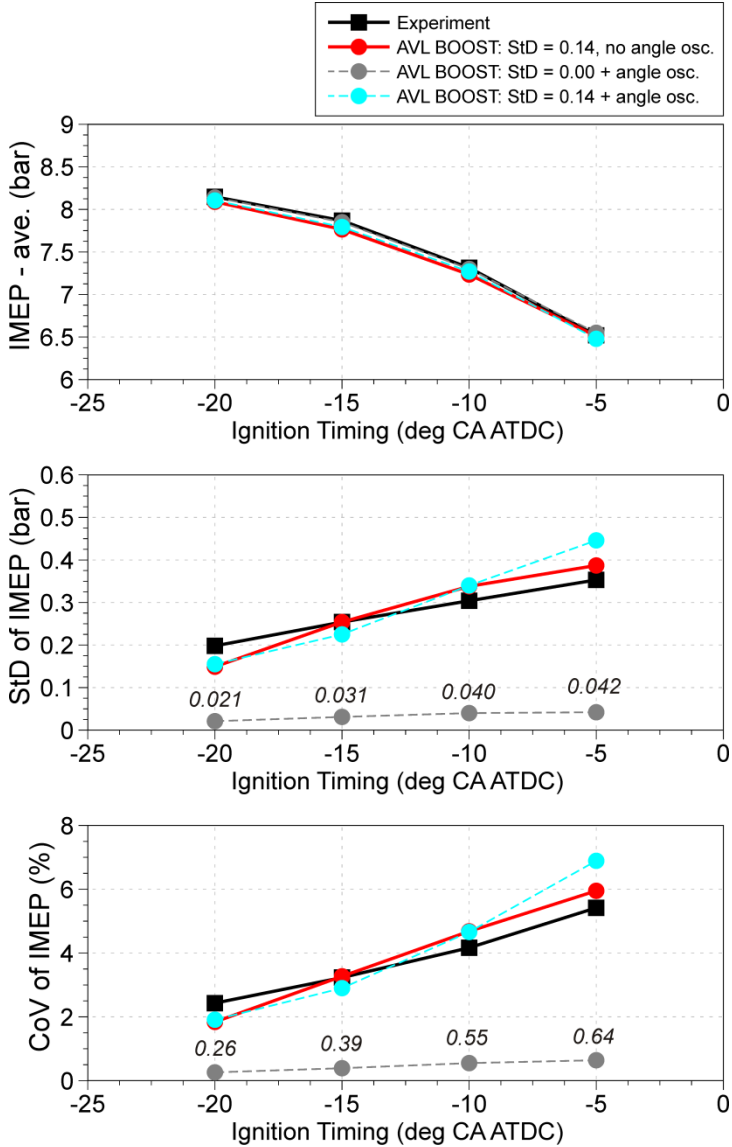


Figure 85. Influence of variation of the cross-flow velocity direction on the statistic results of IMEP at all considered operating points ST5 – ST20.

Therefore, from the considered CFR engine and four operating points that represent the full load conditions and low engine speed it is impossible to define the general contribution of the flow angle variations to the overall CCV in combustion. The effect of flow angle oscillation depends on the combustion chamber geometry as well as on the operating points in terms of engine speed and load.

It is already mentioned that the presented modeling of CCV in combustion neglects all other effects that contribute to the CCV in combustion. The simulations were performed with the fully homogeneous mixtures, although the variations of overall flow pattern in the cylinder can produce significant mixture stratification. The local mixture stratification in the combustion chamber influences the local flame speeds that can change the overall combustion burning rate. Due to simplicity of the cycle-simulation model and unavailability of the 3-D CFD results of CFR engine, necessary for the correct definition of mixture stratification, it was decided that modeling of mixture stratification will not be made. The complex 3-D interactions between the flame and the in-cylinder turbulent structures can also contribute to the CCV in combustion. Such phenomena cannot be captured with the presented quasi-dimensional combustion and 0-D turbulence sub-models.

The effects of variation of both, in-cylinder turbulence level and flow angle from cycle-to-cycle become noticeable at operating points where the spark timing is retarded. As it was previously described, the larger variations of IMEP at the operating points whose spark timing is retarded can be attributed to the longer period during the expansion in which the individual in-cylinder pressure profiles deviate from the averaged pressure profile.

In order to check the simulation results of the early flame kernel growth when the flow angle and in-cylinder turbulence variations are imposed simultaneously, the flame kernel positions for the ST5 operating point are shown in Figure 86.

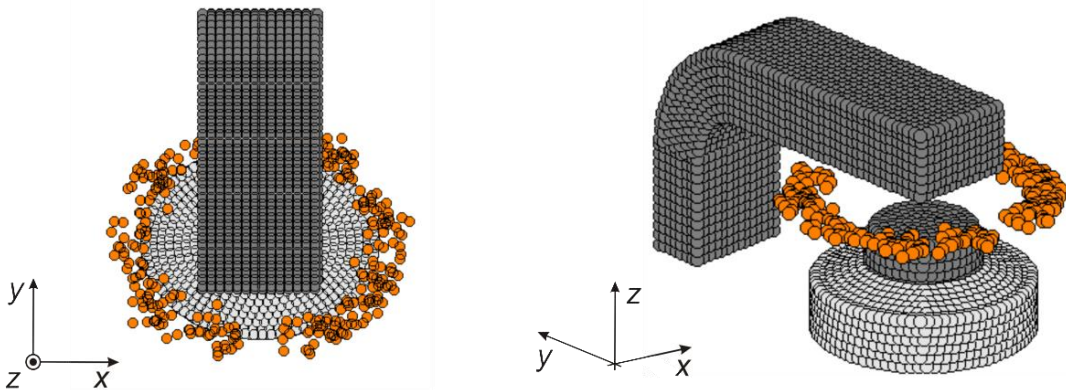


Figure 86. Visualization (top and isometric view) of the flame kernel shifting (at the end of kernel calculation) for the operating point ST5 ( $\sigma_{rel, S10} = 0.14$ ).

On the left side of Figure 86 the top view is shown, while the isometric view is given on the right side. The orange circle markers represent the final flame center when the kernel burned mass reached the critical value described by equation (3.16). After that, the flame front has grown enough to be considered as the turbulent flame and hence its movement is not considered anymore. The shifting of the flame kernel center during the phase of early kernel growth is defined by the cross-flow velocity profile and flow angle. Due to the low engine speed the cross-flow velocities are low (about 1.3 m/s) and therefore the flame centers remain close to the spark plug electrodes. The values of the flame kernel shifting for the considered operating points ST5 are in the range of 1.8 to 2.8 mm. It can be seen that the achieved flow angles defined as random angles that follow uniform distribution are within the desired angles  $\alpha_1^*$  and  $\alpha_2^*$  that are specified in Figure 84. The response of cycle-simulation model shown in Figure 86 confirms that the variation of flow angle from cycle-to-cycle is in accordance with the defined model.

The cycle-simulation results with the variation of in-cylinder turbulence level and flow angle where the CA5 is plotted against the CA10-90 are shown in Figure 87 and the results are compared to the experimental data. If the cycle-simulation results from AVL BOOST shown in Figure 81 are compared with the ones presented in Figure 87, it can be seen that the flow angle variation has slightly spread the 'I' shaped form. Such behavior is obtained because the random variation of flow angle is independent on the variation of in-cylinder turbulence. In other words, the cycles whose flow angle contributes to the longer ignition delay (due to high heat loss) can have the higher or lower in-cylinder turbulence level influencing the faster or slower main turbulent combustion.

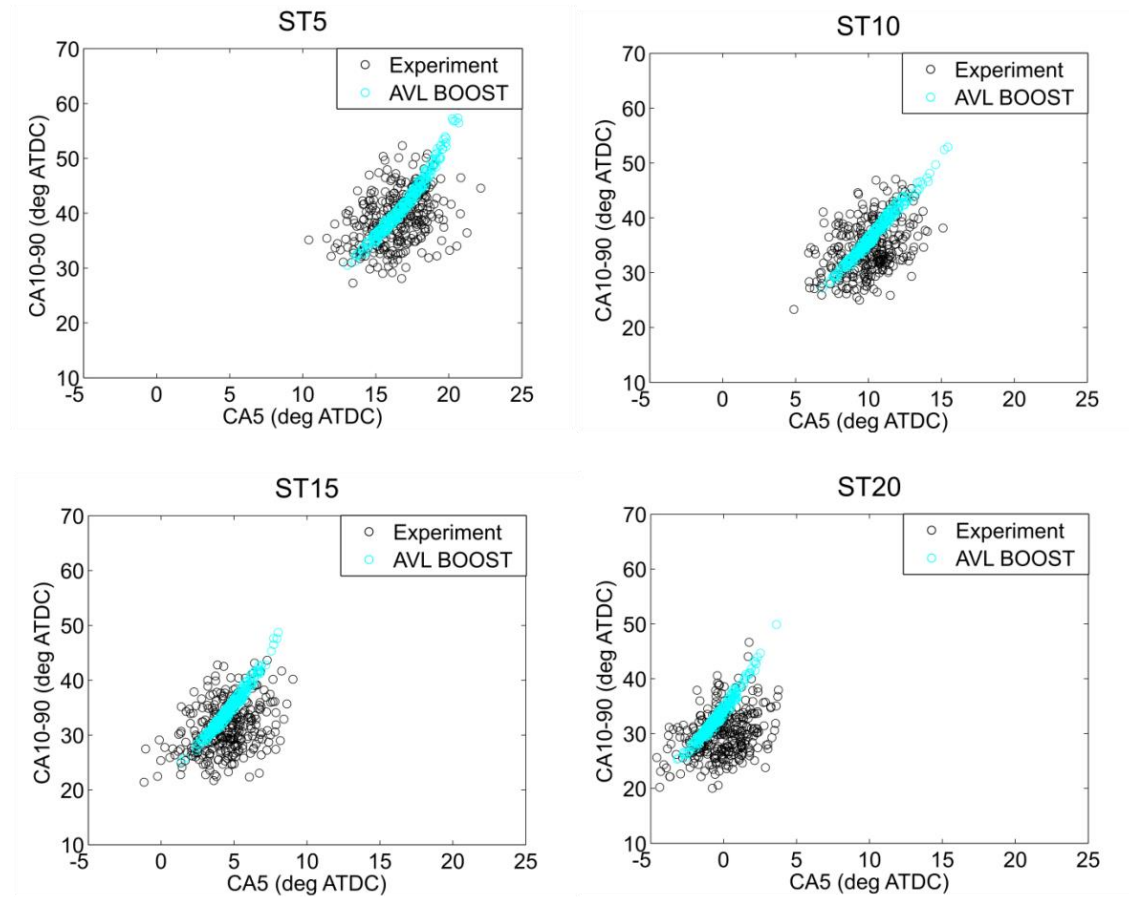


Figure 87. Comparison of experimental and cycle-simulation results of CA5 vs. CA10-90 for all considered operating points and sample size of 300 cycles with the oscillation of in-cylinder turbulence and flow angle from cycle-to-cycle.

Although the flow angle and in-cylinder turbulence level were varied simultaneously from cycle-to-cycle, representing more physical solution, Figure 87 shows that there are other effects that contribute to the CCV in combustion of SI engine. The mixture stratification can significantly change the individual burning rate as it was demonstrated on the test cases in [81]. Furthermore, the local complex 3-D interactions between the flame and turbulent structures can produce CCV in combustion.



## 7. General Overview and Conclusions

Within the framework of the presented study, new physically based sub-models for the simulation of turbulence, ignition and combustion phenomena are developed and integrated into the cycle-simulation model of AVL BOOST. The validation of cycle-simulation results was performed by comparison with the available 3-D CFD results and with the experimental data of CFR engine.

The modeling of turbulence presented in the second chapter is divided into three main parts representing the single zone modeling during the high pressure cycle, two zone modeling during the combustion and the full cycle modeling during the entire engine cycle. The validation of the single zone  $k-\varepsilon$  turbulence model applied during the high pressure cycle required the specification of initial in-cylinder turbulence at the beginning of the high pressure cycle. The initial values of in-cylinder turbulence and dissipation rate at the beginning of the high pressure cycle and for different engine geometries and operating points were defined from the 3-D CFD results. Although the turbulence is very complex 3-D phenomenon whose nature is still not fully clear today, it was shown that by implementing specific modifications of the single zone  $k-\varepsilon$  turbulence model, and by using the specific parameter that adjusts for the model inability to calculate specific phenomena, the model can predict the progress of total in-cylinder turbulent kinetic energy during the high pressure cycle that is close to the 3-D CFD results. The comparison of cycle-simulation and 3-D CFD results required the manual tuning of new user-defined constant  $C_\varepsilon$  for every operating point showing that the constant should be set in the range from 2.00 to 2.55. At the same time, the combustion process was calculated by the original quasi-dimensional combustion model based on the fractal theory. The application of under-relaxation function  $I_f$ , that depends on the value of user-defined parameter  $r_{f, \text{ref}}$ , restricts to reach the maximum values of fractal dimension  $D_{3, \text{max}}$  when the maximum wrinkling of the flame front occurs. The mentioned under-relaxation function is used for the smooth transition from laminar to fully developed turbulent flame. In order to obtain the combustion results that are close to the 3-D CFD results from AVL FIRE, by the fractal combustion model, the manual tuning of four combustion model constants for each operating point of the engine was required. The first parameter  $f_{D_{3, \text{max}}}$  represents the parameter that influences the maximum fractal dimension; the constant  $c_{\text{ign}}$  is used to modify the ignition delay period; the reference flame front radius  $r_{f, \text{ref}}$  represents the assumed flame front radius when the maximum wrinkling of the flame front is

achieved, defining the initial combustion phase and the last constant  $x_B$  is used to slow down the burning rate at the late part of the combustion process. The manual tuning of four combustion constants and one turbulence model constant for each operating point of the engine is not a user friendly approach.

To achieve the better, and physically more accurate, prediction of the combustion process, the two zone  $k$ - $\varepsilon$  turbulence model was developed. The two zone turbulence model is applied only during the combustion process when the cylinder mixture is divided into the unburned and the burned zone. The calculation of the unburned zone turbulence is performed simultaneously with the total in-cylinder turbulence, while the turbulence quantities of the burned zone can be explicitly calculated from the total and the unburned zone turbulence. Such approach represents significantly simplified modeling of the unburned zone turbulence with only one new user-defined constant  $C_\varepsilon^{UZ}$  that has to be specified. The initial values of the unburned zone turbulence are defined from the total in-cylinder turbulence (calculated with the previously developed single zone model) at the start of combustion. For the considered SI engines and operating points the constant  $C_\varepsilon^{UZ}$  was defined in the range from 3.0 to 7.5. When the two zone  $k$ - $\varepsilon$  turbulence model was utilized in a simulation that used the fractal combustion model, the flame front propagation across the combustion chamber of SI engine depends on the unburned zone turbulence and the artificial wall combustion mode for the calculation of the late part of combustion process can be fully omitted. Therefore, by applying the developed two zone turbulence model a better and physically more accurate prediction of combustion process of SI engines is achieved with the same number of user-defined constants.

In order to fully eliminate the dependency of the turbulence model on the initial values of turbulence quantities at the beginning of the high pressure cycle, the single zone  $k$ - $\varepsilon$  turbulence model was extended to the gas exchange phase. The specific extension of the  $k$  and  $\varepsilon$  differential equation requires the specification of two user-defined constants for each operating point of the engine representing the intake  $k$  and  $\varepsilon$  production constant. The validation of the proposed full  $k$ - $\varepsilon$  turbulence model showed that by manual tuning of the two intake production constants the model can correctly reproduce the progress of in-cylinder turbulent kinetic energy during the intake at low and middle engine speed. At higher engine speed, the progresses of in-cylinder turbulent kinetic energy calculated by the 0-D model are shifted earlier, when compared with the 3-D CFD results. This behavior occurs because the 0-D turbulence model considers the instantaneous transfer of the mean flow kinetic energy (that

enters into the cylinder over the intake valve cross section) to the level of turbulent kinetic energy.

To avoid the manual tuning of ignition delay period and early combustion phase for different operating conditions of the engine, the new quasi-dimensional ignition model (QDIM) and modified transition from laminar to fully developed turbulent flame were applied to the cycle-simulation model of AVL BOOST. Developed QDIM is based on the AKTIM model usually available in the 3-D CFD models of combustion in SI engines. Several main conclusions regarding the developed QDIM can be written:

- Ignition delay period and early flame kernel growth depend on a large number of physical properties such as: spark plug geometry, cross-flow velocity, heat transfer effects, energy of secondary electric circuit, etc.
- The misfire conditions can be captured by the model. When there is a large heat transfer and low kernel energy received from the electric spark, the flame kernel will not be able to grow enough and the misfire will occur.
- The QDIM is capable of handling multiple electrical breakdowns that may occur at high cross-flow velocities. When the voltage between the electrodes  $V_{ie}$  reaches the breakdown voltage  $V_{bd}$  the new breakdown is obtained and the new spark is formed increasing the kernel expansion speed. This phenomenon is described and demonstrated in Figure 53.
- The QDIM is able to simulate the cycle-to-cycle variations in combustion when the specific perturbations of constants that influence QDIM are set. The oscillations of ignition delay period can be induced by the oscillations of cross-flow velocity and/or by the oscillations of flow angle at the vicinity of the spark plug, as it is demonstrated in the last chapter.

The analysis of intake constants of the turbulence model and of the upper limit of fractal dimension showed that the models for parameterization of the changes of these constants can be defined. The intake  $k$  production constant  $S_{in}$  was correlated to the instantaneous mean flow velocity at the intake valve cross section, while the intake  $\varepsilon$  production constant  $C_{in}$  was defined as the linear function of the instantaneous in-cylinder pressure during the intake process. Instead of manual setting of constants  $S_{in}$  and  $C_{in}$  for each operating point of the engine, the parameterization model requires the specification of four constants:  $S_{00}$ ,  $S_{10}$ ,  $C_{00}$  and  $C_{10}$ . The specification of these four constants is made by the optimization which is

performed at several operating points of SI engine simultaneously. The optimization process using the genetic algorithm resulted in the single set of turbulence model constants showing a good agreement of the turbulent kinetic energy during the combustion and expansion with the 3-D CFD results. The optimization of the intake constants  $S_{00}$ ,  $S_{10}$ ,  $C_{00}$  and  $C_{10}$  is performed for each engine together with the proposed parameterization model of the fractal dimension. The maximum value of the fractal dimension that is reached during the developed turbulent flame is expressed as a linear function of the ratio of turbulence intensity to laminar flame speed. The application of single sets of constants related to the turbulence, ignition and combustion model on considered engines (Engines 1 – 4) showed a very good agreement with the 3-D CFD results at different operating conditions. The proposed parameterization models of the turbulence model constants and of the upper limit of fractal dimension are derived based on the validation with the available 3-D CFD results. For extreme engine operating conditions (engine speed above 7000 rpm and high boost levels) the validity of the parameterization model has to be rechecked.

The presented cycle-simulation model that includes the developed sub-models for turbulence, ignition and combustion was applied in the simulation of CCV in combustion of CFR engine. Four different operating points were evaluated with the spark timing of  $5^\circ$ ,  $10^\circ$ ,  $15^\circ$  and  $20^\circ$  CA BTDC. The considered spark sweep enables the analysis of operating points with different levels of CCV in combustion. The fully stoichiometric mixture was analyzed, with the intake pressure and temperature that correspond to the ambient conditions. The measured in-cylinder pressure traces were stored with the resolution of  $0.1^\circ$  CA over 300 working cycles. The offline application for the calculation of heat release from the measured pressure traces was used as one of the most commonly used techniques for the measure of combustion rate.

The modeling of CCV in combustion was performed by imposing the perturbations of only one turbulence production constant that produced oscillations in the in-cylinder turbulence level from one cycle to another. The perturbations of turbulence production constant follow the Gaussian distribution around the mean value with defined relative standard deviation which was chosen to mimic the CCV in combustion close to the one observed in the experiment. Although the cycle-simulation model has the possibility to simulate the effects of in-cylinder non-homogeneity in mixture composition, it was not considered here due to the simplicity and unavailability of the input data necessary for the definition of the mixture stratification. All operating points analyzed within the presented

study were simulated with the single set of turbulence, ignition and combustion model constants. The influence of different relative standard deviations of the turbulence production constant was also investigated in terms of statistical results of IMEP. Since the flow angle at the vicinity of the spark plug can cause the variations in combustion of SI engine, the random variation of flow angle was defined and the achieved results were compared with the experimental data.

The overall capability of the presented cycle-simulation model to simulate the CCV in combustion was demonstrated in Figures 75 - 87. The cycle-averaged, cycle-resolved and statistical results were processed and compared with the experimental data. Bearing in mind that homogeneous mixture was simulated and the fact that the single set of model parameters with the same value of relative standard deviation of turbulence production constant over the spark sweep was applied, the presented cycle-simulation model seems to be detailed enough to reproduce the CCV in combustion.

The overall analysis of the experimental results showed that the earlier spark timing increases the mean IMEP while its oscillations expressed as CoV and StD of IMEP are reduced. The statistical analysis of the in-cylinder pressure traces and combustion rates have been performed and the following conclusions are drawn:

- The experimental results showed that individual cycles with faster kernel development do not necessarily have to have faster main turbulent combustion. This indicates the presence of in-cylinder non-homogeneities in terms of temperature, composition, flow and turbulence as well as complex interactions between flame and turbulent structures that always have 3-D behavior and that cannot be predicted by the 0-D models.
- The simulation results achieved by the variation of in-cylinder turbulence level showed that individual cycles with faster kernel development have faster main turbulent combustion and vice versa.
- Cycle-averaged results of the in-cylinder pressure and normalized HR matched the experimental data very well.
- The predictions of CCV in combustion are very close to the ones that were observed in the experiment.
- Perturbation of turbulence production constant that follows the Gaussian distribution around the mean value seems to be the correct one.
- Although the ignition, combustion and turbulence sub-model used in the cycle-simulation are based on the 0-D approach, the mentioned sub-models that are

integrated into the cycle-simulation are detailed enough to reproduce the global effects of CCV in turbulence and combustion, although the complex flame-turbulence interactions [117] are not captured.

- Because of the limitations of the 0-D approach all possible influencing factors on CCV are not taken into account (i.e. non-homogeneities of mixture composition, temperature, flow and turbulence as well as complex 3-D interactions between the flame and turbulent structures) which limits the possibility for full match of the simulation with the experimental results. For the comprehensive analysis of CCV in combustion, the above mentioned influencing factors should be analyzed and studied either by measurement or 3-D CFD (LES) multi-cycle simulations.

The presented cycle-simulation and modeling of the CCV in combustion by means of random variation of the in-cylinder turbulence level and of the flow angle at the spark plug location represent a simple, fast and well-promising solution for engineering work. Such simulation model is a good base for the improved modeling of knock occurrence, fuel consumption and exhaust gas emissions which in the presence of CCV may significantly deviate from the ones obtained by mean cycle.

The computational time of the presented cycle-simulations of 300 cycles with the imposed CCV in turbulence and combustion was around 50 minutes per operating point on the standard personal computer (Intel Xeon E5-1620, 3.6 GHz).

## 7.1. Original scientific contribution

The research of the modeling of turbulence, ignition and combustion phenomena for the cycle-simulation of SI engine presented in this thesis resulted in the following scientific contribution:

- The development of new single zone  $k-\varepsilon$  turbulence sub-model that is able to predict the progress of total in-cylinder turbulence level during the combustion and expansion close to the 3-D CFD results.
- The simplified approach for the modeling of unburned zone turbulence was applied for improving the prediction of combustion process at different engine operating conditions.
- The development of new quasi-dimensional ignition model (QDIM) that is able to capture the effects of different in-cylinder conditions and spark plug designs on the early flame kernel growth as well as the multiple breakdowns and misfire conditions in the 0-D environment.

- Definition of parameterization model for the turbulence constants and for the upper limit of fractal dimension so that the single set of constants for one engine geometry can be used in the simulation of entire engine map.
- Possibility to simulate the cycle-to-cycle variations in combustion of SI engine with the variation of in-cylinder turbulence and/or flow angle at the spark plug location that reproduces statistical simulation results close to the experimental results.
- Possibility to analyze the effects of different engine parameters such as spark plug design, ignition energy, heat transfer at spark plug, combustion chamber design on the engine output performances with the presence of CCV.
- Possibility to better predict the engine conditions for the more accurate modeling of knock combustion and exhaust gas emissions with the presence of CCV in flow and combustion.

## **7.2. Possible directions of further work**

According to the achieved results with the application of the developed sub-models for the simulation of averaged cycle and CCV in combustion of SI engine, a several possible directions of future work can be specified:

- Application of developed sub-models with the single set of constants on the simulation of entire SI engine (multi-cylinder engine) in the entire engine operating map and by integrating knock combustion sub-model.
- Extension of the spark plug geometry model for the description of spark plugs with two- and three-ground electrodes.
- Analysis of influence of different spark plug designs on SI engine performances with the presence of cycle-to-cycle variations in flow and combustion.
- Research of particular effects (variation of flow angle, variation of in-cylinder turbulence and flow, mixture stratification) that affect cycle-to-cycle variations in SI engine in order to create more comprehensive picture regarding the CCV phenomena in combustion of modern SI engines.
- Development of the new quasi-dimensional combustion model that will include more 3-D local effects (turbulence non-homogeneity, flame quenching, etc.).
- Extension of the 0-D turbulence model that will be detailed enough to physically predict the variations of in-cylinder flow and turbulence from cycle-to-cycle.

- The application of the developed cycle-simulation model in the analysis of exhaust gas emissions, fuel consumption and performance output of SI engine with the presence of CCV in combustion.



## References

1. Versteeg, H. K. and Malalasekera, W., *An Introduction to Computational Fluid Dynamic*, The Finite Volume Method, second edition, Pearson Education, 2007
2. Vitek, O., Macek, J., Poetsch, C., and Tatschl, R., *Modeling of Cycle-to-Cycle Variations in 0-D/1-D Simulation by Means of Combustion Model Parameter Perturbations based on Statistics of Cycle-Resolved Data*, SAE Technical Paper 2013-01-1314, 2013, doi:[10.4271/2013-01-1314](https://doi.org/10.4271/2013-01-1314).
3. Coble, A., Smallbone, A., Bhave, A., Mosbach, S. et al., *Implementing Detailed Chemistry and In-Cylinder Stratification into 0/1-D IC Engine Cycle Simulation Tools*, SAE Technical Paper 2011-01-0849, 2011, doi:[10.4271/2011-01-0849](https://doi.org/10.4271/2011-01-0849).
4. <https://www.avl.com/fire>
5. Ramos J. I., *Internal Combustion Engine Modeling*, Hemisphere Publishing Corporation, USA, 1989
6. Wilcox D. C., *Turbulence Modeling for CFD*, DCW Industries, Inc., California, 1993
7. Lander B. E. and Spalding D. B., *Mathematical Models of Turbulence*, Academic Press, London, 1972
8. Morel T. and Mansour N. N., *Modeling of Turbulence in Internal Combustion Engines*, SAE Technical Paper 820040, 1982
9. Polous S. G. and Heywood J. B., *The Effect of Chamber Geometry on Spark-Ignition Engine Combustion*, SAE Technical Paper 830334, 1983
10. Tabaczynski R. J., *Turbulence Measurements and Modelling in the Reciprocating Engines – an Overview*, IMechE, C51/83, 1983
11. Agarwal A., Filipi Z. S., Assanis N. D. and Baker D. M., *Assessment of Single- and Two-Zone Turbulence Formulations for Quasi-Dimensional Modeling of Spark-Ignition Engine Combustion*, Comb. Sci. and Tech., Vol. 136, pp. 13-39, 1998
12. Grill M., Billinger T. and Bargende M., *Quasi-Dimensional Modeling of Spark Ignition Engine Combustion with Variable Valve Train*, SAE Technical Paper 2006-01-1107, 2006
13. Verhelst S. and Sheppard C.G.W., *Multi-zone thermodynamic modeling of spark-ignition engine combustion – An overview*, Energy Conversion and Management 50, pp. 1326 – 1335, 2009
14. Watanabe K., Ito S. and Tsurushima T., *A New Quasi-Dimensional Combustion Model Applicable to Direct Injection Gasoline Engine*, SAE Technical Paper 2010-01-0544, 2010
15. Blizard N. C. and Keck J. C., *Experimental and Theoretical Investigation of Turbulent Burning Model for Internal Combustion Engines*, SAE Technical Paper 740191, 1974
16. Rakopoulos C.D., Michos, C.N. and Giakoumis, E.G., *Thermodynamic Analysis of SI Engine Operation on Variable Composition Biogas-Hydrogen Blends Using a Quasi-Dimensional, Multi-Zone Combustion Model*, SAE Technical Paper 2009-01-0931, 2009
17. Gouldin F. C., *An Application of Fractals to Modeling Premixed Turbulent Flames*, Combustion and Flame, Vol. 68, pp. 246-266, 1987

18. Cintosun E., Smallwood G. J. and Gülder O. L., *Flame Surface Fractal Characteristics in Premixed Turbulent Combustion at High Turbulence Intensities*, AIAA Journal, Vol. 45, No. 11, 2007
19. Bozza F., Gimelli A., Merola S. S. and Vaglieco B. M., *Validation of a Fractal Combustion Model through Flame Imaging*, SAE Technical Paper 2005-01-1120, 2005
20. Perini F., Paltrinieri F. and Mattarelli E., *A quasi-dimensional combustion model for performance and emissions of SI engines running on hydrogen-methane blends*, International Journal of Hydrogen Energy 35, 2010, pp. 4687-4701, doi:10.1016/j.ijhydene.2010.02.083.
21. Lee T-K. and Filipi Z. S., *Improving the Predictiveness of the Quasi-D Combustion Model for Spark Ignition Engines with Flexible Intake Systems*, International Journal of Automotive Technology, Vol. 12, No. 1, pp. 1-9, 2011
22. Wu C-M., Roberts C. E., Matthews R. D. and Hall M. J., *Effects of Engine Speed on Combustion in SI Engines: Comparisons of Predictions of a Fractal Burning Model with Experimental Data*, SAE Technical Paper 932714, 1993, doi:10.4271/932714.
23. Ballal D. R. and Lafebvre A. H., *The Influence of Spark Discharge Characteristics on Minimum Ignition Energy in Flowing Gases*, Combustion and Flame, vol. 24, pp. 99 – 108, 1975
24. Mansour M., Peters N. and Schrader L-U., *Experimental study of turbulent flame kernel propagation*, Experimental, Thermal and Fluid Science 32, pp. 1396-1404, 2008
25. Pischinger S. and Heywood J. B., *A Model for Flame Kernel Development in a Spark-Ignition Engine*, 23rd International Symposium on Combustion, Vol. 1, pp. 1033-1040, The Combustion Institute, 1990
26. Dahms, R. N., Fansler, T. D., Drake, M. C., Kuo, T.-W., Lippert, A.M. and Peters, N., *Modeling ignition phenomena in spray-guided spark-ignited engines*, Proceedings of the Combustion Institute, Vol. 32, pp. 2743-2750, 2009
27. Colin O. and Truffin, K., *A spark ignition model for large eddy simulation based on an FSD transport equation (ISSIM-LES)*, Proceedings of the Combustion Institute, Vol. 33, pp. 3097-3104, 2010
28. Duclos J-M. and Colin O., *Arc and Kernel Tracking Ignition Model for 3D Spark-Ignition Engine Calculations*, COMODIA 5: 343-350, 2001
29. Brehob, D. and Newman, C., *Monte Carlo Simulation of Cycle by Cycle Variability*, SAE Technical Paper 922165, 1992, doi:10.4271/922165.
30. Ji, C., and Ronney, P., *Modeling of Engine Cyclic Variation by a Thermodynamic Model*, SAE Technical Paper 2002-01-2736, 2002, doi:10.4271/2002-01-2736.
31. Mehrani, P., and Watson, H., *Modeling the Effects of Mixture Composition on Cyclic Variability*, SAE Technical Paper 2007-01-0672, 2007, doi:10.4271/2007-01-0672.
32. Abdi Aghdam, E., Barluka, A., Hattrell, T., Liu, K., et al., *Study of Cyclic Variation in an SI Engine Using Quasi-Dimensional Combustion Model*, SAE Technical Paper 2007-01-0939, 2007, doi:10.4271/2007-01-0939.
33. Poinso T. and Veynante D., *Theoretical and Numerical Combustion*, R. T. Edwards. Inc. USA, 2001

34. Bozza F., Gimelli A., Russo F., Torella E., Strazzullo L. and Mastrangelo G., *Application of a Quasi-Dimensional Combustion Model to the Development of a High-EGR VVT SI Engine*, ICE, 2005
35. Tatschl R. et al., *LES Simulation of Flame Propagation in a Direct-Injection SI-Engine to Identify the Causes of Cycle-to-Cycle Combustion Variations*, SAE Technical Paper 2013-01-1084, 2013
36. Pera C., Richard, S., and Angelberger, C., *Exploitation of Multi-Cycle Engine LES to Introduce Physical Perturbations in 1D Engine Models for Reproducing CCV*, SAE Technical Paper 2012-01-0127, 2012, doi:[10.4271/2012-01-0127](https://doi.org/10.4271/2012-01-0127).
37. Merker G. P., Schwarz C., Stiesch G., and Otto F., *Simulating Combustion, Simulation of combustion and pollutant formation for engine-development*, Springer-Verlag, Berlin Heidelberg, 2006
38. Šoda, A., Mannini, C. and Sjerić, M., *Investigation of Unsteady Air Flow Around Two-Dimensional Rectangular Cylinders*, Transactions of Famera, XXXV-2, ISSN 1333-1124, University of Zagreb, 2011
39. Heywood, J. B. *Internal Combustion Engine Fundamentals*, McGraw-Hill Inc., New York, 1988
40. Prucka, R. G., Lee, T., Filipi, Z. and Assanis, Z., *Turbulence Intensity Calculation from Cylinder Pressure Data in a High Degree of Freedom Spark-Ignition Engine*, SAE Technical Paper 2010-01-0175, 2010
41. Dent, J. C. and Salama, N. S., *The Measurement of the Turbulence Characteristics in an Internal Combustion Engine Cylinder*, SAE Technical Paper 750886, 1975
42. Hall, M. J., and Bracco, F. V., *A Study of Velocities and Turbulence Intensities Measured in Firing and Motored Engines*, SAE Technical Paper 870453, 1987
43. Davidson, L., *An Introduction to Turbulence Models*, Publication 97/2, Chalmers University of Technology, Sweden, 2003
44. <http://www.cd-adapco.com/industries/defense>
45. <http://www.ozeninc.com/products/hpc/features/>
46. Launder, B. E., Reece, G. J. and Rodi, W., *Progress in the Development of a Reynolds-Stress Turbulent Closure*, Journal of Fluid Mechanics, Vol. 68 (3), pp. 537-566., 1975
47. Launder, B. E. and Spalding, D. B., *The Numerical Computation of Turbulent Flows*, Comp. Methods Appl. Mech. Eng., Vol. 3, pp. 269-289., 1974
48. Launder, B. E. and Sharma, B. I., *Application of the Energy Dissipation Model of Turbulence to the Calculation of Flow Near a Spinning Disc*, Letters in Heat and Mass Transfer, vol. 1, no. 2, pp. 131-138., 1974
49. Ahmadi-Befrui, B. and Gosman, A. D., *Assessment of Variants of the  $k-\varepsilon$  Turbulence Model for Engine Flow Applications*, International Journal for Numerical Methods in Fluids, Vol. 9, 1073-1086, 1989
50. Borgnakke, C., Arpaci, V., and Tabaczynski, R., *A Model for the Instantaneous Heat Transfer and Turbulence in a Spark Ignition Engine*, SAE Technical Paper 800287, 1980, doi:[10.4271/800287](https://doi.org/10.4271/800287).
51. Wong, V. and Hoult, D., *Rapid Distortion Theory Applied to Turbulent Combustion*, SAE Technical Paper 790357, 1979, doi:[10.4271/790357](https://doi.org/10.4271/790357).

52. Sjerić M., Kozarac D. and Bogensperger M., *Implementation of a Single Zone  $k-\epsilon$  Turbulence Model in a Multi Zone Combustion Model*, SAE Technical Paper, 2012-01-0130, 2012
53. Lämmle, C., *Numerical and Experimental Study of Flame Propagation and Knock in a Compressed Natural Gas Engine*, PhD Thesis, Swiss Federal Institute of Technology Zurich, 2005
54. Heywood, J. B., *Combustion and its Modeling in Spark-Ignition Engines*, International Symposium COMODIA 94, 1994
55. Aghajani, H., Mehdizadeh, S.N., Tabejamaat, S., *Analytical modeling of flame kernel development in SI engines*, 2<sup>nd</sup> ICSCCE, 5-8 July 2006, Athens, Greece
56. Dahms, R., *Modeling of Combustion in Spray-Guided Spark-Ignition Engines*, PhD Thesis, RWTH Aachen University, 2010
57. Fan, L. and Reitz, R., *Development of an ignition and combustion model for spark-ignition engines*, SAE Technical Paper 2000-01-2809, 2000, doi:[10.4271/2000-01-2809](https://doi.org/10.4271/2000-01-2809).
58. Alger, T. et al., *The Effect of Sparkplug Design on Initial Flame Kernel Development and Sparkplug Performance*, SAE Technical Paper 2006-01-0224, 2004, doi:[10.4271/2006-01-0224](https://doi.org/10.4271/2006-01-0224).
59. Lee, Y. G. and Boehler, J. T., *Flame Kernel Development and its Effects on Engine Performance with Various Spark Plug Electrode Configurations*, SAE Technical Paper 2005-01-1133, 2005, doi:[10.4271/2005-01-1133](https://doi.org/10.4271/2005-01-1133).
60. Tan, Z. and Reitz, R., *Modeling Ignition and Combustion in Spark-ignition Engines Using a Level Set Method*, SAE Technical Paper 2003-01-0722, 2003, doi:[10.4271/2003-01-0722](https://doi.org/10.4271/2003-01-0722).
61. Tan, Z., Kong, S., and Reitz, R., *Modeling Premixed and Direct Injection SI Engine Combustion Using the G-Equation Model*, SAE Technical Paper 2003-01-1843, 2003, doi:[10.4271/2003-01-1843](https://doi.org/10.4271/2003-01-1843).
62. Bohbot, J., Gillet, N., and Benkenida, A., *IFP-C3D: an Unstructured Parallel Solver for Reactive Compressible Gas Flow with Spray*, Oil & Gas Science and Technology, Vol. 64, No. 3, pp. 309-335, 2009.
63. Pashley, N., Stone, R., Roberts, G., *Ignition System Measurement Techniques and Correlations for Breakdown and Arc Voltages and Currents*, SAE Technical Paper 2000-01-0245, doi:[10.4271/2000-01-0245](https://doi.org/10.4271/2000-01-0245).
64. Verhoeven, D., *Spark Heat Transfer Measurements in Flowing Gases*, REVUE DE L'INSTITUT FRANÇAIS DU PÉTROLE, Vol. 52, N° 4, JUILLET-AOÛT, 1997.
65. Eisazadeh-Far, K., Parsinejad, F., Metghalchi, H., and Keck, J. C., *On flame kernel formation and propagation in premixed gases*, Combustion and Flame, Vol. 157, pp. 2211-2221, 2010
66. Verhelst, S., Sierens, R., *A quasi-dimensional model for the power cycle of a hydrogen fuelled ICE*, Int. Journal of Hydrogen Energy, 2007;32: 3545-54.
67. Song, J., and Sunwoo, M., *Flame kernel formation and propagation modelling in spark ignition engines*, IMechE, Vol. 215 Part D, 2001
68. Metghalchi, M. and Keck, J. C., *Laminar Burning Velocity of Propane-Air Mixtures at High Temperature and Pressure*, Combustion and Flame 38, 1980, pp. 143-154

69. Tan, Z., and Reitz, R. D., *An ignition and combustion model based on the level-set method for spark ignition engine multidimensional modelling*, *Combustion and Flame*, Vol. 145, pp. 1 – 15, 2006
70. Schmid, P. J, and Henningson D. S., *Optimal energy density growth in Hagen-Poiseuille flow*, *Journal of Fluid Mechanics*, Volume 277, pp. 197-225, 1994
71. Shichida, T. et al., *Numerical Simulation for Ignitability of Spark Plug using Detailed Chemical Kinetics*, SAE Technical Paper, 2014-01-1234, 2014, doi:[10.4271/2014-01-1234](https://doi.org/10.4271/2014-01-1234).
72. Piock, W. F., Weyand, P., Wolf, E., and Heise, V., *Ignition Systems for Spray-Guided Stratified Combustion*, SAE Technical Paper 2010-01-0598, 2010
73. Goschütz, M., Schulz, C. and Kaiser, S., *Endoscopic Imaging of Early Flame Propagation in a Near-Production Engine*, *SAE Int. J. Engines* 7(1):2014, doi:[10.4271/2014-01-1178](https://doi.org/10.4271/2014-01-1178).
74. Shen, H., Hinze, P., and Heywood, J., *A Study of Cycle-to-Cycle Variations in SI Engines Using a Modified Quasi-Dimensional Model*, SAE Technical Paper 961187, 1996, doi:[10.4271/961187](https://doi.org/10.4271/961187).
75. Gettel, L. E., and Tsai, K.C., *Flame Kernel Development with the Multiple Electrode Spark Plug*, *Combustion and Flame*, Vol. 54, pp. 225-228, 1983
76. Graf, J., Lauer, T. and Geringer, B., *Ignition Systems for Highly-Supercharged Downsized Engines*, *MTZ* 11/2013, Vol. 74, 2013
77. Herweg, R., and Ziegler, G. F. W., *Flame Kernel Formation in a Spark-Ignition Engine*, *International Symposium COMODIA 90*, pp. 173-178, 1990.
78. Kaminski, C. F., Bai, X. S., Hult, J., Dreizler, A., Lindenmaier, S., and Fuchs, L. *Flame growth and wrinkling in a turbulent flow*, *Applied Physics. B* 71, pp. 711-716, 2000
79. Matthews, R. D., Hall, M. J., Dai, W. and Davis, G. C., *Combustion Modeling in SI Engines with Peninsula-Fractal Combustion Model*, SAE Technical Paper 960072, 1996
80. Filipi, Z. and Assanis, D. N., *Quasi-Dimensional Computer Simulation on the Turbocharged Spark-Ignition Engine and its Use for 2- and 4-Valve Engine Matching Studies*, SAE Technical Paper 910075, 1991, doi:[10.4271/910075](https://doi.org/10.4271/910075).
81. Sjerić, M., Kozarac, D. and Šagi, G., *Development of a Stratified Fractal Combustion Model*, 23<sup>rd</sup> JUMV International Automotive Conference with Exhibition, Belgrade, Serbia, 19-21<sup>st</sup> April, 2011
82. Peters, N., *Laminar Flamelet Concept in Turbulent Combustion*, 21<sup>st</sup> Symposium (International) on Combustion, The Combustion Institute, pp. 1231-1250, 1986
83. North, G. L. and Santavicca, D. A., *The Fractal Nature of Premixed Turbulent Flames*, *Combust. Sci. and Tech.*, Vol. 72, pp. 215-232, 1990
84. Metgalchi, M. and Keck, J., *Burning Velocities of Air with Methanol, Isooctane and Indolene at High Pressure and Temperature*, *Combustion and Flame*, Vol. 48, pp. 191-210, 1982
85. Bozza, F. et al., *A Theoretical Comparison of Various VVA Systems for Performance and Emission Improvements of SI-Engines*, SAE Technical Paper 2001-01-0670, 2001, doi:[10.4271/2001-01-0670](https://doi.org/10.4271/2001-01-0670).

86. AVL BOOST - version 2010, Users Guide and Theory, Edition 11/2010
87. Marble, F. E. and Broadwell, J. E., *The Coherent Flame Model for Turbulent Chemical Reactions*, Project Squid Report TRW-9-PU, Purdue University, 1977
88. Colin, O., and Benkenida, A., *The 3-Zones Extended Coherent Flame Model (ECFM3Z) for Computing Premixed/Diffusion Combustion*, Oil & Gas Science and Technology – Rev. IFP., Vol. 59, No. 6, pp. 593-609, 2004
89. Keck, J. C., and Heywood, J. B., *Early Flame Development and Burning Rates in Spark Ignition Engines and Their Cyclic Variability*, SAE Technical Paper 870164, 1987
90. Lim, M. T., Anderson, R. W., and Arpaci, V. S., *Prediction of Spark Kernel Development in Constant Volume Combustion*, Combustion and Flame, Vol. 69, pp. 303-316, 1987
91. Dahms, R. N., Drake, M.C., Fansler, T.D., Kuo, T.-W. and Peters, N., *Understanding ignition processes in spray-guided gasoline engines using high-speed imaging and the extended spark-ignition model SparkCIMM. Part A: Spark channel processes and the turbulent flame front propagation*, Combustion and Flame, Vol. 158, pp. 2229-2244, 2011
92. Dahms, R. N., Drake, M.C., Fansler, T.D., Kuo, T.-W. and Peters, N., *Understanding ignition processes in spray-guided gasoline engines using high-speed imaging and the extended spark-ignition model SparkCIMM. Part B: Importance of molecular fuel properties in early flame front propagation*, Combustion and Flame, Vol. 158, pp. 2245-2260, 2011
93. Pitt, P. L., Clements, R. M., and Topham, D. R., *The Early Phase of Spark Ignition*, Combustion Science and Technology, 78:4-6, pp. 289-314, 1991
94. Boulouchos, K., Steiner, T. and Dimopoulos, P., *Investigation of Flame Speed Models for the Flame Growth Period during the Premixed Engine Combustion*, SAE Technical Paper 940476, 1994, doi:[10.4271/940476](https://doi.org/10.4271/940476).
95. Arpaci, V. S., Ko, Y., Taek Lim, M. and Lee, H. S., *Spark kernel development in constant volume combustion*, Combustion and Flame, Vol. 135, pp. 315-322, 2003
96. North, G. L. and Santavicca, D. A., *Fractal Analysis of Premixed Turbulent Flame Structure*, Presented at the Eastern States Section of the Combustion Institute Fall Meeting, San Juan, Puerto Rico, 1986
97. Mantzaras, J., Felton, P. G., and Bracco, F., V., *Fractals and Turbulent Premixed Engines*, Combust. Flame, 1989
98. Santavicca, D. A., Liou, D., and North, G. L., *A Fractal Model of Turbulent Flame Kernel Growth*, SAE Technical Paper 900024, 1990, doi:[10.4271/900024](https://doi.org/10.4271/900024).
99. Smith, J. E., *Introduction to Evolutionary Computing*, Springer-Verlag, Berlin, Germany, 2003
100. Peterson, B., and Sick, V., *High-speed flow and fuel imaging study of available spark energy in a spray-guided direct-injection engine and implications on misfires*, International Journal of Engine Research, Vol. 11, 2010
101. Ozdor, N., Dulger, M., and Sher, E., *Cyclic Variability in Spark Ignition Engines – A Literature Survey*, SAE Technical Paper 940987, 1994, doi:[10.4271/940987](https://doi.org/10.4271/940987).

102. Mickelsen, W.R., and Ernstein, N.E., *Growth Rates of Turbulent Free Flames*, IV<sup>th</sup> Symp. (Int.) on Combustion, pp. 325-333, Baltimore, 1953, Williams & Wilkins
103. Stone, C. R., Brown, A. G., and Beckwith, P., *Cycle-by-Cycle Variations in Spark Ignition Engine Combustion – Part II: Modeling of Flame Kernel Displacements as a Cause of Cycle-by-Cycle Variations*, SAE Technical Paper 960613, 1996, doi:[10.4271/960613](https://doi.org/10.4271/960613).
104. Holmström, K., and Denbratt, I., *Cyclic Variation in an SI Engine Due to the Random Motion of Flame Kernel*, SAE Technical Paper 961152, 1996, doi:[10.4271/961152](https://doi.org/10.4271/961152).
105. Lacour, C. and Pera, C., *An Experimental Database Dedicated to the Study and Modelling of Cyclic Variability in Spark-Ignition Engines with LES*, SAE Technical Paper 2011-01-1282, 2011, doi:[10.4271/2011-01-1282](https://doi.org/10.4271/2011-01-1282).
106. Vermorel, O., Richard, S., Colin, O., Angelberger, C. et al., *Multi-Cycle LES Simulations of Flow and Combustion in a PFI SI 4-Valve Production Engine*, SAE Technical Paper 2007-01-0151, 2007, doi:[10.4271/2007-01-0151](https://doi.org/10.4271/2007-01-0151).
107. Vitek, O., Macek, J., Tatschl, R., Pavlovic, Z. et al., *LES Simulation of Direct Injection SI-Engine In-Cylinder Flow*, SAE Technical Paper 2012-01-0138, 2012, doi:[10.4271/2012-01-0138](https://doi.org/10.4271/2012-01-0138).
108. Manzie, C., and Watson, H., *Modelling Combustion Variability in LPG Injected Engines for Improved Engine Performace at Idle*, SAE Technical Paper 2004-01-0420, 2004, doi:[10.4271/2004-01-0420](https://doi.org/10.4271/2004-01-0420).
109. Kulzer, A., Lejsek, D., Keifer, A., and Hettinger, A., *A Pressure Trace Analysis Methods to Analyze Combustion Features and Cyclic Variability of Different Gasoline Combustion Concepts*, SAE Technical Paper 2009-01-0501, 2009, doi:[10.4271/2009-01-0501](https://doi.org/10.4271/2009-01-0501).
110. Van Blarigan, A., Kozarac, D., Seiser, R., Chen, J.Y, Cattolica, R. and Dibble, R., *Spark-ignited engine NO<sub>x</sub> emissions in a low-nitrogen oxycombustion environment*, Applied Energy, Vol. 118, pp. 22-32, 2014
111. <https://www.avl.com/boost1>
112. Ma, F., Shen, H., Liu, C., Wu, D. et al., *The Importance of Turbulence and Initial Flame Kernel Center Position on the Cyclic Combustion Variations for Spark-Ignition Engine*, SAE Technical Paper 961969, 1996, doi:[10.4271/961969](https://doi.org/10.4271/961969).
113. Brown, A., Stone, C., and Beckwith, P., *Cycle-by-Cycle Variations in Spark Ignition Engine Combustion - Part I: Flame Speed and Combustion Measurements and a Simplified Turbulent Combustion Model*, SAE Technical Paper 960612, 1996, doi:[10.4271/960612](https://doi.org/10.4271/960612).
114. Dai, W., Trigui, N., and Lu, Y., *Modeling of Cyclic Variations in Spark-Ignition Engines*, SAE Technical Paper 2000-01-2036, 2000, doi:[10.4271/2000-01-2036](https://doi.org/10.4271/2000-01-2036).
115. Sjerić, M., Kozarac, D., Tomić, R., *Development of a Two Zone Turbulence Model and its Application to the Cycle-Simulation*, Thermal Science, 2013, doi:[10.2298/TSCI130103030S](https://doi.org/10.2298/TSCI130103030S).
116. Woschni, G., *A Universally Applicable Equation for the Instantaneous Heat Transfer Coefficient in the Internal Combustion Engine*, SAE Technical Paper 670931, 1967, doi:[10.4271/670931](https://doi.org/10.4271/670931).

117. Vermorel, O. et al., *Towards the understanding of cyclic variability in a spark ignited engine using multi-cycle LES*, *Combustion and Flame* 156, 2009, pp. 1525-1541
118. Ma F. et al., *Development and validation of a quasi-dimensional combustion model for SI engines fuelled by HCNG with variable hydrogen fractions*, *International Journal of Hydrogen Energy* 33, pp. 4863-4875, 2008
119. Gouldin F. C., Hilton S. M. and Lamb T., *Experimental Evaluation of the Fractal Geometry of Flamelets*, 22<sup>nd</sup> Symposium (International) on Combustion 1988; The Combustion Institute, Pittsburgh, pp. 541 – 550, 1988



## **Carriculum Vitae in English**

### Personal data

First name: Momir  
Last name: Sjerić  
Date of birth: 3<sup>rd</sup> October 1985  
Place of birth: Bjelovar, Croatia  
Email: [momir.sjeric@fsb.hr](mailto:momir.sjeric@fsb.hr)

### Education

2009 – 2014 PhD student, postgraduate study at Faculty of Mechanical Engineering and Naval Architecture, University of Zagreb, course: Teory of constructions  
2008 – 2009 Master degree in mechanical engineering (MEng Mech), Faculty of Mechanical Engineering and Naval Architecture, University of Zagreb, course: Engineering modeling and computational simulations  
2004 – 2008 Bachelor degree in mechanical engineering (BEng Mech), Faculty of Mechanical Engineering and Naval Architecture, University of Zagreb, course: Engineering modeling and computational simulations  
2000 – 2004 Technical high school, Kutina, Croatia  
1992 – 2000 Elementary school, Garešnica, Croatia

### Employment

2011 – Junior Researcher, Faculty of Mechanical Engineering and Naval Architecture, University of Zagreb  
2010 – 2011 Project Associate, Faculty of Mechanical Engineering and Naval Architecture, University of Zagreb

### Foreign languages

English – very good (written and spoken)

### Publications

- For the list of publications please visit the page:  
<http://bib.irb.hr/lista-radova?autor=323056&lang=EN>

## **Carriculum Vitae in Croatian**

### Osobni podaci

Ime: Momir  
Prezime: Sjerić  
Datum rođenja: 3. listopada 1985.  
Mjesto rođenja: Bjelovar, Hrvatska  
Email: [momir.sjeric@fsb.hr](mailto:momir.sjeric@fsb.hr)

### Obrazovanje

2009. – 2014. Student na doktorskom studiju Fakulteta strojarstva i brodogradnje, Sveučilišta u Zagrebu, smjer: Teorija konstrukcija  
2008. – 2009. Magistar inženjer strojarstva, Fakultet strojarstva i brodogradnje, Sveučilišta u Zagrebu, smjer: Inženjersko modeliranje i računalne simulacije  
2004. – 2008. Prvostupnik strojarske struke, Fakultet strojarstva i brodogradnje, Sveučilišta u Zagrebu, smjer: Inženjersko modeliranje i računalne simulacije  
2000. – 2004. Srednja tehnička škola, Tehnička škola Kutina  
1992. – 2000. Osnovna škola, Garešnica

### Zaposlenje

2011. – Znanstveni novak, Fakultet strojarstva i brodogradnje, Sveučilište u Zagrebu  
2010. – 2011. Stručni suradnik na projektu, Fakultet strojarstva i brodogradnje, Sveučilište u Zagrebu

### Strani jezici

Engleski – vrlo dobro (u pisanju i govoru)

### Bibliografija

- Za listu publikacija posjetiti web stranicu:  
<http://bib.irb.hr/lista-radova?autor=323056>

## APPENDIX

### *Derivation of k-ε differential equations for 0-D approach*

Initial equations for derivation of turbulence model are Reynolds decomposition of flow velocity (1), continuity equation (2) and Navier-Stokes equation of Newtonian fluid (3):

$$u_i = \bar{u}_i + u_i' \quad (1)$$

$$\rho_{,t} + (\rho u_i)_{,i} = 0 \quad (2)$$

$$(\rho u_i)_{,t} + (\rho u_i u_j)_{,j} = -p_{,i} + \tau_{ij,j} + f_i \quad (3)$$

where  $\rho$  (kg/m<sup>3</sup>) is fluid density,  $u$  (m/s) is flow velocity,  $p$  (Pa) is pressure,  $\tau$  (N/m<sup>2</sup>) is stress tensor and  $f$  (N/m<sup>3</sup>) represents body forces acting on the fluid.

If the Reynolds decomposition for the flow velocity represented with equation (1) is inserted into Navier-Stokes equation (3) and if the body forces, pressure and density fluctuations are neglected, the following equation may be written:

$$(\rho(\bar{u}_i + u_i'))_{,t} + (\rho(\bar{u}_i + u_i')(\bar{u}_j + u_j'))_{,j} = -\bar{p}_{,i} + (\bar{\tau}_{ij} + \tau_{ij}')_{,j} \quad (4)$$

Integration of equation (4) over the time leads to the time averaged Navier-Stokes equation (bearing in mind that the mean value of any pulsating property is zero):

$$(\rho u_i)_{,t} + (\rho u_i u_j)_{,j} = -p_{,i} + \tau_{ij,j} - \overline{\rho u_i' u_j'}_{,j} \quad (5)$$

where the last term  $\overline{\rho u_i' u_j'}$  on the right hand-side represents the Reynolds stress tensor as an additional fluid stress due to velocity fluctuations  $u'$ .

If equation (3) is subtracted from equation (5), multiplication the result by  $u'$  and time averaging yields to equation of turbulent kinetic energy  $k$ :

$$(\rho k)_{,t} + (\rho k u_i)_{,i} = -\overline{\rho u_i' u_j'}_{,i} u_{i,j} - \rho \frac{\overline{u_i' u_i' u_j' u_j'}}{2}{}_{,j} - \overline{p_{,i} u_i'} + \overline{\tau_{ij}' u_i'}_{,j} - \overline{\tau_{ij}' u_i'}_{,i,j} \quad (6)$$

where turbulent kinetic energy is calculated as:

$$k = \frac{1}{2} \overline{u_i' u_i'} \quad (7)$$

At high Reynolds numbers the fourth term on the right-hand side of equation (6) is smaller than the first and can be neglected as well as the pressure-velocity correlations represented by third term on the right-hand side. The first term on the right-hand side represents the production of turbulent kinetic energy that can be approximated by well-known Boussinesq correlation:

$$-\rho \overline{u_i' u_j'} = \mu_t (u_{i,j} + u_{j,i}) - \frac{2}{3} \delta_{ij} (\mu_t u_{k,k} + \rho k) \quad (8)$$

where  $\mu_t$  (Pa·s) is turbulent (eddy) viscosity and  $\delta_{ij}$  is Kronecker delta symbol. The Boussinesq assumption states that the Reynolds stress tensor is proportional to the mean strain rate tensor.

If the Boussinesq correlation is substituted into equation (6) the following differential equation of turbulent kinetic energy can be written:

$$(\rho k)_{,t} + (\rho k u_i)_{,i} = \left( \frac{\mu_t}{\sigma_k} k_{,i} \right)_{,i} + P - \rho \varepsilon \quad (9)$$

The dissipation rate of turbulent kinetic energy is defined as:

$$\varepsilon = \frac{\overline{\tau_{ij}' u'_{i,j}}}{\rho} \quad (10)$$

When the values of  $\mu_t$  and  $\sigma_k$  are specified and when the dissipation rate of turbulent kinetic energy is defined, equation (6) can be closed. Differential equation of dissipation rate of turbulent kinetic energy can be written by analogy with equation (6):

$$(\rho \varepsilon)_{,t} + (\rho \varepsilon u_i)_{,i} = \left( \frac{\mu_t}{\sigma_\varepsilon} \varepsilon_{,i} \right)_{,i} + \frac{\varepsilon}{k} (C_1 P - C_2 \rho \varepsilon) + C_3 \rho \varepsilon u_{i,i} \quad (11)$$

The effects of compressibility in  $k$  and  $\varepsilon$  equations appear through the production term  $P$ :

$$P = \mu_t (u_{i,j} + u_{j,i}) \mu_{i,j} - \frac{2}{3} \delta_{ij} (\mu_t u_{k,k}^2 + \rho k u_{k,k}) \quad (12)$$

where the first term represents the shear effects while the second term is dilatation effect on the turbulent kinetic energy.

Equations (9) and (11) represent differential equations of  $k$ - $\varepsilon$  turbulence model for multi-dimensional models. In order to transform such equations for 0-D models, a homogeneous and isotropic turbulent flow field is assumed. The total velocity divergence can be expressed from the continuity equation (2) if density is uniform in space but may vary in time:

$$u_{i,j} = -\frac{1}{\rho} \frac{d\rho}{dt} \quad (13)$$

If equation (13) is applied to the definition of the strain rate tensor  $S_{ij}$ , only members on the main diagonal exist:

$$S_{ij} = \frac{1}{2} (u_{i,j} + u_{j,i}) = \begin{bmatrix} u_{1,1} & 0 & 0 \\ 0 & u_{2,2} & 0 \\ 0 & 0 & u_{3,3} \end{bmatrix} \quad (14)$$

and the total strain rate (total velocity divergence) of cylinder for the 0-D approach is equal to:

$$S_{ij}^{\text{tot}} = u_{i,j}^{\text{tot}} = -\frac{1}{\rho} \frac{d\rho}{dt} \quad (15)$$

If the homogeneous and isotropic turbulent flow field is assumed, the convection and diffusion terms do not exist. By addition of differential equations (9) and (11) over the index  $i$  for 3-D case and by the application of equation (15) for the total velocity divergence, and with the assumption of  $C_1 = 1.44$ ,  $C_3 = -0.373$ , it is possible to write resulting differential equations for 0-D model:

$$\frac{dk}{dt} = \frac{2}{3} \frac{k}{\rho} \frac{d\rho}{dt} - \varepsilon \quad (16)$$

$$\frac{d\varepsilon}{dt} = \frac{4}{3} \frac{\varepsilon}{\rho} \frac{d\rho}{dt} - C_2 \frac{\varepsilon^2}{k} \quad (17)$$

where  $C_2$  (-) is user-defined constant usually set to 1.92.

Equations (16) and (17) neglect the fluxes of  $k$  and  $\varepsilon$  associated with combustion. Under the equilibrium condition between the production and dissipation of turbulent kinetic energy, differential equations can be extended (detail derivation of new terms can be found in [5]):

$$\frac{dk}{dt} = \frac{2}{3} \frac{k}{\rho} \frac{d\rho}{dt} - \frac{2}{3} \frac{k}{\nu} \frac{d\nu}{dt} - \varepsilon \quad (18)$$

$$\frac{d\varepsilon}{dt} = \frac{4}{3} \frac{\varepsilon}{\rho} \frac{d\rho}{dt} + \frac{5}{12} \frac{\varepsilon}{\nu} \frac{d\nu}{dt} - C_2 \frac{\varepsilon^2}{k} \quad (19)$$

where  $\nu$  ( $m^2/s$ ) is the kinematic viscosity of fluid.

### Basic conservation equations

The single zone approach for the description of in-cylinder state during the engine cycle is illustrated below in Figure 88.

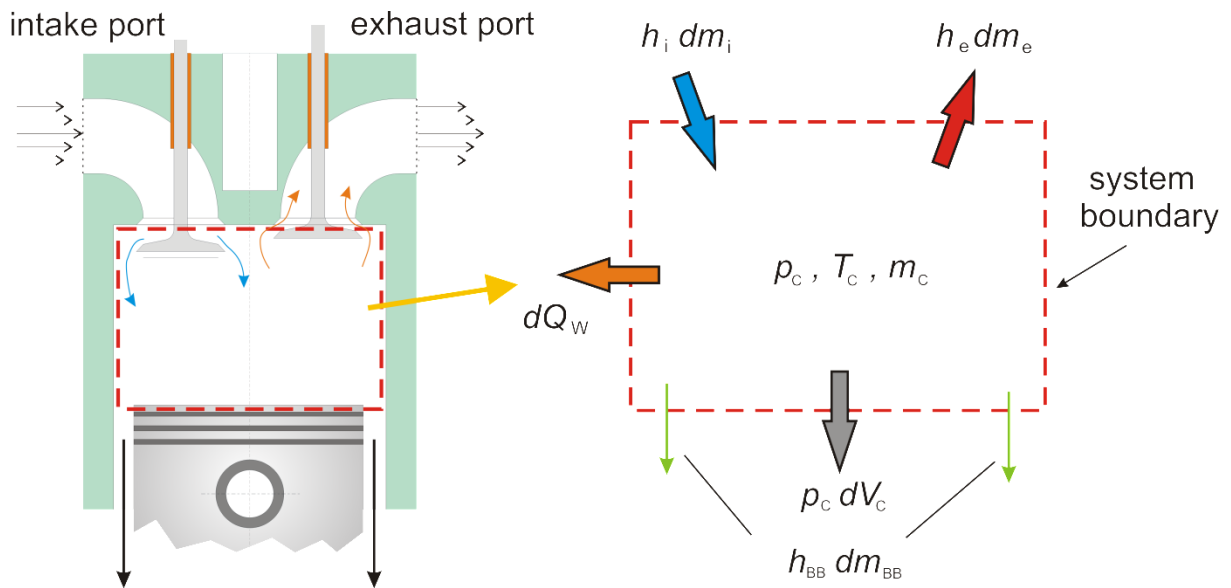


Figure 88. Energy balance of the cylinder – single zone description of cylinder domain.

The thermodynamic state of the cylinder can be calculated using the first law of thermodynamics:

$$\begin{aligned} \frac{d(m_C \cdot u)}{d\alpha} = & -p_C \cdot \frac{dV}{d\alpha} + \frac{dQ_F}{d\alpha} - \sum \frac{dQ_W}{d\alpha} - h_{BB} \cdot \frac{dm_{BB}}{d\alpha} + \dots \\ & \dots + \sum \frac{dm_i}{d\alpha} \cdot h_i - \sum \frac{dm_e}{d\alpha} \cdot h_e - q_{ev} \cdot f \cdot \frac{dm_{ev}}{d\alpha} \end{aligned} \quad (20)$$

where are:

$\frac{d(m_C \cdot u)}{d\alpha}$  the change of internal energy in the cylinder over the time,

$-p_C \cdot \frac{dV}{d\alpha}$  piston work caused by its movement,

$\frac{dQ_F}{d\alpha}$  rate of heat release caused by the combustion of fuel,

$\sum \frac{dQ_W}{d\alpha}$  the change of wall heat losses,

$h_{BB} \cdot \frac{dm_{BB}}{d\alpha}$  enthalpy flow due to blow-by,

$\sum \frac{dm_i}{d\alpha} \cdot h_i$  enthalpy flow of the inflow mass,

$\sum \frac{dm_e}{d\alpha} \cdot h_e$  enthalpy flow of mass that flows out the cylinder,

$q_{ev} \cdot f \cdot \frac{dm_{ev}}{d\alpha}$  rate of evaporation heat.

The variation of in-cylinder mass can be calculated as the sum of in-flowing and out-flowing masses:

$$\frac{dm_C}{d\alpha} = \sum \frac{dm_i}{d\alpha} - \sum \frac{dm_e}{d\alpha} - \frac{dm_{BB}}{d\alpha} + \frac{dm_{ev}}{d\alpha} \quad (21)$$

where the first and second terms correspond to inflow and outflow mass, respectively. The third term is blow-by flow while the last one represents the mass flow caused by the in-cylinder evaporation (fuel injection). In-cylinder temperature at each time step during the engine cycle excluding the combustion period can be calculated from equation (20) that can be solved using a Runge-Kutta method. Once the cylinder temperature is calculated, in-cylinder pressure can be obtained from the gas equation:

$$p_C = \frac{1}{V} \cdot m_C \cdot R_C \cdot T_C \quad (22)$$

During the combustion, when the quasi-dimensional combustion model is used, the cylinder mixture is divided into the burned and unburned mass (two zone approach). For each particular mass, the conservation of mass and energy equation are applied and given below.

### *Multi-zone combustion model – pressure and temperature derivatives*

In order to derive the expressions for the pressure and temperature derivative, the gas equation for each zone and for the entire cylinder mass as well as energy equation should be written:

$$p_c V_i = m_i R_i T_i \quad (23)$$

$$p_c V_c = \sum_{i=1}^N m_i R_i T_i \quad (24)$$

$$\frac{d(m_i u_i)}{d\alpha} = \frac{dQ}{d\alpha} - p_c \frac{dV_i}{d\alpha} + \sum_{j=1}^M \frac{dm_{ij}}{d\alpha} \quad (25)$$

where N (-) and M (-) represents the number of zones and number of species, respectively. Time derivatives of equations (23) and (24) lead to the following expressions:

$$p_c \frac{dV_i}{d\alpha} = R_i T_i \frac{dm_i}{d\alpha} + m_i T_i \frac{dR_i}{d\alpha} + R_i m_i \frac{dT_i}{d\alpha} - V_i \frac{dp_c}{d\alpha} \quad (26)$$

$$\frac{dp_c}{d\alpha} V_c = \sum_{i=1}^N \left( m_i R_i \frac{dT_i}{d\alpha} + m_i T_i \left( \frac{\partial R_i}{\partial T_i} \frac{dT_i}{d\alpha} + \frac{\partial R_i}{\partial p_c} \frac{dp_c}{d\alpha} + \sum_{j=1}^M \frac{\partial R_i}{\partial x_j} \frac{dx_{ji}}{d\alpha} \right) + \frac{dm_i}{d\alpha} R_i T_i \right) - p_c \frac{dV_c}{d\alpha} \quad (27)$$

The gas constant and internal energy for the real gases are considered as function of pressure, temperature and mixture composition. Therefore, their time derivatives are:

$$\frac{dR_i}{d\alpha} = \frac{\partial R_i}{\partial T_i} \frac{dT_i}{d\alpha} + \frac{\partial R_i}{\partial p_c} \frac{dp_c}{d\alpha} + \sum_{j=1}^M \frac{\partial R_i}{\partial x_j} \frac{dx_{ji}}{d\alpha} \quad (28)$$

$$\frac{du_i}{d\alpha} = \frac{\partial u_i}{\partial T_i} \frac{dT_i}{d\alpha} + \frac{\partial u_i}{\partial p_c} \frac{dp_c}{d\alpha} + \sum_{j=1}^M \frac{\partial u_i}{\partial x_j} \frac{dx_{ji}}{d\alpha} \quad (29)$$

If equations (26), (28) and (29) are inserted into the energy equation (25) it is possible to calculate the time derivative of zone temperature. After that, the rate of change of in-cylinder pressure can also be expressed:



$$\frac{dT_i}{d\alpha} = - \frac{1}{\left( \frac{\partial u_i}{\partial T_i} + R_i + T_i \frac{\partial R_i}{\partial T_i} \right)} \left[ \left( T_i \frac{\partial R_i}{\partial p_c} - \frac{R_i T_i}{p_c} + \frac{\partial u_i}{\partial p_c} \right) \frac{dp_c}{d\alpha} + \sum_{j=1}^M \frac{\partial u_i}{\partial x_j} \frac{dx_{ji}}{d\alpha} + T_i \left( \sum_{j=1}^M \frac{\partial R_i}{\partial x_j} \frac{dx_{ji}}{d\alpha} \right) + \frac{1}{m_i} \left( h_i \frac{dm_i}{d\alpha} - \sum_{j=1}^M \frac{dm_{ij}}{d\alpha} h_j - \frac{dQ_j}{d\alpha} \right) \right] \quad (30)$$

$$\frac{dp_c}{d\alpha} = \frac{\sum_{i=1}^N m_i T_i \left( \sum_{j=1}^M \frac{\partial R_i}{\partial x_j} \frac{dx_{ji}}{d\alpha} \right) + R_i T_i \frac{dm_i}{d\alpha}}{\left( \frac{\partial u_i}{\partial T_i} + R_i + T_i \frac{\partial R_i}{\partial T_i} \right)} \left( R_i + T_i \frac{\partial R_i}{\partial T_i} \right) - p_c \frac{dV_c}{d\alpha} \quad (31)$$

$$V_c = \sum_{i=1}^N m_i \left[ \left( R_i + T_i \frac{\partial R_i}{\partial T_i} \right) \left( - \frac{\frac{\partial u_i}{\partial T_i} + R_i + T_i \frac{\partial R_i}{\partial T_i}}{p_c} + T_i \frac{\partial R_i}{\partial p_c} \right) + T_i \frac{\partial R_i}{\partial p_c} \right]$$

Equations (30) and (31) represent the general equations for the calculation of rate of change of zone temperature and of in-cylinder pressure assuming that all zones have the same pressure. In terms of definition of gas properties and composition (species transport), a two different approaches are available: *Classic Species Transport* and *General Species Transport*. Using the option of Classic Species Transport the mixture is considered as consisted of air, fuel vapor and combustion products. In the case of General Species Transport the mixture composition is described by an arbitrary number of species that is defined by user. The minimum number of species is 7: fuel, O<sub>2</sub>, N<sub>2</sub>, CO<sub>2</sub>, H<sub>2</sub>O, CO and H<sub>2</sub>. In this study the Classic Species Transport and two zone combustion model were used.